Structural Analysis of Protein Complexes

Dissertation

der Mathematisch-Naturwissenschaftlichen Fakultät

der Eberhard Karls Universität Tübingen

zur Erlangung des Grades eines

Doktors der Naturwissenschaften

(Dr. rer. nat.)

vorgelegt von

M. Sc. Natascha Bartlick

aus Reutlingen

Tübingen

2022

Gedruckt mit Genehmigung der Mathematisch-Naturwissenschaftlichen Fakultät der Eberhard Karls Universität Tübingen.

Tag der mündlichen Qualifikation:	30.01.2023
Dekan:	Prof. Dr. Thilo Stehle
1. Berichterstatter/-in:	Prof. Dr. Thilo Stehle
2. Berichterstatter/-in:	Prof. Dr. Frank Böckler

TABLE OF CONTENTS I

ABBREVIATIONS

Table 1: Abbreviations.

ApmTri	Aminoheptanedioic acid-ε-3-methyl-1,2,4-triazole
ArnA	Bifunctional polymyxin resistance protein ArnA
ASU	Asymmetric unit
αTAT	α-Tubulin N-acetyltransferase
AVP	Adenovirus encoded protease
BD	Bromodomain
BET	Bromodomain and extra-terminal domain
BETs	BET family BD containing proteins
BID	Basic residue-enriched interaction domain
BRDs	Bromodomain containing proteins
CAR	Coxsackievirus and adenovirus receptor
CBP	Cyclic adenosine monophosphate (cAMP) response element-binding protein (CREB) binding protein
CC	Coiled-coil
CCP	Complement control protein
CD	Circular dichroism
CDV	Cidofovir
CMC	Critical micelle concentration
Con A	Concanavalin A
COVID-19	Coronavirus disease 2019
CSPGs	Chondroitin sulfate proteoglycans
CTD	C-terminal domain
CV	Column volume
DDM	N-Dodecyl-β-D-maltopyranoside
DLS	Dynamic light scattering
DM	N-Decyl-β-D-maltopyranoside
dMiro	*Drosophila melanogaster* Miro
Drp1	Dynamin-1-like protein
DSG2	Desmoglein-2
ERMCS	ER-mitochondria contact sites
ERMES	ER-mitochondria encounter structure
ESI-MS	Electrospray ionisation mass spectrometry
FBS	Fetal bovine serum
FPLC	Fast protein liquid chromatography
GABA	γ-Aminobutyric acid
GMPPNP	Guanosine-5'-[(β,γ)-imido]triphosphate
GNAT	General control non-depressible 5 (GCN5)-related N-acetyltransferase
GST	Glutathione S-transferase
H	Histone
HAdV	Human adenovirus
HAdVG52-FK	Human adenovirus species G 52 fibre knob
HAP1	Huntington-associated protein 1
HATs	Histone acetyltransferases
HDAC6	Histone deacetylase 6
HDACs	Histone deacetylases
HGS	Hepatocycte growth factor-regulated tyrosine kinase substrate
HMT	Histone methyltransferase
HVR	Hyper variable regions
IEx	Ion exchange chromatography
IMAC	Immobilised metal affinity chromatography
IMS	Intermembrane space
ISWI	Imitation SWI
KAc	Lysine acetylation

Table 1, continued: Abbreviations.

KHC	Kinesin heavy chain
LRRK2	Leucine-rich repeat kinase 2
MAG	Myelin-associated glycoprotein
MBP	Maltose binding protein
MBS	Miro binding site
Mdm	Mitochondrial distribution and morphology protein
MFL	Nanobody identifier
Mfn	Mitofusin
MIB	Mitochondrial intermembrane space bridging complex
MICOS	Mitochondrial contact site and cristae organisation system
Mim	Mitochondrial import complex
MIM	Mitochondrial inner membrane
Mim1/2	Mitochondrial import protein 1/2
Miro	Mitochondrial Rho GTPase
MOI	Multiplicity of infection
MOM	Mitochondrial outer membrane
MST	Microscale thermophoresis
MWCO	Molecular weight cut-off
Myo19	Unconventional myosin 19
NAbs	Neutralising antibodies
NCS-1	Neuronal calcium sensor 1
NLS	Nuclear localisation sequence
NMC	NUT midline carcinoma
NPC	Nuclear pore complex
NTD	N-terminal domain
NUT	Nuclear protein in testis
OG	N-Octyl-β-D-glucopyranoside
OGT	*O*-linked β-N-acetylglucosamine (*O*-GlcNAc) transferase
PCAF	P300/CBP associated factor
PD	Parkinson's disease
PDB	Protein Data Bank
PINK1	Phosphatase and tensin homologue (PTEN)-induced putative kinase 1
pLDDT	Per-residue confidence score
PML	Promyelocytic leukemia
PVDF	Polyvinylidene difluoride
RhoA	Transforming protein RhoA
RMSD	Root-mean-square deviation
SAM	Sorting and assembly machinery
SARS-CoV-2	Severe acute respiratory syndrome coronavirus type 2
SEC	Size exclusion chromatography
SEC-SAXS	Size exclusion chromatography (SEC) small angle X-ray scattering
SIRT	Sirtuin deacetylases
SLS	Swiss Light Source
SP	Speckled protein
STP	Serine/threonine/proline-rich
SUMO	Small ubiquitin-related modifier
SWI/SNF	Switch/sucrose non-fermentable
TM	Transmembrane domain
TOM	Translocase of the outer membrane
Tom70	Mitochondrial import receptor subunit Tom70
TP	Terminal protein
TRAK	Trafficking kinesin-binding protein
TSA	Thermal shift assay
WD	Tryptophan-aspartic acid motif
XDS	X-ray detector software

ABSTRACTS

A. Mitochondria travel over long distances to their sites of function to meet local energy requirements and maintain calcium homeostasis. Alterations in mitochondrial distribution in neurons are closely linked to neurodegenerative diseases such as Parkinson's disease. Key regulators of mitochondrial trafficking are the calcium-sensing GTPase Miro and the motor adaptor protein TRAK, which couple mitochondria to the motor proteins. Despite increasing evidence for the role of Miro in many cellular processes including mitochondrial distribution, dynamics and turn-over, the underlying mechanistic details remain elusive. Understanding the conformational changes Miro might undergo upon calcium-binding, GTP hydrolysis or protein-protein interactions is the focus of this study. For this purpose, we established an expression and purification protocol for the two human Miro proteins, namely hMiro1 and hMiro2. hMiro1 was characterised in terms of stability, folding and for the first time regarding the GTPase activity in context of the full-length protein. Furthermore, we implemented the expression and purification of the hMiro1 binding site of hTRAK2, one of the two human TRAK proteins. We were able to form a complex between hMiro1 and hTRAK2 demonstrating that recombinant hMiro1 is functional. The hMiro1 purified in this study has been used by Funmi Fagbadebo (group of Prof. Rothbauer, Pharmaceutical Biotechnology, University of Tübingen) to immunise alpacas and to select, enrich and characterise hMiro1-specific nanobodies obtained from corresponding blood samples. The established protocol is applicable to Parkinon's disease-derived mutations of hMiro1 thus enabling important future research. Taken together, this project provides a platform for the investigation of the structure-function relationship of hMiro1 and its interacting partners.

B. Bromodomains (BD) are unique structural modules that specifically recognise N-ε-lysine acetylation motifs. BD-containing proteins of the Bromodomain and Extra-Terminal domain (BET) family share a common domain architecture comprising two structurally conserved BDs. They serve as transcriptional regulators and epigenetic markers by association with acetylated histones throughout the cell cycle. Malfunction of BET proteins has been linked to a broad spectrum of diseases. BRD4, a member of this protein family, has been shown to be responsible for the regulation of growth-promoting genes in chronic lymphocytic leukaemia and has been identified as component of chromosomal translocation in nuclear protein in testis midline carcinoma. Despite the importance of studying these proteins, one major obstacle remains the deacetylation of BD targets in *in vivo* experiments. In 2010 *Filippakopoulos et al.* published a BET family specific, cell-permeable small molecule BD inhibitor, called JQ1, based on which Sören Kirchgäßner (group of Prof. Schwarzer, Interfaculty Institute of Biochemistry, University of Tübingen) designed the acetyl lysine mimicking artificial amino acid ApmTri used in this study. Affinity measurements and crystallisation experiments showed that BET BDs bind peptides comprising ApmTri with comparable affinity, high specificity and in a similar structural fashion compared to peptide substrates comprising acetyl lysine. We thereby introduce a new and versatile tool for the utmost important *in vivo* research on BD-containing proteins. We have built a solid foundation for the future

design of peptide-based co-inhibitors, capable of inhibiting both BDs of BET family proteins at once, thus increasing the affinity and selectivity of the inhibitors.

C. Human adenoviruses (HAdV) are the cause for many respiratory, ocular and gastrointestinal diseases. They shield their double-stranded DNA core with an icosahedral capsid formed by three major proteins, the hexon, the fibre and the penton base. For virus entry, the major capsid proteins need to interact with host cell receptors to trigger virus internalisation. While the fibre knob is well-established as the interaction partner for primary receptors and the penton base is known to engage with integrins, recent data suggest a role for the hexon protein in receptor interaction. Based on infection data the interaction between the complement regulatory protein CD46 and the HAdV-D species was established, but additional research will be required to assess if the hexon is responsible for the interaction beyond the two genotypes that were investigated, HAdV-D56 and HAdV-D26. In order to elucidate which epitopes in the hyper variable region of the trimeric hexon protein engage in CD46 binding, we aim to obtain structural data on HAdV D-type hexons in complex with CD46. For this purpose, we established complex formation with five different D-species hexons and optimised the hexon to receptor ratio to improve sample quality. Initial negative staining images of the HAdV receptor complex highlight the quality of the hexon sample and reveal the prevalent hexon orientation for each genotype. With these experiments we have laid the foundations for subsequent cryoEM experiments. The soon to be obtained structures will broaden our understanding of HAdV receptor interaction and help elucidating the potential of new HAdV genotypes as vaccine vectors.

ZUSAMMENFASSUNGEN

A. Mitochondrien legen weite Distanzen zu ihren Zielorten zurück um den lokalen Energiebedarf zu decken und die Kalzium Homöostase aufrecht zu erhalten. In Neuronen werden Veränderungen in der Verteilung der Mitochondrien mit Neurodegenerativen Erkrankungen wie beispielsweise Parkinson in Verbindung gebracht. Die Kalzium-bindende GTPase Miro und das Motoradaptorprotein TRAK sind zentrale Regulatoren des mitochondrialen Transports und verbinden Mitochondrien mit den Motorproteinen. Obwohl es eine stetig wachsende Anzahl an Hinweisen für die Aufgaben von Miro in vielen verschiedenen zellulären Prozessen gibt, unter anderem in dem Transport, der Dynamik und der Erneuerung von Mitochondrien, bleiben die zugrundeliegenden mechanistischen Prozesse unentdeckt. Der Fokus dieser Studie liegt auf dem Verstehen der Konformationsänderungen die Miro während der Bindung an Kalzium, der GTP Hydrolyse oder der Interaktion mit anderen Proteinen durchläuft. Zu diesem Zweck haben wir ein Expressions- und Reinigungsprotokoll für die zwei humanen Miro Proteine, hMiro1 und hMiro2, etabliert. Die Stabilität und Faltung von hMiro1 wurde charakterisiert und zum ersten Mal wurde die Aktivität der GTPase im Kontext des Volllängenproteins analysiert. Darüber hinaus haben wir die Reinigung und Expression der hMiro1 Bindestelle von hTRAK2 etabliert. Wir konnten einen Komplex aus hMiro1 und hTRAK2 bilden und somit die Funktionalität von rekombinantem hMiro1 nachweisen. Das in dieser Studie gereinigte hMiro1 wurde von Funmi Fagbadebo (Gruppe von Prof. Rothbauer, Pharmazeutische Biotechnologie, Universität Tübingen) für die Immunisierung von Alpakas verwendet, um hMiro1 spezifische Nanobodys aus entsprechenden Blutproben zu selektieren, anzureichern und zu charakterisieren. Das etablierte Protokoll zur Reinigung von hMiro1 kann auf Parkinson spezifische Mutanten von hMiro1 angewendet werden und ermöglicht dadurch wichtige zukünftige Forschung. Zusammengefasst ermöglicht dieses Projekt weitere Untersuchungen der Zusammenhänge zwischen der Struktur und der Funktionen von hMiro und seiner Interaktionspartner.

B. Bromodomänen sind einzigartige strukturelle Module die gezielt N-ε-Lysin Acetylierungsmotive erkennen. Bromodomänen-enthaltende Proteine der Bromodomänen und Extra-Terminalen Domänen (BET) Familie haben einen gemeinsamen Domänenaufbau der zwei strukturell konservierte Bromodomänen umfasst. Durch ihre Assoziation mit acetylierten Histonen im Verlauf des Zellzykluses, dienen sie als Transkriptionsregulatoren und epigenetische Marker. BET Proteine mit Fehlfunktionen wurden mit einem breiten Spektrum an Krankheiten in Verbindung gebracht. Es wurde gezeigt, dass BRD4, ein Mitglied dieser Protein Familie, verantwortlich ist für die Regulation von Wachstumsfördernden Genen in Altersleukämie und BRD4 wurde darüber hinaus als Komponente der chromosomalen Translokation in NUT (Nukleares Protein im Hoden)-Mittellinienkarzinomen identifiziert. Obwohl das Studieren dieser Proteine von höchster Wichtigkeit ist, bleibt ein wesentliches Hindernis die Deacetylierung von Bromodomänen Substraten während *in vivo* Experimenten. Bereits 2010, publizierten *Filippakopoulos et al.* den BET Familien-spezifischen, Zell-durchdringenden

niedermolekularen Bromodomänen Inhibitor JQ1. Basierend auf diesem Inhibitor hat Sören Kirchgäßner (Gruppe von Prof. Schwarzer, Interfakultäres Institute für Biochemie, Universität Tübingen) die, in dieser Studie verwendete, artifizielle Acetlylysin-imitierende Aminosäure, genannt ApmTri, designt. Affinitätsmessungen und Kristallisationsexperimente haben gezeigt, dass BET Bromodomänen ApmTri-enthaltende Peptide mit vergleichbarer Affinität, hoher Spezifität und auf vergleichbare strukturelle Weise binden wie Acetyllysine-enthaltende Peptide. ApmTri stellt ein neues, vielseitiges Werkzeug für die dringende und wichtige *in vivo* Forschung an Bromodomänen-enthaltenden Proteinen dar. Wir haben damit eine solide Basis für das Design von zukünftigen Peptid-basierten Co-Inhibitoren geschaffen, die in der Lage sind beide Bromodomänen der BET Family zeitgleich zu inhibieren und dadurch die Affinität und Selektivität der Inhibitoren erhöhen.

C. Humane Adenoviren (HAdV) sind die Ursache für viele Darm-, Augen- und Atemwegserkrankungen. Sie schützen ihre doppelsträngige DNA durch ein icosaedrisches Kapsid das aus drei Hauptproteinen, dem Hexon, dem Fiber Protein und der Penton Basis, aufgebaut ist. Für den Eintritt des Virus in die Zielzelle müssen die Hauptkapsidproteine mit den Rezeptoren auf der Zelloberfläche interagieren um die Internalisierung des Virus auszulösen. Im Gegensatz zu der etablierten Interaktion zwischen dem Fiber Knob und primären Rezeptoren oder der Penton Basis die mit Integrin Rezeptoren interagiert, wurde die Rolle des Hexon Proteins in der Interaktion mit Rezeptoren erst kürzlich entdeckt. Basierend auf Infektionsdaten wurde die Interaktion mit CD46, einem Komplementsystem-regulierenden Protein, und der HAdV D-Spezies etabliert. Zukünftige Forschung wird zeigen ob das Hexon auch in anderen HAdV Genotypen außer den beiden untersuchten Genotypen HAdV-D56 und HAdV-D26 eine tragende Rolle für die Interaktion spielt. Welche Bindeepitope in den hypervariablen Regionen des trimeren Hexonproteins für die Interaktion mit CD46 verantwortlich sind, möchten wir mit strukturellen Daten verschiedener HAdV D-Typ Hexone in Komplex mit CD46 aufklären. Zu diesem Zweck haben wir die Komplexbildung mit fünf verschiedenen D-Typ Hexonen etabliert und das Verhältnis von Hexon zu Rezeptor für eine optimale Probenqualität verbessert. Initiale Kontrastelektronenmikroskopie Bilder des HAdV Rezeptor Komplexes zeigen die hohe Qualität der Hexonprobe und offenbaren die vorherrschende Orientierung des Hexons für den jeweiligen Genotyp. Mit diesen Experimenten haben wir eine solide Basis für nachfolgende cryo-Elektronenmikroskopie Experimente geschaffen. Auf dieser Grundlage erlangte Strukturen werden unser Verständnis für HAdV Rezeptor Interaktionen erweitern und mithelfen das Potential von neunen HAdV Genotypen als Impfstoffvektoren einzuschätzen.

A. Structure-function analysis of the human mitochondrial GTPase Miro and its interacting partners

A.1 INTRODUCTION

Mitochondria are central organelles that regulate cellular functions by providing adenosine triphosphate (ATP) and buffering calcium. In addition, mitochondria have an important role in cellular lipid homeostasis as they take part in the synthesis of membrane phospholipids, steroids and terpenes [1]. Moreover, mitochondria coordinate apoptotic signalling as their surface serves as meeting platform for antiapoptotic and proapoptotic proteins [2]. The spatial separation of apoptotic activators and their targets inside mitochondria prevents apoptosis in healthy cells. During their life cycle, mitochondria are dynamic as they frequently undergo fission, fusion and changes in morphology in order to maintain their shape, distribution and size [3]–[5]. Throughout these processes, the inner organisation of mitochondria comprising the mitochondrial outer membrane (MOM), the intermembrane space (IMS), the mitochondrial inner membrane (MIM) and the mitochondrial matrix has to remain intact [6], [7]. Due to their functional importance it is crucial that mitochondria are transported to their target sites. Cells with high energy metabolism including neurons and muscle cells display a higher mitochondrial content and enhanced mitochondrial activity and biogenesis [8], [9]. In such polarised cells, mitochondria need to travel over long distances to reach their site of function and they are required to be healthy and functional upon arrival [10]. The diversity of polarised cells requires individually adapted mitochondrial trafficking, one example being the different organisation of mitochondrial transport in dendrites and axons of neurons, adjusting to the directionality of the transport [11]. Mitochondrial transport in neurons is mostly organised along microtubules. In vertebrates, microtubules in axons and distal dendrites have a preferential plus-end-out orientation [12], [13] while proximal dendrites display mixed orientations of microtubules [14]. In contrast, in invertebrates, dendritic microtubules are oriented exclusively minus-end-out [15]. Mitochondrial transportation accommodates to the individual requirements with several modes of transportation and a wide-spread regulatory network. Mitochondrial dysfunction and deficiencies in mitochondrial motility have implications in neurodegenerative disorders such as Parkinson's disease (PD) [16]–[18].

A.1.1 Mitochondrial transport

In neurons, about half of the mitochondria are stationary, and the mean transport velocity of moving mitochondria lies within the range of 0.1-2.0 µm/s [19]–[21]. About 30% of axonal mitochondria are mobile at resting conditions with a similar velocity and motility in anterograde and retrograde direction [21]. Cytosolic calcium levels regulate mitochondrial motility [22], which decreases at elevated calcium levels and increases in the absence of cytosolic calcium [23], [24]. The long-distance bi-directional transport of mitochondria is organised along microtubules [11] and requires the interplay of the motor

protein kinesin and the dynein motor complex (Fig. A.1) [25]. In axons, kinesin-1 and dynein cooperate to achieve bi-directional mitochondrial movement. In contrast, in dendrites, bi-directional motility depends solely on dynein [25]. Mitochondria can be additionally transported along actin filaments by the myosin 19 (Myo19) motor protein, highlighting the versatility of mitochondrial trafficking [26]–[28].

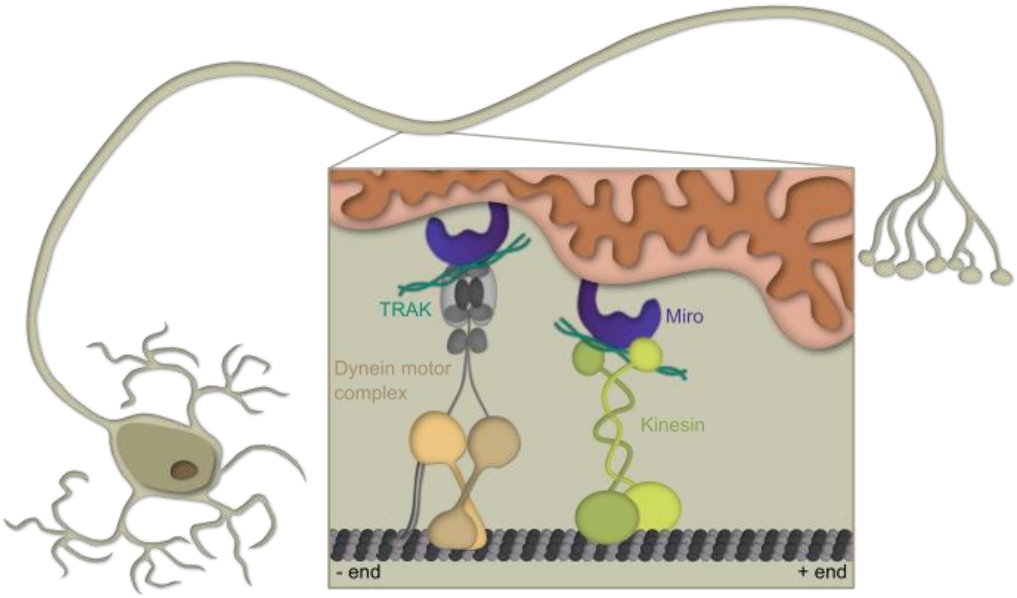

Figure A.1: Mitochondrial trafficking along microtubules in neurons. Long-distance transport in neurons is organised along microtubules and facilitated by the motor proteins kinesin and dynein. Microtubules in axons have a preferred plus-end-out orientation, therefore, kinesin is the key motor for anterograde transport from the cell body towards the synapse. The dynein motor complex is not only responsible for retrograde transport of mitochondria in axons but is predominantly responsible for mitochondrial motility in dendrites.

Key players of mitochondrial trafficking on the mitochondrial surface are the mitochondrial Rho guanosine triphosphate (GTP) hydrolase (GTPase) (Miro) [21], [29], [30], an abundant mitochondrial receptor protein, and the trafficking kinesin-binding protein (TRAK) (Fig. A.1) [31], [32]. hMiro directly interacts with kinesin-1 in the absence of calcium, independent of the presence of hTRAK [29]. If mitochondrial arrest is achieved by 1) kinesin-1 uncoupling from hMiro upon calcium binding [29], 2) kinesin-1 dissociating from microtubules upon calcium binding by hMiro [21] or if 3) docking of the mitochondrial through syntaphilin (SNPH) [33] is required, needs to be clarified. Moreover, hMiro acts as receptor for Myo19 thus enabling mitochondrial trafficking along actin filaments [27], [28], [34]. hTRAK interacts not only with hMiro but additionally binds to the cargo binding domain of kinesin-1 heavy chain [31], [32], [35]. Experiments in *Drosophila melanogaster* have shown that TRAK and the kinesin light chain might bind the kinesin heavy chain (KHC) competitively [36]. In addition, hTRAK interacts with the dynein motor complex for retrograde transport of mitochondria [25]. In hMiro knockout cells, hTRAK remains associated to mitochondria [28] and although fast long-ranged mitochondrial transport is inhibited, mitochondria are distributed in axons [28], [37], indicating the presence of additional hTRAK receptors on the mitochondrial surface [38], [39].

A.1.2 Human mitochondrial Rho GTPase Miro

Two human Miro proteins, hMiro1 and hMiro2, were identified as GTPases from the public deoxyribonucleic acid (DNA) sequence database of the human genome projects [30]. The two proteins share about 61% sequence identity. Although originally classified as members of the Rho family of GTPases [30], the structures of the GTPase domains of hMiro [40], [41] display a number of divergences, most notably the lack of the conserved 13 amino acid rho-helix [30], [41]–[43]. Due to the characteristic features of the Miro GTPases and the unique overall domain organisation, the Miro proteins are now considered to be members of their own protein family. Miro comprises N-terminal and C-terminal GTPase domains, (nGTPase and cGTPase, respectively) that flank two calcium-binding EF hand domains, and a C-terminal membrane anchor (Fig. A.2, A) [30]. Klosowiak et al. [40] introduced a shortend nomenclature for the hMiro domains labelling the nGTPase as A, the EF hand domains as B_1 and B_2, respectively, the cGTPase as C and the transmembrane domain as D (Fig. A.2, A).

The GTPases of hMiro1 and the cGTPase of hMiro2 share a common fold that is typical for GTPases and comprises five distinct motifs: The P-loop motif engages with the phosphate groups of bound GTP, the Switch 1 and Switch 2 motifs that are displaced upon GTP hydrolysis, the G4 motif that mediates interactions with the guanine base and the G5 motif that stabilises the exocyclic oxygen of GTP [40]. The nGTPase of hMiro1 shares only 22% sequence identity with the cGTPase with an overall Root-mean-square deviation (RMSD) of 3.88 Å, indicating that the GTPase domains of Miro might be mechanistically distinct (Fig. A.2, E) [41]. The cGTPase of hMiro has been previously predicted to be catalytically inactive, but a recent study with recombinant protein identified the cGTPase of hMiro as nucleotide triphosphate (NTP) hydrolase [44]. The EF hand domains (EF1/EF2) of hMiro1 each comprise a canonical EF hand (EFH1/EFH2) as well as a non-canonical hidden EF hand (LM-EFH1/LM-EFH2). The EF hands each consist of a canonical helix-loop-helix motif. While the canonical EF hands engage in calcium binding, the hidden EF hands stabilise EFH1 and EFH2 with their antiparallel β-scaffold (Fig. A.2, B) [45]. The hidden EF hands each comprise an additional helix that has been termed ligand-mimicking helix (LM) based on a structural comparison with the EF hand domains of the neuronal calcium sensor 1 (NCS-1) [45]. In NCS-1, a C-terminal loop segments folds into a caviety formed by the EF hand domains mimicking a ligand in the absence of an interaction partner [46]. The calcium binding EF hands of hMiro carry canonical calcium binding loops that coordinate calcium in a pentagonal bipyramidal fashion (Fig. A.2, D). The aspartic acid in the Y and Z position, the backbone oxygen interaction in the -Y position and the glutamic acid contributing two oxygens in the -Z position form the corners of the pentagonal plane. An aspartic acid sits in the X position above the pentagonal plane and a water molecule is coordinated in the -X position below in both EFH1 and EFH2 in the structure of calcium bound hMiro1[40]. Although calcium-binding by Miro has been demonstrated [29], [47] the structural data does not explain underlying conformational changes in response to ligand binding. The human Miro proteins are C-terminally anchored to the MOM via an α-helical single transmembrane domain [30], [48].

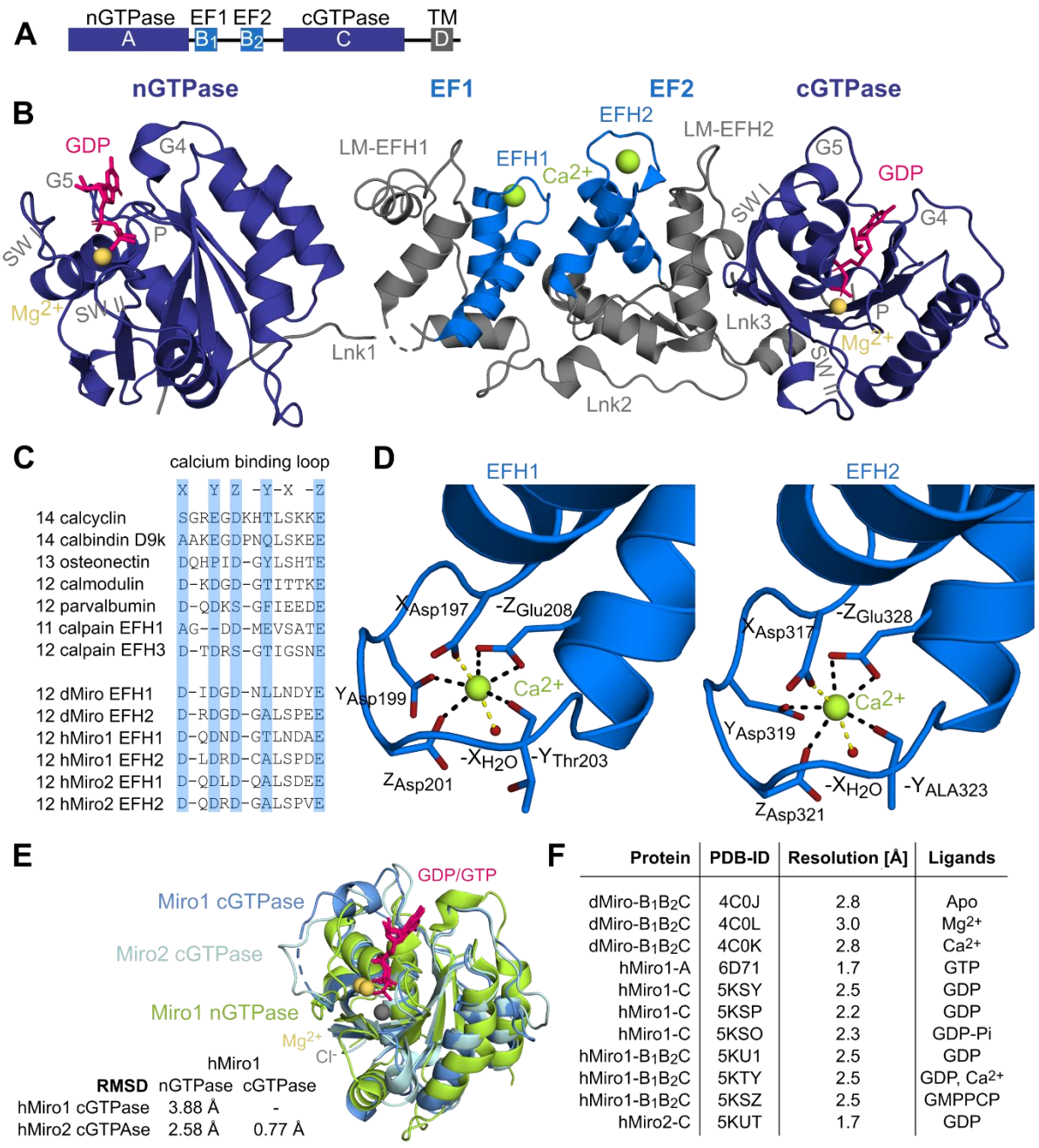

Figure A.2: The human mitochondrial GTPase Miro. (**A**) Domain organisation of the human Miro proteins. The two GTPase domains (dark blue) corner the EF hand domains (blue) and the α-helical transmembrane anchor (grey) is located at the C-terminus. The nomenclature of the hMiro domains reads as follows starting from the N-terminus: A for the nGTPase, B_1 and B_2 for the EF hand domains, C for the cGTPase and D for the transmembrane helix. (**B**) Cartoon representation of the hMiro1 structures of the nGTPase (PDB-ID: 6D71) and the EF hand domains (EF1/EF2) with the cGTPase (PDB-ID: 5KTY) in the GDP-bound state. The canonical calcium binding EF hands (EFH1/2) are highlighted in light blue. GTPase specific motifs and the hidden ligand mimicking EF hands (LM-EFH1/2) are indicated. Lnk = linker, SWI/II = Switch I/II, P = P-loop. (**C**) Alignment of the calcium binding motifs of hMiro1/2 and dMiro with other typical GTPases. Residues engaging in the interaction with the calcium ion are highlighted in light blue. (**D**) Structure of the calcium binding canonical EF hands (blue) (PDB-ID: 5KTY) displaying the helix-loop-helix motif with loop residues interacting with the calcium ion (lime green). The pentagonal bipyramidal coordination of the calcium with the respective conserved positions is indicated. (**E**) Structural alignment and RMSD calculation of the hMiro1 cGTPase (light blue) and nGTPAse (lime green) (PDB-ID: 6D71, 5KSP) and the hMiro2 cGTPase (cyan) (PDB-ID: 5KUT). (**F**) List of the available human and *Drosophila melanogaster* Miro structures and the corresponding Protein Data Bank (PDB) accession codes.

Orthologues of Miro can be found in eukaryotic organisms, including *Saccharomyces cerevisiae*, were Miro is called Gem1p, *Schizosaccharomyces pombe*, *Caenorhabditis elegans*, *Arabidopsis thaliana*, *Drosophila melanogaster* (dMiro) and *Mus musculus* [30]. Several isoforms of hMiro1 and hMiro2 are produced by alternative splicing of the C-terminus, most of them maintaining the transmembrane anchor. The physiological significance of the individual isoforms of hMiro is yet to be determined. hMiro1 and hMiro2 are both abundantly expressed in all tissues. Mouse knockout (KO) studies revealed, that while $Miro2^{KO}$ could be compensated by Miro1, the function of Miro1 in late development is critical and cannot be compensated by Miro2 in $Miro1^{KO}$ embryos [28].

The high-resolution structural data on the Miro proteins are to date limited to apo, magnesium or calcium bound structures of dMiro comprising the cGTPase and both EF hand domains [45] and similar guanosine diphosphate (GDP), Guanosine-5'-[(β,γ)-methyleno]triphosphate (GMPPCP) or GDP and calcium-bound structures of hMiro1 [40]. In addition, a GTP-bound structure of the nGTPase of hMiro1 [41] and GDP-bound structures of the cGTPase of hMiro1 and hMiro2 [40] have been solved (Fig. A.2, F). Taken together, the structural data reveal how GTP and calcium binding is organised within the Miro proteins. Additional size exclusion chromatography (SEC) small angle X-ray scattering (SEC-SAXS) experiments reveal that in solution the conformation of hMiro1 is bent between the nGTPase and the first EF hand domain [41]. The organisation of the hMiro proteins on the mitochondrial surface has to be determined. Recent super resolution microscopy experiments indicate that hMiro1 and hMiro2 might engage in a macromolecular complex forming protein interaction platforms with a median diameter of 100 nm [49].

A.1.3 Human Trafficking kinesin-binding protein

Mammals possess two distinct TRAK proteins, namely TRAK1 and TRAK2 [50], [51]. In 2002, TRAK2 from rat was identified in a yeast two-hybrid screen with the γ-Aminobutyric acid $(GABA)_A$ receptor β2-IL during a search for interaction partners of the receptor [52]. Therefore, TRAK2 was originally named $GABA_A$ receptor interacting factor 1 (GRIF-1) [52]. The two human TRAK proteins were found in the same year in a yeast two-hybrid screen for interaction partners of the β-*O*-linked *N*-acetylglucosamine (*O*-GlcNAc) transferase (OGT) and due to their direct interaction they were named OGT interacting protein 98 (OIP98, TRAK2) and OIP106 (TRAK1), respectively [51], [53]. In *Drosophila melanogaster* only one TRAK protein, called Milton is present that was identified in 2002 as an important component of the mitochondrial transport systems in *Drosophila* neurons and likely interaction partner of KHC [50]. Based on these experiments, an additional study in 2005 revealed that the human TRAK proteins engage in an interaction with KHC similar to Milton [31].

The TRAK proteins are less conserved in sequence compared to Miro (Fig. A.3, C). Nevertheless, they share a common N-terminal Huntington-associated protein 1 (HAP1)-like coiled-coil domain whereas the C-terminal part of the TRAK proteins is more divergent and engages in protein-protein interactions (Fig. A.3, A). However, most of the protein interaction sites on TRAK are not well defined. While the

TRAK proteins likely interact with KHC via the N-terminal part of the protein [36], a recent study revealed that the C-terminal region of TRAK1 (amino acids (AA) 636-953) is sufficient for the association with microtubules [35]. The hTRAK proteins have been shown to play distinct roles in the directionality of mitochondrial transport by their interaction with kinesin-1 and the dynein motor complex [25]. However, how exactly hTRAK1/2 interact with dynein remains elusive.

Milton has been shown to associate with mitochondria independent of Miro via the C-terminal part of the protein (AA 847-1116) [36], indicating the presence of a potential MOM affine domain in the C-terminal part of Milton. In hMiro1/2 knockout cells, hTRAK1/2 and their associated motor proteins are able to associate with mitochondria [28], suggesting an additional Miro independent MOM anchoring mechanism. Moreover, co-expression of hTRAK1/2 with KHC is sufficient for mitochondrial transport [28], hinting towards the existence of additional hTRAK1/2 receptors on the MOM. One possible hTRAK1/2 receptor would be mitofusin 1/2 (Mfn1 and Mfn2, respectively) that interact with hMiro1/2 and hTRAK1/2 [38], [39].

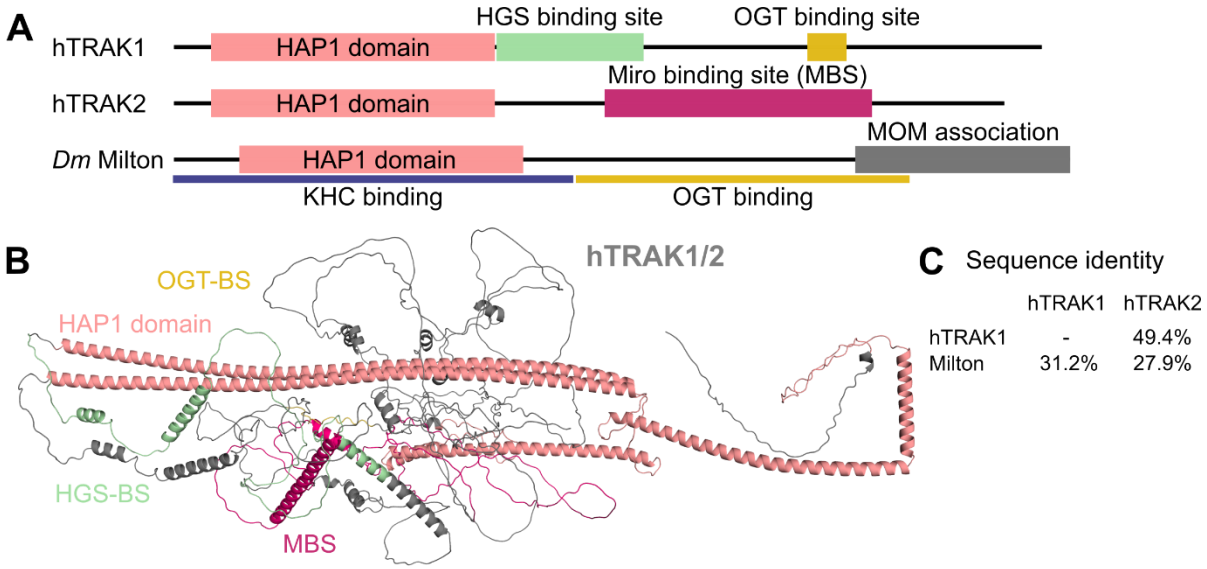

Figure A.3: Trafficking kinesin-binding proteins. (**A**) Domain organisation of the human TRAK proteins and the *Drosophila melanogaster* TRAK protein, called Milton. Protein regions which are sufficient for the binding to interaction partners are only poorly defined by experiments. HAP1 domain (salmon), Hepatocyte growth factor-regulated tyrosine kinase substrate (HGS) binding site (mint green), OGT binding site (yellow), Miro binding site (MBS) (pink) and KHC binding site (dark blue). (**B**) Alphafold [54], [55] structure prediction models of hTRAK1 and hTRAK2. Only the conserved coiled-coil HAP1 domain (salmon) aligns well. The C-terminal protein interaction domains are mostly unstructured and might only become fully folded upon binding to the corresponding interaction partner. The Miro1 binding site (pink) of hTRAK2 is predicted as mostly unstructured and has to date not been defined well. (**C**) Sequence identity of the hTRAK proteins and Milton based on a whole sequence alignment.

Recently reported structure predictions of hTRAK1/2 (Fig. A.3, B) in the Alphafold Protein Structure Database [54], [55] suggest that the N-terminal coiled coil domain of hTRAK1/2 is the only intrinsically ordered part of the protein. Large stretches of the protein are predicted to be unstructured and might only be able to fold into a three-dimensional structure upon interaction with one or more interaction partners. The interaction between the human Miro proteins and hTRAK1/2 is well established [21], [56]. The

hMiro1 binding site of hTRAK2 is located within a C-terminal section of hTRAK2 comprising amino acid 476-700, referred to as MBS [57], whereas the nGTPase of hMiro1 is sufficient for the binding to hTRAK2 [56]. The Miro and TRAK proteins cooperate to coordinate mitochondrial transport, however, they also form the bridge between mitochondrial trafficking, mitochondrial dynamics and the communication with the endoplasmic reticulum (ER).

A.1.4 The concerted transport of MIM and MOM

The MIM and the MOM are connected by the mitochondrial contact site and cristae organising system (MICOS) on the MIM and the sorting and assembly machinery (SAM) on the MOM [58]–[62]. The MICOS complex is required for maintenance of the cristae organisation and mitochondrial metabolism [59] whereas the SAM complex mediates the assembly of β-barrel proteins in the MOM [63], [64]. hMiro1/2 co-purifies with components of the mitochondrial intermembrane space bridging complex (MIB) comprising MICOS and SAM and super resolution microscopy revealed the association of hMiro macromolecular complexes on the MOM surface with MICOS nanoclusters [49]. Knockout of both hMiro proteins disrupts the mitochondrial cristae organisation and Miro-depleted mitochondria show a reduction of MICOS clusters on the MOM during transport [49]. The results of this study suggest a role for Miro in coordinating the concerted transport of both mitochondrial membranes in order to maintain the internal mitochondrial organisation during long-distance transport.

A.1.5 Mitochondrial transport is regulated by the acetylation of Miro

Histone deacetylase 6 (HDAC6) has been identified as α-tubulin deacetylase [65] that operates beyond its nuclear functions by shuttling to the cytoplasm [66], [67]. Inhibition of HDAC6 increases α-tubulin acetylation leading to the formation of stabilised microtubules (Fig. A.4) which has been shown to be important for axon regeneration in injured spinal cords [68]. In contrast, the central nervous system growth inhibitors myelin-associated glycoprotein (MAG) and chondroitin sulfate proteoglycans (CSPGs) decrease the stability of the α-tubulin N-acetyltransferase (αTAT) thus decreasing α-tubulin acetylation [69]. Recent research established a connection between the inhibition of αTAT and the activation of HDAC6 through MAG and CSPGs initiated transforming protein RhoA (RhoA) signalling [70]. RhoA activation increases cytoplasmic calcium levels, which leads to the calcium-dependent activation of HDAC6 [71]. As a result, α-tubulin is deacetylated by HDAC6 [72] and further acetylation is inhibited.

The mammalian Miro proteins undergo posttranslational modifications (PTMs) at different positions (Fig. A.5, A). Acetylation can occur at three distinct sites (Fig. A.5, A): Within the nGTPAse (K92), the cGTPase (K512) and near the transmembrane domain (K616) [73], [74]. Rat Miro1 has been identified as a substrate of the deacetylase HDAC6 (Fig. A.4) [71]. Deacetylation of Miro1 at K92 decreases

mitochondrial membrane potential and transport in axons. Moreover, the acetyl-mimetic mutation of Miro K92Q prevents calcium-dependent mitochondrial arrest [71], suggesting a role of Miro acetylation in altering the calcium sensitivity of the protein. The mechanisms controlling Miro acetylation and how the calcium sensitivity of Miro is affected by the K92 acetylation remain to be determined.

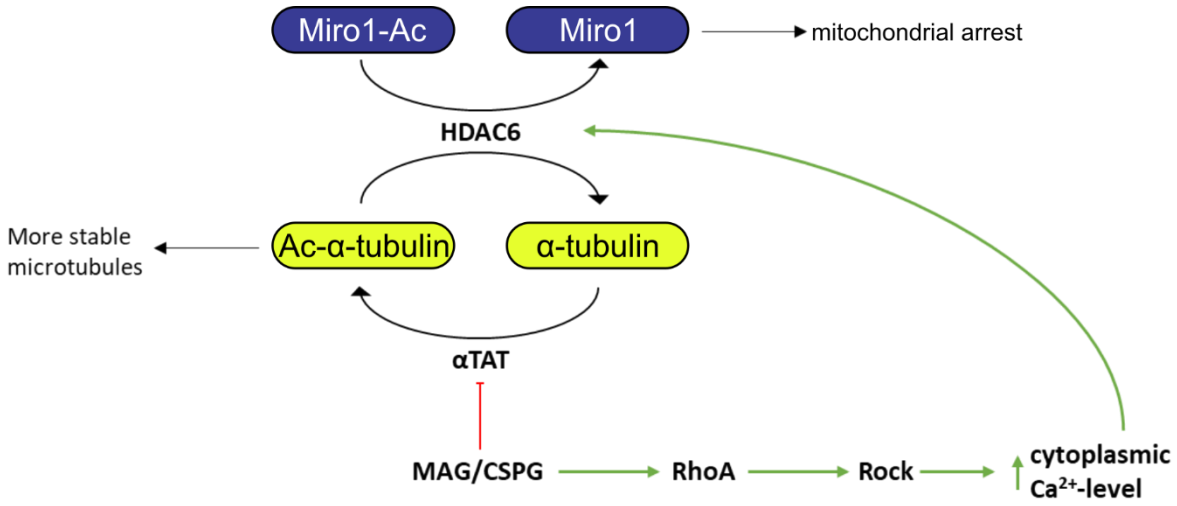

Figure A.4: Regulation of actin depolymerisation in axons. αTAT is responsible for the acetylation of α-tubulin which leads to the generation of microtubules with increased stability. MAG and CSPGs inhibit αTAT and activate the α-tubulin deacetylase HDAC6 through RhoA signalling. Activated HDAC6 additionally deacetylates Miro1 which leads to mitochondrial arrest. Rock = Rho-associated protein kinase.

A.1.6 Peroxisomal trafficking is mediated by Miro and TRAK

Peroxisomes are small organelles that carry high concentrations of metabolic enzymes which are important for many cellular functions such as beta oxidation, the neutralisation of reactive oxygen species, bile acid synthesis or maintaining the redox equilibrium [75]. Similar to mitochondria, they need to be transported towards their site of function. A Miro1 splice variant comprising an additional C-terminal insertion [76] between the cGTPase and the transmembrane domain localises to peroxisomes with the help of a cytosolic peroxin (Pex19p) receptor [77], [78]. Peroxisomal transport is dependent on the function of the hMiro1 nGTPase, as peroxisomes are not targeted to the cell periphery in the presence of a dominant-negative mutant of the nGTPase but are instead scattered throughout the cytoplasm [78]. While retrograde transport of peroxisomes along microtubules is organised similarly to mitochondrial transport via hTRAK1/2 and the dynein motor complex [25], anterograde transport utilises hMiro, kinesin 14B and peroxisome biogenesis factor 1 (Pex1) [79]. Further studies are needed to elucidate whether peroxisomal trafficking depends on calcium-sensing by Miro, similar to mitochondrial arrest occurring at elevated calcium levels.

A.1.7 hMiro in mitochondrial fission and fusion

hMiro's functions are not strictly limited to trafficking, but extended to other aspects of mitochondrial dynamics, including fission and fusion. Mitochondria constantly undergo fission and fusion thereby changing their morphology to adapt to the cellular environment. Mitochondrial fission plays a central role in the distribution of mitochondria during cell division and the removal of damaged parts of the mitochondrial network during heightened cellular stress [80]. Fusion is critical in embryonic development and at later developmental stages allowing cells to adapt to higher demands of oxidative metabolism [81], [82]. While deletion of Gem1p, the yeast Miro, only affects the mitochondrial morphology without interfering with fission and fusion processes [83], Miro in higher eukaryotes is directly contributing to fission and fusion. The depletion of dMiro or hMiro1/2 considerably alters mitochondrial morphology [28], [84] dependent on hMiro calcium binding [48] and the nucleotide state of the nGTPase of Miro [30], [56]. Moreover, the Miro proteins directly influence mitochondrial and peroxisomal fission by inhibiting the recruitment of the dynamin-1-like protein (Drp1), the master regulator of mitochondrial fission, by the mitochondrial fission protein 1 (Fis1) receptor [48], [85]. The role of Miro in mitochondrial fusion is less explored, however, the close linkage of the Miro-TRAK complex to the mitochondrial fusion proteins Mfn1/2 [38], [39] prompts towards a potential connection. Notably, hTRAK1 has been demonstrated to influence mitochondrial fragmentation in Hela cells [39]. Moreover, hTRAK1 co-localises with Mfn1/2 but not Drp1 on the MOM indicating the linkage with mitochondrial fusion rather than fission. Although there is evidence for a role of the Miro-TRAK complex in the control of mitochondrial morphology, it is not clear how mitochondrial dynamics and trafficking are connected by these proteins.

A.1.8 hMiro at ER-mitochondria contact sites

Calcium and phospholipid exchange between mitochondria and the ER occur at ER-mitochondria contact sites (ERMCS) [86]. The physical bridge between the ER and mitochondria is formed by a multitude of proteins [87]. While the composition of the contact sites in yeast, called ER-mitochondria encounter structure (ERMES) is well established [88], fewer details are known for the ERMCS in mammals. In yeast, the ER anchored Maintenance of mitochondrial morphology protein 1 (Mmm1) forms a complex with the Mitochondrial distribution and morphology protein 12 (Mdm12) and Mdm34 which are engaging in the interaction with the MOM tether β-barrel protein Mdm10 [89]. Gem1p, the yeast orthologue of Miro regulates formation of the ERMES complex and the regulation depends on the functionality of the GTPase domains of Gem1p [83], [90], [91]. Furthermore, a calcium-binding deficient mutation of the EFH1 of Gem1p reduces localisation to the ERMES complex and ERMES formation, similarly to inactive or GTP-binding deficient nGTPase mutants [47], [90]. Likewise, mammalian Miro plays a critical role in the formation and functionality of ERMCS. Double knockout of hMiro1 and hMiro2 significantly reduces ER-mitochondria contacts [49]. Moreover, Miro interacts

with the ERMCS proteins Mfn2 and Disrupted in schizophrenia protein 1 (DISC1) [38], [92]–[94], thus establishing a link between the concerted transport of the mitochondrial membranes through MIB and the regulation of the ERMCS formation.

A.1.9 The role of hMiro in PINK1/Parkin mediated mitophagy

Damaged and dysfunctional mitochondria are cleared from cells in a process called mitophagy [95], [96]. The Phosphatase and tensin homologue (PTEN)-induced putative kinase 1 (PINK1)-Parkin pathway (Fig. A.5, B) initiates ubiquitin-dependent mitophagy of depolarised mitochondria [97].

In healthy mitochondria, PINK1 gets imported into the mitochondrial matrix through the Translocase of the outer membrane (TOM) complex [98] and cleaved by the Presenilins-associated rhomboid-like protein (PARL) [99]. In contrast, in depolarised mitochondria, PINK1 interacts with the TOM complex, is stabilised on the MOM and dimerizes before it cross phosphorylates itself to become active [100]. Subsequently, PINK1 phosphorylates Parkin and ubiquitin. Phosphorylated Parkin undergoes conformational changes, binds to phosphorylated ubiquitin, transiently localises to the MOM and binds the E2 ubiquitin-conjugating human enzyme 8 (UbcH8) [101]. Fully active Parkin ubiquitinates its substrates on the MOM in an E2-dependent manner.

hMiro initially associates with the Leucine-rich repeat kinase 2 (LRRK2) [102], and PINK1 phosphorylates hMiro1 at AA S156, T298 and T299 (Fig. A.5, A) [103], [104] prior to the ubiquitination of hMiro by Parkin [105]. Although many ubiquitination sites have been reported for hMiro, Parkin preferentially ubiquitinates hMiro at lysine K572 in the cGTPase [40], [106]. The recruitment of Parkin to the MOM of depolarised mitochondria is dependent on hMiro calcium binding and hMiro1 ubiquitination at lysine K572 [107] or phosphorylation of hMiro2 at serines S325 and S430 by PINK1 [108]. Hereafter, PINK1 phosphorylates ubiquitin chains on Parkin substrates which accelerates the formation of the ubiquitin chain. Mutations in PINK1 [109], Parkin [110] and LRRK2 [102] have been shown to cause early-onset PD and mutations of hMiro can be found in PD patients [111]–[113] indicating the importance of the removal of hMiro from the surface of depolarised mitochondria for mitochondrial clearance.

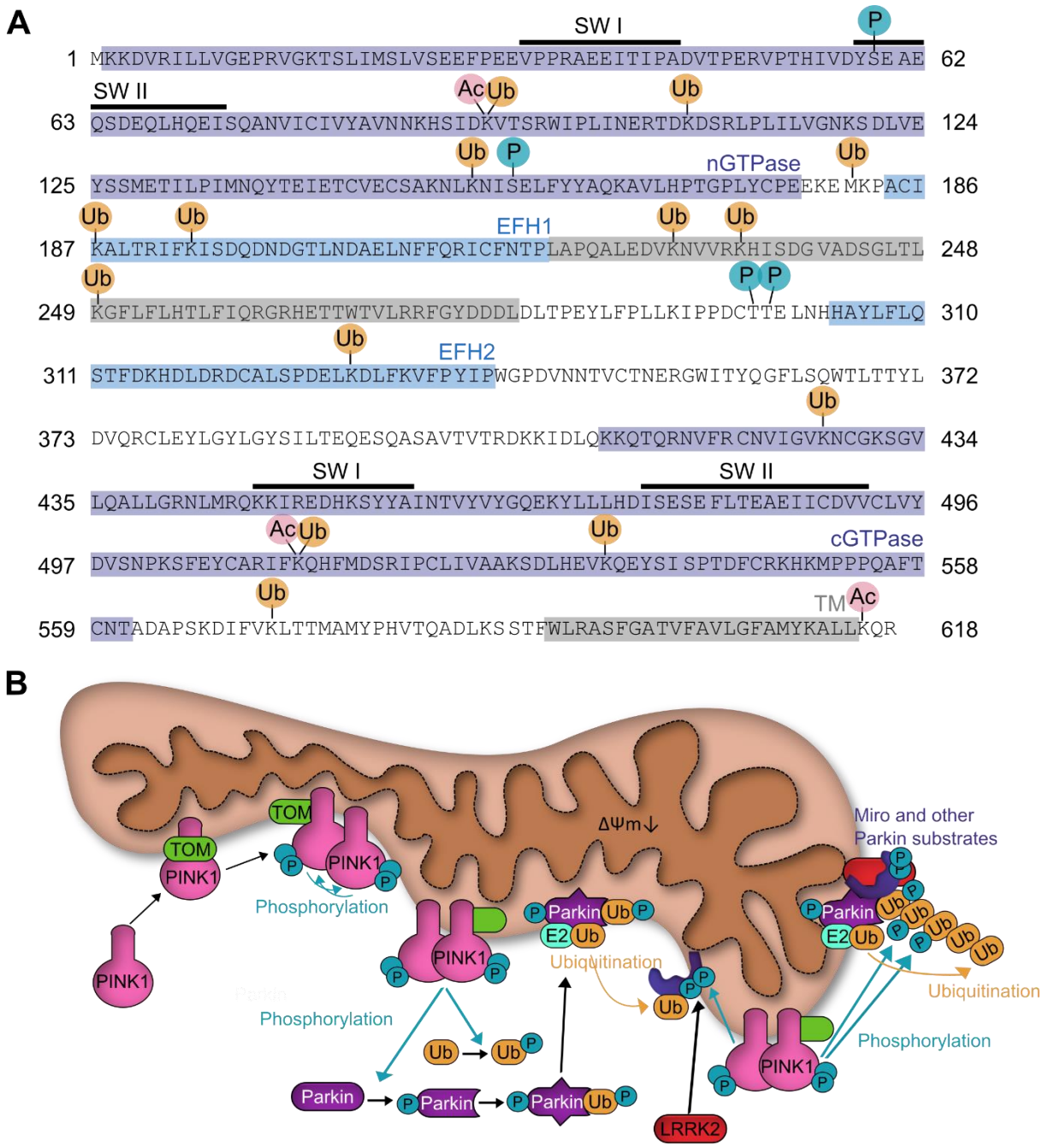

Figure A.5: hMiro is a substrate of Parkin in the PINK1/Parkin pathway of mitophagy. (**A**) PTMs in the sequence of hMiro1, including acetylation sites (Ac, rose), phosphorylation sites (P, cyan) and ubiquitination sites (Ub, orange). The domain organisation of hMiro1 and the nucleotide stabilising Switch I and the nucleotide hydrolysis regulating Switch II regions of the GTPase domains are indicated. (**B**) Model of PINK1/Parkin mediated mitophagy. Upon membrane depolarisation PINK1 is stabilised by the TOM complex on the MOM, dimerises and cross-phosphorylates itself. LRRK2 is activated and interacts with Miro and PINK1 phosphorylates Miro. PINK1 phosphorylates ubiquitin and Parkin, and phosphorylated Parkin undergoes conformational changes and binds phosphorylated ubiquitin to become fully active. Parkin is transiently stabilised on the MOM and starts ubiquitinating substrates. PINK1 phosphorylates ubiquitin chains on substrates, thus accelerating the ubiquitination by Parkin.

A.1.10 The yeast mitochondrial import protein MIM2

Mitochondria originate from an ancient endosymbiontic event [114] and have since then acquired numerous additional cellular functions. The small number of genes in the mitochondrial DNA is in stark contrast to the large number of mitochondrial proteins. As a consequence, mitochondria carry multiple protein complexes responsible for protein translocation within the MOM and the MIM. The main protein translocase of the MOM is the TOM complex [115], which acts as the access gateway for most of the nuclear-encoded mitochondrial proteins [116]. In addition, the SAM complex functions in the insertion of β-barrel proteins into the MOM [117], [118]. However, most proteins of the MOM carry α-helical single-span or multiple-span transmembrane anchors. In yeast, they are inserted into the membrane with the help of the MOM protein Mitochondrial Import (Mim) complex.

The Mim complex consists of the 13 kDa Mitochondrial Import protein 1 (Mim1) [119], [120] and the 10 kDa Mim2 [121]. Recent research established three independent mechanisms for Mim assisted protein integration into the MOM [122]. (1) The Mim complex accepts single-span or multiple-span precursor proteins from the Tom70 receptor (Fig. A.6, A) [119], [120], (2) Mim independently integrates single-spanning proteins [122], [123] and (3) Mim promotes the assembly of TOM subunits in cooperation with the SAM complex [123]–[127], rendering Mim a versatile protein translocase.

Although the Mim complex is fungi-specific and not conserved in mammals, sequentially distinct functional analogues of the Mim complex can be found in other organisms. A candidate for a protein that facilitates integration of α-helical MOM proteins similarly to Mim, is the Peripheral archaic translocase of the outer membrane 36 (pATOM36) of the protozoan *Trypanosoma brucei* [128]. Only recently, the human mitochondrial carrier homolog 2 (MTCH2) protein has been identified as insertase for α-helical MOM proteins [129].

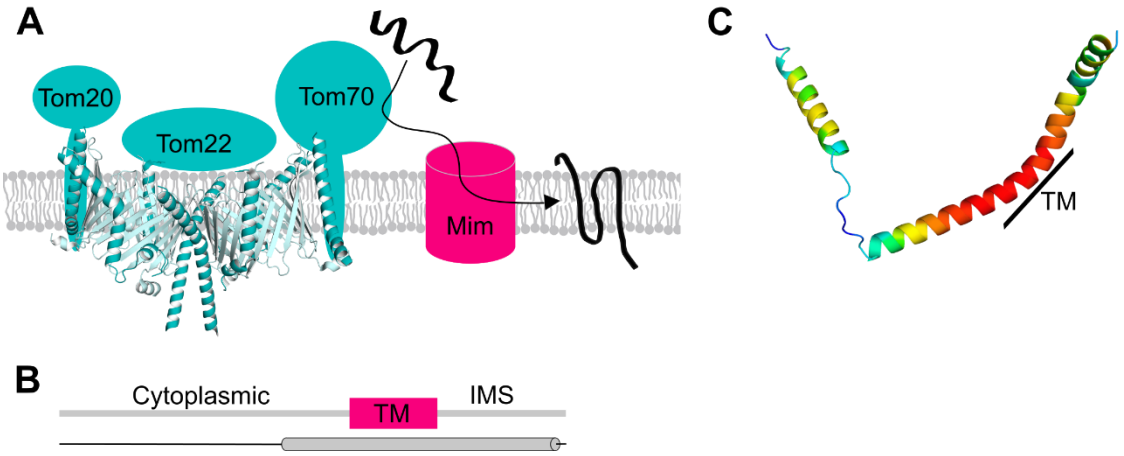

Figure A.6: Mim2 is a component of the mitochondrial outer membrane import machinery. (**A**) Model of the Mim complex (pink) functioning as translocase for α-helical outer membrane proteins. (**B**) Domain organisation of MIM2 including the transmembrane α-helix. The N-terminus of Mim2 is negatively charged and located at the cytoplasmic site of the MOM. The C-terminus comprises many positively charged residues and points towards the IMS. (**C**) Alphafold [54], [55] model of Mim2 from *Saccharomyces cerevisiae* colored for per-residue confidence score (pLDDT). Very high pLDDT (>90) in red and very low pLDDT (<50) in blue. The transmembrane domain (TM) is indicated by a black line.

Mim2 was identified in an immunoprecipitation assay coupled to stable isotope labelling with amino acids in cell culture (SILAC) as interaction partner of Mim1 [121]. Although Mim2 is conserved in fungi such as *Schizosaccharomyces pombe*, it has no homologues in higher eukaryotes. Mim2 is an integral protein of the MOM with the C-terminus facing the IMS (Fig. A.6, B) [121]. Recently reported structure prediction models from the Alphafold database [54], [55] suggest a high α-helical secondary structure content for Mim2 (Fig. A.6, C) and a lack of tertiary structure motifs, likely due to the small size of the protein. However, Mim1 and Mim2 are components of a high molecular weight complex [123], [126], [130], [131], likely formed by several copies of the two proteins. Moreover, Mim1 and Mim2 have been shown to function in the same molecular pathway. Deletion of Mim2 changes mitochondrial morphology and reduces the biogenesis of mitochondrial proteins. Furthermore, the import of multi-spanning proteins into the MOM is compromised in mitochondria lacking Mim2 [121]. Structural data on the whole Mim complex would be of assistance in understanding how integration of proteins with α-helical transmembrane anchor into the MOM is achieved.

A.2 OBJECTIVES

The focus of the first project of this dissertation is the structural and functional characterisation of the hMiro proteins. To date, high-resolution structural data on hMiro1/2 are limited to parts of the proteins and do not explain the underlying conformational changes the proteins are expected to undergo in order to fulfil their multifaceted functions. The so far obtained structural data on hMiro1/2 [40], [41] has been determined with recombinant protein without the help of crystallisation chaperones. Low-resolution SEC-SAXS experiments [41] indicate the existence of a potentially flexible connection between the nGTPase and EF1 of hMiro1 that likely is crucial for mediating structural changes. To increase the chances for successful structure determination and to stabilise the flexibly linked nGTPase, the development of hMiro1 specific nanobodies binding to different parts of the protein in collaboration with Funmi Fagbadebo (group of Prof. Rothbauer, Pharmaceutical Biotechnology, University of Tübingen) was planned. For this purpose, the expression and purification of hMiro1 short and full-length constructs was established and optimised. Thereafter, the tasks at hand comprised:

- Stabilisation of the protein with the aim of determining structural data
- Characterisation of the protein in presence of its non-protein ligands
- Transfer of established protocols to hMiro2

Moreover, patient-derived PD related mutations of hMiro1 (group of Dr. Julia Fitzgerald, Hertie Institute for Clinical Brain Research, University of Tübingen) that induce altered cellular properties were purified and characterised. Through this, the connection between structural alterations of hMiro and the disruption of the interaction of hMiro with PINK1 and Parkin was supposed to be addressed.

Furthermore, the interaction with the well-established binding partner of hMiro in mitochondrial trafficking, hTRAK2, was analysed. To date, no three-dimensional structural information of TRAK is available, likely due to extended flexible stretches within the protein. Proper folding of the hMiro1 binding site of hTRAK might happen in a hMiro1-dependent manner upon interaction, therefore, establishing a complex between the proteins will be crucial for the characterisation of hTRAK.

The second part of the project focussed on the optimisation of the purification of Mim2 and the analysis of the crystallisation potential of the protein. Mim2 as part of the Mim complex is responsible for the incorporation of proteins harbouring an α-helical transmembrane anchor, such as Miro, into the MOM in yeast. Obtaining structural data will help to understand the mechanism of membrane incorporation and increase the chances for finding functional homologues in higher eukaryotes.

A.3 MATERIALS AND METHODS

A.3.1 Materials

A.3.1.1 Chemicals

Table A.1: List of chemicals and suppliers used in the hMiro1 project.

Acetic acid	Roth
Acrylamide-bisacrylamide solution Rotiphorese® 30% (v/w) gel	Roth
Agar-agar	Roth
Agarose	Roth
N-Z-amine AS	Sigma-Aldrich
Ammonium persulfate (APS)	Roth
Ammonium sulfate ($(NH_4)_2SO_4$)	Merck
Ampicillin	Sigma-Aldrich
Bluo-gal	Biomol
Bromophenol blue	Roth
Calcium chloride ($CaCl_2$)	Sigma-Aldrich
Chloramphenicol	Sigma-Aldrich
N-Decyl-β-D-maltopyranoside (DM)	Cube Biotech
Desoxy nucleoside triphosphate (dNTP)	Genaxxon bioscience
Dimethyl sulfoxide (DMSO)	Sigma-Aldrich
Dipotassium hydrogen orthophosphate (K_2HPO_4)	Sigma-Aldrich
Disodium hydrogen phosphate (Na_2HPO_4)	Sigma-Aldrich
Dithiothreitol (DTT)	Sigma-Aldrich
N-Dodecyl-β-D-maltopyranoside (DDM)	Cube Biotech
Ethanol	Roth
Ethylenediaminetetraacetic acid (EDTA)	Roth
Fetal bovine serum (FBS)	Thermo Fisher Scientific
Gentamycin	Roth
Glacial acetic acid	Roth
D-(+)-Glucose	Sigma-Aldrich
L-Glutamine	Thermo Fisher Scientific
L-Glycine	Sigma-Aldrich
GDP	Sigma-Aldrich
GTP	Sigma-Aldrich
Guanosine-5'-[(β,γ)-imido]triphosphate (GMPPNP)	Sigma-Aldrich
Heparin, tissue culture grade	Sigma-Aldrich
(4-(2-hydroxyethyl)-1-piperazineethanesulfonic acid (HEPES)	Roth
Imidazole	Roth
Isopropanol	Sigma-Aldrich
Isopropyl-β-D-thiogalactopyranoside (IPTG)	VWR International
Kanamycin	Sigma-Aldrich
α-Lactose	Sigma-Aldrich
Lysogeny broth (LB) Miller	Roth
Magnesium chloride ($MgCl_2$)	Sigma-Aldrich
Magnesium sulfate ($MgSO_4$)	Sigma-Aldrich
β-Mercaptoethanol	Sigma-Aldrich
Methanol	Merck
Milk powder (MP)	Roth
3-(N-Morpholino)propanesulfonic acid (MOPS)	Sigma-Aldrich
N-Octyl-β-D-glucopyranoside (OG)	Cube Biotech
Polyethylene glycol 500 (PEG 500)	Sigma-Aldrich
Polyethylene glycol 6000 (PEG 6000)	Fluka Analytical
Ponceau S	Roth
Potassium chloride (KCl)	Sigma-Aldrich
Potassium dihydrogen phosphate (KH_2PO_4)	Sigma-Aldrich

Table A.1, continued: List of chemicals and suppliers used in the hMiro1 project.

Reduced glutathione	Sigma-Aldrich
Sodium chloride (NaCl)	Roth
Sodium dodecyl sulfate (SDS)	Roth
Tetracycline	Roth
Tetramethylethylenediamine (TEMED)	Roth
Tris(2-carboxyethyl)phosphine (TCEP)	Sigma-Aldrich
Tris(hydroxymethyl)aminomethane (Trizma®-Base, Tris Base)	Sigma-Aldrich
Tris(hydroxymethyl)aminomethane hydrochloride (Tris HCl)	Sigma-Aldrich
Tryptone	Roth
TWEEN®-20	Sigma-Aldrich
Yeast Extract	Roth

A.3.1.2 Vectors, enzymes and cloning material

Table A.2: Cloning vectors for hMiro1/2 and hTRAK1/2 constructs as provided by manufacturer.

pET28a(+)	BioCat, Germany or Genscript Biotech, Netherlands
pFastBAc1	BioCat, Germany or Genscript Biotech, Netherlands
pGEX-4T-1	Genscript Biotech, Netherlands
pMAL-c4x	Genscript Biotech, Netherlands

Table A.3: Enzymes used for cloning, protein purification and tag cleavage.

BamHI-HF™	New England BioLabs
Benzonase® nuclease	Sigma-Aldrich
BglII	New England BioLabs
DpnI	New England BioLabs
EcoRI-HF™	New England BioLabs
ExactRun-DNA Polymerase	Genaxxon bioscience
HindIII-HF™	New England BioLabs
NcoI-HF™	New England BioLabs
NdeI	New England BioLabs
NotI-HF™	New England BioLabs
Q5® high-fidelity DNA Polymerase	New England BioLabs
TEV protease	In-house production
XbaI	New England BioLabs
XhoI	New England BioLabs

Table A.4: Sequencing primer for bacmid cloning control PCR.

pUC/M13 forward	5′-CCCAGTCACGACGTTGTAAAACG-3′
pUC/M13 reverse	5′-AGCGGATAACAATTTCACACAGG-3′

Table A.5: DNA purification and virus extraction kits.

BaculoQUANT™ ALL-IN-ONE Virus extraction and titration kit	Oxford expression technologies
GenElute™ HP Plasmid Miniprep Kit	Sigma-Aldrich
PureLink HiPure Plasmid DNA Miniprep kit	Invitrogen

A.3.1.3 Buffers and media

Table A.6: Protein purification and other buffers.

1% Agarose in TAE	10g/L agarose, 20 mL TAE buffer 50x, to 1 L with H_2O
Cobalt IMAC buffer	25 mM HEPES pH 7.5, 300 mM NaCl, 1 mM $MgCl_2$, 1 mM DTT, 10 mM imidazole pH 8.0
Cobalt IMAC solubilisation buffer	25 mM HEPES pH 7.5, 300 mM NaCl, 1 mM $MgCl_2$, 1 mM DTT, 10 mM imidazole pH 8.0
Dialysis buffer	25 mM HEPES pH 7.5, 300 mM NaCl, 1 mM $MgCl_2$, 1 mM DTT
HAdVG52-FK buffer	30 mM Tris pH 7.5, 150 mM NaCl
GST buffer	25 mM HEPES pH 7.5, 300 mM NaCl, 1 mM $MgCl_2$, 1 mM DTT
GST elution buffer	25 mM HEPES pH 7.5, 300 mM NaCl, 1 mM $MgCl_2$, 1 mM DTT, 10 mM reduced glutathione
GST solubilisation buffer	25 mM HEPES pH 7.5, 300 mM NaCl, 1 mM $MgCl_2$, 1 mM DTT
IEx buffer low salt	25 mM HEPES pH 7.5, 20 mM NaCl, 1 mM $MgCl_2$, 1 mM DTT
IEx buffer high salt	25 mM HEPES pH 7.5, 1 M NaCl, 1 mM $MgCl_2$, 1 mM DTT
Intein elution buffer	20 mM HEPES pH 8.0, 500 mM NaCl, 1 mM $MgCl_2$, 30 mM DTT
Intein high salt buffer	20 mM HEPES pH 7.4, 1 M NaCl, 1 mM $MgCl_2$
Intein low salt buffer	20 mM HEPES pH 7.4, 100 mM NaCl, 1 mM $MgCl_2$
Intein solubilisation buffer	20 mM HEPES pH 7.4, 500 mM NaCl, 1 mM $MgCl_2$
Intein wash buffer	20 mM HEPES pH 8.0, 500 mM NaCl, 1 mM $MgCl_2$
IMAC elution buffer	25 mM HEPES pH 7.5, 300 mM NaCl, 1 mM $MgCl_2$, 1 mM DTT, 500 mM imidazole pH 8.0
Nickel IMAC buffer	25 mM HEPES pH 7.5, 300 mM NaCl, 1 mM $MgCl_2$, 1 mM DTT, 20 mM imidazole pH 8.0
Nickel IMAC solubilisation buffer	25 mM HEPES pH 7.5, 300 mM NaCl, 1 mM $MgCl_2$, 1 mM DTT, 20 mM imidazole pH 8.0
Ponceau red staining solution	50 mg ponceau S, 2.5 mL acetic acid, 47.5 mL H_2O
4x SDS sample buffer	30 mL glycerol, 10 mL 10% SDS, 1.63 mL 0.5 M EDTA pH 8.0, 4 mL β-mercaptoethanol, 20 mg bromphenol blue, 13 mL H_2O
SEC buffer	25 mM HEPES pH 7.5, 300 mM NaCl, 1 mM $MgCl_2$, 1 mM DTT
SEC buffer Mim2	20 mM MOPS pH 8.0 , 300 mM NaCl
SEC buffer Mim2 phosphate	20 mM sodium phosphate buffer pH 8.0, 300 mM NaCl
TAE buffer 50x	242 g/L Trizma base, 57.2 mL glacial acetic acid, 10 mL 0.5 M EDTA pH 8.0, to 1 L with H_2O
TB buffer 10x	23.1 g/L KH_2PO_4, 125.4 g/L K_2HPO_4
TBS-T	20 mM Tris pH 7.5, 150 mM NaCl, 0.5% TWEEN®-20
TBS-T with milk powder	20 mM Tris pH 7.5, 150 mM NaCl, 0.5% TWEEN®-20, 5% MP
Transferbuffer	3.025 g Tris base, 14.4 g L-glycine, 200 mL methanol, 800 mL H_2O

Table A.7: *E. coli* growth media.

5052 50x	250 g glycerol, 25 g D-(+)-glucose, 100 g α-lactose, 730 mL H_2O
LB medium	25 g/L LB Miller in H_2O
LB agar	25 g/L LB Miller, 15 g/L agar-agar in H_2O
NPS 20x	66 g/L $(NH_4)_2SO_4$, 136 g/L KH_2PO_4, 142 g/L Na_2HPO_4 in H_2O
SOC medium	2% tryptone, 0.5% yeast extract, 10 mM NaCl, 2.5 mM KCl, 10 mM $MgCl_2$, 10 mM $MgSO_4$, 20 mM glucose in H_2O
TB	12 g/L tryptone, 24 g/L yeast extract, 5 g/L glycerol in H_2O
TB medium	90% TB, 10% TB buffer 10x
ZY	10 g/L N-Z-amine AS, 5 g/L yeast extract in H_2O
ZY medium	2% 5052 50x, 5% NPS 20x, 1 mM $MgSO_4$, 93% ZY

A.3.1.4 Cells and culture medium

Table A.8: *E. coli* and insect cells and corresponding culture growth media.

Cell line	Manufacturer	Medium	Manufacturer
ArcticExpress	In-house production	ZY medium	
BL21 (DE3)	In-house production	TB medium ZY medium	
DH10Bac	In-house production	LB medium SOC medium	
DH5α	In-house production	LB medium	
SF9	Thermo Fisher Scientific	SF9-900™ II SFM	Thermo Fisher Scientific
		Grace's insect cell medium unsupplemented	Thermo Fisher Scientific
High Five™	Thermo Fisher Scientific	Express Five™ medium	Thermo Fisher Scientific
Rosetta 2 (DE3)	In-house production	LB medium	
Shuffle® T7	In-house production	ZY medium	

A.3.1.5 Reagents and screens

Table A.9: List of reagents used in the hMiro1 project.

Cellfectin™ II reagent	Thermo Fisher Scientific
cOmplete™ EDTA-free protease inhibitors	Roche
CutSmart® Buffer	New England BioLabs
ECL™ Western blotting detection reagents	Sigma-Aldrich
ExactRun buffer	Genaxxon bioscience
Gel Filtration Calibration Kits (Low/High molecular weight)	GE Healthcare
GelRed®	Biotium
GeneRuler 1 kb Plus DNA Ladder	Thermo Fisher Scientific
Goat α-mouse antibody	Novagen
Instant blue®	Abcam
Izit Crystal Dye	Hampton Research
Malachite Green Phosphate Assay Kit	Sigma-Aldrich
Mouse α-his antibody	Novagen
Protein Thermal Shift Dye Kit™	Applied Biosystems
Q5® GC enhancer	New England BioLabs
Q5® reaction buffer	New England BioLabs
Page Ruler™ prestained protein ladder	Fermentas
Page Ruler™ unstained protein ladder	Fermentas
Penicillin-Streptomycin solution 100x	Genaxxon bioscience
Purple loading dye 6x	New England BioLabs
Rotiphorese® 10x running buffer	Roth

Table A.10: Commercial crystallisation screens.

The Cation Suite	Qiagen
Crystal Screen HT™	Hampton Research
JCSG+ Suite	Qiagen
Morpheus®	Molecular Dimensions
PEG/Ion HT™	Hampton Research
Wizard Classic 1 and 2 Block	Molecular Dimensions
Wizard Classic 3 and 4 Block	Molecular Dimensions

A.3.1.6 SDS-PAGE

Table A.11: Protocol for casting of SDS gels.

Chemicals	Stacking gel	Separating gel 12%	Separating gel 15%
Rotiphorese® gel 30%	5.85 mL	27 mL	33.8 mL
1.5 M Tris/HCl pH 8.8		16.9 mL	16.9 mL
1.5 M Tris/HCl pH 6.8	7.5 mL		
10% SDS (w/v)	450 µL	677 µL	677 µL
TEMED	45 µL	67.5 µL	67.5 µL
10% APS (w/v)	450 µL	677 µL	677 µL
H_2O	27.5 mL	22.5 mL	15.7 mL

A.3.1.7 Consumables

Table A.12: Overview of consumable materials used in the hMiro1 project.

Amicon® Ultra 0.5 mL centrifugal filters (MWCO 10 kDa)	Merck
Amylose Resin	New England BioLabs
Blotting paper 703	VWR North america
Chitin Resin	New England BioLabs
ColiRollers™ plating beads	Novagen
Corning®-Costar®-Spin-X® centrifugal filters (0.22 µM)	Corning
Corning® Erlenmeyer culture flask (125 mL, 250 mL, 500 mL)	Merck
Cover slides 12-542-C	Fischer Band
Cryotubes	Greiner Bio-One
Glutathione Agarose Resin	Serva
Gravity flow columns, empty	Bio-Rad
GSTrap™ FF column 5 mL	Cytiva
HisPur™ Cobalt Resin	Thermo Fisher Scientific
HisTrap FF Crude column 5 mL	Cytiva
HiTrap™ Q FF column 5 mL	Cytiva
HiTrap™ Talon™ Crude column 5 mL	Cytiva
INTELLI-PLATE® 96	Art Robbins Instruments
Membrane filter (0.22 µM)	Millipore
MicroAmp™ optical 8 cap PCR strips	Applied Biosystems
MicroAmp™ optical adhesive film	Applied Biosystems
Microtiter plate, 96-well	Greiner Bio-One
Pasteur pipettes, glass	neoLab
PCR tubes (0.2 mL)	Peqlab
Petri dishes	Greiner Bio-One
Pierce™ protein concentrators PES (MWCO 30 kDa)	Thermo Fisher Scientific
Pipette tips	Herbe Plus
Plastic cuvettes	Sarstedt
Polyolefin cover foil	HJ-Bioanalytik GmbH
Reaction tubes (1.5 mL, 2.0 mL, 15 mL, 50 mL)	Greiner Bio-One
Rothi®-PVDF membrane (0.45 µM)	Roth
Serological pipettes (2 mL, 5 mL, 10 mL, 25 mL, 50 mL, 100 mL)	Greiner Bio-One
Slide-A-Lyzer® Mini dialysis devices	Thermo Fisher Scientific
Spectra/Por™ dialysis membrane MWCO 6-8 kDa	Thermo Fisher Scientific
Syringes (1 mL, 5 mL, 10 mL, 30 mL)	Greiner Bio-One
Syringe-top filters (0.22 µM)	VWR international
Tissue Culture Plates 6 well	Greiner Bio-One
Vivaspin™ 20 centrifugal concentrators (MWCO 10 kDa, 30 kDa, 50 kDa, 100 kDa)	Sartorius

A.3.1.8 Instruments

Table A.13: List of hardware and instruments.

ÄKTA Basic	Amersham Pharmacia Biotech
ÄKTA Micro (Ettan LC)	GE Healthcare
ÄKTA Prime Plus	GE Healthcare
Autoclave VX 95	Systenic
Centrifuge 5415 D	Eppendorf
Centrifuge Heraeus™ multifuge 1 L-R	Thermo Fisher Scientific
CERTOMAT® R/HK	Sartorius
ChemiDoc™ MP Imaging System	Bio-Rad
CP323S-0CE scale	Sartorius
Cryo loops (0.05-0.5 mm)	Molecular dimensions
Digital Sonifier	Branson
DNA electrophoresis cell	Bio-Rad
Enzyme mini cooler	VWR International
Eppendorf Thermomixer comfort	Eppendorf
FastGene®	NIPPON Genetics Europe
Fiberlite™ bottle for SLC4000 rotor	VWR International
Gryphon crystallisation robot	Art Robinson Instruments
Heating block Neoblock 1	neoLab
Hellma macro cuvette 110-QS 1 mm	Hellma
Hellma ultra-micro cuvette 105.201-QS 3 mm	Hellma
Heraeus™ function line incubator	Thermo Fisher Scientific
HERAsafe®	Thermo Fisher Scientific
HiLoad Superdex™ 75 16/600 column	Cytiva
HiLoad Superdex™ 200 16/600 column	Cytiva
iCycler™ Thermal Cycler	Biorad
IKAMAG® magnetic stirrer Mini MR standard	VWR International
Infors HT Multitron incubation shaker	Infors HT
Intelli-Mixer™ RM-2L rotator	ELMI
MAR345 detector	Mar
MicroMax™-007 HF microfocus X-ray generator	Rigaku
Microscope Leica DMIL	Meyer Instruments
Microscope Leica MZ 16	Meyer Instruments
Microscope Leica MZ 95	Meyer Instruments
Microwave	Parasonic
Milli-Q-Nerj	Millipore
Mini-PROTEAN electrophoresis system	Bio-Rad
Nalgene® Mr. Frosty	Sigma-Aldrich
Nanodrop ND-1000	Thermo Fisher Scientific
Neubauer improved counting chamber	Marienfeld Superior
Nylon and pins	GE Healthcare
Peristaltic pump (EconoPump)	Bio-Rad
Polyallomer bottles 50 mL for SS-34 rotor	Beranek
pH meter BP11	Sartorius
Pump P-500 (Fast protein liquid chromatography (FPLC))	Pharmacia
QuantStudio™ Real-Time-PCR	Thermo Fisher Scientific
Sartorius ME premium semi micro scale	Sartorius
SLC4000 rotor	Thermo Fisher Scientific
SmartSpec™ Plus spectrophotometer	Bio-Rad
Sorvall™ RC 6 Plus centrifuge	Thermo Fisher Scientific
Spectropolarimeter J-720	JASCO
SS34 rotor	Thermo Fisher Scientific
Superdex™ increase 3.2/300 column	Cytiva
Superdex™ 75 PC 3.2/30	GE Healthcare

Table A.13, continued: List of hardware and instruments.

Tecan infinite M200 plate reader	TECAN
Thermolyne Labquake Rotisserie tube rotators	Barnstead International
Transblot SD Semi-Dry transfer cell	Bio-Rad
Vortex Genie 2™	Bender & Hobein AG
Zetasizer Nano ZS	Malvern Panalytical

A.3.1.9 Software

Table A.14: Software and online tools.

Alphafold	EMBL-EBI, DeepMind [54], [55]
Basic Local Alignment Search Tool (BLAST)	National Center for Biotechnology Information [132]
Clustal Omega	EMBL-EBI [133]
ExPASy Protparam, translate	Swiss Institute of Bioinformatics [134]
GenSmart™ Codon Optimisation	Genscript Biotech
PyMOL 2.5	DeLano Scientific LLC [135]
Unicorn™ chromatography software	Cytiva

A.3.2 Methods

A.3.2.1 Molecular biology

Construct design

Full-length constructs of hMiro1 (UniprotKB: Q8IXI2) and hMiro2 (UniprotKB: Q8IXI1) comprise the nGTPase, both EF hand domains and the cGTPase including amino acid 1-592 of hMiro1 and 1-588 of hMiro2. The C-terminal α-helical transmembrane anchor was truncated and constructs were codon optimised for *E. coli* or insect cell expression by GenSmart™ Codon Optimisation, respectively. The complementary DNA (cDNA) of hMiro1 was synthesised for *E. coli* expression with either a N-terminal Spot-tag® and a tobacco etch virus (TEV) cleavable C-terminal hexa-histidine tag (His_6-tag) and cloned into the pET28a(+) vector (Biocat, Germany) or with a TEV cleavable N-terminal maltose binding protein (MBP) tag and cloned into pMAL-c4x (Genscript Biotech, Netherlands). hMiro2 cDNA was synthesised for *E. coli* expression with a N-terminal Spot-tag® and a TEV cleavable C-terminal His_6-tag in pET28a(+) (Biocat, Germany) or it was cloned into the pGEX-4T-1 vector providing a N-terminal TEV cleavable glutathione S-transferase (GST) tag (Genscript Biotech, Netherlands). The corresponding constructs of hMiro1 and hMiro2 for insect cell expression were designed with a TEV cleavable C-terminal His_6-tag and cloned into pFastBac1 (Genscript Biotech, Netherlands).

The cDNA of N-terminally Spot-tagged® full-length hTRAK1 (UniprotKB: Q9UPV9) (Genscript Biotech, Netherlands) or N-terminally Spot-tagged® full-length hTRAK2 (UniprotKB: O60296) was cloned into a pFastBac1 vector for insect cell expression (Biocat, Germany). For *E. coli* expression, the amino acid sequence of hTRAK2 was truncated to the MBS [57] comprising amino acids 476-700 including a C-terminal serine-rich region of 6 amino acids (AS 701-706). The cDNA was codon optimised (GenSmart™ Codon Optimisation) and cloned into a pGEX4T-1 vector providing a N-terminal, TEV cleavable GST-tag (Genscript Biotech, Netherlands).

Site-directed mutagenesis

Proceeding from the constructs described above, constructs of shorter length, with altered tags or including PD related mutations were cloned by site-directed mutagenesis (see Extended data, Table A.21 for an overview of all cloned constructs). Primer pairs (Extended data, Table A.24) were designed with complementary sequences up- and down-stream of the region of interest, excluding the to be truncated parts. Point-mutations were implemented by changing up to 3 bases in the complementary sequence of the primer. Additional small tags were incorporated via loop-in strategy through extended primers. The site-directed mutagenesis was accomplished by polymerase chain reaction (PCR) as described in Table A.15 and the template DNA was removed by overnight DpnI digest at 37 °C.

Table A.15: PCR mix and protocol for site-directed mutagenesis. The complementary primer pairs include 5' overhangs to decrease risk of self-hybridisation.

PCR mix	Reagents	Volume [µL]
	Template (~100 ng/µL)	1
	Forward primer (10 µM)	2.5
	Reverse primer (10 µM)	2.5
	5x Q5 reaction buffer	10
	5x Q5 High GC enhancer	10
	dNTPs (10 mM)	1
	Q5® high-fidelity DNA Polymerase	0.5
	H2O	22.5

PCR protocol	Step	Repeats	Temperature [°C]	Time [s]
	1	1	98	120
	2	4	98	10
			54	30
			72	420
	3	4	98	10
			57	30
			72	420
	4	4	98	10
			60	30
			72	420
	5	4	98	10
			63	30
			72	420
	6	4	98	10
			66	30
			72	420
	7	4	98	10
			69	30
			72	420
	8	4	98	10
			72	30
			72	420
	9	1	72	120
	10	1	4	∞

Heat-shock transformation

The PCR products of the site-directed mutagenesis were transformed into chemically competent *E. coli* DH5α cells by heat-shock. 50 µL cells were thawed on ice for 20 min prior to incubation with 100 ng DNA for 20 min on ice. Heat-shock was performed in an Eppendorf Thermomixer comfort for 35 s at 42 °C. Thereafter, cells were cooled on ice for 2 min before they were incubated with 300 µL LB medium at 37 °C for 1 h, shaking at 900 rpm. The cell suspension was streaked on LB agar plates containing antibiotics according to the plasmid encoded resistance, and plates were incubated overnight at 37 °C.

Plasmid amplification and purification

Positive clones from the heat-shock transformation were retrieved from the LB agar plates and used to inoculate 20 mL LB medium containing the corresponding selection marker. Cells were cultivated at 37 °C, shaking at 180 rpm and harvested after ≥14 h by centrifugation at 4,500x g for 15 min. The plasmid DNA was extracted from the cell pellet with the GenElute™ HP Plasmid Miniprep Kit as described in the user protocol [136].

Enzymatic digestion and agarose gel electrophoresis

Successful generation of shorter hMiro1/2 or hTRAK1/2 constructs was controlled by cutting the plasmid DNA before and after the shortened gene of interest with the respective restriction enzymes and a subsequent agarose gel electrophoresis with a 1% agarose gel stained with GelRed® nucleic acid gel stain run at 120 mA for 45 min in 1x Tris-acetate EDTA (TAE) buffer. Clones with the appropriate length of the cut DNA fragment were sent for sequencing.

Sequencing

The plasmid DNA (100 ng/µL) of correct clones identified by agarose gel electrophoresis or constructs that could not be analysed by enzymatic digestion was sequenced with Sanger sequencing at Microsynth Seqlab (Göttingen, Germany). Vector specific primers allowing the sequencing of the gene of interest were either provided or by request specifically synthesised at Micorsynth Seqlab.

Bacmid cloning

For cloning of the gene of interest in the required bacmid DNA, 1 ng pFastBac1 vector carrying the gene of interest was transformed into DH10Bac *E. coli* by heat-shock for 45 sec at 42 °C [137]. After chilling of the cells on ice for 2 min, 900 µL room temperature (RT) super optimal broth with catabolite repression (SOC) medium was added and cells were incubated for 5-6 h at 37 °C, shaking at 225 rpm. Thereafter, cells were plated for blue/white selection as 1:10 dilution with SOC medium on LB agar plates containing 100 µg/mL bluo-gal, 50 µg/mL kanamycin, 7 µg/mL gentamycin, 10 µg/mL tetracycline and 40 µg/mL isopropyl-β-D-thiogalactopyranoside (IPTG), and plates were incubated for 48 h at 37 °C. Positive colonies were restreaked to confirm white phenotype. Single white colonies were picked after restreaking and used to inoculate 10 mL LB medium containing antibiotics as described above. Cells were grown over night at 37 °C in an orbital shaker at 250 rpm and 1.5 mL culture volume was harvested on the following day by centrifugation at 9,000x g for 15 min. Recombinant bacmid DNA was extracted using the PureLink HiPure Plasmid DNA Miniprep kit by gravity flow as described [138]. Successful transfer of the gene of interest into the bacmid DNA was confirmed by PCR (Table A.16)

with pUC/M13 forward and reverse primers and subsequent analysis of the PCR product by agarose gel electrophoresis [137].

Table A.16: PCR mix and protocol for confirmation of successful bacmid cloning.

PCR mix	Reagents	Volume [µL]
	Template (~100 ng/µL)	1
	pUC/M13 forward (10 µM)	2.5
	pUC/M13 reverse (10 µM)	2.5
	5x ExactRun buffer	10
	dNTPs (10 mM)	1
	ExactRun-DNA Polymerase	0.5
	H2O	32.5

PCR protocol	Step	Repeats	Temperature [°C]	Time [s]
	1	1	94	180
	2	35	94	45
			55	45
			72	300
	3	1	72	420
	4	1	4	∞

A.3.2.2 Cell culture

Maintenance of Sf9 and High Five™ cells

SF9 insect cells were cultivated in SF9-900™ II SFM at 28 °C, shaking at 130 rpm and split at a density above $1.5x10^6$ cells/mL every 3-4 days to a final concentration of $0.6\text{-}0.7x10^6$ cells/mL in fresh medium. High Five™ cells were grown in Express Five™ SFM with 20 mM L-glutamine at 27 °C, shaking at 130 rpm and split similarly to the SF9 insect cells. Freshly thawed High Five™ cells required the addition of 10 U/mL heparin and cells were slowly starved from heparin once they showed high viability. For cryo preservation, highly viable SF9 or High Five™ cells of low passage number were frozen at $1x10^7$ cells/mL in 10% (v/v) DMSO.

Transfection and viral stock production

Sf9 insect cells were transfected with bacmid DNA containing the gene of interest using Cellfectin™ II Reagent [137]. For this purpose, $8x10^5$ SF9 cells per well were seeded in 6 well plates into 2 mL unsupplemented Grace's Insect Medium and allowed to attach for 15 min at RT. 8 µL Cellfectin™ II Reagent was mixed with 200 µL unsupplemented Grace's Insect Medium and 500 ng bacmid DNA and incubated for 15-30 min at RT. The DNA transfection mixture was added to the cells and incubated at 27 °C for 5 h. Thereafter, the transfection mixture was removed and the cells were fed with 2 mL SF-900™ II SFM and incubated for another 72 h at 27 °C until the SF9 cells showed signs of late-stage viral infection such as growth stop, granular appearance and detachment from the 6 well plate. P1 viral stock was isolated from the transfected cells by separation of the virus containing medium from the remaining cells and cell debris through centrifugation at 1,000x g for 10 min.

To produce a high-titer baculovirus stock, SF9 cells were infected with P1 with a multiplicity of infection (MOI) of 0.07 pfu/cell and an expected virus titer of the P1 stock of $1x10^6$-$1x10^7$ pfu/mL). The titration of the P2 virus stock was performed by quantitative polymerase chain reaction (qPCR) (Table A.17) according to baculoQUANT [139] and final P3 stocks were determined by infection of SF9 cells with P2 virus stock at a MOI of 0.1 pfu/cell. Viral stocks were stored at 4°C, protected from light with 2% FBS for up to 6 months.

Table A.17: PCR mix, lysis and PCR protocol for virus titration by qPCR. 80 µL of P2 viral stock are harvested at 16,000x g for 5 min and the pellet is resuspended in 20 µL baculoQUANT lysis buffer prior to cell lysis and subsequent qPCR.

PCR mix	Reagents	Volume [µL]
	qPCR low carboxyrhodamine mix	12.5
	RNAse free water	7.5
	Probe and primer solution	3
	Virus or control	2

Lysis protocol	Step	Repeats	Temperature [°C]	Time [min]
	1	1	65	15
	2	1	96	2
	3	1	65	4
	4	1	96	1
	5	1	65	1
	6	1	96	0.5
	7	1	20	∞

PCR protocol	Step	Repeats	Temperature [°C]	Time [s]
	1	1	95	600
	2	40	95	15
			60	60
	3	1	4	∞

A.3.2.3 Heterologous expression

Expression in *E. coli*

For the purpose of expression, the *E. coli* codon optimised constructs were transformed by heat shock into BL21 (DE3) *E. coli*, Shuffle® T7 competent *E. coli* or ArcticExpress competent cells, respectively. Cells were plated on LB agar plates containing 50 µg/mL kanamycin or 100 µg/mL ampicillin according to the selection marker carried by the respective vector and grown overnight at 37 °C. On the following day, colonies were scratched from the agar plates with 5 mL LB medium and used to inoculate either 50 mL Terrific broth (TB) medium or ZY auto induction medium for small scale test expressions or 3.6 L ZY auto induction medium for large scale expression. Small scale test expressions were used to determine the expression of the constructs and to establish medium-dependent expression temperature time for optimal protein yield. Once appropriate amounts of soluble protein were obtained, the gained knowledge was transferred to large scale expressions. Cultures were inoculated at an optical density $(OD)_{600}$ of 0.05 and grown to an OD_{600} of 1.0-1.2 at 37 °C while shaking at 100 rpm. Once the desired OD_{600} was reached, expression in TB medium was induced by the addition of 200 mM IPTG and cultures

were cooled to 18 °C for overnight expression (20-22 h). 2 mL of test expressions were harvested by centrifugation at 10,000x g for 5 min to be analysed for protein content by sodium dodecyl sulfate-polyacrylamide gel electrophoresis (SDS-PAGE). Large scale expressions in 3.6 L ZY medium were harvested by centrifugation at 9,220x g for 15 min and the pellets were stored at -20 °C until usage.

The Drp1 plasmid was provided by Andreas Jenner (group of Prof. Garcia-Saez, Institute for Genetics, University of Cologne) and the protein was expressed and purified according to established protocols [140]. Drp1 was expressed in Rosetta 2 (DE3) *E. coli* in 4 L LB Miller containing 100 µg/mL ampicillin and 34 mg/mL chloramphenicol. Expression was induced at an OD_{600} of 0.6 by the addition of 1 mM IPTG and the temperature was lowered to 20 °C for expression. Cells were harvested after ≥18 h and stored as described above.

Insect cell expression

Insect cell expression was performed in 50-200 mL highly viable SF9 or High Five™ cultures at a density of $2x10^6$ cells/mL, infected with P3 baculovirus stock at a MOI of 10 pfu/cell. Infected cells were incubated for 72 h at 27 °C before harvesting at 1,000x g for 5 min and storage at -20 °C.

Cell lysis

E. coli expression pellets were thawed and solubilized on ice in 5 mL per g pellet of the corresponding solubilisation buffer (Table A.6). Due to their small size, insect cell expression pellets were generally solubilised in 20 mL solubilisation buffer. Prior to cell lysis, cOmplete™ EDTA-free protease inhibitors and 5 µL Benzonase® nuclease were added. *E. coli* cells were lysed at 50% amplitude with 0.5s on-/ 2.0 s off-pulse for 5 min while insect cells were sonicated at 30% amplitude with 0.5s on-/2.0s off pulse for 30 sec. The cell lysate was centrifuged at 34,541x g for 45 min to separate the protein containing supernatant from remaining cells and cell debris.

A.3.2.4 Protein purification

Unless otherwise stated, all steps of the protein purification were performed at 4 °C with pre-chilled, filtered buffers as listed in Table A.6.

Immobilised metal affinity chromatography

His_6-tagged hMiro1/2 constructs were purified by immobilised metal affinity chromatography (IMAC) with either a 5 mL HisTrap™ FF Crude column or a 5 mL HiTrap™ Talon™ Crude column. For this purpose, cells were solubilised and lysed in IMAC buffer containing 20 mM imidazole or 10 mM

imidazole, respectively. After centrifugation, the protein containing supernatant was loaded cyclically onto the equilibrated column for ≥15 h. Loaded columns were connected to an Äkta Prime Plus system for washing and elution. For nickel IMAC, columns were washed with IMAC buffer containing 20 mM imidazole and subsequently with IMAC buffer containing 68 mM imidazole prior to the elution at an imidazole concentration of 116 or 164 mM in dependency of the hMiro construct. As hMiro1/2 constructs eluted at lower imidazole concentration from HiTrap™ Talon™ Crude columns, these columns were washed at an imidazole concentration of 34.5 mM and protein was eluted in IMAC buffer containing 255 mM imidazole in a single step. Elution fractions containing the protein of interest were identified by SDS-PAGE.

GST affinity purification

GST-hTRAK2-MBS and GST-hMiro2 expression pellets were solubilised in GST buffer without reduced glutathione. After cell lysis and centrifugation, the protein containing supernatant was loaded cyclically for ≥15 h onto an equilibrated 5 mL GSTrap™ FF column. Thereafter, the column was washed with GST buffer on an Äkta Prime Plus system before elution of the protein with GST buffer containing 5 mM reduced glutathione. Elution fractions were analysed by SDS-PAGE for protein content according to the elution profile.

Dialysis and enzymatic tag cleavage

In order to cleave the affinity tag of constructs with the help of the TEV protease, protein of interest containing fractions were pooled after the IMAC or GST affinity purification according to the corresponding SDS-PAGE and transferred into Spectra/Por™ dialysis membrane with a molecular weight cut-off (MWCO) of 6-8 kDa. After the addition of 2 mL of 0.6 mg/mL TEV protease, the dialysis of the protein was performed at 4 °C for ≥15 h in 2 L SEC buffer for subsequent preparative SEC or low salt IEx buffer for subsequent ion exchange chromatography (Table A.6).

Preparative size exclusion chromatography

For the preparative SEC, the protein of interest was either concentrated directly from the protein containing fractions of the affinity purification or after dialysis and cleavage of the affinity tag. Proteins were concentrated in Pierce™ protein concentrators Polyether sulfone (PES) with a suitable MWCO chosen according to the calculated size of the corresponding protein construct (Table A.18). The volume of the protein solution had to be reduced to 3-4 mL to be loaded onto the preparative SEC column, therefore proteins were concentrated in several subsequent steps of 10 min at 2,000x g. In-between centrifugation steps, the protein solution was monitored for signs of visible aggregation and mixed to

avoid the formation of areas with exceedingly high protein concentrations within the concentrators. If the protein was not dialysed into SEC buffer before, the protein was diluted 1:10 with SEC buffer during the concentrating process to reduce high imidazole or reduced glutathione concentrations. The concentrated protein was loaded onto an equilibrated HiLoad Superdex 75 16/600 or HiLoad Superdex 200 16/600 column, according to the size of the protein, installed on either an Äkta Basic system or a Pharmacia Pump P-500 FPLC system. The protein was eluted over 1.2 column volumes (CV) with SEC buffer, the elution was monitored by the ultra violet (UV) absorbance at 280 nm and fractions were analysed for protein content by SDS-PAGE. If required for subsequent experiments, fractions containing the protein of interest were pooled and concentrated to the desired target concentration, as desribed before.

Table A.18: Calculated molecular masses of hMiro1/2 and hTRAK2 constructs. Molecular masses were calculated with Expasy ProtParam. A comprehensive list of all constructs can be found in Extended data, Table A.21. N- or C-terminal tags as well as mutations are indicated and the domain nomenclature is explained in Fig. A.2, A.

Protein construct	Calculated molecular mass	Number of amino acids
hMiro1-His	70.0 kDa	610
MBP-hMiro1	109.4 kDa	970
hMiro1	67.9 kDa	592
hMiro1(R272Q)-His	70.0 kDa	610
hMiro1(R450C)-His	69.9 kDa	610
hMiro1-AB$_1$B$_2$-His	50.0 kDa	435
hMiro1-AB$_1$-His	35.2 kDa	308
hMiro1-AB$_1$(1-281)-His	34.2 kDa	300
hMiro1-AB$_1$(1-275)-His	33.4 kDa	293
hMiro1-A-His	22.6 kDa	198
hMiro1-A(1-167)-His	21.1 kDa	185
GST-hMiro2	91.6 kDa	817
hMiro2-His	67.1 kDa	606
hMiro2-AB$_1$-His	34.6 kDa	308
GST-hTRAK2-MBS	51.7 kDa	461
His-hTRAK2-MBS	27.4 kDa	253

Intein-mediated affinity purification

Drp1 expression pellets were dissolved in intein solubilisation buffer and sonicated as described above. For the intein mediated affinity purification, Drp1 containing supernatant was loaded onto 1.5 mL equilibrated chitin resin for 2 h prior to washing of the beads with 20 mL intein solubilisation buffer followed by 20 mL intein wash buffer. The protein was eluted from the chitin resin trough self-splicing of the intein tag over 48 h in the presence of 30 mM dithiothreitol (DTT). During the elution, occurring aggregates were separated from soluble protein by centrifugation at 16,100x g for 20 min. Hereafter, the protein was either directly concentrated to 0.5 mg/mL for usage in the GTPase assay or further purified by ion exchange chromatography.

Ion exchange chromatography

To increase the purity of hMiro1(R450C)-His and Drp1 an additional ion exchange chromatography (IEx) purification step was performed. For this purpose, hMiro1(R450C)-His was dialysed in low salt IEx buffer and Drp1 was diluted 1:5 with Intein low salt buffer. Proteins were loaded cyclically onto a 5 mL HiTrap™ Q FF column for 2-3 h. The loaded column was washed with either low salt IEx buffer or Intein low salt buffer, respectively. Proteins were eluted via a sodium chloride (NaCl) gradient of 0-1000 mM over 20 CV and protein containing fractions were analysed by SDS-PAGE. Thereafter, Drp1 was concentrated in a Pierce™ protein concentrators PES with a MWCO of 30 kDa to 0.5 mg/mL.

A.3.2.5 Analytics

SDS-PAGE

Expression samples and affinity chromatography, ion exchange chromatography and preparative SEC samples were analysed by SDS-PAGE to identify fractions containing the protein of interest and to analyse the quality and quantity of the purified protein. Samples were mixed in a 3:1 ratio with 4x sodium dodecyl sulfate (SDS) sample buffer (Table A.6) and heated to 98 °C for 5 min. Thereafter, they were centrifuged for 2 min at 16.100x g and 6-12 µL sample were loaded onto 12-15% SDS polyacrylamide gels (Table A.11). The gel electrophoresis was run in 1x SDS-PAGE buffer for 45 min at 220 V and gels were stained with InstantBlue™ staining solution.

Western blotting

To confirm the identity of the protein of interest in expression and purification samples, corresponding SDS gels were Western blotted. For this procedure, the SDS gel, a polyvinylidine fluoride (PVDF) membrane and blotting paper were soaked for 15 min with transfer buffer (Table A.6). The SDS gel was stacked on top of the PVDF membrane and sandwiched between four layers of blotting paper on each side for semi-dry transfer. The proteins were transferred onto the PVDF membrane during blotting for 1 h at 20 V. Successful blotting was confirmed by Ponceau red staining of the PVDF membrane and InstantBlue™ staining of the SDS gel. After washing off the Ponceau red staining solution, the membrane was blocked with Tris-buffered saline with Tween20 (TBS-T) buffer (Table A.6) supplemented with 5% (w/v) milk powder (MP) for 1 h. The membrane was decorated with mouse α-His primary antibody diluted 1:10.000 in TBST-T buffer with 5% (w/v) MP at 4 °C. After ≥12 h of incubation, the primary antibody was removed in three washing steps of 10 min with TBS-T buffer. The PVDF membrane was incubated with goat α-mouse antibodies diluted 1:5.000 in TBS-T buffer for 1 h at RT before the secondary antibody was removed in four subsequent washing steps of 10 min with TBS-T buffer. For visualisation of the secondary antibody by chemiluminescence, the PVDF membrane

was covered with ECL™ Western blotting developmental solution and developed for 1-10 min while images were recorded at a wavelength of 428 nm.

ESI-MS

Samples of *E. coli* and insect cell expressed hMiro1-His and insect cell expressed hMiro2-His as well as GST-hTRAK2-MBS and of the putative hMiro1-His/GST-hTRAK2-MBS complex were analysed regarding the identity of the proteins of interest by electrospray ionisation mass spectrometry (ESI-MS) at the Proteome Center Tübingen (PCT) by Katharina Zittlau (group of Prof. Maček, Quantitative Proteomics, Interfaculty Institute for Cell Biology, Eberhard Karls University Tübingen). For this purpose, the samples were analysed by SDS-PAGE and bands running at sizes similar to the proteins of interest were cut and sent for analysis.

Analytical SEC

The stability of the protein of interest, the formation of aggregates and the oligomeric state of the protein samples were monitored by analytical SEC. Unless indicated otherwise, samples were typically concentrated to 1-2 mg/mL with Amicon® Ultra-0.5 mL centrifugal filters and filtered with Corning®-Costar®-Spin-X® centrifugal filters. If an exchange of buffer was needed, small sample volumes of 100-200 µL were dialysed into the target buffer for ≥15 h in Slide-A-Lyzer® MINI Dialysis devices with a MWCO of 20 kDa. Protein samples were analysed on a Superdex™ 200 Increase 3.2/300 column installed on an Äkta Micro Ettan LC system. For the hMiro1/2 and hTRAK2 constructs, standard SEC buffer was used and modified as indicated at the individual experiment by adding additional buffer components such as calcium chloride ($CaCl_2$), nucleotides or detergents. Mim2 samples, expressed and purified by Janani Natarajan (group of Prof. Rapaport, Interfaculty Institute of Biochemistry, University of Tübingen), were analysed via analytical SEC using a Superdex™ 75 PC 3.2/30 column in Mim2 SEC buffer supplemented with detergents. Mim2 elution was monitored by the UV absorption at 280 nm and the size of the eluted protein was estimated according to a pre-determined standard curve.

Complex formation and pulldown experiments

For complex formation between hMiro1-His and GST-hTRAK2-MBS, the proteins were mixed in a 1:1 ratio in SEC buffer and incubated at 4 °C for 4 h. Thereafter, the putative complex was purified by preparative SEC and fractions containing both proteins were identified by SDS-PAGE. Peak fractions of the elution profile containing both proteins were split equally and incubated with either 40 µL HisPur™ Cobalt Resin or 40 µL glutathione agarose resin for 1 h. In addition, hMiro1-His and GST-hTRAK2-MBS were individually loaded onto the opposing resin as controls. The resin was

washed three times with SEC buffer and proteins were eluted in 20 µL SDS sample buffer (Table A.6) by heating of the samples to 98 °C for 5 min. The formation of a complex between hMiro1-His and GST-hTRAK2-MBS after 2 h of incubation in SEC buffer was also monitored by analytical SEC using a Superdex™ 200 Increase 3.2/300 column.

To increase the stability of hMiro1-His for crystallisation, hMiro1 specific nanobodies [141] were isolated from immunised alpacas or identified from synthetic nanobody libraries by F. Fagbadebo. hMiro1-His was mixed in a 1:1 ratio with the nanobodies in SEC buffer and incubated ≥18 h at 4 °C to enable complex formation. Thereafter, the stability and oligomerisation of hMiro1-His with the nanobodies was analysed by analytical SEC.

Circular dichroism spectroscopy

The folding of hMiro1-His and Mim2 was analysed by circular dichroism (CD) spectroscopy with a JASCO J-720 spectropolarimeter. Samples were diluted to 0.15-0.3 mg/mL with H_2O to reduce the concentration of buffer components and thus improve the signal-to-noise ratio. Spectra were collected at the range of 195-250 nm in the far-UV in a 1 mm quartz cuvette with a scanning speed of 20 nm/min and a band width of 1.0 nm. Ten accumulation cycles were recorded and averaged prior to a background correction by subtraction of similarly collected buffer signal. To estimate the secondary structure content, the recorded ellipticity signals were compared to theoretical spectra of purely α-helical, β-sheet or random coil proteins.

Dynamic light scattering

To determine the size distribution profile of hMiro1-AB_1-His before and after cleavage of the His_6-tag by the TEV protease, dynamic light scattering (DLS) was used. 20 µL of hMiro1-AB_1 at a concentration of 1.0 mg/mL were transferred in an ultra-micro 105.201-QS quartz cuvette and measured three times in a Zetasizer Nano ZS. The size distribution by mass was plotted for analysis of the polydispersity in the protein sample.

Thermal shift assay

The unfolding of Mim2 in different buffer compositions was monitored in a thermal shift assay (TSA) to establish improved buffer conditions for the purification of Mim2. For this purpose, protein at a concentration of 0.5-1.0 mg/mL was mixed with Protein Thermal Shift™ Dye [142] according to Table A.19. The protein melt reaction was performed in a QuantStudio™ Real-Time-PCR system at 25-99 °C with a ramp rate of 0.05 °C/s. Data was recorded with an excitation filter at 580 nm and an emission filter at 623 nm.

Table A.19: TSA reaction mix and melt reaction protocol [142]**.**

TSA reactions	Component	Volume [µL]
	Protein Thermal Shift™ Buffer	5.0
	Protein diluted to 0.1-1.0 mg/mL in buffer	12.5
	Protein Thermal Shift™ Dye (8x)	2.5

TSA run protocol	Step	Temperature [°C]	Time [s]
	1	25	120
	2	25 – 99 °C	+ 0.05 °C/s
	3	99	120
	4	25	∞

Endpoint malachite green GTPase activity assay

The GTPase activity of recombinant hMiro1-His expressed in High Five™ cells was determined one or two days post purification with an endpoint malachite green phosphate assay [143]. For this purpose, the protein was concentrated to 1.5 mg/mL and diluted to concentrations ranging from 0.25-6.43 µM in SEC buffer. To determine the functionality of the assay, recombinant Drp1, a GTPase involved in the fission of the mitochondria, was expressed and purified [140] and used as positive control at a concentration of 0.25-0.5 µM. The basal turnover rate of GTP in the presence of non-GTPase proteins was determined using the recombinant trimeric human adenovirus species G 52 fibre knob (HAdVG52-FK), expressed and purified by Katja Vonmetz (group of Prof. Stehle, Interfaculty Institute of Biochemistry, University of Tübingen). The size of HAdVG52-FK (67.2 kDa) is comparable to hMiro1-His and it was used at similar concentrations to hMiro1-His (1.0-5.0 µM) as negative control in the assay. To determine the GTPase activity of the proteins, samples were incubated with 0.1 mM GTP for 5-22 h at RT in SEC buffer with and without 2 mM $CaCl_2$. Ten to thirty minutes after the addition of the reaction reagents [143], the malachite green, molybdate and free orthophosphate formed a green complex that was quantified using a TECAN plate reader at 620 nm. The concentration of free phosphate resulting from the enzymatic activity of the protein was calculated with the help of a phosphate standard after correction of the baseline by subtraction of the absorption in control samples without protein. The experiments were reproduced in triplicates and the standard deviation was calculated. The usage of long-term stored GTP resulted in high free phosphate concentrations in some of the assays, which led to a decreased signal-to-noise ratio and increased errors.

A.3.2.6 Structure determination

Crystallisation

Concentrations of 1.9 mg/mL, 5.1 mg/mL or 10.4 mg/mL of *E. coli* expressed hMiro1-His and concentrations of 1.9 mg/mL, 4.7 mg/mL or 8.0 mg/mL of insect cell expressed hMiro1-His were used for crystallisation. Initial screens to identify crystallisation conditions for hMiro1(R450C)-His were set up at 5.2 mg/mL and for the hMiro1-His/GST-hTRAK2-MBS complex at a concentration of 4.9 mg/mL.

Potential aggregates were removed by either centrifugation at 16,100x g for 10 min or by filtering with a 0.22 µM filter. Crystallisation conditions were screened in 96-well sitting drop plates with commercial screens as indicated in Table A.22. Screens and protein drops were set up with a Gryphon pipetting robot. Crystallisation was ought to be achieved by vapour diffusion with 200 µL reservoir solution and a 400 nL protein drop comprising 200 nL concentrated protein and 200 nL reservoir solution. To allow for crystal growth, the sitting drop plates were incubated at 4 °C or 20 °C for up to 6 months.

For crystallisation, Mim2 was purified in 20 mM 3-(*N*-morpholino)propanesulfonic acid (MOPS) and 300 mM NaCl or 20 mM sodium phosphate buffer and 300 mM NaCl. Initial screening of crystallisation conditions for Mim2 were performed as described above except for the altered drop size of 200, 400 or 600 nL comprising protein at a concentration of 1.7 mg/mL, 3.0 mg/mL or 4.0 mg/mL and reservoir solution mixed in a 1:1 ratio. The used commercial screens are listed in Table A.20. Mim2 honey comb crystals were tested for their protein content by transfer of a few crystals in a drop of fresh mother liquor mixed with 0.1 µL Izit Crystal Dye.

Table A.20: Screening of crystallisation conditions for Mim2.

Protein	Concentration [mg/mL]	Temperature [°C]	Buffer	Drop ratio	Drop size [nL]	Commercial Screens
MIM2	1.7	20	MOPS	1:1	200	Wizard Classic 1 and 2 Block (Molecular dimensions) Wizard Classic 3 and 4 Block (Molecular dimensions)
	3.0	20	MOPS	1:1	600	Crystal Screen HT™ (Hampton Research)
	4.0	20	Sodium phosphate buffer	1:1	400	Crystal Screen HT™ (Hampton Research)

Crystal harvesting, cryo-protection and data collection

Crystals grown in Mim2 crystallisation trials were tested for their protein content and their ability to diffract in a RT diffraction experiment on a Rigaku MicroMax™-007 HF microfocus X-ray generator equipped with a MAR345 detector. For this purpose, crystals were mounted directly from the crystallisation drop onto 0.05-0.5 mm loops and tested with an exposure time of 5 min per image and an increment of 90 °C between single images. After elimination of crystals that showed diffraction patterns resembling salt crystals, the remaining crystals or crystals of similar appearance were transferred into cryo-protection solution (Table A.23) and then mounted into 0.05-0.5 mm loops. Test shots were obtained at beamline X06DA (PILATUS 2M-F detector) of the Swiss Light Source (SLS), Paul Scherer Institute, Villigen, Switzerland with a beam transmission of 100%, exposure time of 0.2 s and 90° rotations between single images.

A.4 RESULTS

This chapter comprises the results of the hMiro1 project. Purified hMiro1-AB$_1$-His and hMiro1-His have been used in Fagbadebo et al., 2022 [141] for alpaca immunisation, enrichment and selection of hMiro1 specific nanobodies and characterisation of the nanobodies. The manuscript of the purification of hMiro1-His from High Five™ cells is currently in preparation.

Annkathrin Scheck (AS), Sophia Kieferle (SK), Hsin-Yin Chang (HC), Leonard Jahnke (LJ), Funmi Fagbadebo (FF), Andreas Jenner (AJ), Katja Vonmetz (KV), Janani Natarajan (JN) and N. Bartlick (NB) have contributed to the work below. Corresponding affiliations are listed in the appendix section.

The study was designed by NB. All hMiro1/2 and hTRAK1/2 constructs were designed by NB and AS and SK assisted NB with cloning the constructs. Bacmid cloning of all constructs for insect cell expression and cell maintenance was carried out by NB. Expression and purification protocols for all hMiro1/2 constructs were established by NB. hMiro1 short constructs were expressed and purified by FF and NB for alpaca immunisation. Miro1 specific nanobodies were selected, enriched and characterised by FF. Nanobodies were expressed and purified by FF for binding analysis experiments carried out by NB in this study. Purification of hMiro1 short constructs was optimised by NB, AS and HC. Full-length hMiro1-His has been expressed in *E. coli* by NB, HC and LJ and in insect cells by NB. The expression and purification of hMiro1-His and hMiro2-His was optimised by NB and LJ. hMiro1-His from *E. coli* and hMiro1-His and hMiro2-His from insect cells were characterised by NB. Crystallisation trials of hMiro1-His were performed by NB, LJ and HC. AS and HC were responsible for the optimisation of the hMiro1(R450C)-His purification and AS for the crystallisation experiments. HC worked on the optimisation of the hMiro1(R272Q)-His purification. GST-hTRAK2-MBS was expressed and purified and complex formation with hMiro1-His was analysed by NB and LJ. SK and AS worked as assisting scientists under the supervision of NB on the project. NB supervised the lab rotation of HC and the project module and bachelor thesis of LJ during which they worked on the hMiro1 project. The Drp1 construct for the GTPase assay and the corresponding purification protocol was provided by AJ and the protein was purified by NB. The HAdVG52-FK protein used in the GTPase assay was expressed and purified by KV. JN provided purified protein for all Mim2 experiments. The SEC experiments were performed by NB and JN and the crystallisation and CD experiments were carried out by NB.

The constructs comprising PD related mutations of hMiro1 were designed based on previous findings by Lisa Schwarz (group of Dr. Fitzgerald, Department of Neurodegeneration, Hertie Institute for Clinical Brain Research, University of Tübingen) [113], [unpublished data], Julia Fitzgerald (Department of Neurodegeneration, Hertie Institute for Clinical Brain Research, University of Tübingen) and others [111].

A.4.1 Purification of hMiro1 short constructs

When we initiated our research on hMiro1, structural data of hMiro1 was limited to both EF hand domains and the cGTPase [40]. We suspected that determination of a full-length crystal structure would be dependent on the stabilisation of the likely more flexible nGTPase of hMiro1. Therefore, the production of hMiro1 specific nanobodies was initiated since such nanobodies were expected to serve as crystallisation chaperones, stabilising the nGTPase. As we initially struggled to express full-length hMiro1 and the production of nanobodies against the nGTPase of hMiro1 did not necessarily require full-length protein for the alpaca immunisation, smaller constructs, comprising only the nGTPase of hMiro1 and no, one or both EF hand domains were cloned, respectively. In accordance with the constructs used for hMiro1-B_1B_2C crystallisation [40], hMiro1-A, hMirol-AB_1 and hMiro1-AB_1B_2 were C-terminally His_6-tagged (Fig. A.7, A). Moreover, we tried to express constructs (Extended data, Table A.21) comprising an additional N-terminal Spot-Tag®, which specifically binds to Spot nanobodies. We planned to utilize the Spot nanobodies as crystallisation chaperones, however Spot®-tagged constructs never expressed, therefore, we focused on the initial plan to produce hMiro1 specific nanobodies.

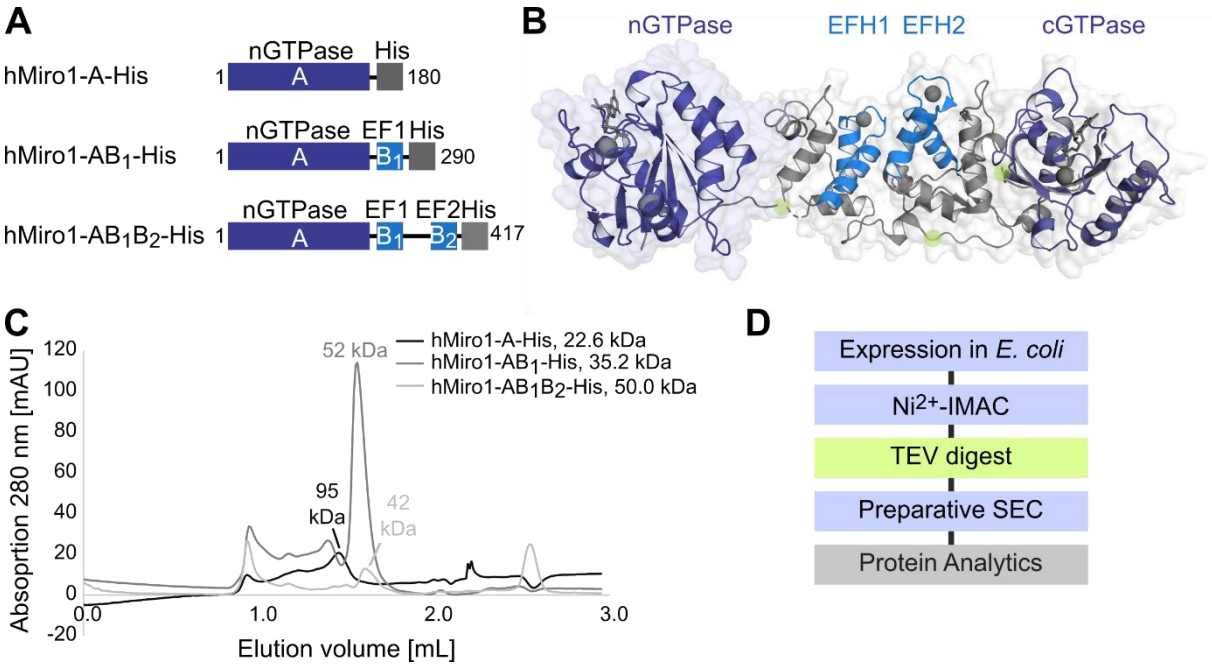

Figure A.7: hMirol-AB_1-His is more stable compared to other hMiro1 short constructs. (**A**) Construct design of the hMiro1 short constructs expressed in *E. coli* comprising the nGTPase (A, dark blue) and EF hand domains (B_1 and B_2, light blue). All functional constructs are C-terminally His_6-tagged. (**B**) Cartoon and surface representation of the structures of the nGTPase (PDB-ID: 6D71) [41] and the two EF hand domains and the cGTPase (PDB-ID: 5KTY) [40] of hMiro1. Construct boundaries are indicated in lime green. (**C**) Analytical SEC profiles of hMiro1 short constructs. hMiro1-AB_1-His elutes mainly in one species corresponding to a monomer or dimer (without cleavage of the His_6-tag) and was thus used for alpaca immunisation. (**D**) Purification strategy for the hMiro1 short constructs. The cleavage of the His_6-tag by TEV protease proved to be intolerable for the protein and was therefore not included in the purification strategy of later constructs.

hMiro1 short constructs were expressed in *E. coli* BL21 cultures, overnight at 18 °C. To determine soluble protein, it was critical to quickly reach and maintain 18 °C in the expression phase. The constructs were purified with a trimmed version of the purification protocol described in Klosowiak et al., 2016 [40] comprising an initial nickel IMAC, followed by cleavage of the C-terminal tag by TEV protease and a preparative SEC (Fig. A.7, D). The identites of the protein constructs were confirmed by Western blotting (Extended data, Fig. A.23).

hMiro1-A-His (Extended data, Fig. A.19) showed solid and reproducible expression and the majority of impurities could be removed during the initial nickel IMAC. The subsequent cleavage of the His_6-tag was confirmed by SDS-PAGE and the protein solution remained clear of visible aggregates. However, during the following concentration step the membrane of the concentrators tended to get clogged and the protein solution showed colour changes from colorless to yellow indicating that precipitation might be ongoing. Analysis of the protein by analytical SEC after the nickel IMAC revealed that the smallest peak (Extended data, Fig. A.19, E, peak 3) elutes at a volume of 1.45 mL, which corresponds to an expected molecular weight of around 95 kDa. Since hMiro1-A-His has a calculated molecular mass of 22.6 kDa, the protein clearly did not elute as a monomer from the analytical SEC. During the final preparative SEC, after TEV cleavage, the majority of the protein elutes in the void volume, revealing the instability of the protein.

As for hMiro1-A-His, expression of hMiro1-AB_1-His (Extended data, Fig. A.20) worked reliably and a substantial amount of protein was obtained during the first purification step. Because we could not confirm successful cleavage of the His_6-tag by SDS-PAGE, we analysed the protein before and after cleavage by analytical SEC, CD spectroscopy and DLS. The analytical SEC revealed a substantial reduction of the peak eluting at 1.56 mL corresponding to monomeric or dimeric protein (Extended data, Fig. A.20, E, peak 4) and the DLS showed that most of the protein shifted to larger species (Extended data, Fig. A.20, G). The circular dichroism spectrum (Extended data, Fig. A.20, F) indicated underlying changes in the secondary structure of hMiro1-AB_1. However, the results were not conclusive, hence, we decided against cleaving of the His_6-tag.

hMiro1-AB_1B_2-His was expressed in smaller amounts than hMiro1-A-His and hMiro1-AB_1-His and the protein was unable to saturate the 5 mL HisTrap™ FF Crude column (Extended data, Fig A.21, B-C), allowing a lot of impurities to bind to the column as well. Upscaling or switching to a smaller column would have solved that issue, however, the subsequent preparative SEC (Extended data, Fig. A.21, D) revealed significant aggregation of the protein making the construct unsuitable for our purposes. We planned to optimise the hMiro1 short constructs by removing C-terminal linker regions that were left in the initial construct design. Especially the long linkers between EF1 and EF2 of hMiro1 and EF2 and the cGTPase of hMiro1 show potential for optimisation (Fig. A.7, B). However, the linkers are all located at the bottom side of hMiro1 and form an extended platform that could be important for the stability and integrity of the protein. We optimised our construct design and the new constructs showed

similar expression levels compared to the established constructs except for the highly desired optimised hMiro1-AB_1B_2-His construct.

At this point, we assessed the quality of the hMiro1-His constructs as optimisation of the new constructs proved to be time consuming and we had to proceed with the animal immunisation. The comparison of the analytical SEC chromatograms of the hMiro1-His short constructs (Fig. A.7, C) reveals that hMiro1-AB_1-His was the only suitable candidate, as it showed less aggregation and a substantial fraction of the protein eluted as monomeric peak. Hence, we isolated the monomeric peak after the preparative SEC and used it for the alpaca immunisation. Shortly after the immunisation was performed, we found suitable expression conditions for full-length hMiro1-His. Therefore, the optimisation of the hMiro1 short constructs was discontinued.

A.4.2 Purification of full-length hMiro1-His

Starting from our previous results on the purification of hMiro1 short constructs, we initially expressed hMiro1-His in *E. coli* BL21 cells. We tested differentially tagged constructs (Extended data, Table A.21) including hMiro1 fused to a N-terminal MBP-tag, a N-terminal Spot-Tag®, a C-terminal His_6-tag or both a N-terminal Spot-tag® and a C-terminal His_6-tag. All constructs comprised both the nGTPase and the cGTPase and the calcium-binding EF hand domains (AA 1-592) of hMiro1. The C-terminal α-helical transmembrane anchor (AA 593-618) was excluded to increase the solubility of hMiro1 and simplify downstream experiments. hMiro1-His was the only construct showing significant expression levels when expressed overnight in auto induction medium. We confirmed the identity of the expressed protein with a size of 70.0 kDa by ESI-MS and Western blotting (Extended data, Fig. A.23). As previously reported [40], [41], the expression temperature had to be set to a maximum of 18 °C to gain soluble protein. Our additional attempts to express hMiro1-His in *E. coli* Shuffle® T7 or ArcticExpress cells to account for the temperature sensitivity remained unsuccessful. Based on previously published results [34], [40], [41] and our results on the hMiro1 short constructs, we established a two-step purification protocol for hMiro1-His comprising an initial nickel IMAC followed by a preparative SEC. Since the expression level of hMiro1-His was comparably low with about 4-8 mg protein per 40 g *E. coli* pellet eluting from the nickel IMAC many impurities were able to bind to the unsaturated column material. To minimise unspecific binding during the affinity purification, the column was switched to a HiTrap™ Talon™ crude column, which has a higher selectivity for His-tagged proteins and a five times smaller binding capacity (Extended data, Fig. A.22, A-D). hMiro1-His purified by cobalt IMAC also showed less aggregation during the subsequent concentration step. The following preparative SEC revealed that hMiro1-His does not elute as single monomeric species (Extended data, Fig. A.22, E-F) but instead elutes as multiple distinct peaks and a large fraction of the protein elutes in the void volume of the column indicating ongoing aggregation.

In order to stabilise hMiro1-His in its monomeric form, the elution profile of hMiro1-His upon altering buffer components such as the salt concentration, the concentration of reducing reagents or the addition of detergents was monitored by analytical SEC. For this purpose, the smallest species (Extended data, Fig. A.22, E-F, peak 3) eluting as distinct peak from the preparative SEC was isolated and used for downstream experiments. hMiro1-His obtained as a result, elutes during analytical SEC experiments at an elution volume corresponding to approximately 90 kDa (Fig. A. 10, B and D, peak 2). The calculated molecular weight of hMiro1-His of 70.0 kDa suggest that this species is likely monomeric, hence we will from now on refer to this species as monomeric hMiro1-His.

In previous studies [40], [41] hMiro1 constructs have been purified by ion exchange chromatography after dialising the protein against low salt buffers. Our *E. coli* expressed hMiro1-His construct showed visible white aggregates when transferred in low or high salt buffer with no significant change in the ratio between monomeric and oligomeric hMiro1-His (Fig. A.8, A). For this reason, the additional ion exchange chromatography was excluded in our purification strategy. hMiro1-His has 18 cysteine residues of which four are surface exposed, two at the junction between the nGTPase and EF1, C175 and C185, and two within the EF2 domain, C322 and C350, respectively (Extended data, Fig. A.24, C). In our experiments the presence of reducing reagents during the purification of hMiro1-His was critical to determine soluble protein but the occurrence of oligomeric hMiro1-His could not be prevented even by adding high concentrations of DTT and TCEP (Extended data, Fig. A.24, A-B). Since hMiro1 is a membrane protein with an α-helical transmembrane anchor we considered the addition of detergents to stabilise hMiro1-His. However, in the presence of 0.2 % N-Decyl-β-D-maltopyranoside (DM) (Fig. A.8, B) or 0.02% Tween-20 the ratio between monomeric and oligomeric hMiro1-His was unaltered, whereas the addition of 1% OG led to the formation of white aggregates.

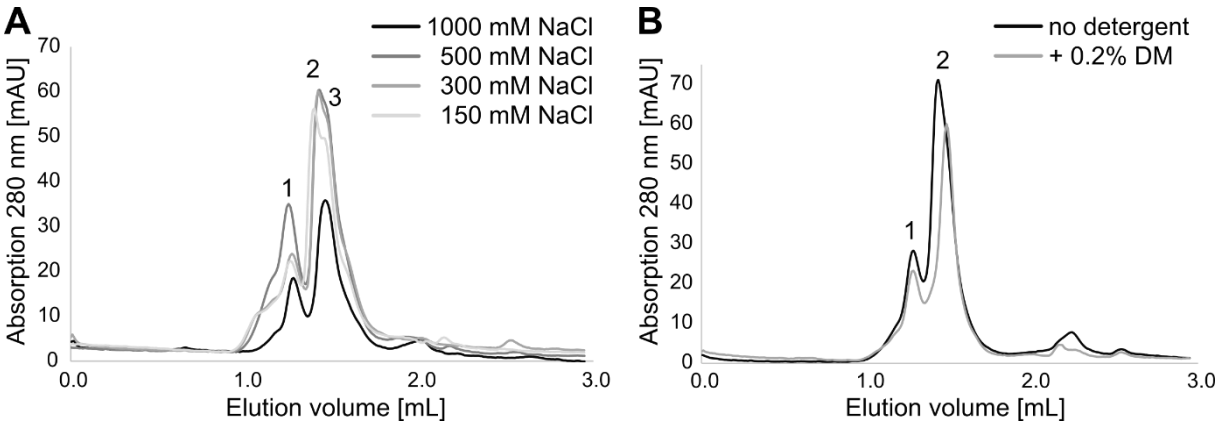

Figure A.8: Optimisation of the buffer components during hMiro1-His purification. (**A**) Analytical SEC of hMiro1-His in the presence of different NaCl concentrations. The intensity of hMiro1-His with 1000 mM NaCl is reduced as the protein precipitated visibly and less protein could be loaded onto the column after filtering. (**B**) In the presence of 0.2 % DM, the peak position of monomeric hMiro1-His (peak 2) shifts during the analytical SEC.

During the optimisation of the *E. coli* hMiro1-His purification conditions we recognised, that the peak position of monomeric hMiro1-His shifted within a 20 kDa range between runs. In some cases, we even observed two individual peaks (Fig. A.8, A, peak 2 and 3) leading us to the assumption hMiro1-His

could undergo conformational changes. Although we could not test our theory, the reported SEC-SAXS data on full-length hMiro1-His [41] shows that hMiro1 is indeed not a linear protein but rather L-shaped. We propose that the nGTPase is flexibly linked to the EF1 domain as a shift from an L-shaped conformation to a more linear conformation could explain the different elution profiles of hMiro1-His in our analytical SEC experiments.

When we confirmed the identity of *E. coli* expressed hMiro1-His by ESI-MS, the co-purification of the *E. coli* bifunctional polymyxin resistance protein ArnA (ArnA) with a size of 74.3 kDa was determined. Although ArnA was only detected in the wash fractions of the cobalt IMAC, the bands in the SDS-PAGE reveals that its size is very similar to hMiro1-His and remaining ArnA would be difficult to separate during the preparative SEC. Another aspect that prevented a comprehensive characterisation of hMiro-His from *E. coli* were the issues we faced regarding the reproducibility of the protein expression and the repeated signs of aggregation during the subsequent purification. Since we also were unable to determine structural data of hMiro1-His from *E. coli*, we reappraised our strategy.

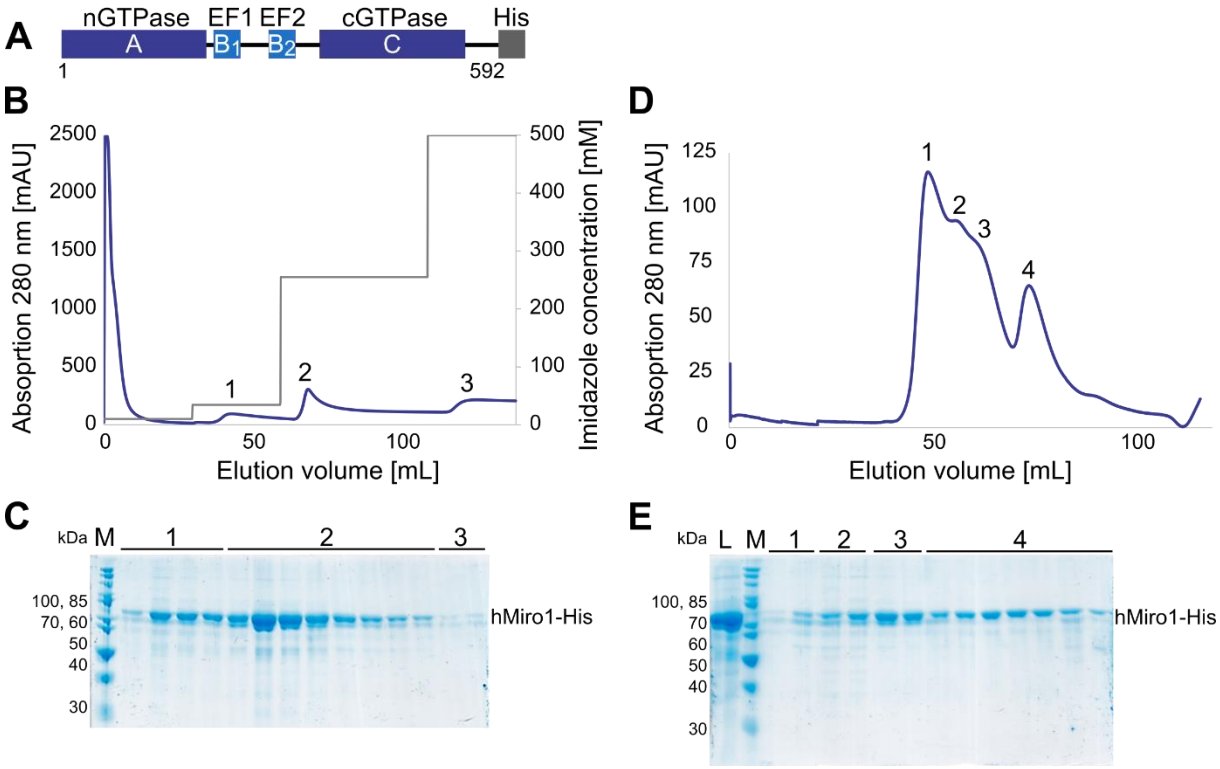

Figure A.9: hMiro1-His can be purified from High Five™ cells with a two-step protocol. (**A**) hMiro1-His construct design for both *E. coli* and insect cell expression with two GTPase domains (dark blue) flanking the EF hand domains (light blue). The construct was codon optimised and C-terminally His_6-tagged. (**B**-**C**) The elution profile and corresponding SDS-PAGE analysis of the hMiro1-His cobalt IMAC reveal, that the target protein is separated from most impurities. (**D**-**E**) The chromatogram of the preparative SEC reveals that hMiro1-His does not elute as single monomeric peak. The corresponding SDS-PAGE reveals the presence of hMiro1-His in all peak fractions. (**B**-**D**) Loading of the peak fractions of the cobalt IMAC and the preparative SEC onto the SDS-PAGE gels as indicated by numbers. Recombinant hMiro1 has a calculated molecular mass of 70.0 kDa and runs above the 70 kDa marker band. L = load, M = marker

hMiro1 is a heavily post-translationally modified protein [40], [71], [104], [144], [145] that displays strong phenotypes [28], [48], [56] when over-expressed, even across species [36]. The expression of a similar codon-optimised hMiro1-His construct (Fig. A.9, A) in High Five™ insect cells gave rise to sufficient amounts of soluble protein and, although carried out at 27 °C, led to reliable and reproducible results. The optimised two-step purification protocol from *E. coli* hMiro1-His was transferable to hMiro1-His expressed in insect cells (Fig. A.9, B-D). Insect cell expressed hMiro1-His also displayed two distinct bands in the SDS-PAGE analysis of the cobalt IMAC and the following preparative SEC. In contrast to *E. coli* expressed hMiro1-His, both bands were identified as hMiro1-His in ESI-MS experiments. The expression in High Five™ cells probably produced differentially post-translationally modified versions of hMiro1-His.

Although insect cell expressed hMiro1-His appeared to be comparably stable during the purification process and no signs of precipitation were recognisable, the final preparative SEC revealed that hMiro1-His eluted in several peaks, indicating distinct species (Fig. A.9, D). If isolated, monomeric hMiro1-His does not remain stable but instead forms new oligomers within hours, hinting at an equilibrium between monomeric and oligomeric hMiro1.

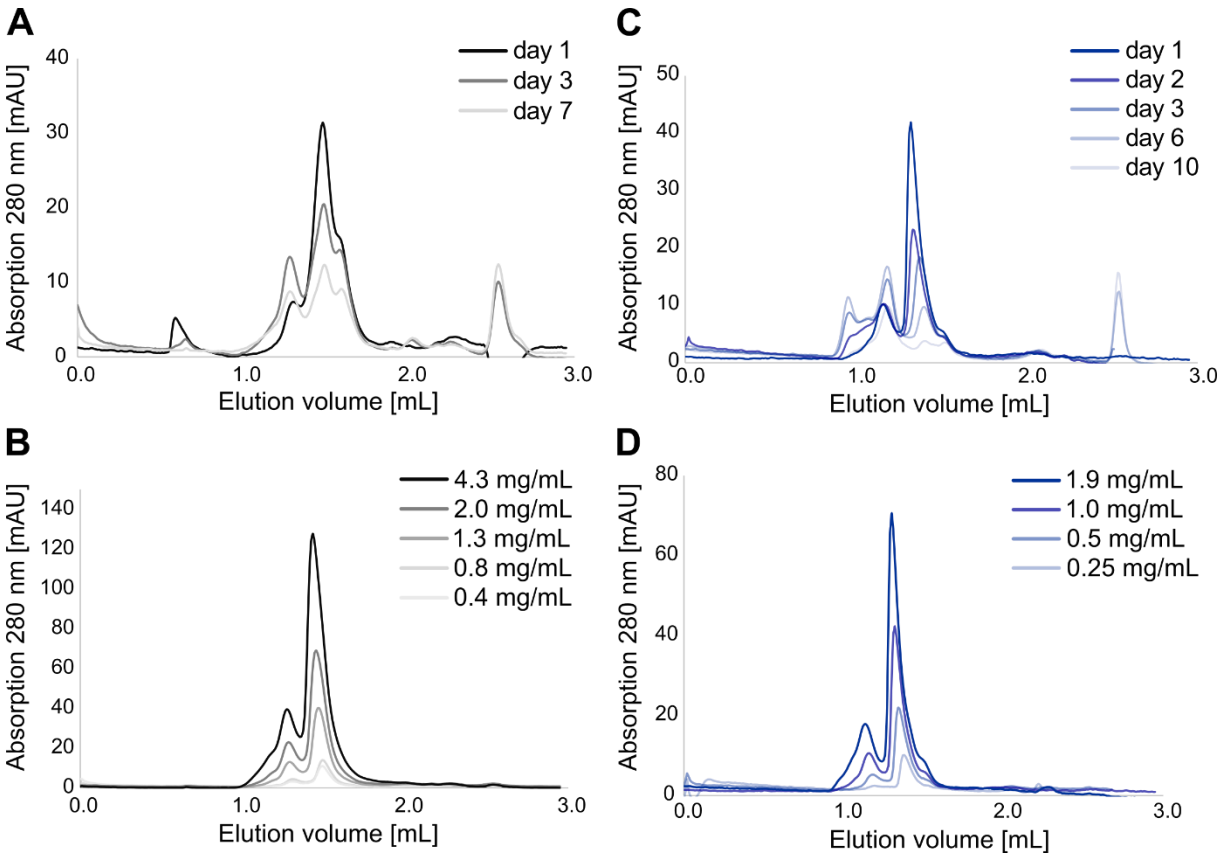

Figure A.10: Analysis of the oligomeric state of hMiro1-His from *E. coli* BL21 and High Five™ insect cells. Elution profiles of analytical SEC runs of hMiro1-His expressed in (**A**-**B**) *E. coli* (grey-black) or (**C**-**D**) insect cells (blue) (**A** and **C**) monitored over time or (**B** and **D**) at increasing concentrations. hMiro1-His oligomerises in a time-dependent manner but concentration-independent.

As the aim of this study was the determination of a crystal structure of full-length hMiro1-His, we worked with comparably high concentrations during the purification process, far beyond physiological concentrations. To address if the high concentrations of hMiro1-His caused the appearance of oligomers, samples of hMiro1-His with increasing concentrations were compared by analytical SEC. A comparison of the results for hMiro1-His from *E. coli* and insect cells reveals that, independent of the expression host, increasing concentrations do not alter the ratio between monomeric and oligomeric hMiro1-His (Fig. A.10, B, D). Instead, monomeric hMiro1-His shifts from the monomeric to oligomeric state in a time dependent manner, ultimately resulting in precipitated protein (Fig. A.10, A, C).

Since super-resolution studies on hMiro1/2 on the mitochondrial outer membrane [49] indicate that hMiro1/2 is not necessarily monomeric *in vivo*, we decided to investigate the oligomerisation tendency of hMiro1-His in the context of its ligands as described below. Full-length hMiro1-His from *E. coli* and High Five™ cells, expressed and purified as described here, has been used by F. Fagbadebo for the selection, enrichment and characterisation of hMiro1 specific nanobodies [141].

A.4.3 Characterisation of hMiro1-His in the presence of its non-protein ligands

The hMiro1 regulated mitochondrial trafficking has been shown to be dependent on cytosolic calcium levels [21], [29], [48]. Since hMiro1 harbours two calcium binding EF hands it is highly likely that calcium binding by hMiro1 induces conformational changes within the protein leading either to a displacement of the motor proteins from the microtubule track [21] or to a disconnection of the motor proteins from the mitochondrial acceptor hMiro1 [29]. To test the influence of calcium on the stability of hMiro1-His, the protein was monitored in analytical SEC experiments with 1 mM magnesium, 2 mM calcium or none of the aforementioned ions. *E. coli* expressed hMiro1-His precipitated significantly during the dialysis into calcium containing buffer, which interfered with the analysis of the results (Extended data, Fig. A.25, D). We recognised an overall reduction of soluble hMiro1-His protein in the presence of calcium ions and a shift in the ratio of monomeric and oligomeric hMiro1-His towards more oligomeric protein in the absence of both ions. Since *E. coli* expressed hMiro1-His generally had stability issues throughout the purification process and High Five™ expressed hMiro1-His showed overall improved behaviour, we repeated the experiments with insect cell expressed hMiro1-His. hMiro1-His displayed a clear tendency for oligomerisation and aggregation in both the presence of calcium ions (Fig. A.11, A) and the absence of both magnesium and calcium (Extended data, Fig. A.25, A). In contrast, the shift from monomeric to oligomeric hMiro1-His is slowed down in the presence of magnesium ions (Extended data, Fig. A.25, B). In summary these experiments show that magnesium ions have a positive effect on the stability of hMiro1-His, but they cannot prevent the oligomerisation entirely.

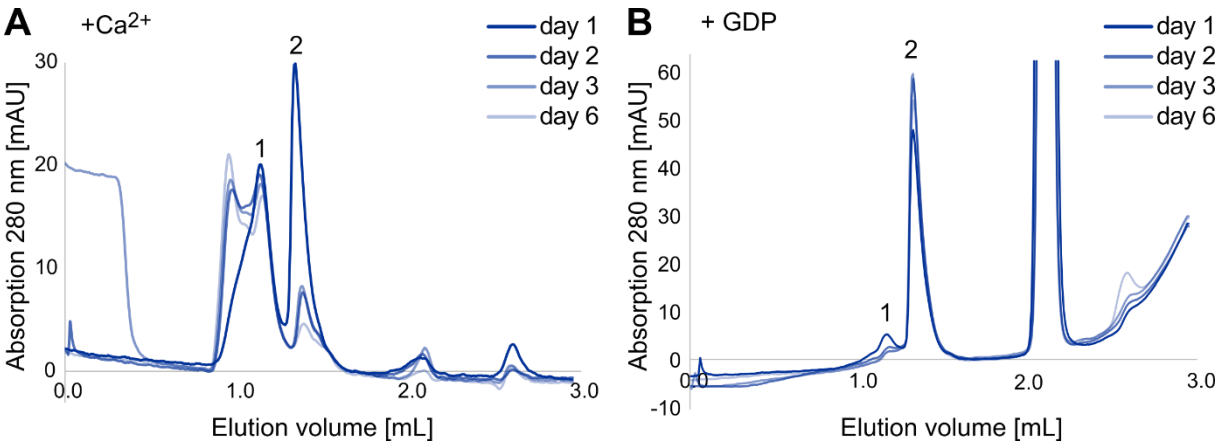

Figure A.11: hMiro1-His in the presence of non-protein ligands. (**A**) hMiro1-His expressed in insect cells, in the presence of 2 mM $CaCl_2$ over the course of 6 days. The analytical SEC shows the shift of monomeric hMiro1-His (peak 2) towards oligomeric hMiro1-His. (**B**) Addition of 2 mM GDP stabilises the insect cell expressed hMiro1-His monomer. Samples for the analytical SEC were stored at approximately 4 °C between runs.

The Miro proteins carry an atypical domain organisation including two Ras-like GTPAses, which makes them a unique protein family [[40], [56], [146]]. While the role of the calcium-binding EF hands of hMiro1 has been explored extensively [21], [22], [29], [147], the role of the GTPase domains regarding the diverse functions of hMiro1 remains elusive. A recent publication has analysed the GTPase activity of the hMiro1/2 GTPAse domains, revealing that both domains harbour the capability of hydrolysing GTP [44]. We investigated if nucleotides could be involved in the stabilisation of hMiro1 in order to obtain a sample suitable for crystallisation. We used either 2 mM GDP or 2 mM GMPPNP, a non-hydrolysable GTP analogue in our analytical SEC experiments. *E. coli* hMiro1-His showed severe signs of aggregation during storage at 4 °C, which made it very difficult to load comparable amounts of protein onto the SD200 3.2/300 column, leading to inconclusive results (Extended data, Fig. A.26, A-C). In contrast, insect cell expressed hMiro1-His displayed a significant increase in stability of the monomer in the presence of either GDP (Fig. A.11, B) or GMPPNP (Extended data, Fig. A.26, E). We additionally tested if the presence of GDP throughout the purification process would stabilise monomeric hMiro1-His and if already oligomerised hMiro1-His could be rescued by the addition of GDP or GMPPNP. However, it appears that previously oligomerised protein cannot be transferred back into the monomeric state. We conclude that binding of nucleotides by the GTPase domains of hMiro1 stabilises the protein in its monomeric form and propose that the nucleotide-bound state of hMiro1 might be important for the regulation of the oligomerisation of hMiro1 *in vivo* [49].

A.4.4 hMiro1 has a high α-helical secondary structure content

The structures of hMiro1-B_1B_2C (PDB-ID: 5KTY) and hMiro1-A (PDB-ID: 6D71) display a high overall α-helical secondary structure content of 46.3% in the GTPase and EF hand domains which are connected by extended coil-coil linkers (39.5%) [40], [41]. To ensure that our hMiro1-His constructs are properly folded we analysed their secondary structure by far-UV CD spectroscopy.

Both hMiro1-His purified from *E. coli* and insect cells showed the expected negative peaks for α-helical structure content at 208 and 222 nm and a positive slope below 195 nm (Fig. A.12, A-B). A comparison to a hMiro1-His sample that was frozen (Fig. A.12, A, grey) between the purification and the CD experiment reveals the negative impact of freezing on the folding of hMiro1-His. Since both GDP and GMPPNP absorb strongly in the far-UV, the experiments could only be performed in the absence of both nucleotides. Nevertheless, especially for insect cell expressed hMiro1-His we observed the expected α-helical fold, even in the absence of any nucleotides.

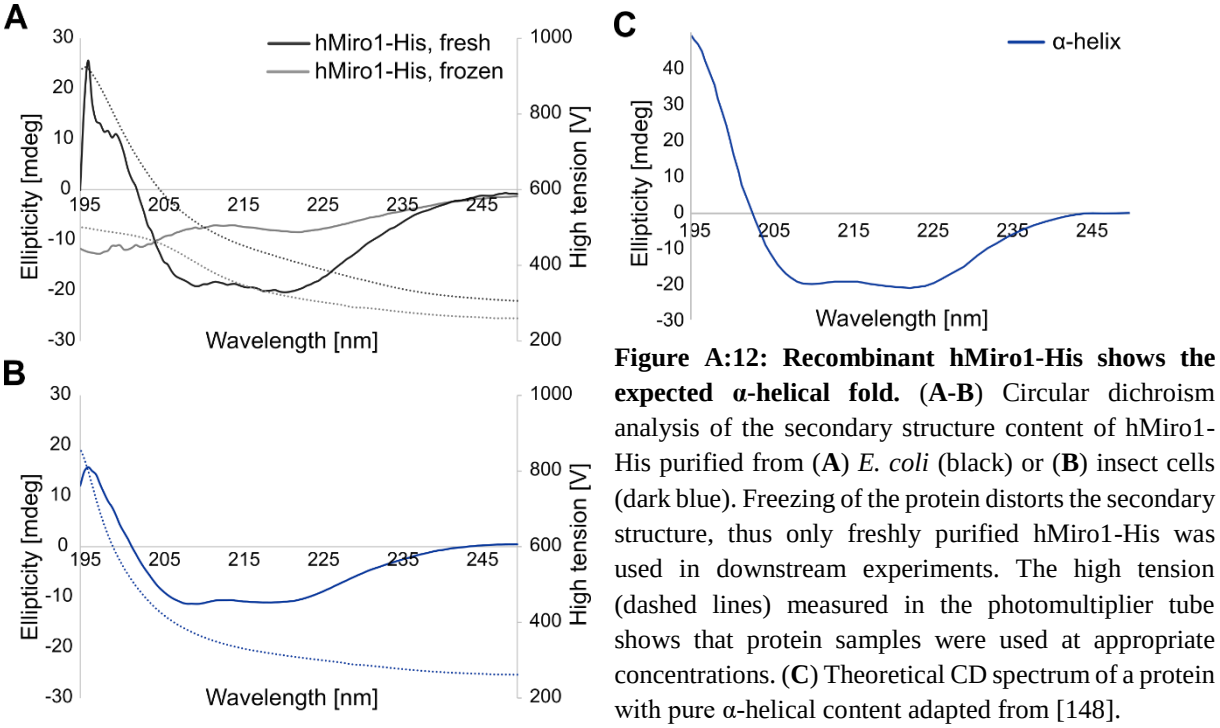

Figure A:12: Recombinant hMiro1-His shows the expected α-helical fold. (**A-B**) Circular dichroism analysis of the secondary structure content of hMiro1-His purified from (**A**) *E. coli* (black) or (**B**) insect cells (dark blue). Freezing of the protein distorts the secondary structure, thus only freshly purified hMiro1-His was used in downstream experiments. The high tension (dashed lines) measured in the photomultiplier tube shows that protein samples were used at appropriate concentrations. (**C**) Theoretical CD spectrum of a protein with pure α-helical content adapted from [148].

A.4.5 Crystallisation attempts with hMiro1-His

Previous structural studies on the hMiro proteins [40], [41] were unable to determine high-resolution structures on the full-length proteins. For hMiro1, the flexibility between the nGTPase and the remaining portion of the protein likely hinders the crystallisation. However, for the purpose of determining structural data on full-length hMiro1 our strategy included the stabilisation of the nGTPase of hMiro1 by hMiro1 specific nanobodies [141]. Throughout this study, we tested a variety of hMiro1 specific nanobodies derived from either immunised alpacas or synthetic nanobody libraries [149] for their capability of stabilising hMiro1 in analytical SEC experiments (Extended data, Fig. A.27, A-C). Albeit some nanobodies were able to alter the elution profile of hMiro1, none of them were able to stabilise monomeric hMiro1 and some even accelerated the shift from monomeric to oligomeric hMiro1. One major issue in these experiments was the incompatibility of the buffer conditions of hMiro1 and the nanobodies. Especially the DTT needed to prevent hMiro1 from aggregating critically impacted the proper folding of some of the nanobodies.

Since we did not observe significant improvements in the stability of hMiro1 through the addition of nanobodies, we proceeded with crystallising hMiro1 without the hMiro1 specific nanobodies. We tested both *E. coli* and insect cell expressed hMiro1 at different concentrations and at 4 °C or 20 °C (Extended data, Table A.22). As the oligomeric state of hMiro1 is under discussion in recent literature [49], we also tried to crystallise oligomeric hMiro1, although we were unable to isolate a specific oligomeric species of the protein. Once we recognised the promising stabilisation of monomeric hMiro1 through the addition of GDP (Fig. A.11, B), we were optimistic that the presence of GDP would aid the crystallisation of hMiro1. However, to date none of our crystallisation attempts yielded any protein crystals.

A.4.6 hMiro1 is an active GTPase

Our unsuccessful attempts to crystallise full-length hMiro1 made us question, if recombinant hMiro1, although displaying folding in the CD experiments, is fully functional and can be used in *in vitro* experiments to study hMiro1. The GTPase activity of the individual GTPase domains of hMiro1 and hMiro2 has been qualitatively shown for recombinantly expressed single domain proteins [44]. We determined the GTPase activity of High Five™ expressed hMiro1-His with a similar endpoint malachite green GTPase activity assay. To ensure the functionality of the assay, we included the HAdVG52-FK, a trimeric protein of similar size to hMiro1-His with no GTPase domain, and Drp1, a GTPase of the MOM that is required for mitochondrial fission [150], as negative and positive control, respectively. As the dynamin-related protein Drp1 is expected to display strong GTPase activity it had to be used at 10 times lower concentrations of 0.2-0.5 µM to function within the range of the malachite green assay. In contrast, hMiro1 and HAdVG52-FK were used at higher concentrations up to 6.43 µM.

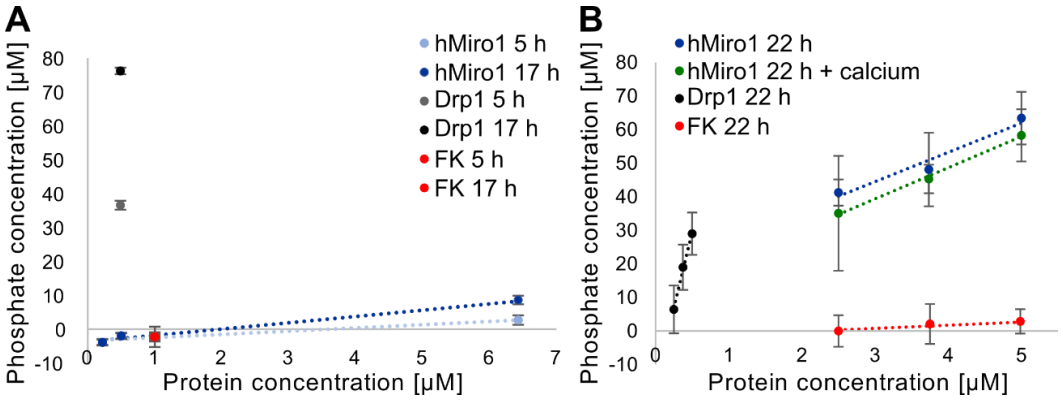

Figure A.13: Recombinant hMiro1-His shows GTPase activity. (**A**-**B**) Endpoint malachite green GTPase activity assay of insect cell expressed hMiro1-His after (**A**) 5 h incubation, 17 h incubation or (**B**) 22 h incubation with GTP. The GTPase Drp1 and the HAdVG52-FK (FK) are used as positive and negative control, respectively. Error bars in (**B**) are increased due to the usage of long-term stored GTP, which resulted in high free phosphate levels within the assay.

As expected, HAdVG52-FK showed no GTPase activity throughout the assay, while Drp1 displayed strong GTPase activity, which lead to increasing phosphate concentrations according to the increase in

concentration of Drp1 or the incubation time. On the contrary, hMiro1-His shows slow, calcium-independent GTPase activity (Fig. A.13, A-B), hinting towards a proper folding and functionality of the protein. The activity of hMiro1-His could only be determined qualitatively as the assay was executed at RT which influenced the stability of hMiro1-His and the used GTP. Moreover, the results were strongly influenced by the time delay between the purification of the protein and the assay execution, which indicates that oligomeric hMiro1 might not be as active as monomeric hMiro1. Our assay demonstrates that hMiro1-His is not only properly folded but also an active, functional GTPase.

A.4.7 Purification of patient derived hMiro1 PD mutants

hMiro1 is a phosphorylation target of PINK1 [151] in the PINK1/Parkin-mediated mitophagy pathway for damaged mitochondria and gets subsequently ubiquitinated by Parkin [40], [106], [152], [153]. Recent studies identified mutations in *RHOT1*, the gene encoding hMiro1, in PD patients and characterised the resulting cellular phenotypes [111], [112]. With the aim of a structural characterisation of two of the PD-related mutations of hMiro1, R272Q (Fig. A.14, A) and R450C (Fig. A.14, C) [111], [113], we cloned the mutations into the hMiro1-His construct for *E. coli* expression.

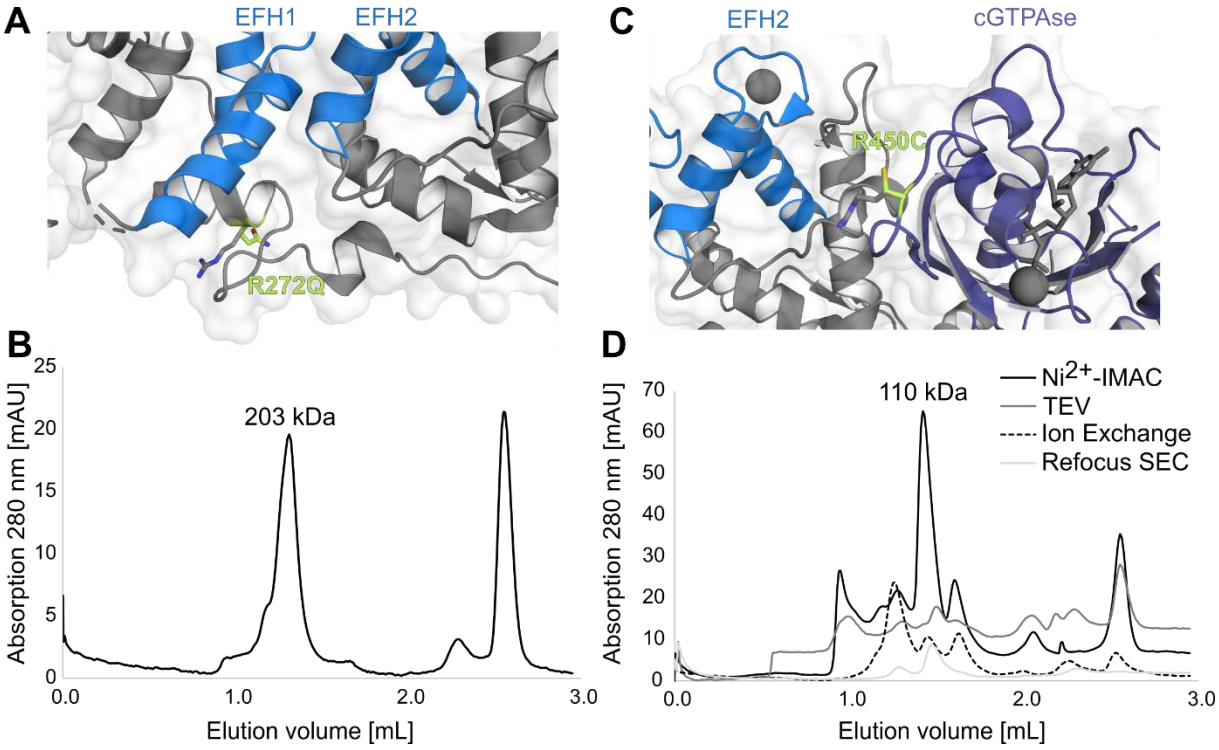

Figure A.14: Analysis of PD-related mutations of hMiro1. (**A, C**) Structure of hMiro1-B_1B_2C (PDB-ID:5KTY) in surface and cartoon representation with highlighted position of the PD related mutations (**A**) R272Q or (**C**) R450C in lime green stick representation. Mutations were implemented by Pymol™ 2.4.1 and both the wt residues and the mutations are shown. Calcium-binding EF hands are light blue and the cGTPase is dark blue. (**B**, **D**) Analytical SEC elution profiles of (**B**) hMiro1(R272Q)-His and (**D**) hMiro1(R450C)-His. The oligomeric state of hMiro1(R272Q)-His was analysed after the preparative SEC, while hMiro1(R450C)-His was analysed at different steps of the purification process as indicated.

Both hMiro1(R272Q)-His and hMiro1(R450C)-His were expressed in conditions similar to those used for hMiro1-His. The expression levels of hMiro1(R272Q)-His were slightly reduced compared to the wild type (wt) while hMiro1(R450C)-His was expressed at a similar rate compared to hMiro1-His. The expression of the hMiro1 PD mutants was confirmed by Western blotting (Extended data, Fig. A.23). For hMiro1(R272Q)-His, the two-step purification protocol of hMiro1-His, comprising an initial nickel IMAC followed by a preparative SEC, was adapted (Extended data, Fig. A.28). In contrast to wt hMiro1-His, hMiro1(R272Q)-His showed increased signs of aggregation during the SEC and did not elute as monomer from the SD200 16/60 column. Instead, the elution volume of the peak containing the smallest version of hMiro1(R272Q)-His rather fits to the size of a dimer or trimer of hMiro1 (Extended data, Fig. A.28, D, peak 3). To further estimate the size of the hMiro1(R272Q)-His oligomer we loaded the protein on an analytical SEC, where it eluted at an elution volume corresponding to 200 kDa (Fig. A.14, B). The hMiro1-His monomer elutes earlier than expected from the calculated molecular mass (70.0 kDa) at an elution volume corresponding to 90-110 kDa, likely due to the elongated shape of the protein. Moreover, we noticed that the position of the monomeric peak slightly varies between runs, hinting towards possibly ongoing alterations in the conformation of hMiro1-His. Based on the elution profile of monomeric hMiro1-His, we propose that hMiro1(R272Q)-His likely exists as dimer or trimer in the preparative and analytic SEC. Because hMiro1(R272Q)-His showed severe signs of aggregation during the purification process and lacked stability once purified, we did not proceed towards crystallisation of this PD-related mutant.

During the purification of hMiro1(R450C)-His (Extended data, Fig. A.29), we noticed that this mutant did behave similarly to wt hMiro1-His throughout the purification process. hMiro1(R450C)-His was expressed at similar rates and eluted with a comparable elution profile during the nickel IMAC (Extended data, Fig. A.29, B-C). The protein significantly aggregated upon cleavage of the His_6-tag by TEV protease as evident from the analytical SEC experiments (Fig. A.14, D). To increase the purity of the protein we tried to establish an ion exchange chromatography (Extended data, Fig. A.29, D-E) as an additional purification step between the initial nickel IMAC and the final preparative SEC, however, hMiro1(R450C)-His precipitated heavily in the low salt buffer (20 mM NaCl). Moreover, after the ion exchange chromatography, the protein did not elute as a monomer in the analytical SEC. Therefore, we kept the original two-step purification protocol and used the purified protein after the preparative SEC (Extended data, Fig. A.29, F-G) for downstream crystallisation experiments. In contrast to hMiro1(R272Q)-His, hMiro1(450C)-His did elute in the range of monomeric hMiro1-His from the analytical SEC, at 110 kDa. Our attempts to crystallise hMiro1(R450C)-His at 4 °C did not lead to the formation of any protein crystals. Due to time restrains we focused on the optimisation of the wt hMiro1-His expression and purification.

A.4.8 Purification of full-length hMiro2 from insect cells

Studying hMiro2 has proven to be a big challenge in previous studies as Miro1 can substitute for many functions of hMiro2 [28]. Especially in mitochondrial trafficking, the role of hMiro2 is likely limited to connecting mitochondria to microtubules, while the motility of mitochondria is not significantly reduced in the absence of hMiro2 [28], [37]. To date, the structural data on hMiro2 is limited to a high resolution structure of the cGTPase [40] and additional low resolution SEC-SAXS data [41] on the full-length protein.

In order to obtain additional structural data on full-length hMiro2, we initially attempted to express a C-terminally His_6-tagged construct, similar to hMiro1-His, in *E. coli*. Because we could not see any expression for hMiro2-His, we tested different construct lengths and tags (Extended data, Table A.21). Among the tested constructs, an N-terminally GST-tagged construct comprising both GTPase domains and the EF hand domains, GST-hMiro2, and a C-terminally His_6-tagged construct comprising only the nGTPase and the EF1 domain, hMiro2-AB_1-His showed significant expression levels. However, the purification of these constructs remained challenging as both GST-hMiro2 and hMiro2-AB_1-His showed strong tendencies to form inclusion bodies during expression and aggregated during purification.

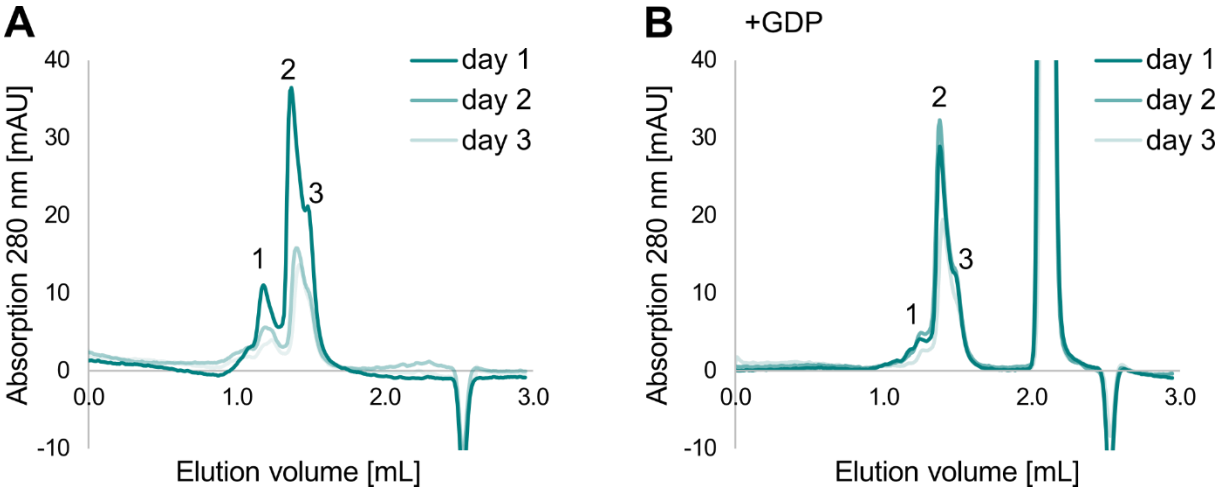

Figure A.15: hMiro2-His stability in the presence and absence of 2 mM GDP. Analytical SEC experiments with purified hMiro2-His at one, two or three days after purification. (**A**) Without GDP, hMiro2-His quickly aggregates after purification. A significant portion of the protein elutes on day 1 as monomer at 90 kDa (peak 2) and as dimer/trimer at approximately 205 kDa (peak 1). (**B**) With 2 mM GDP hMiro2-His gets partially stabilised. A reduction in monomeric protein can only be seen at day 3.

On the basis of the promising results from insect cell expressed hMiro1-His, we designed a similar construct for full-length hMiro2 (Extended data, Fig. A.30, A) expression in High Five™ cells. The two-step purification protocol from hMiro1-His was adapted for hMiro2-His including a cobalt IMAC and a follow-up preparative SEC (Extended data, Fig. A.30, B-E). Although most of hMiro2-His eluted as oligomers and aggregates from the preparative SEC (Extended data, Fig. A.30, D-E), we were able to isolate a small portion of monomeric hMiro2-His for downstream experiments. Analytical SEC experiments revealed the aggregation and reduction in monomeric hMiro2-His (Fig. A.15, A, peak 2)

setting in quickly after purification. Since monomeric hMiro1-His was stable in the presence of 2 mM GDP, we tested if GDP has a similar stabilisation effect on hMiro2-His. GDP did partially stabilise hMiro2-His as evident from the invariable appearance of oligomeric hMiro2-His and the reduction in monomeric hMiro2-His appearing only on day 3 (Fig. A.15, B, peak 2). Although we were not able to purify and stabilise enough hMiro2-His to allow us to perform crystallisation experiments, the purified recombinant protein can be used for other assays requiring smaller quantities of protein, such as the testing of the specificities of hMiro1/2 antibodies.

A.4.9 Purification of the hTRAK2 Miro1 binding site

Shortly after the identification of hMiro1/2 [30] and hTRAK1/2 [51], [52] and their relevance for mitochondrial trafficking [30], [31], the direct interaction between the proteins has been established [21], [29], [56]. To date, no three-dimensinal structural information, except for recent structure predicions by AlphaFold [54], [55], for the hTRAK proteins and the interaction with hMiro1/2 is available. On the basis of recently published protocols for the expression of hTRAK1/2 in mammalian cells [35], we planned to initiate expression of full-length hTRAK1 and hTRAK2 proteins in insect cells.

A variety of constructs was tested, including different tags and construct length (Extended data, Table A.21), but none of them showed expression in SF9 or High Five™ insect cells. As of yet, the interaction between hMiro1 and hTRAK2 has been studied in most detail, identifing a subdomain of hTRAK2 [57], comprising AS 476-700, which is sufficient for the interaction with hMiro1. Because we could not find a suitable construct for the expression of hTRAK1/2 in insect cells, we focussed on the expression of the MBS of hTRAK2 in *E. coli*. The construct design comprised an N-terminal GST-tag fused to the MBS, comprising AS 476-700 of hTRAK2 and a short serine rich region (AS 701-706) of hTRAK2 (Fig. A.16, A). While a similar N-terminally His_6-tagged construct did not yield significant amounts of soluble protein, GST-hTRAK2-MBS could be reproducibly expressed in BL21 *E. coli*. While both hMiro1-His and GTS-hTRAK2-MBS could be individually expressed, co-expression was not successful.

We established a two-step purification protocol for GST-hTRAK2-MBS comprising an initial GST affinity purification (Fig. A.16, B-C) followed by a preparative SEC (Fig. A.16, D-E). The protein was purified in similar buffer conditions to hMiro1-His to enable subsequent complex formation. When compared to batch incubation with amylose beads, purification via a GSTrap™ FF column significantly increased the obtained amounts of soluble protein. However, the low expression levels of GST-hTRAK2-MBS resulted in the co-purification of a significant amount of impurities (Fig. A.16, C, E). To ensure the identity of GST-hTRAK2-MBS, serveral bands of the GST affinity purification were analysed by ESI-MS. A band slightly above the 50 kDa marker was identified as hTRAK2.

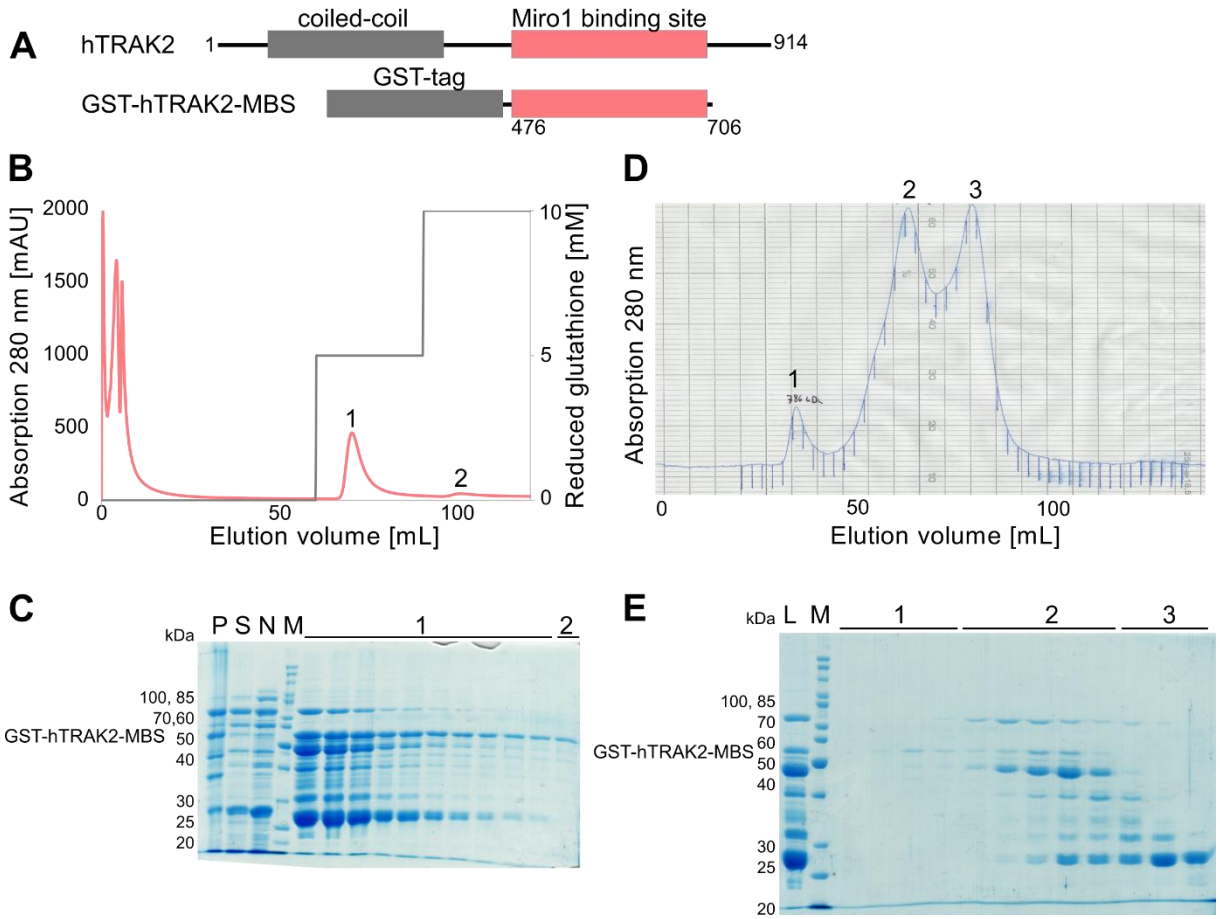

Figure A.16: The purification of GST-hTRAK2-MBS. (**A**) Domain organisation of hTRAK2 with the conserved coiled-coil domain (AS 134-354) highlighted in grey and the hMiro1 binding site (AS 476-700) highlighted in salmon. The protein likely carries a mitochondrial localisation element towards the C-terminus [36]. The KHC binding site of hTRAK2 is located within the coiled-coil region at AS 124-283 [32]. The GST-hTRAK2-MBS construct comprises the MBS of hTRAK2 N-terminally fused to a GST-tag. (**B**-**E**) Elution profiles and corresponding SDS gels of the two-step purification protocol for GST-hTRAK2-MBS including (**B**-**C**) a GST affinity chromatography and (**D**-**E**) a preparative SEC. P = lysate pellet after centrifugation, S = lysate supernatant after centrifugation, N = non bound protein, M = marker, L = load.

The subsequent preparative SEC revealed that GST-hTRAK2-MBS elutes at an elution volume correpsonding to approximately 150 kDa (Fig. A.16, D, peak 2), and thus three times the calculated size of GST-hTRAK2-MBS (51.7 kDa). We further analysed the elution profile of GST-hTRAK2-MBS by analytical SEC (Fig. A.16, C), further refining the apparent size of the protein to 190 kDa. Based on the data we suspect, that GST-hTRAK2-MBS dimerises through the GST-tag, however, this does not fully explain the elution of GST-hTRAK2-MBS at elution volumes corresponding to 190 kDa during the SEC runs. Further analysis of the oligomeric state of GST-hTRAK2-MBS through cleavage of the GST-tag proved to be impossible as hTRAK-MBS was insoluble. Although there was clearly scope for improvement of the purification conditions of GST-hTRAK2-MBS, we proceeded towards complex assembly with *E. coli* expressed hMiro1-His.

A.4.10 GST-hTRAK2-MBS directly interacts with hMiro1-His

Once we had established that recombinant hMiro1-His showed the expected folding and GTPase activity, the next step was to investigate if recombinant hMiro1-His (purified from *E. coli*) is able to interact with the Miro1 binding site of hTRAK2. For this purpose, we incubated a 1:1 ratio of hMiro1-His and GST-hTRAK2-MBS for 4 hours to allow for complex formation. The analysis of the putative complex by preparative SEC showed two distinct peaks corresponding to 260 kDa and 190 kDa (Fig. A.17, A) and the corresponding SDS gel revealed that both proteins were present in peak 1 and peak 2 (Fig. A.17, B). Based on our knowledge regarding the oligomerisation of hMiro1-His and the potential dimerisation of GST-hTRAK2-MBS, the interpretation of these results was difficult.

Therefore, we analysed samples of the individual proteins and the putative complex by analytical SEC in the presence of 2 mM GDP. The comparison of the elution profiles reveals the formation of a larger species (Fig. A.17, C) in the hMiro1-His/GST-hTRAK2-MBS sample as compared to hMiro1-His or GST-hTRAK2-MBS alone.

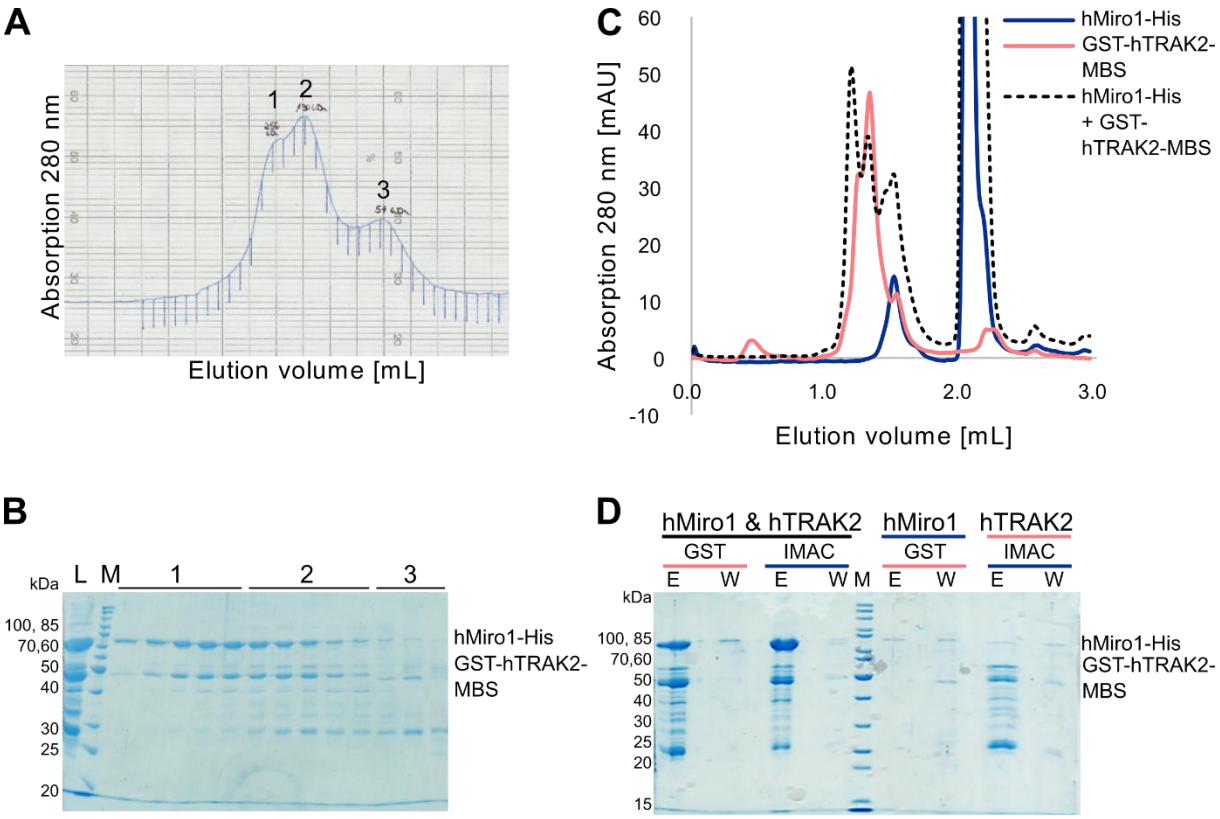

Figure A.17: Analysis of the complex formation between recombinant hMiro1-His and GST-hTRAK2-MBS. (**A**) Preparative SEC of hMiro1-His with GST-hTRAK2-MBS, mixed in a 1:1 ratio, 4 h prior to the purification. (**B**) Corresponding SDS-PAGE analysis of the SEC purification of the putative complex. Both hMiro1-His (70.0 kDa) and GST-hTRAK2-MBS (51.7 kDa) elute over the entire range of peak 1 and 2. Peak fractions are loaded as indicated by numbers. L = load, M = marker. (**C**) Analytical SEC elution profiles for hMiro1-His or GST-hTRAK2-MBS alone or mixed at a 1:1 ratio. While some protein remains unbound, the formation of a larger species can be recognised. (**D**) Pulldown experiment with peak 2 of (**A**-**B**) the preparative SEC. The hMiro1-His/GST-hTRAK2-MBS complex was analysed by GST affinity purification (GST) or cobalt IMAC (IMAC) with beads. GST-hTRAK2-MBS is able to pull down hMiro1-His on glutathione resin. As control the individual proteins were loaded onto the opposite resin. E = Elution, W = wash.

To further confirm the formation of a complex, fractions of peak 2 of the preparative SEC (Fig. A.17, A) were used in a pulldown assay (Fig. A.17, D). Comparable amounts of hMiro1-His, GST-hTRAK2-MBS and the putative complex were loaded on cobalt or glutathione agarose resin, respectively. As expected, GST-hTRAK2-MBS showed unspecific binding to the cobalt resin, likely due to the impurities remaining in the protein sample after purification. In contrast, hMiro1-His showed no unspecific binding to the glutathione agarose resin. In the sample of the pre-formed hMiro1-His/GST-hTRAK2-MBS complex, bands for both hMiro1-His and GST-hTRAK2-MBS can be seen on either type of resin, clearly hinting towards the formation of a complex. The corresponding bands at 70 kDa and 50 kDa, respectively, were analysed by ESI-MS and the presence of hMiro1-His and GST-hTRAK2-MBS was confirmed. At the time, a further analysis of the complex was not possible due to the instability of both *E. coli* expressed hMiro1-His and GST-hTRAK2-MBS. We tried to obtain crystals of the complex (Extended data, Table A.22), but to date, the complex did not crystallise.

A.4.11 The folding of Mim2 depends on the surrounding detergent

In yeast, Mim2, a component of the Mim complex, is required for the incorporation of MOM proteins carrying α-helical transmembrane domains [121]. To date, no high-resolution structure of Mim2 has been reported and three-dimensional structure predictions tools, such as Alphafold [54], [55], predict the protein to be mainly α-helical with a high degree of variability in the predictions. For the purpose of structure determination, J. Natarajan established the purification of Mim2 from cell-free protein expression systems. The His_6-tagged protein was purified by nickel IMAC and subsequent preparative SEC. Initially, the protein appeared to be soluble in phosphate buffer and we proceeded with crystallisation. However, magnesium ions, carried over from the cell-free expression, rendered crystallisation in phosphate buffer impossible due to a large quantity of magnesium phosphate crystals growing in many different conditions (Extended data, Fig. A.31, B).

To avoid the formation of salt crystals, we exchanged the buffer to MOPS and investigated the folding of Mim2 to ensure ideal starting conditions for further crystallisation attempts. To our surprise, Mim2 showed the expected α-helical folding only after the addition of the detergent N-Dodecyl-β-D-maltopyranoside (DDM) to the buffer. We checked the folding of Mim2 in both phosphate and MOPS buffer and tried to rescue protein that was purified in the absence of detergent. The results indicate that Mim2 needs detergent to display any secondary structure content and protein purified without detergent could not be rescued, likely due to the formation of aggregates (Fig. A.18, A). Further analysis of the protein stability by TSA proved to be difficult as Mim2 does not have a hydrophobic core, that could be exposed upon unfolding (Extended data, Fig. A.31, F).

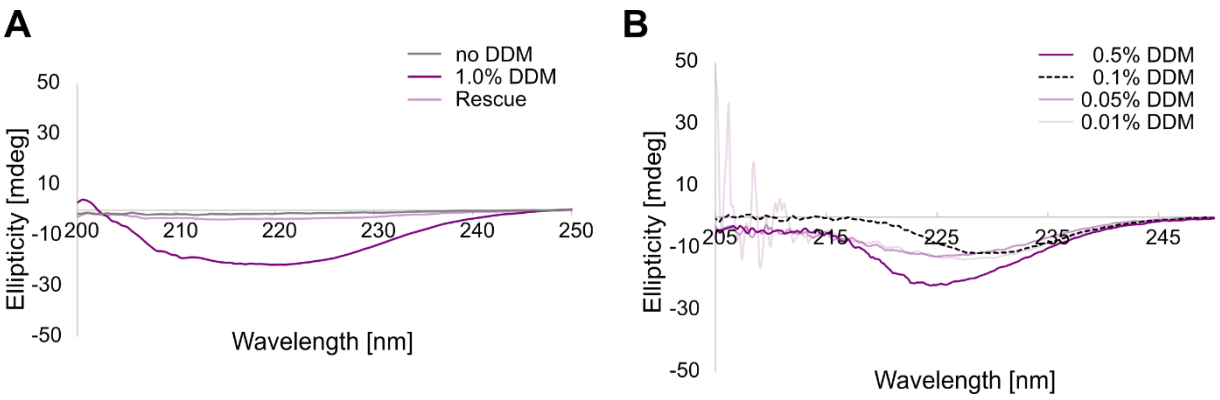

Figure A.18: Mim2 shows α-helical folding in detergent containing buffer conditions. (**A**-**B**) CD experiments with Mim2 in (**A**) buffer with and without DDM during purification and with DDM added after purification (Rescue) or in (**B**) buffer with increasing DDM concentrations during the purification from the *in vitro* cell-free expression system.

Additional crystallisation trials (Extended data, Table A.23) gave rise to honeycomb shaped crystals that grew in small clusters of 3-10 connected hexagons (Extended data, Fig. A.31, A). In contrast to the magnesium salt crystals (Extended data, Fig. A.31, B, D), the soft honey comb shaped crystals did not show any diffraction (Extended data, Fig. A.31, C), but tested positive for protein content when tested with Izit Crystal Dye (Hampton Research).

We further investigated if the used detergent or the detergent concentration could be altered to benefit the stability of Mim2 by analytical SEC and CD spectroscopy. The analytical SEC elution profiles suggest (Extended data, Fig. A.32, B, D and F), that Mim2 remained stable in all tested detergent conditions, as the peaks eluting were sharp. However, the CD spectra of Mim2 in the different detergents displayed distinct peaks, indicating that the folding of Mim2 changes dependent on the used detergent. Moreover, the peak position in the spectra of Mim2 is depending on the concentration of the used detergent (Fig. A.18, B and Extended data, Fig. A.32, A, C and E). We propose, that the folding of Mim2 adjusts to the micelles formed by the detergent (Fig. A.18, B and Extended data, Fig. A.32, A, C and E). Likely, the length of the membrane-spanning α-helix can adjust to the micelle size and shape due to the lack of tertiary structure which would explain the range of spectra we obtained. Higher detergent concentrations were generally beneficial for Mim2 folding, highlighted by increasing signal-to-noise ratios below 215 nm if the detergent concentration was near the critical micelle concentration (CMC). The flexibility in the folding of Mim2 displayed in the CD experiments and by the soft honey comb crystals led us to the conclusion that Mim2 would be an suitable candidate for structure determination by nuclear magnetic resonance (NMR) spectroscopy rather than crystallography.

A.5 DISCUSSION

A.5.1 Heterologous expression of the hMiro proteins

Despite increasing evidence for the role of hMiro in mitochondrial trafficking, dynamics and turnover, knowledge about the underlying mechanisms within hMiro and its interaction partners remains limited. We established an expression and purification protocol for recombinant, full-length hMiro1 that yields stable, folded and functional protein. Our work will enable future research on the interaction network of hMiro to shed light onto the coordination and regulation of mitochondrial function by hMiro.

Parts of hMiro were structurally characterised previously [40], [41], however, no high-resolution structure of the full-length protein or structures that are able to explain conformational changes within hMiro have been solved to date. To enhance our chances of success we produced hMiro1 specific nanobodies [141] that, besides their purpose as hMiro visualisation tools, were supposed to serve as crystallisation chaperones. Due to time restraints, the heavy-chain only antibody producing alpacas were immunised with a two domain construct of hMiro1 comprising the nGTPase and EF1 and the Drp1 protein. Albeit the main target, the nGTPase of hMiro1, being present the immune response of the alpacas could have been boosted by using a combination of full-length hMiro, Drp1 and hTRAK or other interaction partners of hMiro [154]. Moreover, initially the nanobody penning and enrichment was performed with unstable *E. coli* expressed hMiro1 that was quite sensitive to the required buffer changes for the experiments. Therefore, we conclude that an improved set of nanobodies could have been isolated and characterised if insect cell expressed full-length hMiro1 would have been available earlier in the process.

Despite many efforts, we were unable to determine three-dimensional structures of hMiro, similarly to other studies before. We planned to utilise the hMiro specific nanobodies as crystallisation chaperones to overcome issues regarding the flexibility of hMiro. Although the nanobodies are able to target specific domains of hMiro [141], they failed to stabilise recombinant hMiro, likely due to the distinct buffer requirements of hMiro and the nanobodies. We could not observe complex formation between GDP stabilised hMiro and the nanobodies, indicating that the interaction might be too weak for our SEC experiments. Though structure determination remains challenging, our recent improvements in the stability of the protein opens new possibilities. On one hand, the expression of hMiro in insect cells coupled to other crystallisation chaperones such as an MBP-tag [155] could increase the chances of successful crystallisation. On the other hand, the GDP-stabilised hMiro could be a target for cryo electron microscopy (cryoEM) if combined with a suitable interaction partner or a specific antibody to increase the size of the protein.

Although the conformational changes within hMiro remain elusive, we were able to observe alterations in the behaviour of the protein during the purification process. For both *E. coli* and insect cell expressed hMiro1 the position of the monomeric peak in SEC experiments shifted in the range of 30 kDa, hinting towards alterations in the hydrodynamic radius of the protein and possibly underlying conformational

changes. Recently published SEC-SAXS experiments on *E. coli* expressed full-length hMiro1 and hMiro2 reveal a bent conformation for hMiro with a kink between the nGTPAse and EF1 of hMiro [41]. In line with our experiments with *E. coli* hMiro1, Smith et al. [41] observed an additional oligomeric peak for hMiro1/2 in their SEC chromatograms in the presence of 2 µM GTP. In contrast, we found significant improvement in the stability of hMiro1 when expressed in insect cells as compared to *E. coli* expression, highlighting the importance of PTMs for the stability and solubility of the protein. We hypothesise that, despite the potential toxicity for the expression host due to strong phenotypes, expression in mammals could further improve the overall behaviour of the protein due to the possible formation of more complex PTMs.

In our experiments, hMiro1 displayed a strong tendency to oligomerise, especially so in the presence of calcium ions. Miro-dependent mitochondrial transport along microtubules is disrupted at elevated calcium levels [21], [29], [48], but mitochondrial transport occurs independently indicating that additional calcium sensors are responsible for calcium-dependent mitochondrial arrest [37], [156]. While the interaction of hMiro1 with hTRAK2 appears to be calcium-independent [29], calcium-binding by hMiro is a requirement for efficient Parkin recruitment by hMiro in PINK1/Parkin induced mitophagy [107], [108]. Recently published data on the acetylation of hMiro1 indicates that the calcium sensitivity of hMiro might be additionally modulated through acetylation at lysine K92 [71]. Although there are many indications for the importance of calcium-buffering by the EF hand domains of hMiro [21], [29], [48], [157], how calcium-binding affects the structure and possibly the oligomerisation of hMiro remains to be determined. The heterologous expression and purification of hMiro mutants deficient of calcium-binding (E208K for EFH1 and E328K for EFH2, respectively) [56], [158] would allow further characterisation of hMiro oligomerisation in response to calcium-binding.

Super-resolution microscopy experiments on hMiro revealed the formation of large hMiro structures comprising hMiro1, hMiro2 and other interacting proteins on the surface of mitochondria [49], indicating that the human Miro proteins are not necessarily monomeric *in vivo*. Since in our experiments the addition of GDP or GMPPNP stabilised monomeric hMiro1, we hypothesise that GTP binding or GTP hydrolysis by the hMiro GTPase domains regulates the formation of larger hMiro structures on the MOM. These structures might be required to stabilise the MIB and to coordinate the concerted transport of the MOM and the MIM. In our experiments, the GTPase activity of hMiro occurred independent of the presence of calcium, similarly to a study analysing the GTP hydrolysis of the individual GTPase domains of hMiro1/2 [44]. In this study, the cGTPase, of hMiro1/2 which was originally thought to be inactive, displayed additional catalytic activity for the hydrolysis of ATP and UTP. Since the nGTPase and the cGTPase domain are structurally distinct it is possible that they fulfil independent functions. However, which role the individual activity of the GTPase domains play in the functions of hMiro and if additional GTPase-activating proteins or nucleotide exchange factors are needed remains yet to be determined. One possibility for a more comprehensive analysis of the GTPase activity of hMiro would

be to include the GTP stabilised (P13V, G425V/K427V) and GDP stabilised (T18N, G430N/S432N) mutants of Miro [56].

Structural data on hMiro2 are limited to a high-resolution structure of the cGTPase of hMiro2 [40]. Therefore, we attempted to purify hMiro2, similarly to hMiro1, from insect cells. Although a substantial amount of protein could be observed, hMiro2 could only partially be stabilised by the addition of GDP, in stark contrast to hMiro1. hMiro1 and hMiro2 have partially overlapping functions in mitochondrial trafficking. However, hMiro1 is able to compensate for loss of hMiro2 in hMiro2 KO neurons, which hMiro2 cannot do in reverse, indicating distinct roles for hMiro1 and hMiro2. This might well be reflected in the differing properties of the proteins regarding their stability and oligomerisation tendency in our experiments. If hMiro1 and hMiro2 indeed form a stable macro molecular complex [49] and the composition of such a complex, yet needs to be established. The pre-requisite for the formation of a complex of recombinant hMiro1 and hMiro2 would be the exchange of the His_6-tag on one of the two proteins, which will require extensive optimisation of expression and purification conditions.

The expression and purification of full-length hTRAK1, fused to large tags for live-cell imaging, has been established before [35]. Establishing a similar protocol for the expression of full-length hTRAK2 in insect cell proved to be difficult. Therefore, we focused on the expression of the hTRAK2-MBS in *E. coli* and we were able to obtain substantial amounts of GST-tagged protein. In our efforts to stabilise the protein, we faced significant solubility and stability issues. To date, the MBS of hTRAK2 has not been refined in much detail [57] and recently published structure predictions of hTRAK2 by Alphafold [54], [55] might allow improved construct design. By all means, the expression of hTRAK-MBS in insect cells could be beneficial for the stability of the protein and would allow for simple PTMs which expression in *E. coli* cannot offer. So far the purification of the hTRAK2-MBS was carried out in conditions optimised for hMiro1, offering a wide range of possible improvements.

The interaction between hMiro1 and hTRAK2 is well established and depends on the MBS of hTRAK comprising AA 476-700 [29]. We attempted to form a complex with recombinant hMiro1 and the hTRAK2-MBS in a pulldown experiment. Although the purified hTRAK2-MBS sample was of low quality, we could still observe hTRAK2-dependent pulldown of hMiro1. However, we cannot exclude that the complex was formed due to unspecific interactions between the tags or the general overall stickiness of partially unfolded GST-hTRAK2-MBS. Moreover, other interaction partners of hMiro such as OGT [51], [53], KHC [21], [29] , PINK1 [151], Adenosine diphosphate (ADP)-ribosylation factor 1 (Arf1) and Golgi-specific brefeldin A-resistance guanine nucleotide exchange factor 1 (GBF1) [159], Drp1 [48] or Metaxin 1/2 [160] might be needed to form a stable complex that can be isolated.

Lastly, the now established purification protocol for wild type full-length hMiro1 can be transferred to the patient-derived hMiro1 PD mutants [111]–[113] enabling the *in vitro* characterisation of these mutations regarding calcium binding, GTP hydrolysis and interaction with other binding partners. The hMiro1 mutations have been identified in two female patients carrying heterozygous R272Q or R450C

mutations, respectively [111]. Additional evidence for the relevance of these mutations for PD came from the same study presenting a phenotype in PD patient derived fibroblasts showing reduced ERMCS, altered calcium homeostasis, increased mitochondrial fragmentation and an increase in mitochondrial clearance. Additional PD-related mutations in hMiro1 have been described since [112], [113] but how the functionality of hMiro1 is altered by these mutations and how the hMiro1 regulated processes are affected remains elusive. Recombinant expression of the hMiro1 PD-related mutants will enable research with a much broader range of techniques.

In summary, we here present a protocol for the expression and purification of hMiro1 from insect cells. Monomeric hMiro1 was stabilised by the addition of GDP or GMPPNP and the recombinant protein showed the expected α-helical folding. Moreover, the present study establishes that recombinant full-length hMiro1 is an active GTPase and able to interact with at least one interaction partner. hMiro1 purified in this study has been used successfully to produce hMiro1 specific nanobodies [141] and we expect the protocol to be of assistance for future research on hMiro1.

A.5.2 Structure determination of Mim2

The yeast Mim2 protein is an integral part of the MOM located Mim complex which in turn is responsible for the integration of proteins with an α-helical anchor such as Miro (Gem1p) into the MOM [121]. We characterised the folding of Mim2 in the presence of detergent to optimise the purification protocol with the purpose of determining the three-dimensional structure of the protein. However, Mim2 displayed high flexibility in our experiments, adjusting its folding to the surrounding micelle. The flexibility of Mim2 might be necessary for the incorporation into the Mim complex. We were able to obtain soft protein crystals that lacked the stability and durability for structure determination. We speculate that the native folding of Mim2 will be better reflected in the context of the Mim complex and propose that due to its small size and stability Mim2 would be a good target for NMR structural and interaction studies. Foremost, the focus of future research should be on establishing the composition of the Mim complex [123], [126], [130], [131] with biochemical and super resolution microscopy techniques. Once the size and stability of the Mim complex has been evaluated, appropriate structural techniques such as cryoEM or NMR spectroscopy can be applied. Our results revealed that recombinant Mim2 needs detergent to display three-dimensional folding and that the protein is highly flexible. Therefore, NMR is perhaps an especially attractive strategy as Mim2 could be stabilised in a quasi-membrane environment using nanodics that contain detergents or lipids.

A.6 OUTLOOK

The results on the expression and purification of recombinant hMiro1 will enable more comprehensive research regarding the multifaceted functions of the hMiro proteins. The herewith developed hMiro1 specific nanobodies will improve confocal microscopy as compared to conventional protein labelling with less specific large sized antibodies. Moreover, these nanobodies will be of advantage as they individually target multiple different domains of hMiro1, thus avoiding the blockage of access for the many interaction partners of hMiro1. The stabilised hMiro1 can now be used to develop an improved set of hMiro1 specific nanobodies, further boosting the specificity and selectivity of the nanobodies. hMiro antibodies are prone to label not only the protein of interest but also endogenous hMiro1 or hMiro2. Recombinant hMiro1/2 can be used to characterise the hMiro binding capability of those antibodies, which are still frequently used in confocal microscopy. Moreover, the distinct functions of hMiro2 and the interaction network of hMiro2 are not well understood. Recombinant hMiro2 could be used to establish to which extent the interaction networks of hMiro1 and hMiro2 overlap and to identify new interaction partners with mass spectrometry techniques. The purification protocol for hMiro1 established in this thesis can be optimised for PD-related mutants of hMiro1, thus enabling *in vitro* experiments to characterise the altered properties of the mutations.

Finally, recombinant hMiro1 will be used in *in vitro* assays to study Drp1-dependent fission by Yannic Lurz (group of Prof. Schäffer, Center for Molecular Biology of Plants, University of Tübingen). Miro1 has been shown to be important for the formation of membrane protrusions at microtubules for downstream vesicle generation by Drp1 [161]. Y. Lurz plans to establish a combination of Drp1 fission and kinesin motility assays with hMiro acting at the intersection of the two processes. This demonstrates that our hMiro1 purification protocol will have practical implications in future research on the hMiro proteins.

A.7 EXTENDED DATA

A.7.1 Tables

Table A.21: Overview of the hMiro1 constructs. Most constructs were cloned for this study except for those labelled with *.

Construct name	Protein	Domains	Length (AA)	Mutations	Tag	Host organism	Vector	Expression
1*	hMiro1	AB_1B_2C	1-592	wt	N-Spot, C-6xHis	*E. coli*	pET28a(+)	No
2	hMiro1	AB_1B_2C	1-592	wt	N-Spot	*E. coli*	pET28a(+)	No
hMiro1-His	hMiro1	AB_1B_2C	1-592	wt	C-6xHis	*E. coli*	pET28a(+)	Yes
hMiro1-His*	hMiro1	AB_1B_2C	1-592	wt	C-6xHis	High Five™	pFastBac1	Yes
MBP-hMiro1*	hMiro1	AB_1B_2C	1-592	wt	N-MBP	*E. coli*	pET28a(+)	Yes
hMiro1	hMiro1	AB_1B_2C	1-592	wt	-	*E. coli*	pET28a(+)	Yes
hMiro1(R272Q)-His	hMiro1	AB_1B_2C	1-592	R272Q	C-6xHis	*E. coli*	pET28a(+)	Yes
3	hMiro1	AB_1B_2C	1-592	R450C	N-Spot, C-6xHis	*E. coli*	pET28a(+)	No
hMiro1(R450C)-His	hMiro1	AB_1B_2C	1-592	R450C	C-6xHis	*E. coli*	pET28a(+)	Yes
4	hMiro1	B_1B_2C	181-592	wt	C-6xHis	*E. coli*	pET28a(+)	No
5	hMiro1	AB_1B_2	1-417	wt	N-Spot, C-6xHis	*E. coli*	pET28a(+)	No
hMiro1-AB_1B_2-His	hMiro1	AB_1B_2	1-417	wt	C-6xHis	*E. coli*	pET28a(+)	Yes
6	hMiro1	AB_1B_2	1-417	R272Q	C-6xHis	*E. coli*	pET28a(+)	No
7	hMiro1	AB_1B_2	1-406	wt	C-6xHis	*E. coli*	pET28a(+)	No
8	hMiro1	AB_1B_2	1-406	R272Q	C-6xHis	*E. coli*	pET28a(+)	No
9	hMiro1	AB_1	1-290	wt	N-Spot, C-6xHis	*E. coli*	pET28a(+)	No
hMiro1-AB_1-His	hMiro1	AB_1	1-290	wt	C-6xHis	*E. coli*	pET28a(+)	Yes
10	hMiro1	AB_1	1-290	R272Q	N-Spot, C-6xHis	*E. coli*	pET28a(+)	No
11	hMiro1	AB_1	1-290	R272Q	C-6xHis	*E. coli*	pET28a(+)	No
12	hMiro1	AB_1	1-281	wt	N-Spot, C-6xHis	*E. coli*	pET28a(+)	No
hMiro1-AB_1(1-281)-His	hMiro1	AB_1	1-281	wt	C-6xHis	*E. coli*	pET28a(+)	Yes
13	hMiro1	AB_1	1-281	R272Q	N-Spot, C-6xHis	*E. coli*	pET28a(+)	No
14	hMiro1	AB_1	1-275	wt	N-Spot, C-6xHis	*E. coli*	pET28a(+)	No
hMiro1-AB_1(1-275)-His	hMiro1	AB_1	1-275	wt	C-6xHis	*E. coli*	pET28a(+)	Yes
15	hMiro1	A	1-180	wt	N-Spot, C-6xHis	*E. coli*	pET28a(+)	No
hMiro1-A-His	hMiro1	A	1-180	wt	C-6xHis	*E. coli*	pET28a(+)	Yes
16	hMiro1	A	1-167	wt	N-Spot, C-6xHis	*E. coli*	pET28a(+)	No
hMiro1-A(1-167)-His	hMiro1	A	1-167	wt	C-6xHis	*E. coli*	pET28a(+)	Yes

Table A.21, continued: Overview of the hMiro2 and hTRAK1/2 constructs. Most constructs were cloned for this study except for those labelled with *.

Construct name	Protein	Domains	Length (AA)	Mutations	Tag	Host organism	Vector	Expression
17*	hMiro2	AB_1B_2C	1-588	wt	N-Spot, C-6xHis	*E. coli*	pET28a(+)	No
18	hMiro2	AB_1B_2C	1-588	wt	C-6xHis	*E. coli*	pET28a(+)	No
GST-hMiro2*	hMiro2	AB_1B_2C	1-588	wt	N-GST	*E. coli*	pGEX-4T-1	Yes
hMiro2-His*	hMiro2	AB_1B_2C	1-588	wt	C-6xHis	High Five™	pFastBac1	Yes
19	hMiro2	AB_1B_2C	1-586	wt	C-6xHis	*E. coli*	pET28a(+)	No
20	hMiro2	AB_1B_2C	1-583	wt	C-6xHis	*E. coli*	pET28a(+)	No
21	hMiro2	AB_1B_2C	1-579	wt	C-6xHis	*E. coli*	pET28a(+)	No
22	hMiro2	AB_1B_2	1-415	wt	N-Spot, C-6xHis	*E. coli*	pET28a(+)	No
23	hMiro2	AB_1B_2	1-415	wt	C-6xHis	*E. coli*	pET28a(+)	No
24	hMiro2	AB_1	1-290	wt	N-Spot, C-6xHis	*E. coli*	pET28a(+)	No
hMiro2-AB_1-His	hMiro2	AB_1	1-290	wt	C-6xHis	*E. coli*	pET28a(+)	Yes
25	hMiro2	A	1-180	wt	C-6xHis	*E. coli*	pET28a(+)	No
26	hMiro2	A	1-167	wt	C-6xHis	*E. coli*	pET28a(+)	No
27*	hTRAK1	FL	1-953	wt	N-Spot	High Five™	pFastBac1	No
28	hTRAK2	FL	1-914	wt	N-Spot, C-6xHis	High Five™	pFastBac1	No
29*	hTRAK2	FL	1-914	wt	N-Spot	High Five™	pFastBac1	No
30	hTRAK2	FL	1-914	wt	C-6xHis	High Five™	pFastBac1	No
31	hTRAK2	FL	1-914	wt	N-6xHis	High Five™	pFastBac1	No
32	hTRAK2	FL	1-914	wt	-	High Five™	pFastBac1	No
33	hTRAK2	MBS-CTR	476-914	wt	N-Spot	High Five™	pFastBac1	No
34	hTRAK2	MBS-CTR	476-914	wt	C-6xHis	High Five™	pFastBac1	No
35	hTRAK2	CC-MBS	1-706	wt	N-Spot, C-6xHis	High Five™	pFastBac1	No
36	hTRAK2	CC-MBS	1-706	wt	N-Spot	High Five™	pFastBac1	No
37	hTRAK2	CC-MBS	1-706	wt	C-6xHis	High Five™	pFastBac1	No
38	hTRAK2	MBS	476-706	wt	N-Spot, C-6xHis	High Five™	pFastBac1	No
39	hTRAK2	MBS	476-706	wt	N-Spot	High Five™	pFastBac1	No
40	hTRAK2	MBS	476-706	wt	C-6xHis	High Five™	pFastBac1	No
GST-hTRAK2-MBS*	hTRAK2	MBS	476-706	wt	N-GST	*E. coli*	pGEX-4T-1	Yes
His-hTRAK2-MBS*	hTRAK2	MBS	476-706	wt	N-6xHis	*E. coli*	pET28a(+)-TEV	Yes

Table A.22: Crystallisation experiments with hMiro1-His.

Construct name	Origin	Oligomeric state	Additive	Concentration [mg/mL]	Temperature [°C]	Drop ratio	Size [nL]	Screens
hMiro1-His	*E. coli*	Monomer	-	10.4	20	1:1	400	Wizard Classic 1 and 2 Block (Molecular Dimensions) Wizard Classic 3 and 4 Block (Molecular Dimensions) JCSG+ Suite (Qiagen) PEG/Ion HT™ (Hampton Research)
	E. coli	Monomer	-	1.9	20	1:1	400	Wizard Classic 1 and 2 Block (Molecular Dimensions) Wizard Classic 3 and 4 Block (Molecular Dimensions)
	E. coli	Monomer	-	5.1	4	1:1	400	Wizard Classic 1 and 2 Block (Molecular Dimensions) Wizard Classic 3 and 4 Block (Molecular Dimensions) Crystal Screen HT™ (Hampton Research) PEG/Ion HT™ (Hampton Research) JCSG+ Suite (Qiagen)
	E. coli	Monomer	-	1.9	4	1:1	400	Wizard Classic 1 and 2 Block (Molecular Dimensions) Wizard Classic 3 and 4 Block (Molecular Dimensions)
	E. coli	Oligomer	-	5.1	20	1:1	400	Wizard Classic 1 and 2 Block (Molecular Dimensions) Wizard Classic 3 and 4 Block (Molecular Dimensions) PEG/Ion HT™ (Hampton Research)
	E. coli	Oligomer	-	5.1	4	1:1	400	Wizard Classic 1 and 2 Block (Molecular Dimensions) Wizard Classic 3 and 4 Block (Molecular Dimensions) PEG/Ion HT™ (Hampton Research)

Table A.22, continued: Crystallisation experiments with hMiro1-His.

Construct name	Origin	Oligomeric state	Additive	Concentration [mg/mL]	Temperature [°C]	Drop ratio	Size [nL]	Screens
hMiro1-His	High Five™	Monomer	-	4.7	20	1:1	400	Wizard Classic 1 and 2 Block (Molecular Dimensions) Wizard Classic 3 and 4 Block (Molecular Dimensions) Morpheus® (Molecular Dimensions) Crystal Screen HT™ (Hampton Research) PEG/Ion HT™ (Hampton Research) JCSG+ Suite (Qiagen)
	High Five™	Monomer	-	4.7	4	1:1	400	Wizard Classic 1 and 2 Block (Molecular Dimensions) Wizard Classic 3 and 4 Block (Molecular Dimensions) Morpheus® (Molecular Dimensions) Crystal Screen HT™ (Hampton Research) PEG/Ion HT™ (Hampton Research) JCSG+ Suite (Qiagen) The Cations Suite (Qiagen)
	High Five™	Oligomer	-	1.8	20	1:1	400	Wizard Classic 1 and 2 Block (Molecular Dimensions) Wizard Classic 3 and 4 Block (Molecular Dimensions) Morpheus® (Molecular Dimensions) Crystal Screen HT™ (Hampton Research) JCSG+ Suite (Qiagen)
	High Five™	Oligomer	-	1.8	4	1:1	400	Wizard Classic 1 and 2 Block (Molecular Dimensions) Wizard Classic 3 and 4 Block (Molecular Dimensions) Morpheus® (Molecular Dimensions) Crystal Screen HT™ (Hampton Research) JCSG+ Suite (Qiagen)

Table A.22, continued: Crystallisation experiments with hMiro1-His, hMiro1(R450C)-His and GST-hTRAK2.

Construct name	Origin	Oligomeric state	Additive	Concentration [mg/mL]	Temperature [°C]	Drop ratio	Size [nL]	Screens
hMiro1-His	High Five™	Monomer	2 mM GDP	8.0	20	1:1	400	Morpheus® (Molecular Dimensions) Crystal Screen HT™ (Hampton Research)
	High Five™	Monomer	2 mM GDP	8.0	4	1:1	400	Wizard Classic 1 and 2 Block (Molecular Dimensions) Wizard Classic 3 and 4 Block (Molecular Dimensions) Morpheus® (Molecular Dimensions) Crystal Screen HT™ (Hampton Research) PEG/Ion HT™ (Hampton Research) JCSG+ Suite (Qiagen)
hMiro1(R450C)-His			-	5.2	4	1:1	400	Wizard Classic 1 and 2 Block (Molecular Dimensions) Wizard Classic 3 and 4 Block (Molecular Dimensions) PEG/Ion HT™ (Hampton Research)
hMiro1-His and GST-hTRAK2-MBS	*E. coli*	Monomer	-	4.9	4	1:1	400	Wizard Classic 1 and 2 Block (Molecular Dimensions) Wizard Classic 3 and 4 Block (Molecular Dimensions) Crystal Screen HT™ (Hampton Research)

Table A.23: Crystallisation conditions of Mim2.

Apperance	Salt	Temperature	Buffer	Salt	Precipitant 1	Cryo protection	Crystal
Honeycomb cluster		20 °C	0.1 M Sodium citrate tribasic pH 5.0	0.2 M Ammonium acetate	30 % (w/v) PEG 4000	40% (w/v) PEG 6000	
Honeycomb clusters			0.1 M MES/Sodium hydroxide pH 6.0	0.2 M Ammonium chloride	20% (w/v) PEG 6000	40% (w/v) PEG 6000	**A.31, A**
Single hexagon				0.2 M Magnesium formate	20% (w/v) PEG 3350	40% (w/v) PEG 6000	
Elongated retangles	Yes		0.1 M Sodium acetate trihydrate pH 4.6	0.1 M Cadmium chloride hydrate	30% (v/v) PEG 400	50% PEG 500	
Single retangle	Yes		0.1 M Sodium cacodylate/Hydrochloric acid pH 6.5	0.2 M Zinc acetate	10% (v/v) 2-Propanol	-	
Big cluster	Yes		0.1 M Sodium acetate	0.2 M Calcium chloride dihydrate	20% (v/v) 2-Propanol	-	
Small crosses	Yes		0.1 M HEPES pH 7.5	1.5 M Lithium sulfate		-	
Cross	Yes		0.1 M Tris HCl pH 8.5	0.2 M Lithium sulfate	30% (w/v) PEG 4000	-	**A.31, B**
Fine needles	Yes		0.1 M Imidazole/Hydrochloric acid Ph 8.0	0.2 M Zinc acetate	2.5 M Sodium chloride	-	

Table A.24: Primer sequences for site-directed mutagenesis. Primers were synthesised at biomers.net, Germany or Invitrogen by Thermo Fisher Sientific.

Primer pair	Construct	Sequences
1	2	5' ggatctgaaaagcagcacctttgagatccggctgctaacaaagc 3' 5' gctttgttagcagccggatctcaaaaggtgctgcttttcagatcc 3'
2	hMiro1-His	5' cctctagaaagaaggagatataatgaaaaaagatgtgcgcattc 3' 5' gaatgcgcacatctttttttcattatatctccttctttctagagg 3'
1, 2	hMiro1	5' ggatctgaaaagcagcacctttgagatccggctgctaacaaagc 3' 5' gctttgttagcagccggatctcaaaaggtgctgcttttcagatcc 3' 5' cctctagaaagaaggagatataatgaaaaaagatgtgcgcattc 3' 5' gaatgcgcacatctttttttcattatatctccttctttctagagg 3'
3, 2	hMiro1(R272Q)-His	5' gaaaccacctggaccgtgctgcaacgctttggctatgatgatgatc 3' 5' gatcatcatcatagccaaagcgttgcagcacggtccaggtggtttc 3' 5' cctctagaaagaaggagatataatgaaaaaagatgtgcgcattc 3' 5' gaatgcgcacatctttttttcattatatctccttctttctagagg 3'
4	3	5' cctgatgcgccagaaaaaaatttgcgaagatcataaaagctattatg 3' 5' cataatagcttttatgatcttcgcaaatttttttctggcgcatcagg 3'
4, 2	hMiro1(R450C)-His	5' cctgatgcgccagaaaaaaatttgcgaagatcataaaagctattatg 3' 5' cataatagcttttatgatcttcgcaaatttttttctggcgcatcagg 3' 5' cctctagaaagaaggagatataatgaaaaaagatgtgcgcattc 3' 5' gaatgcgcacatctttttttcattatatctccttctttctagagg 3'
5	4	5' ctctagaaagaaggagatataatgaaaccggcgtgcattaaag 3' 5' ctttaatgcacgccggtttcattatatctccttctttctagag 3'
6	5	5' ccagcgcaacgaaaacctgtattttcagggcgc 3' 5' caggttttcgttgcgctgggtctgtttttctgc 3'
6, 2	hMiro1-AB_1B_2-His	5' ccagcgcaacgaaaacctgtattttcagggcgc 3' 5' caggttttcgttgcgctgggtctgtttttctgc 3' 5' cctctagaaagaaggagatataatgaaaaaagatgtgcgcattc 3' 5' gaatgcgcacatctttttttcattatatctccttctttctagagg 3'

Table A.24, continued: Primer sequences for site-directed mutagenesis.

Primer pair	Construct	Sequences
6, 2, 3	6	5' ccagcgcaacgaaaacctgtattttcagggcgc 3'
		5' caggttttcgttgcgctgggtctgtttttctgc 3'
		5' cctctagaaagaaggagatataatgaaaaaagatgtgcgcattc 3'
		5' gaatgcgcacatctttttttcattatatctccttctttctagagg 3'
		5' gaaaccacctggaccgtgctgcaacgctttggctatgatgatgatc 3'
		5' gatcatcatcatagccaaagcgttgcagcacggtccaggtggtttc 3'
7, 2	7	5' cccgcgataaaaaagaaaacctgtattttcagggcgc 3'
		5' gaaaatacaggttttctttttttatcgcgggtcacggtc 3'
		5' cctctagaaagaaggagatataatgaaaaaagatgtgcgcattc 3'
		5' gaatgcgcacatctttttttcattatatctccttctttctagagg 3'
7, 2, 3	8	5' cccgcgataaaaaagaaaacctgtattttcagggcgc 3'
		5' gaaaatacaggttttctttttttatcgcgggtcacggtc 3'
		5' cctctagaaagaaggagatataatgaaaaaagatgtgcgcattc 3'
		5' gaatgcgcacatctttttttcattatatctccttctttctagagg 3'
		5' gaaaccacctggaccgtgctgcaacgctttggctatgatgatgatc 3'
		5' gatcatcatcatagccaaagcgttgcagcacggtccaggtggtttc 3'
8	9	5' ggaatatctgtttccgctggaaaacctgtattttcagggcg 3'
		5' cgccctgaaaatacaggttttccagcggaaacagatattcc 3'
8, 2	hMiro1-AB$_1$-His	5' ggaatatctgtttccgctggaaaacctgtattttcagggcg 3'
		5' cgccctgaaaatacaggttttccagcggaaacagatattcc 3'
		5' cctctagaaagaaggagatataatgaaaaaagatgtgcgcattc 3'
		5' gaatgcgcacatctttttttcattatatctccttctttctagagg 3'
8, 3	10	5' ggaatatctgtttccgctggaaaacctgtattttcagggcg 3'
		5' cgccctgaaaatacaggttttccagcggaaacagatattcc 3'
		5' gaaaccacctggaccgtgctgcaacgctttggctatgatgatgatc 3'
		5' gatcatcatcatagccaaagcgttgcagcacggtccaggtggtttc 3'

Table A.24, continued: Primer sequences for site-directed mutagenesis.

Primer pair	Construct	Sequences
8, 2, 3	11	5' ggaatatctgtttccgctggaaaacctgtattttcagggcg 3' 5' cgccctgaaaatacaggttttccagcggaaacagatattcc 3' 5' cctctagaaagaaggagatataatgaaaaaagatgtgcgcattc 3' 5' gaatgcgcacatctttttttcattatatctccttctttctagagg 3' 5' gaaaccacctggaccgtgctgcaacgctttggctatgatgatgatc 3' 5' gatcatcatcatagccaaagcgttgcagcacggtccaggtggtttc 3'
9	12	5' ctggatctggaaaacctgtattttcagggcgc 3' 5' tacaggttttccagatccagatcatcatcatagcc 3'
9, 2	hMiro1-AB$_1$(1-281)-His	5' ctggatctggaaaacctgtattttcagggcgc 3' 5' tacaggttttccagatccagatcatcatcatagcc 3' 5' cctctagaaagaaggagatataatgaaaaaagatgtgcgcattc 3' 5' gaatgcgcacatctttttttcattatatctccttctttctagagg 3'
9, 3	13	5' ctggatctggaaaacctgtattttcagggcgc 3' 5' tacaggttttccagatccagatcatcatcatagcc 3' 5' gaaaccacctggaccgtgctgcaacgctttggctatgatgatgatc 3' 5' gatcatcatcatagccaaagcgttgcagcacggtccaggtggtttc 3'
10	14	5' ccgctttggcgaaaacctgtattttcagggcgc 3' 5' tacaggttttcgccaaagcggcgcagcacg 3'
10, 2	hMiro1-AB$_1$(1-275)-His	5' ccgctttggcgaaaacctgtattttcagggcgc 3' 5' tacaggttttcgccaaagcggcgcagcacg 3' 5' cctctagaaagaaggagatataatgaaaaaagatgtgcgcattc 3' 5' gaatgcgcacatctttttttcattatatctccttctttctagagg 3'
11	15	5' gtattgcccggaagaaaaagaagaaaacctgtattttcagggcg 3' 5' cgccctgaaaatacaggttttcttctttttcttccgggcaatac 3'
11, 2	hMiro1-A-His	5' gtattgcccggaagaaaaagaagaaaacctgtattttcagggcg 3' 5' cgccctgaaaatacaggttttcttctttttcttccgggcaatac 3' 5' cctctagaaagaaggagatataatgaaaaaagatgtgcgcattc 3' 5' gaatgcgcacatctttttttcattatatctccttctttctagagg 3'

Table A.24, continued: Primer sequences for site-directed mutagenesis.

Primer pair	Construct	Sequences
12	16	5' gaaagcggtgctggaaaacctgtattttcagggcgc 3' 5' acaggttttccagcaccgctttctgcgcataataaaac 3'
12, 2	hMiro1-A(1-167)-His	5' gaaagcggtgctggaaaacctgtattttcagggcgc 3' 5' acaggttttccagcaccgctttctgcgcataataaaac 3' 5' cctctagaaagaaggagatataatgaaaaaagatgtgcgcattc 3' 5' gaatgcgcacatctttttttcattatatctccttctttctagagg 3'
13	18	5' cctctagaaagaaggagatataatgcgccgcgatgtgcgcattc 3' 5' gaatgcgcacatcgcggcgcattatatctccttctttctagagg 3'
14, 13	19	5' cggaactgcatccggaaaacctgtattttcaggg 3' 5' cctgaaaatacaggttttccggatgcagttccgcatgcaccag 3' 5' cctctagaaagaaggagatataatgcgccgcgatgtgcgcattc 3' 5' gaatgcgcacatcgcggcgcattatatctccttctttctagagg 3'
15, 13	20	5' ggtgcatgcggaagaaaacctgtattttcagggc 3' 5' cctgaaaatacaggttttcttccgcatgcaccagatgc 3' 5' cctctagaaagaaggagatataatgcgccgcgatgtgcgcattc 3' 5' gaatgcgcacatcgcggcgcattatatctccttctttctagagg 3'
16, 13	21	5' gcgtttccgcatctggaaaacctgtattttcagggc 3' 5' cctgaaaatacaggttttccagatgcggaaacgccgccat 3' 5' cctctagaaagaaggagatataatgcgccgcgatgtgcgcattc 3' 5' gaatgcgcacatcgcggcgcattatatctccttctttctagagg 3'
17	22	5' gaaaaaggccagacccagcgcagcgaaaacctgtattttcagggcg 3' 5' cgccctgaaaatacaggttttcgctgcgctgggtctggccttttc 3'
17, 13	23	5' gaaaaaggccagacccagcgcagcgaaaacctgtattttcagggcg 3' 5' cgccctgaaaatacaggttttcgctgcgctgggtctggccttttc 3' 5' cctctagaaagaaggagatataatgcgccgcgatgtgcgcattc 3' 5' gaatgcgcacatcgcggcgcattatatctccttctttctagagg 3'

Table A.24, continued: Primer sequences for site-directed mutagenesis.

Primer pair	Construct	Sequences
18	24	5' ggaatatctgtttccgctggaaaacctgtattttcagggcg 3' 5' cgccctgaaaatacaggttttccagcggaaacagatattcc 3'
18, 13	hMiro2-AB$_1$-His	5' ggaatatctgtttccgctggaaaacctgtattttcagggcg 3' 5' cgccctgaaaatacaggttttccagcggaaacagatattcc 3' 5' cctctagaaagaaggagatataatgcgccgcgatgtgcgcattc 3' 5' gaatgcgcacatcgcggcgcattatatctccttctttctagagg 3'
19, 13	25	5' gtattgcccggaagaaaaagaagaaaacctgtattttcagggcg 3' 5' cgccctgaaaatacaggttttcttcttttttcttccgggcaatac 3' 5' cctctagaaagaaggagatataatgcgccgcgatgtgcgcattc 3' 5' gaatgcgcacatcgcggcgcattatatctccttctttctagagg 3'
20, 13	26	5' gaaagcggtgctggaaaacctgtattttcagggcg 3' 5' cctgaaaatacaggttttccagcaccgctttctgcgc 3'
21	28	5' gatgggtgtgctgaaggaggacgaaaacctgtattttcagggcgcagccgcactcgagcaccaccaccaccaccactaagcggccgctttcgaatctagag 3' 5' ctctagattcgaaagcggccgcttagtggtggtggtggtggtgctcgagtgcggctgcgccctgaaaatacaggttttcgtcctccttcagcacacccatc 3'
21, 22	30	5' gatgggtgtgctgaaggaggacgaaaacctgtattttcagggcgcagccgcactcgagcaccaccaccaccaccactaagcggccgctttcgaatctagag 3' 5' ctctagattcgaaagcggccgcttagtggtggtggtggtggtgctcgagtgcggctgcgccctgaaaatacaggttttcgtcctccttcagcacacccatc 3' 5' gtccgaagcgcgcggaattcatgtcccagtcccagaacgctatcttc 3' 5' gaagatagcgttctgggactgggacatgaattccgcgcgcttcggac 3'
22, 23	31	5' gtccgaagcgcgcggaattcatgtcccagtcccagaacgctatcttc 3' 5' gaagatagcgttctgggactgggacatgaattccgcgcgcttcggac 3' 5' cggtccgaagcgcgcggaattccatatgcaccaccaccaccaccacccatgggaaaacctgtattttcagggcatgtcccagtcccagaacgctatc 3' 5' gatagcgttctgggactgggacatgccctgaaaatacaggttttcccatgggtggtggtggtggtggtgcatatggaattccgcgcgcttcggaccg 3'
22	32	5' gtccgaagcgcgcggaattcatgtcccagtcccagaacgctatcttc 3' 5' gaagatagcgttctgggactgggacatgaattccgcgcgcttcggac 3'
24	33	5' cactggtcctccccctccggtgactccgacctgg 3' 5' gtcaccggaggggggaggaccagtgggacacagcac 3'

Table A.24, continued: Primer sequences for site-directed mutagenesis.

Primer pair	Construct	Sequences
25, 21, 22	34	5' gcggaattcatgccctccggtgactccgacctgg 3'
		5' gtcaccggagggcatgaattccgcgcgcttcg 3'
		5' gatgggtgtgctgaaggaggacgaaaacctgtattttcagggcgcagccgcactcgagcaccaccaccaccaccactaagcggccgctttcgaatctagag 3'
		5' ctctagattcgaaagcggccgcttagtggtggtggtggtggtgctcgagtgcggctgcgccctgaaaatacaggttttcgtcctccttcagcacacccatc 3'
		5' gtccgaagcgcgcggaattcatgtcccagtcccagaacgctatcttc 3'
		5' gaagatagcgttctgggactgggacatgaattccgcgcgcttcggac 3'
26, 21	35	5' cctcctcctcctaagcggccgctttcgaatctag 3'
		5' cggccgcttaggaggaggaggaaccggag 3'
		5' gatgggtgtgctgaaggaggacgaaaacctgtattttcagggcgcagccgcactcgagcaccaccaccaccaccactaagcggccgctttcgaatctagag 3'
		5' ctctagattcgaaagcggccgcttagtggtggtggtggtggtgctcgagtgcggctgcgccctgaaaatacaggttttcgtcctccttcagcacacccatc 3'
26	36	5' cctcctcctcctaagcggccgctttcgaatctag 3'
		5' cggccgcttaggaggaggaggaaccggag 3'
26, 21, 22	37	5' cctcctcctcctaagcggccgctttcgaatctag 3'
		5' cggccgcttaggaggaggaggaaccggag 3'
		5' gatgggtgtgctgaaggaggacgaaaacctgtattttcagggcgcagccgcactcgagcaccaccaccaccaccactaagcggccgctttcgaatctagag 3'
		5' ctctagattcgaaagcggccgcttagtggtggtggtggtggtgctcgagtgcggctgcgccctgaaaatacaggttttcgtcctccttcagcacacccatc 3'
		5' gtccgaagcgcgcggaattcatgtcccagtcccagaacgctatcttc 3'
		5' gaagatagcgttctgggactgggacatgaattccgcgcgcttcggac 3'
26, 24, 21	38	5' cctcctcctcctaagcggccgctttcgaatctag 3'
		5' cggccgcttaggaggaggaggaaccggag 3'
		5' cactggtcctccccctccggtgactccgacctgg 3'
		5' gtcaccggagggggaggaccagtgggacacagcac 3'
		5' gatgggtgtgctgaaggaggacgaaaacctgtattttcagggcgcagccgcactcgagcaccaccaccaccaccactaagcggccgctttcgaatctagag 3'
		5' ctctagattcgaaagcggccgcttagtggtggtggtggtggtgctcgagtgcggctgcgccctgaaaatacaggttttcgtcctccttcagcacacccatc 3'

Table A.24, continued: Primer sequences for site-directed mutagenesis.

Primer pair	Construct	Sequences
26, 24	39	5' cctcctcctcctaagcggccgctttcgaatctag 3' 5' cggccgcttaggaggaggaggaaccggag 3' 5' cactggtcctccccctccggtgactccgacctgg 3' 5' gtcaccggaggggggaggaccagtgggacacagcac 3'
26, 25, 21, 22	40	5' cctcctcctcctaagcggccgctttcgaatctag 3' 5' cggccgcttaggaggaggaggaaccggag 3' 5' gcggaattcatgccctccggtgactccgacctgg 3' 5' gtcaccggagggcatgaattccgcgcgcttcg 3' 5' gatgggtgtgctgaaggaggacgaaaacctgtattttcagggcgcagccgcactcgagcaccaccaccaccaccactaagcggccgctttcgaatctagag 3' 5' ctctagattcgaaagcggccgcttagtggtggtggtggtggtgctcgagtgcggctgcgccctgaaaatacaggttttcgtcctccttcagcacacccatc 3' 5' gtccgaagcgcgcggaattcatgtcccagtcccagaacgctatcttc 3' 5' gaagatagcgttctgggactgggacatgaattccgcgcgcttcggac 3'

A.7.2 Figures

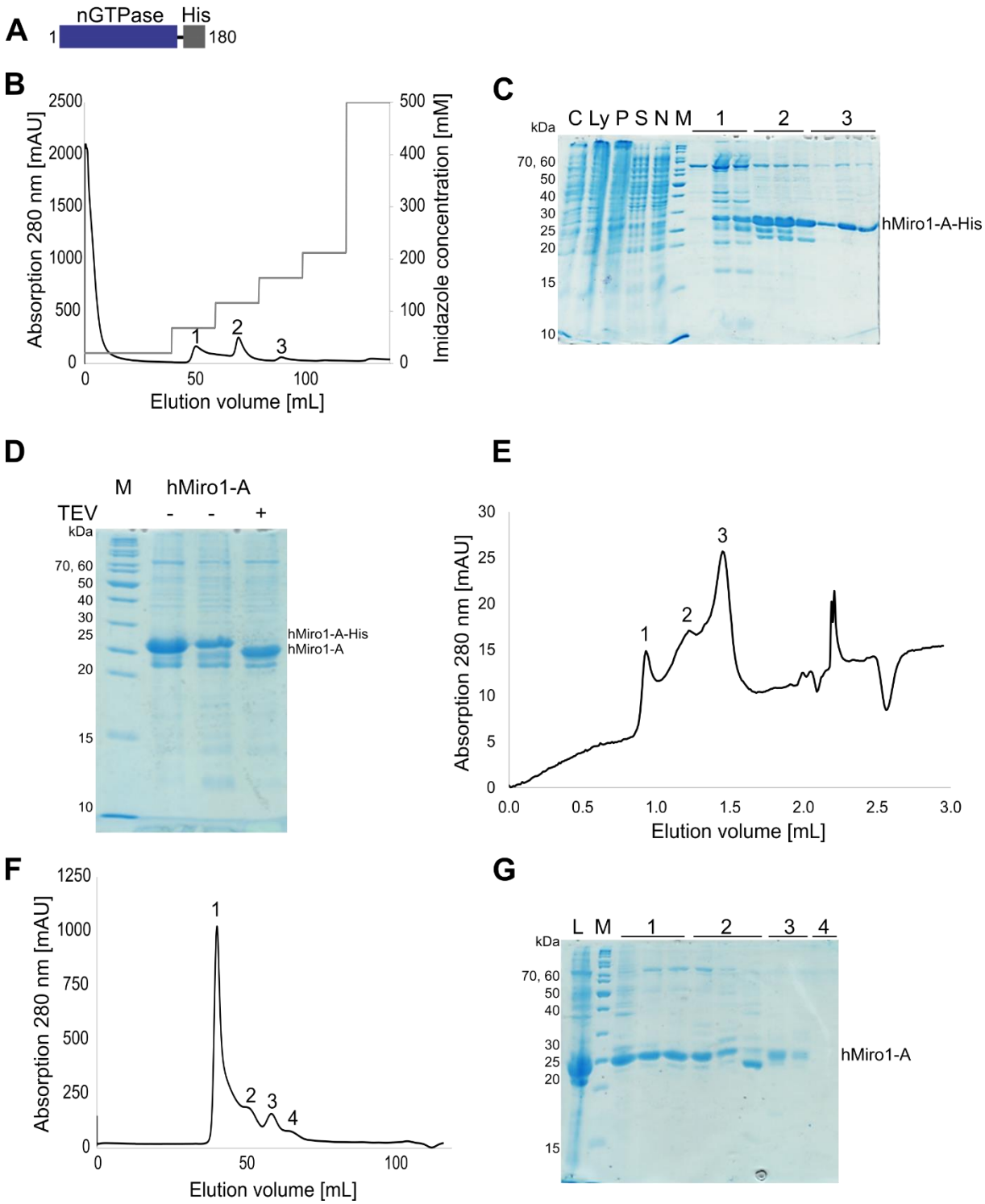

Figure A.19: hMiro1-A-His purification including tag cleavage. (**A**) Construct design for hMiro1-A-His comprising only the nGTPase (dark blue) with a C-terminal His_6-tag. (**B-C**) The majority of hMiro1-A-His elutes at 116 mM Imidazole during the purification by nickel IMAC. (**D**) The SDS-PAGE analysis of the TEV digest of hMiro1-A-His reveals the complete cleavage of the His_6-tag. (**E**) Analytical SEC elution profile of hMiro1-A-His before cleavage of the His_6-tag. Peak 3 elutes at an elution volume corresponding to 95 kDa (peak 3) indicating that hMiro1-A-His (22.5 kDa) is not monomeric. (**F-G**) The preparative SEC of hMiro1-A shows most of the protein eluting in the void volume of the column. (**B-G**) Peaks in the chromatograms and corresponding gels are labelled with corresponding numbers. C = cells, L = lysate, P = pellet after centrifugation, S = supernatant after centrifugation, N = non-bound protein, M = marker.

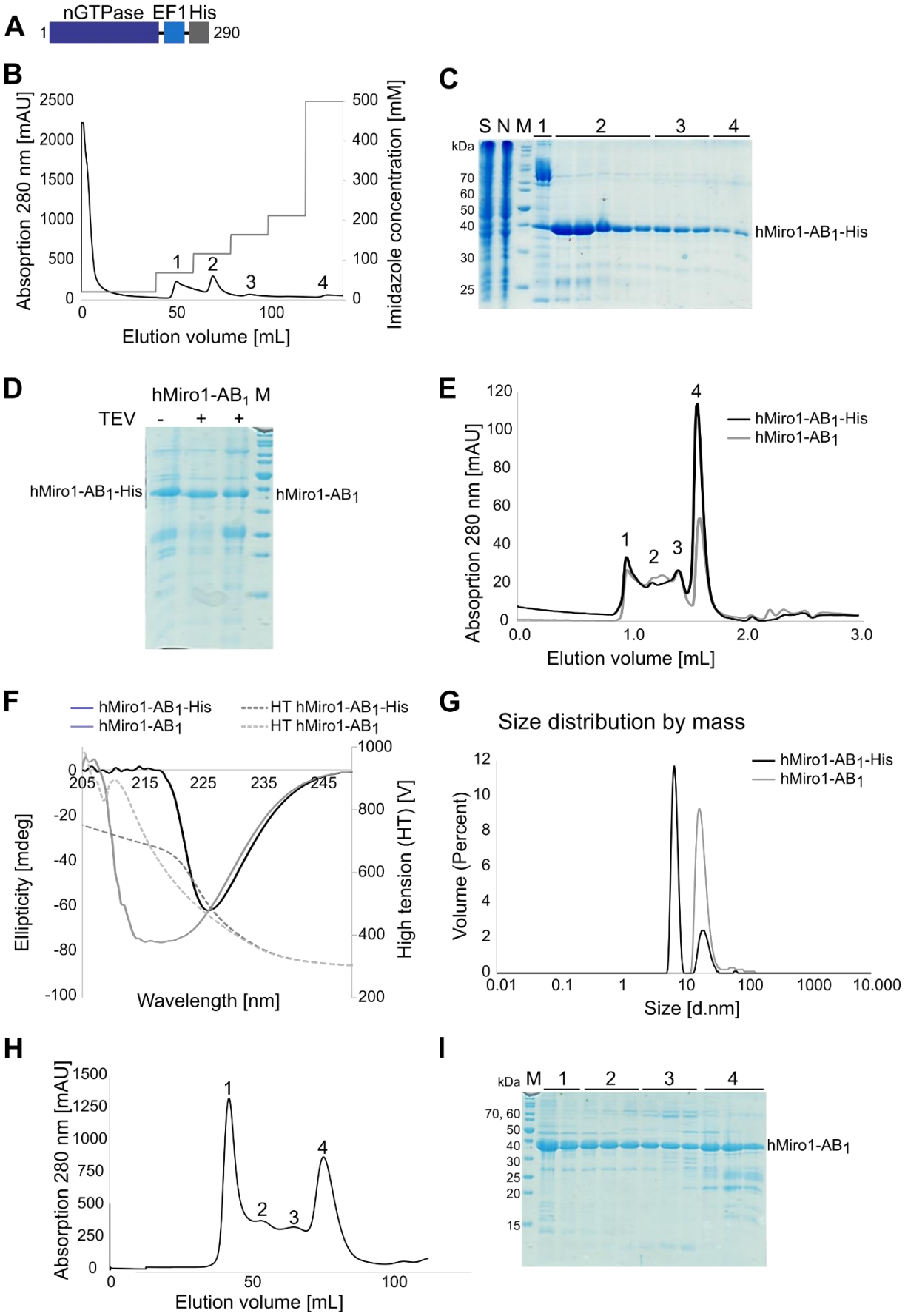

Figure A.20: Purification and characterisation of hMiro1-AB$_1$-His. (**A**) hMiro1-AB$_1$-His construct design comprising the nGTPase, EF1 and a C-terminal TEV cleavable His$_6$-tag. (**B-C**) The nickel IMAC and the corresponding SDS gel of hMiro1-AB$_1$-His show that only few impurities co-purify with the target protein. (**D**) The shift of the bands in the 12% SDS gel after cleavage of the His$_6$-tag of hMiro1-AB$_1$ is not significant. (**E**) The

elution volume of monomeric hMiro1-AB_1 (35.2 kDa) on the SD200 3.2/300 increase column corresponds to 50 kDa (peak 4). Cleavage of the His_6-tag reduced the amount of monomeric hMiro1-AB_1 significantly. (**F**) Circular dichroism spectroscopy of hMiro1-AB_1 before and after the TEV digest reveal differences in the secondary structure. (**G**) Dynamic light scattering analysis of hMiro1-AB_1 before and after cleavage of the His_6-tag. (**H-I**) Even after the TEV digest a substantial fraction of hMiro1-AB_1 elutes as monomer from the preparative SEC. (**C**, **D**, **I**) S = supernatant after centrifugation, N = non-bound protein, M = marker.

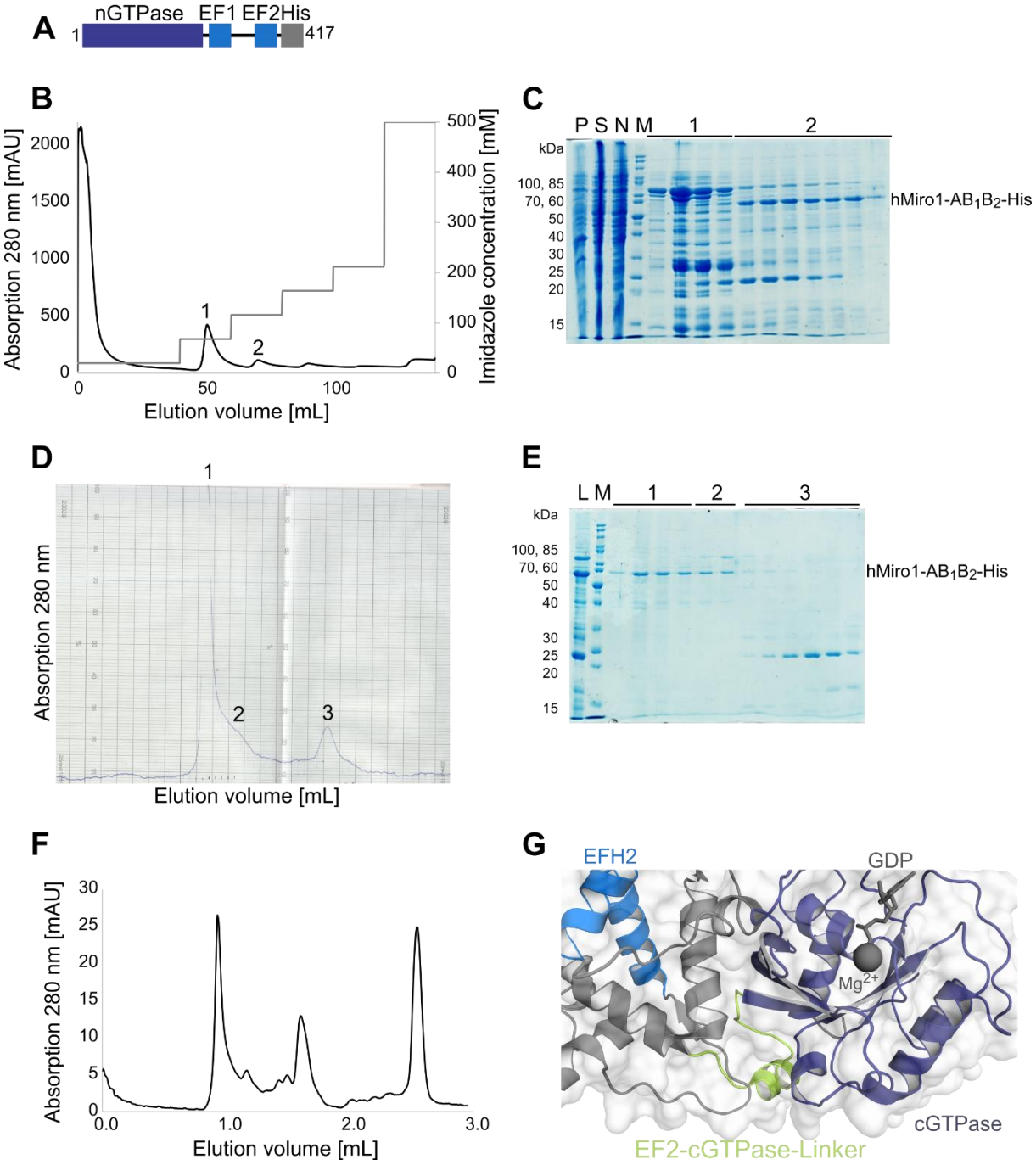

Figure A.21: hMiro1-AB_1B_2-His purification. (**A**) The construct of hMiro1-AB_1B_2-His comprises the nGTPase and both EF hand domains. It is C-terminally His_6-tagged and has a size of 50.0 kDa. (**B-C**) hMiro1-AB_1B_2-His does not saturate the HisTrap™ FF crude column and many impurities remain during the nickel IMAC. (**D-E**) The preparative SEC and (**F**) the analytical SEC reveal that after cleavage of the His_6-tag no monomeric hMiro1-AB_1B_2 was obtained. P = pellet after lysis, S = supernatant after lysis, N = non-bound protein, M = marker, L = load. (**G**) Cartoon and surface representation of hMiro1-B_1B_2C (PDB-ID: 5KTY) with EFH2 (light blue) and the cGTPase (dark blue). The extended linker, that was cut in the revised hMiro1-AB_1B_2 construct is highlighted in lime green.

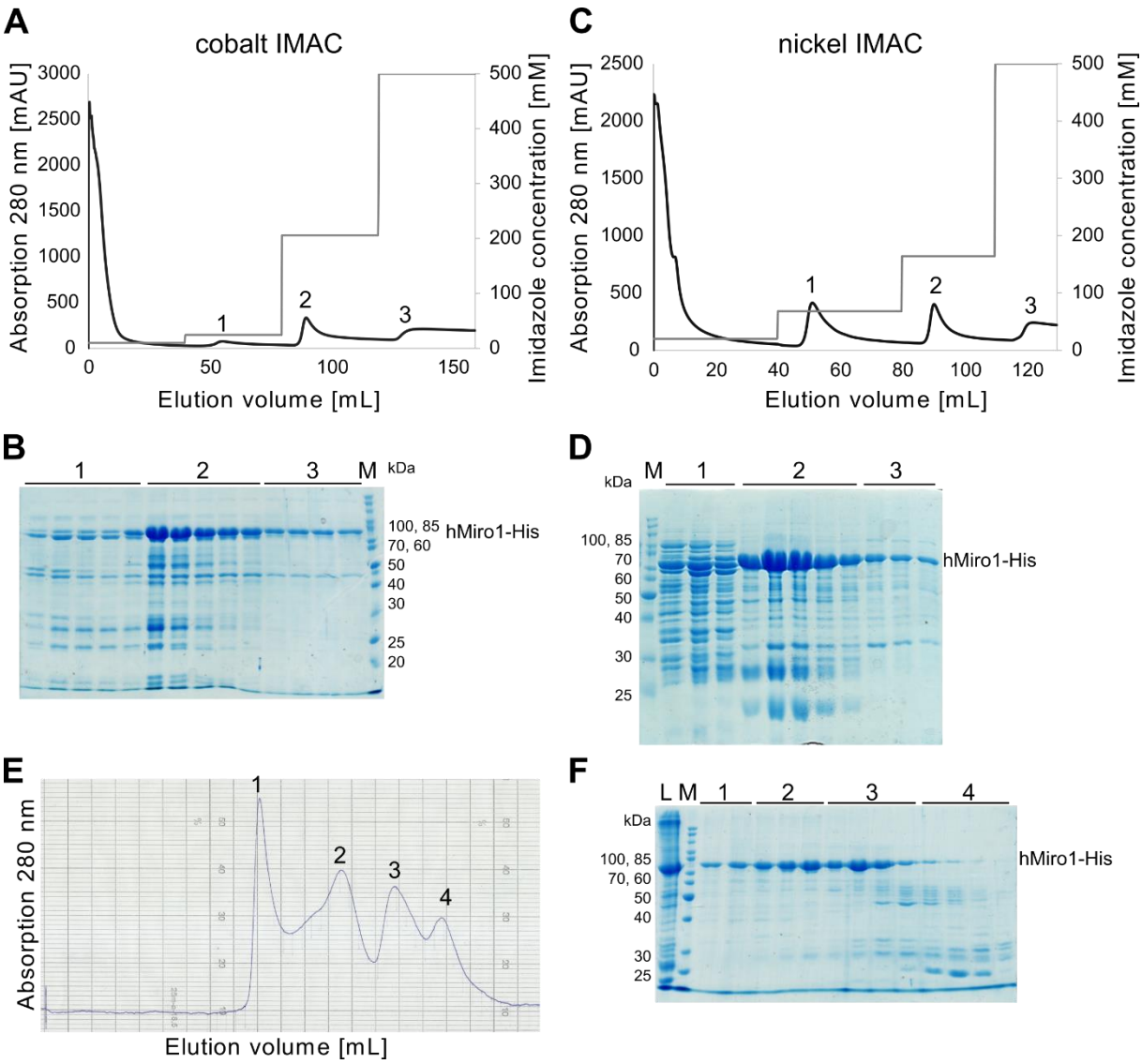

Figure A.22: Purification of full-length hMiro1-His from *E. coli* BL21 cells. (**A-D**) Comparison of (**A-B**) a nickel IMAC or (**C-D**) a cobalt IMAC as initial purification step. During the nickel IMAC the amount of impurities on the column is much higher (compare peak 1 in panel A and C). Peaks in the elution profiles and corresponding SDS gels as indicated by numbers. (**E-F**) A substantial fraction of hMiro1-His elutes as monomer (peak 3) from the SD200 16/600 column during the preparative SEC. L = load, M = marker.

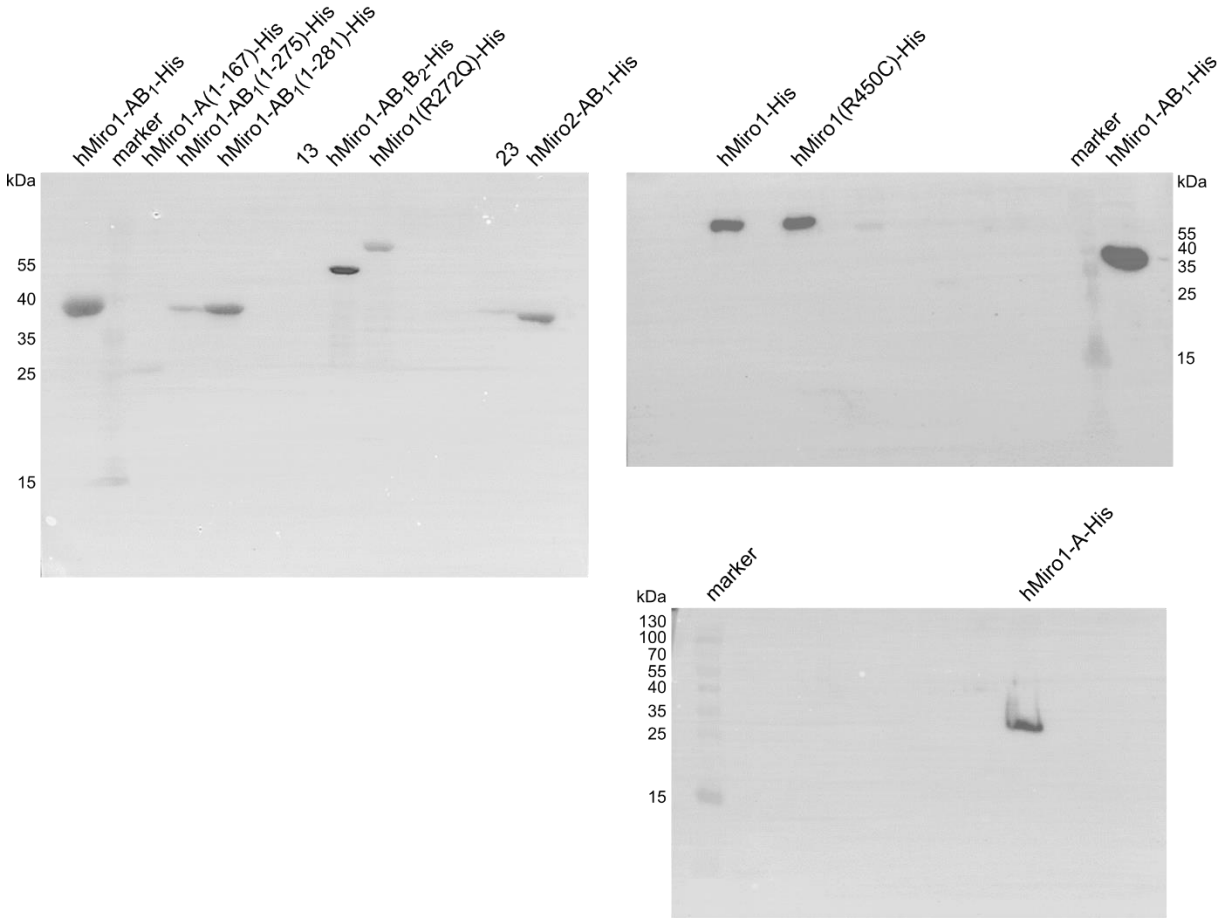

Figure A.23: Western blot analysis of hMiro1/2 samples. To confirm the expression of hMiro1 and hMiro2 constructs, samples were analysed by Western blotting with primary mouse α-His and secondary goat α-mouse antibodies.

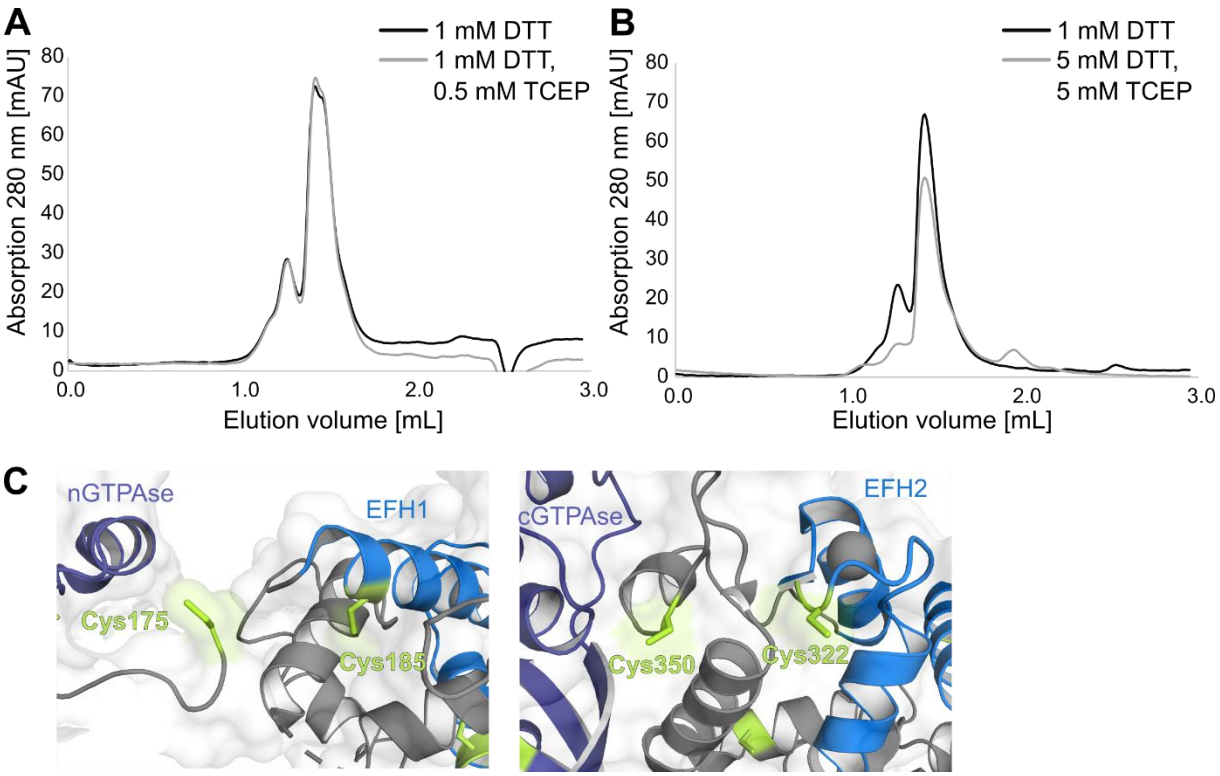

Figure A.24: Optimisation of hMiro1-His purification conditions by adding reducing reagents. (**A-B**) Analytical SEC elution profiles of hMiro1-His purified from *E. coli* at varying concentrations of reducing reagents. No significant improvement in the stability of hMiro1-His was recognisable and the concentrations as high as 5 mM DTT and TCEP did harm the used HiTrap™ Talon™ crude column. (**C**) Surface and cartoon representation of the structures of hMiro1-B_1B_2C and hMiro1-A (PDB-ID: 5KTY and 6D71) with highlighted surface cysteine residues (lime green).

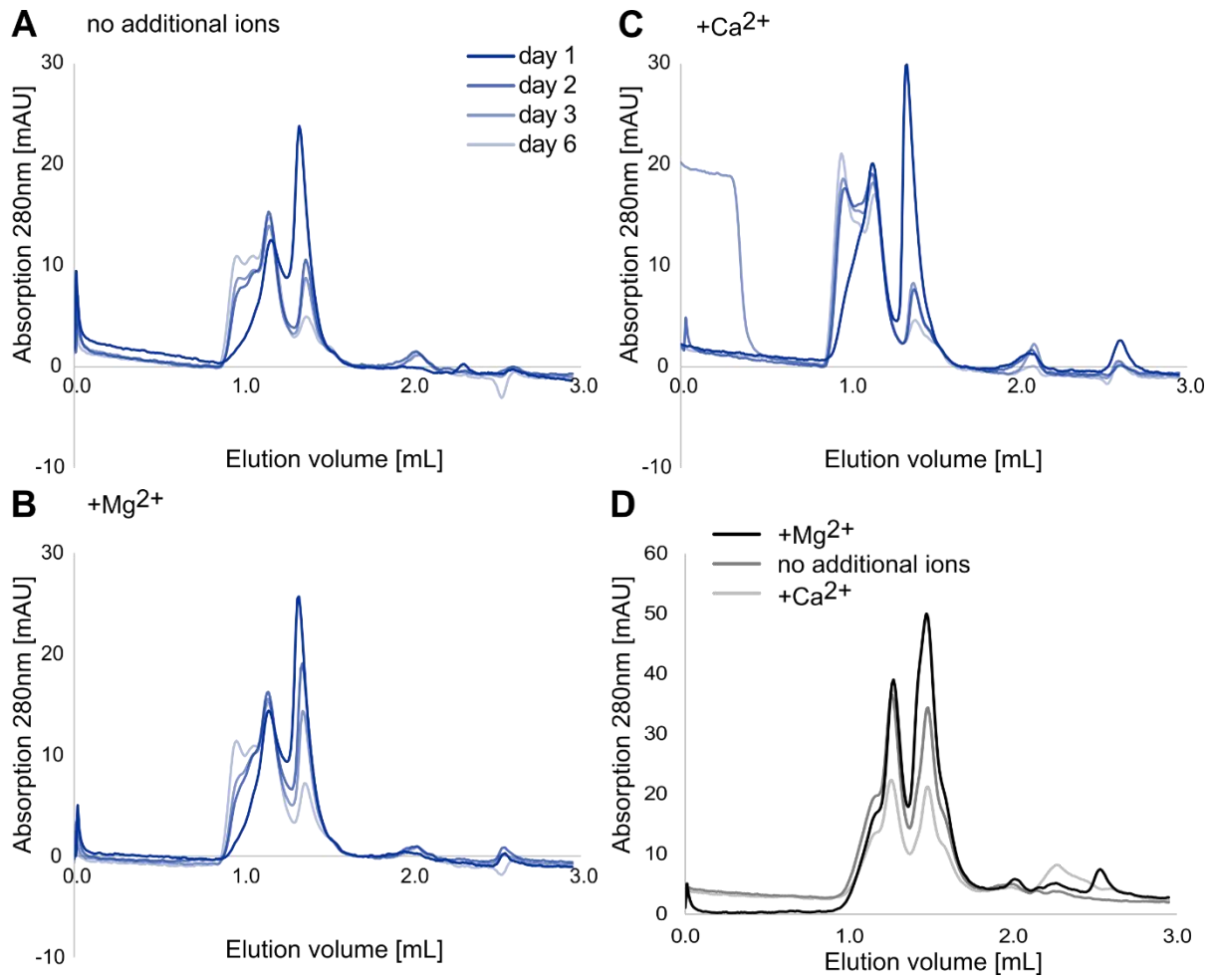

Figure A.25: Analysis of hMiro1-His stability in the presence of calcium or magnesium ions. (**A-C**) Elution profiles of insect cell expressed hMiro1-His (blue) in the presence of either 2 mM $CaCl_2$, 1 mM $MgCl_2$ or both. The presence of calcium ions accelerates the shift from monomeric to oligomeric hMiro1-His significantly while magnesium ions seem to have a stabilising effect. (**D**) The results for *E. coli* hMiro1-His (black/grey) are less conclusive due to the general instability of the protein. The presence of calcium ions increases the ongoing precipitation.

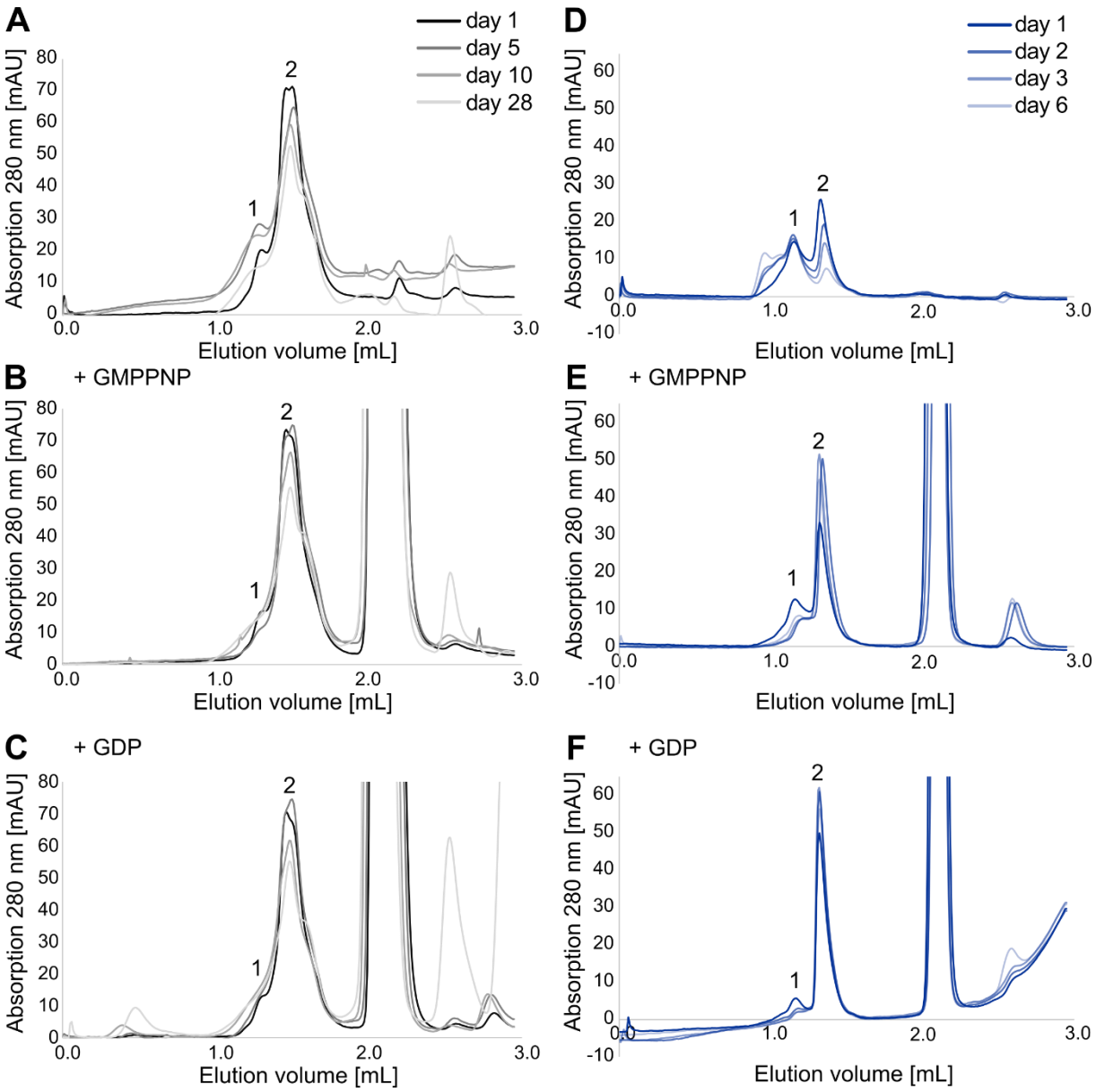

Figure A.26: hMiro1-His stability is dependent on binding to nucleotides. (**A**-**C**) Analytical SEC elution profiles of hMiro1-His expressed in *E. coli* (**A**) without nucleotides or with either (**B**) 2 mM GMPPNP or (**C**) 2 mM GDP. No significant changes in the ratio between monomeric and oligomeric hMiro1-His can be seen. (**D**-**F**) Analysis of the stability of hMiro1-His purified from insect cells in the presence of (**E**) 2 mM GMPPNP, (**F**) 2 mM GDP or (**D**) without nucleotides. Both GMPPNP and GDP significantly reduce the occurrence of oligomeric hMiro1-His over the course of 6 days.

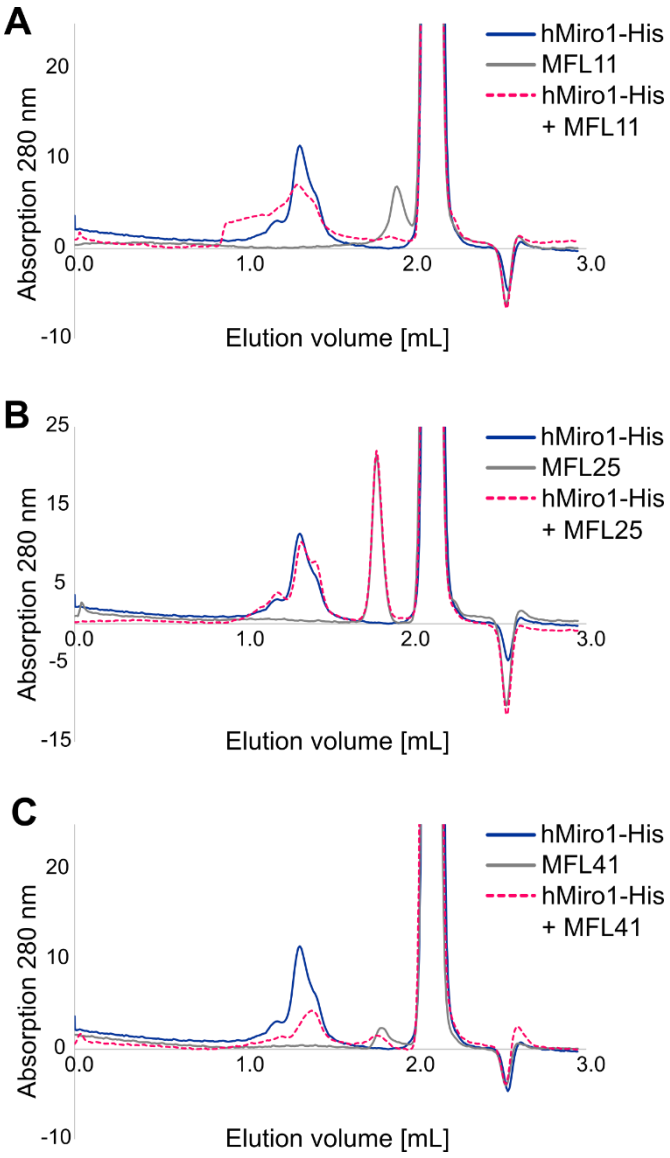

Figure A. 27: hMiro1-His and the hMiro1 specific nanobodies. (**A**-**C**) Analysis of the stability of insect cell expressed hMiro1-His with (**A**) MFL11, (**B**) MFL25 or (**C**) MFL41 by analytical SEC. hMiro1-His and the nanobodies were mixed in 1:1 ratio and 2 mM GDP was added. An exemplary selection of the tested nanobodies is shown.

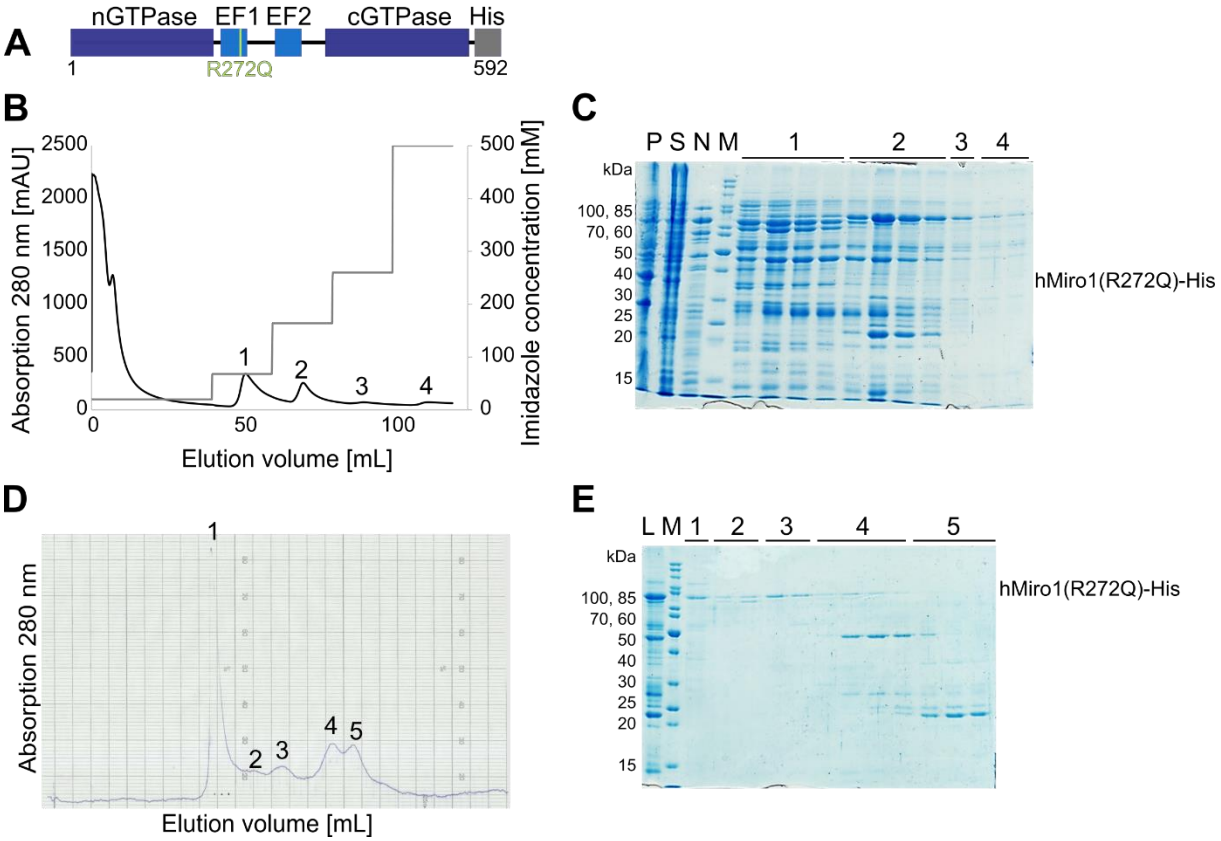

Figure A.28: Purification of hMiro1 carrying the PD-related mutation R272Q. (**A**) hMiro1(R272Q)-His construct design with the position of the mutation highlighted in lime green. (**B**-**E**) Purification of hMiro1(R272Q)-His by (**B**-**C**) nickel IMAC followed by (**D**-**E**) a preparative SEC. Peaks in the elution profiles and corresponding SDS gels as indicated by numbers. hMiro1(R272Q)-His expression levels are lower as compared to the wt and the protein did aggregate during the concentration for the preparative SEC. P = pellet after lysis, S = supernatant after lysis, N = non-bound protein fraction, M = marker, L = load.

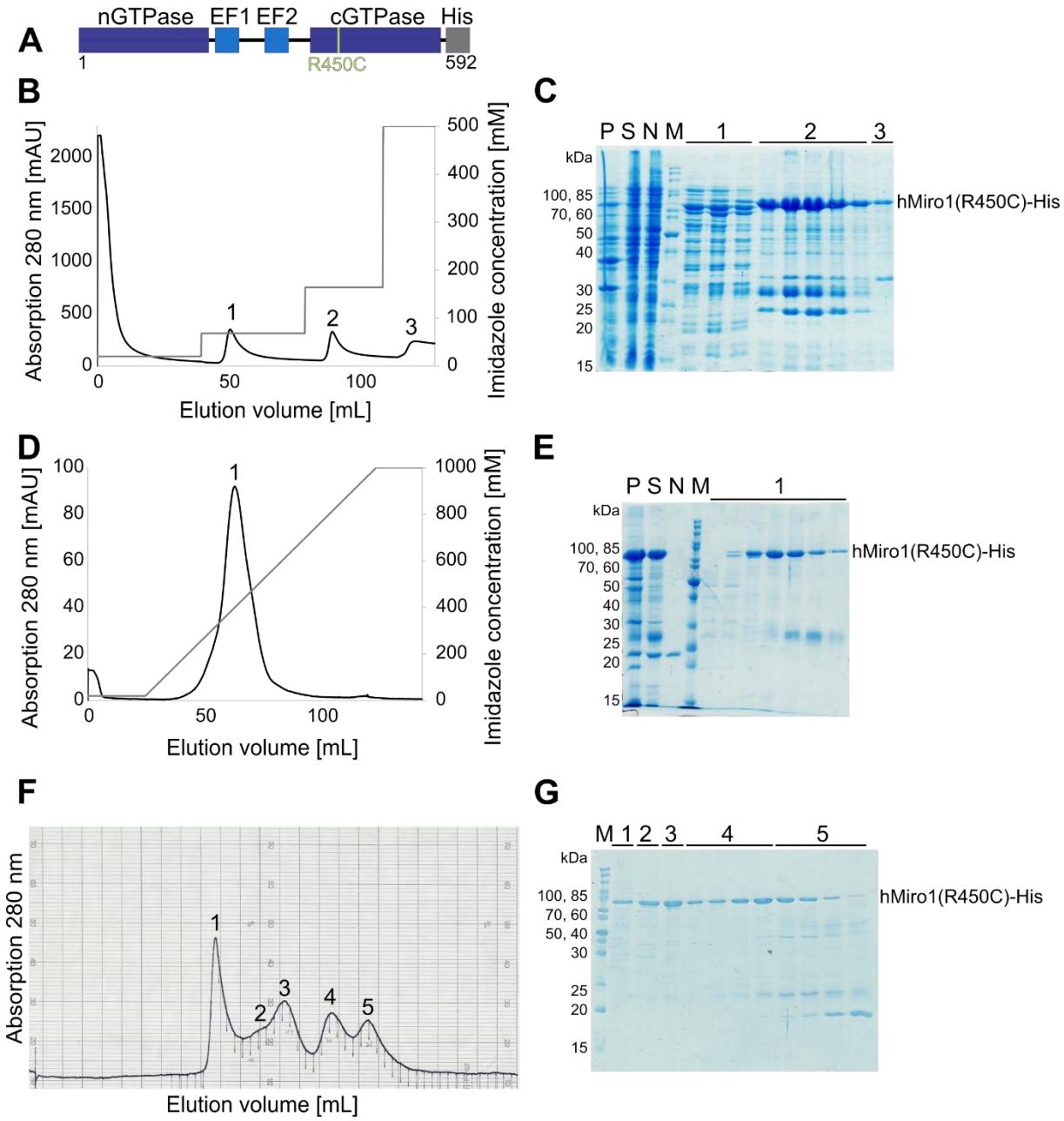

Figure A.29: hMiro1(R450C)-His shows similar behaviour as hMiro1-His during purification. (**A**) Construct design of hMiro1(R450C)-His comprising all soluble domains (blue) of hMiro1 with a C-terminal His_6-tag (grey). The PD-related mutation (lime green) is located at the Switch I region of the cGTPase. (**B**-**G**) hMiro1(R450C)-His purification by (**B**-**C**) nickel IMAC, (**D**-**E**) ion exchange chromatography and (**F**-**G**) preparative SEC. Peak fraction were loaded on SDS gels as indicated by numbers. hMiro1(R450C)-His precipitated significantly during the transfer in low salt buffer for the ion exchange chromatography.

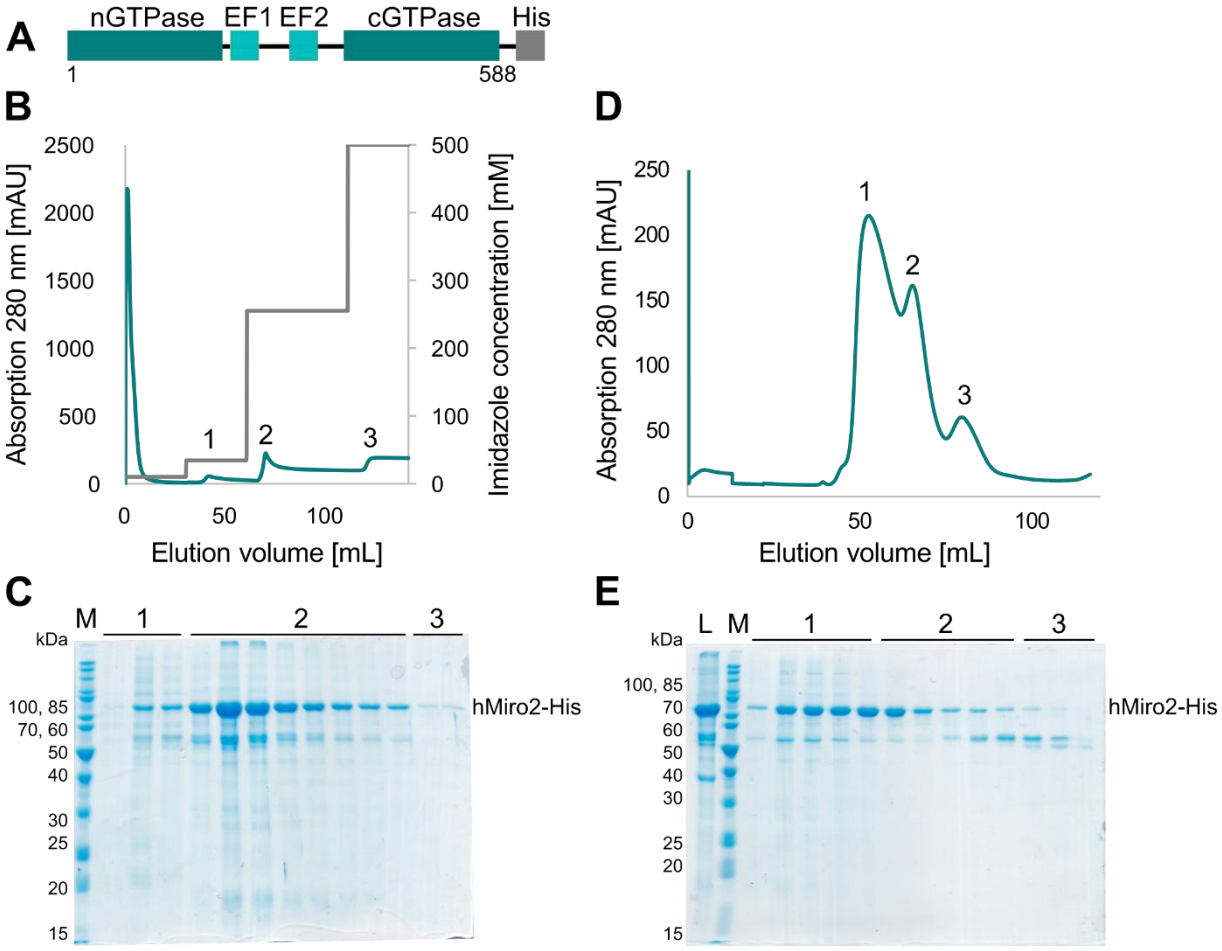

Figure A.30: Two-step purification of hMiro2-His. (**A**) The hMiro2-His construct was similarly designed to hMiro1-His, comprising both GTPase domains (dark cyan) and the calcium-binding EF hand domains (cyan) with a C-terminal His_6-tag (grey). (**B**-**C**) A substantial amount of hMiro2-His can be purified from High Five™ cells by cobalt IMAC. (**D**-**E**) The preparative SEC of hMiro2-His reveals the oligomerisation and aggregation of hMiro2-His. M = marker, L = load.

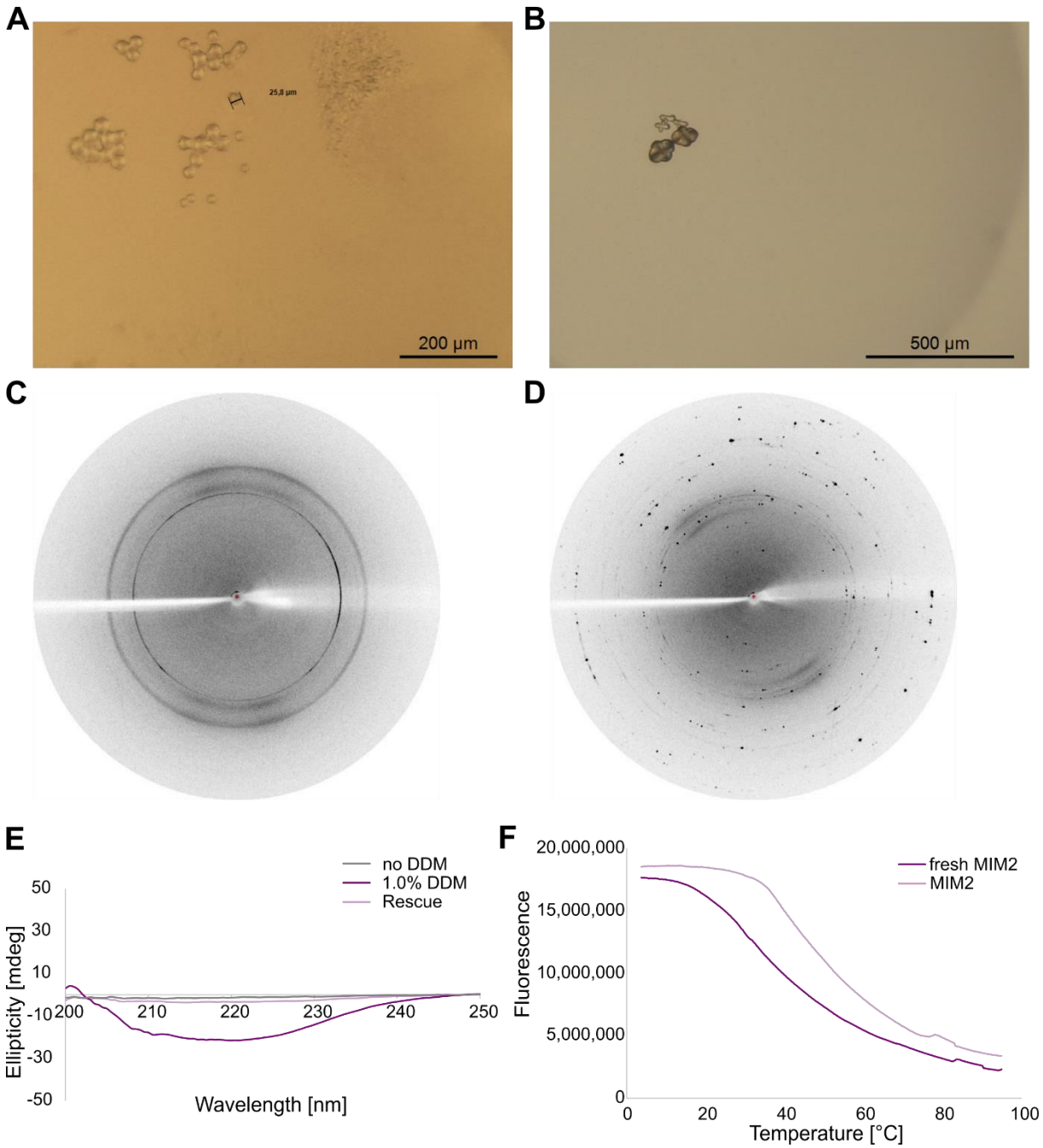

Figure A.31: Crystallisation of Mim2. (**A**-**B**) Microscopic images of the crystals most frequently obtained upon crystallisation of Mim2. Crystals were tested for protein content by the addition of Izit Crystal Dye (Hampton Research) to the crystallisation drop. While (**B**) cross shaped crystals did not incorporate the dye, (**A**) honey comb crystals incorporated the dye and appeared blue coloured shortly before dissolving. (**C**-**D**) Diffraction images collected from (**C**) honey comb shaped crystals or (**D**) cross shaped crystals, respectively. (**E**) CD spectroscopy of Mim2 purified with and without detergent or with detergent added after purification (Rescue). (**F**) Melting curve of fresh or frozen Mim2 determined by TSA. Mim2 does not display a clear melting point due to the absence of a hydrophobic core within the linear α-helical protein.

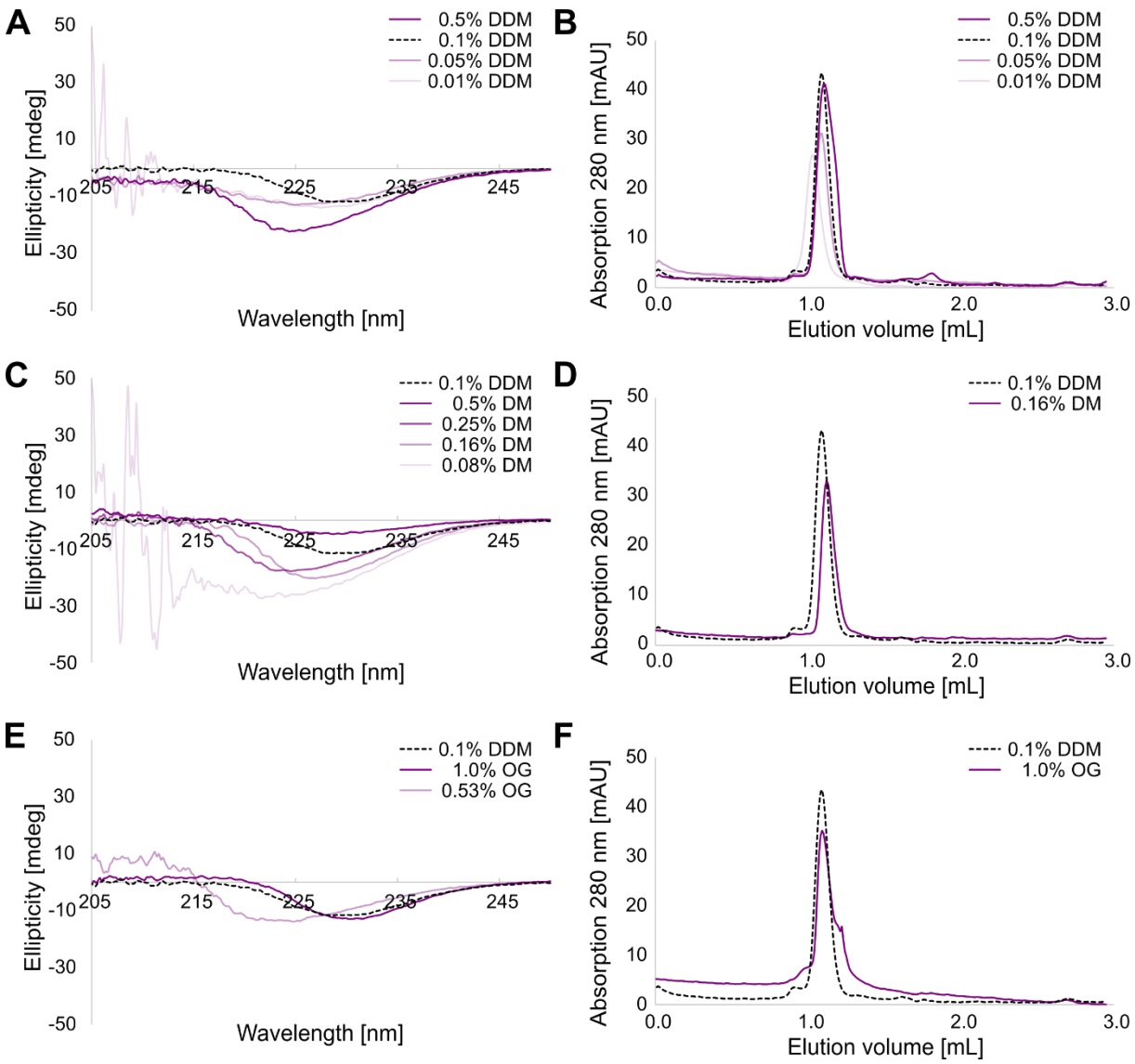

Figure A.32: Mim2 folding adopts to the detergent environment. (**A**, **C**, **E**) Circular dichroism spectroscopy of Mim2 in MOPs buffer containing (**A**) 0.01-0.5% n-dodecyl β-D-maltopyranoside (DDM), (**C**) 0.08-0.5% n-decyl β-D-maltopyranoside (DM) or (**E**) 0.53-1.0% OG. The spectrum with 0.1% DDM is displayed as reference. The peak position of the spectra varies between the different detergents and changes with the detergent concentration. Low detergent concentrations close to the CMC generally led to an increase in the signal-to-noise ratio. (**B**, **D**, **F**) Corresponding analytical SEC elution profiles with (**B**) 0.01-0.5% DDM, (**D**) 0.16% DM or (**F**) 1.0% OG added to the buffer during purification as indicated.

B. Structural analysis of bromodomains bound to acetyl lysine mimicking peptides

B.1 INTRODUCTION

DNA is wrapped around histones to form chromatin in the nucleus of eukaryotic cells. The units forming the chromatin are called nucleosomes. The nucleosome core comprises 146-147 base pairs of DNA organised in a super helix around histone protein octamers. The linker histone H1 binds to the DNA entry and exit sites of the nucleosome core, thus factilitating chromatin condensation. [162]. The histone proteins are overall positively charged, thus counterbalancing the negatively charged DNA backbone and enabling tight packaging of the DNA [163], [164]. PTMs of histone proteins have been shown to be important regulators of chromatin condensation and the corresponding gene transcription [165], [166]. Alterations in the electronic charge and structure of histone tails due to PTMs, such as acetylation, phosphorylation, methylation, ubiquitinylation, sumoylation, carbonylation, biotinylation or ADP-ribosylation, can directly influence the chromatin status [167]. A histone code has been proposed describing the interplay between different combinations of PTMs and the resulting transcriptional status of the gene [167], [168]. Acetylation is one of the most abundant PTMs of the human proteome, neutralising the positive charge of lysine residues. In histone tails, acetylation leads to loosening of chromatin packaging, resulting in enhanced DNA accessibility [169], [170]. Histone acetylation is regulated by counteracting histone acetyltransferases (HATs) and histone deacetylases (HDACs) [171], [172]. The lysine acetylation (KAc) patterns are selectively recognised by bromodomain (BD) containing proteins (BRDs) [173], [174] which are able to recruit downstream proteins for PTM modifications and communicate with a widespread network of transcriptional regulators. Alterations in the lysine acetylation balance due to changes in the abherrant expression pattern of HATs, HDACs and mutations in BDs have been linked to various types of cancer and tumorigenesis [175], indicating that they can serve as targets for the development of specific inhibitors.

B.1.1 Lysine acetylation and deacetylation on histone tails

Although formerly very difficult to identify, modern mass spectrometry based whole proteome analysis methods have established acetylation as a global PTM and highlighted the abundance of lysine acetylation in nuclear and mitochondrial proteins [176]–[180]. The protein core of the nucleosome is built up by an octamere containing two copies of four histone proteins: H2A, H2B, H3 and H4 [181]. The tail of each histone is rich on lysine residues of which many have been found to be targets for lysine acetylation, including eight acetylation modification sites on histone H2A (N-terminal: K5, K9, K13 and K15, C-terminal: K95, K118, K127, K129), ten sites on histone H2B (N-terminal: K5, K12, K15, K20, K24 and K25, C-terminal: K108, K116, K120, K125), nine sites on histone H3 (N-terminal: K4,

K9, K14, K18, K23, K27, K36 and K56, C-terminal: K122) and five sites on histone H4 (K5, K8, K12, K16 and K20) (Fig. B.6, A) [182]–[185].

The acetylation of histones is mediated by HATs which transfer the acetyl group of acetyl-coenzyme A (acetyl-CoA) onto the ε-amine of lysine residues (Fig. B.1). About 37 mammalian proteins have been proposed as HAT family proteins grouped into five major HAT classes: The, from yeast to mammals conserved, General control non-depressible 5 (GCN5)-related N-acetyltransferase (GNAT) family, the HAT1 family and the MYST family, the metazoan specific cyclic adenosine monophosphate (cAMP) response-element binding protein (CREB) binding protein (CBP)/p300 family and the fungal Rtt109 family [186]–[190]. Additionally, several subfamilies including the transcription factor related subfamily and the steroid receptor co-activator subfamily have been described [186], [191]. Both the HATs of the GNAT and the CBP/p300 family carry bromodomains for acetyl lysine recognition in addition to their HAT domains. Proteins of both families are responsible for the recruitment of the transcriptional machinery, thus directly influencing gene expression [182]. In contrast, the MYST family HATs carry a distinct highly conserved MYST domain and interact with transcriptional cofactors to coordinate transcriptional activation and silencing [192].

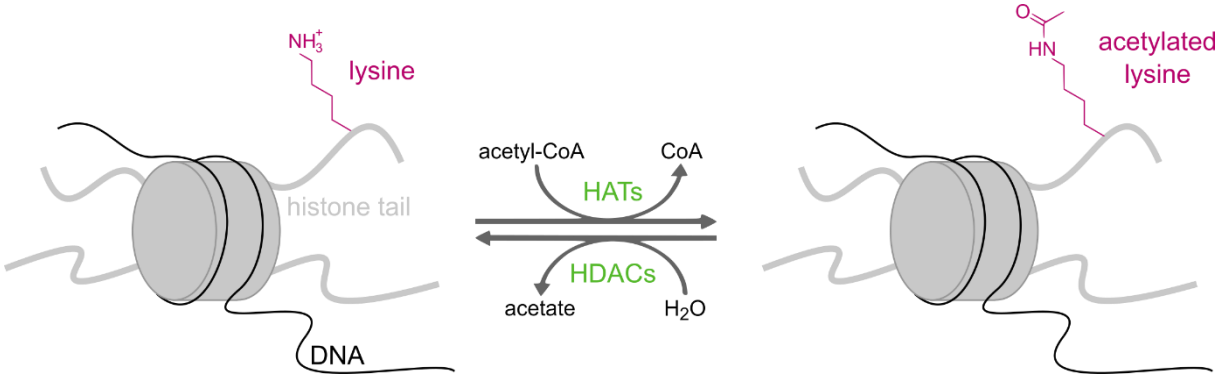

Figure B.1: The acetylation of lysine residues is balanced by histone acetyltransferases and deacetylases. The acetyl group of acetyl-CoA is transferred by histone acetyl transferases (HATs) onto the ε-amide group of lysine residues in histone tails. The process is highly reversible, and the acetyl groups are removed by histone deacetylases (HDACs). Histone acetylation neutralises positive charges of lysine residues leading to the relaxation of the chromatin packing.

Deacetylation of lysine residues is controlled by HDACs which can be grouped into 5 major classes: I, IIa, IIb, III and IV. They can be further distinguished by their co-factor dependency in either Zn^{2+}-dependent HDACs (I, IIa, IIb and IV) or nicotinamide adenine dinucleotide (NAD^+)-dependent sirtuin deacetylases (SIRT) (III) [193]. HDACs of class I, II and IV share a conserved catalytic domain. In mammals, class I HDACs localise to the nucleus forming the core of transcriptional repressor complexes [194]–[196]. In contrast, class II HDACs display only limited lysine deacetylase activity [197], [198]. HDACs of class IIa can still act as transcriptional repressors through transcritptional repressor complexes [199], while class IIb HDACs mainly localise to the cytoplasm, target non-protein histones and display additional functions such as polyamine deacetylase activity [200], [201]. HDAC11, the only member of class IV [202], efficiently removes long-chain fatty-acyl groups from histone peptides rather than displaying deacetylase activity [203], [204]. In contrast to the Zn^{2+}-dependent

HDACs, the catalytic domain of class III HDACs have a conserved NAD^+-binding site [205]. To date, seven distinct SIRT proteins with specific localisation are known in mammals, some of which have weak deacetylase activity [206]–[210]. The low substrate specificity of HDACs allows them to act on several targets and in most cases multiple HDACs can act on a single acetylation site [211], [212].

B.1.2 Bromodomain containing proteins

BDs are protein interaction modules that specifically recognise KAc modifications. They were initially found in *Drosophila melanogaster* in the *brahma* gene [213] and subsequently identified as evolutionary conserved elements in many species [173]. There are 46 BRDs in the human proteome carrying a total of 61 BDs [214]. BRDs are classified into 8 major families based on sequence and structural homology. The first structure of a BD (Fig. B.2) was determined in 1999 in the HAT protein p300/CBP associated factor (PCAF), a member of the GNAT HAT family [174]. The structure was solved in the unliganded state as well as in complex with acetylhistamine, an acetyl lysine analog. A core fold comprising a four-helix bundle (named αZ, αA, αB, and αC, respectively) connected by an extensive ZA loop between αZ and αA and two smaller loops between αA/αB and αB/αC was revealed. The four α-helices are tightly packed in an antiparallel left-handed fashion and although BD modules display sequence variability, their structural fold is highly conserved.

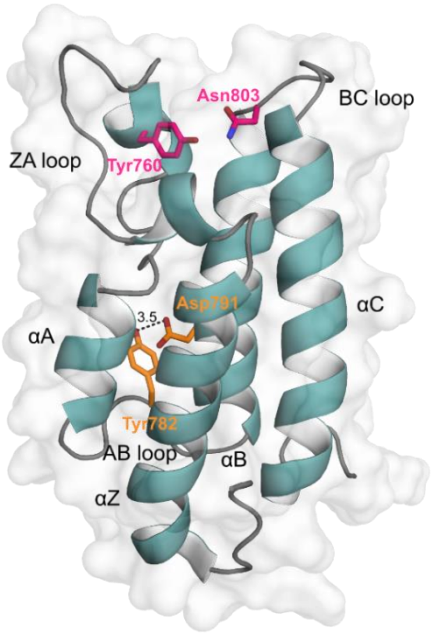

Figure B.2: Structure of the PCAF bromodomain. The first atomic structure of a BD was solved by NMR (PDB-ID: 1N72) [174]. The BD fold of PCAF (teal) comprises a tightly-packed four-helix bundle which is stabilised by the interaction of two conserved residues (Tyr782 and Asp791, orange). The helices are connected by three extended loops, ZA, AB and BC. The ZA and BC loops form the KAc binding pocket. KAc interacts with two conserved residues in the binding pocket, an asparagine (Asn803) and a tyrosine (Tyr760) highlighted in pink. The binding specificity of BDs is mediated by the corresponding surface properties as the BD fold is conserved among all BDs.

The conserved fold is stabilised by a hydrogen bond formed between a conserved tyrosine residue in the AB loop that engages an aspartic acid on the αB helix. The ZA loop and the BC loop form a deep hydrophobic cavity which serves as KAc binding pocket. Two conserved residues mediate the contact between the BD and KAc: An asparagine residue in the BC loop is directly engaging with KAc, whereas a conserved tyrosine residue in the ZA loop interacts indirectly via a water molecule [215]. In some BDs, the ZA loop displays an unusual fold and the conserved asparagine is replaced, mostly by tyrosine

or threonine, suggesting alternative mechanisms for KAc recognition [214], [216]. In most structures, five ordered water molecules can be found at the bottom of the narrow but deep KAc binding pocket engaging in interactions with the KAc. The study revealing the first bromodomain structures also established the specific interaction between bromodomains and KAc [174]. Subsequently, the selectivity of BDs for specific acetylated histone motives was shown to be mainly dependent on the variability ZA and BC loops [215], [217]. Indeed, the association of KAc with BDs is weak unless in context of the flanking histone tail sequences which determine the surface properties and as a consequence the binding specificity [214].

BDs can be found in a diversity of proteins including HATs and HAT associated proteins, transcriptional co-activators and mediators, helicases, methyl transferases, nuclear scaffold proteins and chromatin-remodelling complexes. BRDs prevalently localise to the nucleus and most of their functions are related to chromatin remodelling or transcriptional regulation [214], [218]. They are expressed in a wide variety of tissues displaying a broad and variable expression profile, suggesting a role for BDs in context specific transcriptional control [219]–[221]. Besides catalytic domains, BRDs possess additional motifs such as protein interaction domains. These include methylation recognition domains such as plant homeodomain (PHD) fingers, bromo-adjacent homology (BAH) domains or proline-tryptophan-tryptophan-proline motif (PWWP) domains. Other interaction domains such as kinase-inducible domain (KID)-interacting (KIX) domains and SAND (DNA-binding protein domain) domains can also be found [221].

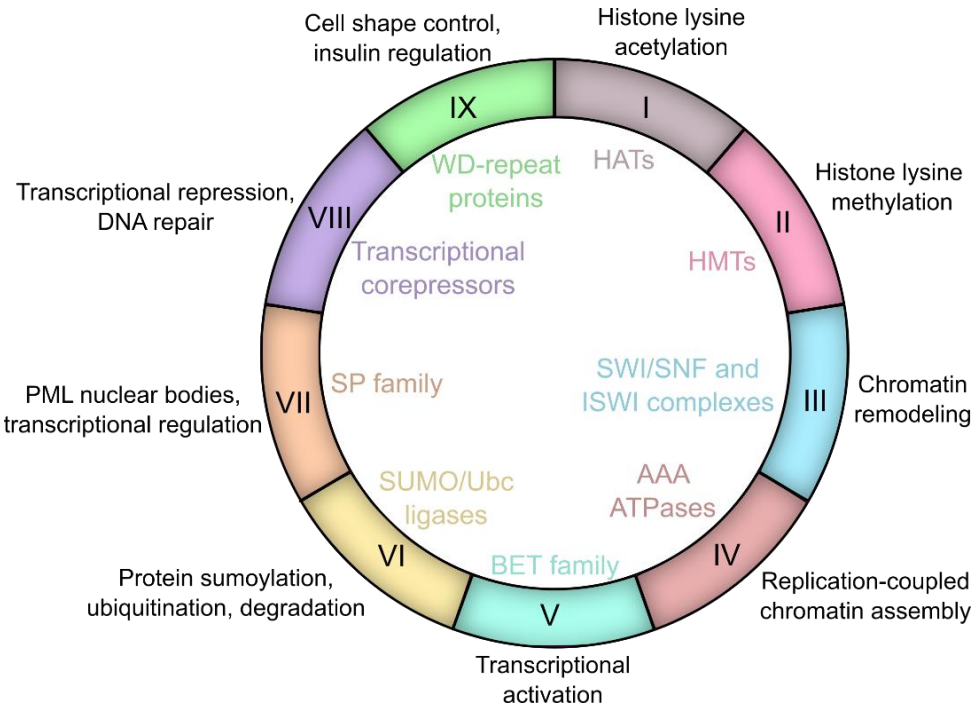

Figure B.3: Function-based classification of the 46 BRDs. Displayed is the function-based classification of BRDs as proposed by N. Zaware and M. Zhou that highlights the roles of BDs in the context of the diverse functions of BRDs [222]. The classification partially overlaps with the structure-based clustering of BDs, particularly the BET family BRD containing proteins. HMT = Histone methyltransferase, PML = promyelocytic leukemia, SP = speckled protein, Ubc = Ubiquitin, SUMO = small ubiquitin-related modifier, SWI/SNF = switch/sucrose non-fermentable, ISWI, imitation SWI.

In 2019, Nilesh Zaware and Ming-Ming Zhou proposed an alternative classification of BD containing proteins based on function [222] in contrast to the structure-based clustering of BDs [214]. The function-based classification includes I) HATs, II) histone methyltransferases, III) chromatin remodelling factors, IV) ATPase associated with diverse cellular activities (AAA ATPase) proteins, V) BET family transcriptional coactivators, VI) E3 SUMO/ubiquitin ligases, VII) SP family proteins of PML nuclear bodies, VIII) transcriptional corepressors and IX) WD-repeat proteins (Fig. B.3). Both classifications display a significant amount of overlap, indicating that structurally related BDs are associated with functionally related BRDs.

Dysfunctional BRDs, caused by overexpression, mutations, chromosomal translocation, or gene fusion, are found to play important roles in multiple diseases [222]. Particularly many BDs have been linked to cancer where BD containing proteins impact oncogene and anti-apoptotic protein expression. Among the BRDs associated with cancer are transcriptional regulators (BRD4), transcriptional repressors (BAZ2A), HATs (CREBBP, EP300), E3 ubiquitin ligases (TRIM24) and chromatin remodelers (BAZ1A) [223]–[229]. BD containing proteins have been linked to metabolic disorders and autoimmune and inflammatory diseases [230]–[233]. Therefore, BRDs have emerged as attractive therapeutic targets. However, the complex interplay between BRDs and their associated protein ligands renders the development of specific inhibitors difficult and requires further research to explain the role of histone modifications in gene transcription.

B.1.3 BET family bromodomains

The Bromodomains and Extra-Terminal (BET) domain family is the most extensively studied group of BD containing proteins. BET family proteins are characterised through their unique domain organisation (Fig. B.4, A) comprising two tandem BD domains with a high level of sequence conservation (Fig. B.4, C), an N-terminal extra-terminal (NET) domain and a more divergent C-terminal protein-interaction domain. Members of the BET family of BRDs are BRD2 [234], BRD3 [234], BRD4 [235] and the testis-specific BRDT [236]. BET family BD containing proteins (BETs) are encoded on paralogous genes and likely evolved due to repeated duplication from a common ancestral gene [237].

The tandem BDs of the BET family, namely BD1 and BD2 (e.g. BRD4(1) and BRD4(2) in case of BRD4), share little homology, enabling the regulation of independent transcriptional processes, however, the critical residues for KAc binding are highly conserved [238]. In contrast to other BDs, the BD1 of the BET family possesses an enlarged binding cavity enabling the cooperative binding of two side-by-side KAc histone modifications [214], [236], [239]. Although different BETs can be found in the same tissue type, they display individual distribution of expression levels, indicating that the BETs are not redundant but accomplish individual functions [240].

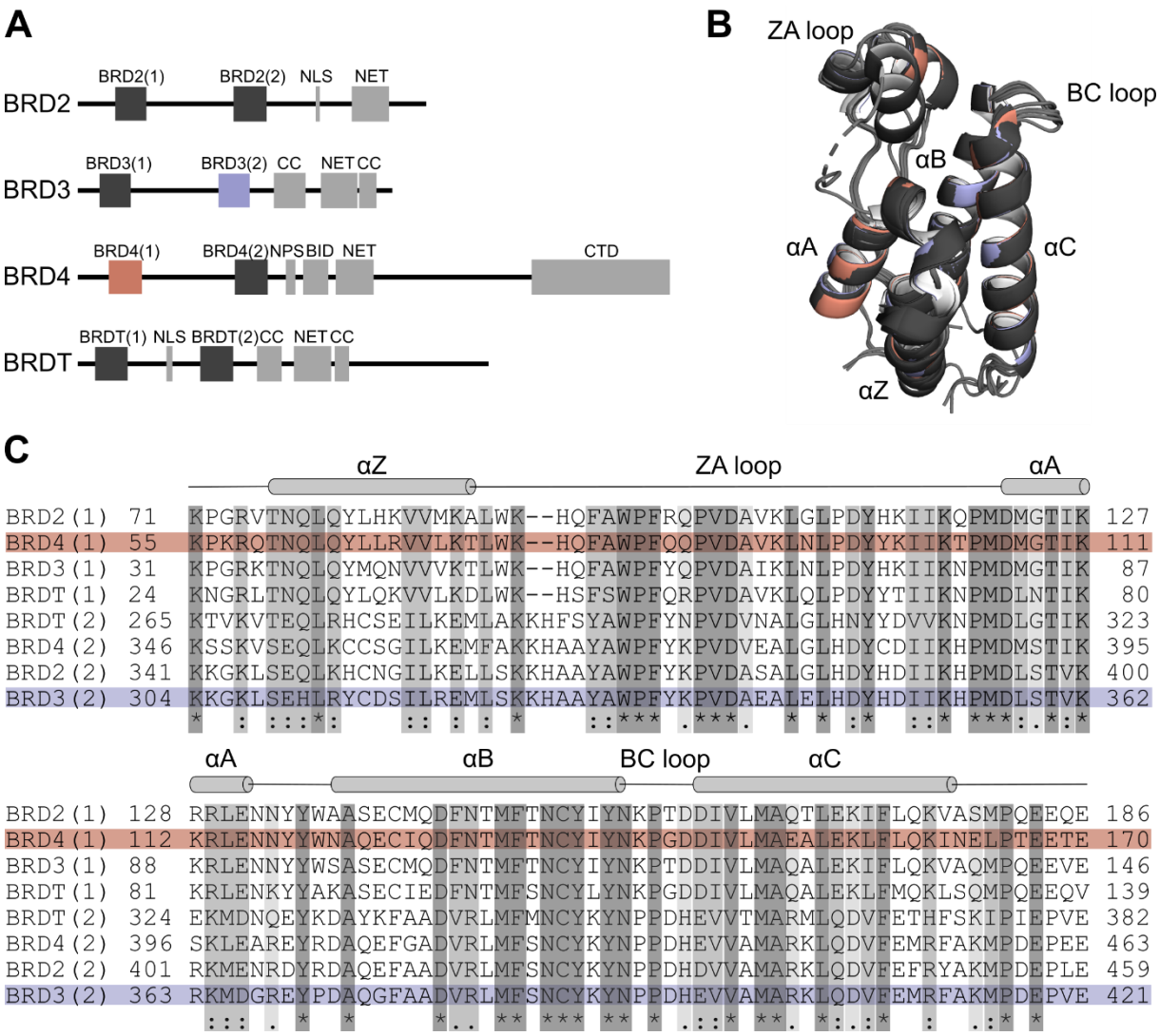

Figure B.4: BET family bromodomains. (**A**) Domain organisation of the BET family proteins BRD2, BRD3, BRD4 and BRDT. The C-terminally located conserved bromodomains are highlighted in dark grey, blue or red. Towards the C-terminus, BET family proteins possess additional protein interaction domains as indicated. NLS = nuclear localisation sequence, CC = coiled-coil, NPS = N-terminal cluster of phosphorylation sites, CTD = C-terminal domain, BID = basic residue enriched interaction domain. (**B**) A Structural alignment of all BDs in the BET family (PDB-IDs: BRD2: 1X0J, 2DVV, BRD3: 2NXB, 2OO1, BRD4: 2OSS, 2OUO, BRDT: 2RFJ, 2WP1) is shown. BRD3(2) is displayed in light blue and BRD4(1) in pale red. On top of the left-twisted four helix bundle, the two variable loops form the KAc binding pocket. (**C**) Sequence alignment of the BET family BDs with structural features indicated. The modifiable residues in the ZA loop majorly contribute to the electrostatic potential of the ligand interaction surface leading to the specificity in substrate recognition. Asterisks mark fully conserved residues and single and double dots indicate groups of residues with weakly or strongly similar properties, respectively.

Alterations in the expression level and mutations of BETs play an important role in many diseases due to the broad spectrum of cellular functions regulated by BETs. BRD2 regulates mitogenesis in lymphoid cells and ß-cells [228]. Additionally, BRD2 levels influence insulin production rendering BRD2 a promising target for diabetes treatment [241]. Elevated BRD2 expression levels have been found in cancers such as mesothelioma and melanoma, and they play a role in acute myocardial infarction. Moreover, α-synuclein induced expression of BRD2 initiates neuroinflammation in PD [242] and BRD2 upregulation can be found in spinal cord injury-induced macrophages and neuronal cells [243], [244].

BRD2 levels are altered in stress-induced inflammation with significant relevance for metabolic processes. BRD2 and BRD3 have partially overlapping functions and similar to BRD2, alterations in the expression level of BRD3 have been found to contribute to cancer, autoimmune diseases and adaptive immunity [245]. BRD3 mutations have been found in gastric cancers [246] and elevated BRD3 levels can be detected in the synovial tissue of arthritis and osteoarthritis patients [247]. BRD4 acts as transcriptional and epigenetic regulator during embryogenesis. It associates with the mediator coactivator complex [248] and recruits the positive transcription elongation factor P-TEFb thus regulating transcriptional elongation by ribonucleic acid (RNA) polymerase II [249], [250]. Notably, many cancer-associated genes are seemingly dependent on BRD4 including c-Myc [251]. In the nuclear protein in testis (NUT) midline carcinoma (NMC), a chromosomal translocation t(15;19) occurs, that produces a BRD4-NUT oncoprotein consisting of the tandem BDs of BRD4 fused to the NUT protein [252], [253]. Similar BRD3-NUT complexes and even three-way translocations have been reported [254], [255]. BRD4s role in diseases is not limited to cancer but it also contributes to inflammatory and autoimmune processes by regulating the activation of the NF-κB pathway. Moreover, BRD4 has essential roles in chronic obstructive pulmonary disease and spinal cord injuries [243], [256], [257]. Finally, BRDT, the fourth member of the BET family, is exclusively present in testis and ovaries [258]. During spermatogenesis, BRDT relocates to the nucleus to initiate acetylation dependent chromatin remodelling, thus controlling meiotic gene expression [259]. Alterations in the expression level of BRDT have been linked to ovarian cancer [260] and oligozoospermia and azoospermia in European men [261]. The transcriptional regulation by BRDs offers tremendous potential for the treatment of diseases through specific inhibition of the interaction between KAc and the BD as highlighted by the ever-increasing amount of patented bromodomain inhibitors.

B.1.4 Inhibition of BET family BDs

The first generation of small-molecule BD inhibitors was developed against the GNAT family HAT PCAF [262], which was quickly followed by inhibitors that block CBP binding to K382Ac of the human tumour suppressor p53 [263]. Subsequently developed highly efficient BET family specific inhibitors were based on thienotriazolodiazepines, a scaffold similar to benzodiazepines [264], [265]. Benzodiazepine-based inhibitors are established as being effective and safe in human treatment [266]. The diazepine-based inhibitors selectively interact with BET family BDs via a triazole ring that acts as acetyl-lysine mimetic and binds deep in the KAc binding pocket near the conserved Asn residue. The diazepine-based inhibitors include I-BET762, MS417, OTX015, CPI-203 but also isoxazole azepine 3, which contains a hydrogen-bond forming ring structure replacing the triazole [267] (Fig. B.5, A-B). Based on the benzodiazepine core, many different inhibitors have been developed by adjusting the groups adjacent to the triazole core in the binding pocket thus altering the affinity and specificity of the inhibitors [266]. JQ1, another diazepine-based inhibitor carrying the BD binding triazole moiety (Fig. B.5, A), has been in focus of researchers due to its effectivity in NMC treatment [268]. Inhibition

of the NMC causing BRD4-NUT fusion oncoprotein by JQ1 leads to tumor regression, growth arrest and squamous differentiation in NMC patient-derived models [253], [254], [268]. Similar positive effects have been seen for other triazolodiazepine inhibitors. MS417 is able to down-regulate the transcriptional activity of NF-κB in human immunodeficiency virus (HIV)-associated nephropathy [269]. CPI-203 shows positive effects in mantle cell lymphoma and pancreatic neuroendocrine tumor [270], [271] and OTX015 exhibits antitumor activity in multiple cancer cell lines [272], [273].

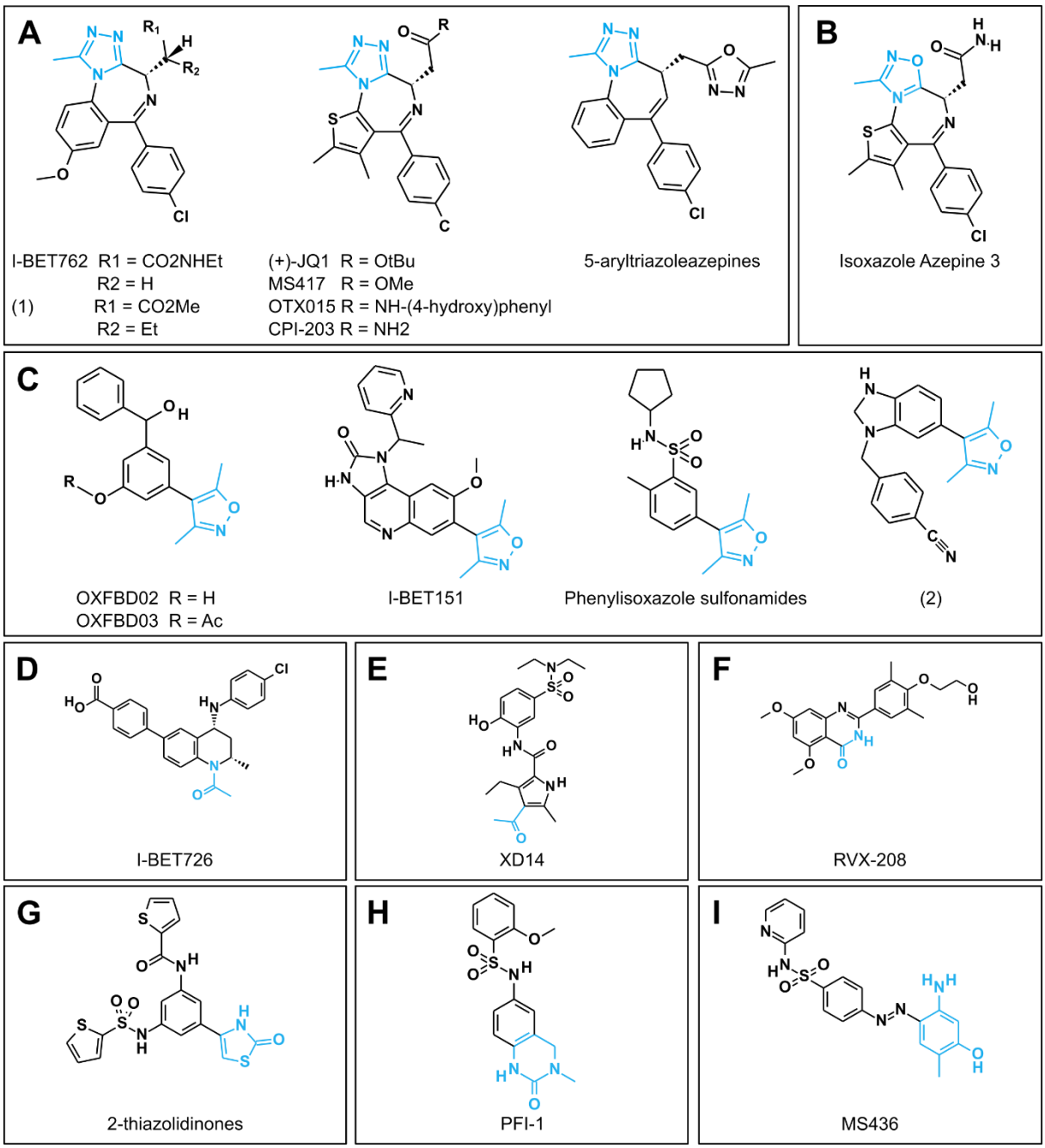

Figure B.5: Selection of important BET family specific BD inhibitors. (**A**-**B**) Diazepine-based inhibitors with (**A**) triazole ring or (**B**) isoxazole ring acetyl-lysine mimetics. (**C**) Dimethylisoxazole BET inhibitors. (**D**) Tetrahydroquinoline-based inhibitor binding to BETs via an acetamide group. (**E**) Acetyl-pyrroles. (**F**) Dimethoxy-quinazolinones (**G**) Dithiazolidinones, (**H**) Dihydroquinazolines, (**I**) Diazobenzenes. (**A**-**I**) The acetyl lysine mimicking group has been coloured in blue. Compounds without specific names were labelled by number. The variety in BD inhibitors is constantly increasing with newly found scaffolds and acetyl-lysine mimetics including xanthins, pyrido-indolones and thiazolidinones.

Recent efforts to expand the BET bromodomain inhibitors beyond the triazolodiazepines has resulted in the development of inhibitors with alternative core structures and new acetyl lysine mimicking groups. Many of these carry a quinoline or quinoline-like scaffold such as I-BET151 [223], I-BET726 [274], RVX-208 [275] or PFI-1 [276] (Fig. B.5, C, D, F, H). I-BET151 carries a 3,5-dimethylisoxazole ring that replaces the triazole ring and has been used in many BET inhibitors [277]. However, researchers constantly develop new inhibitors carrying an increasing spectrum of acetyl lysine mimetics.

The majority of the initially identified inhibitors, especially the diazepine-based inhibitors, are selective for BET family BDs, however, they are unable to distinguish between the individual BDs of the BET family or the two BDs of the same BET protein. Although the residues interacting with KAc are conserved in BET family BDs [215], the two tandem BDs of BETs are structurally distinct [214]. The specificity in the interaction with KAc carrying histone tails comes from the surface area surrounding the KAc binding side, which is formed by the ZA and BC loop of the BDs [214]. Newer generations of BET inhibitors show improved selectivity for BD1 or BD2. Examples for BD1 selective inhibitors are olinone [278], MS436 [279] and MS402 [280], while RVX-208 [275], GSK340 [281] and ABBV-744 [282] display a bias towards BD2. However, BET inhibitors are still mostly unable to distinguish between the BDs of the individual BETs.

Since BDs are solely reader domains that recognise lysine acetylation patterns but harbour no catalytic activities, the development of new inhibitors has recently been oriented towards dual-inhibitors. These dual-inhibitors exploit the close linkage of BDs to functional groups in proteins. The dual BET/HDAC inhibitor TW9 targets BRD4 as well as HDAC1 and is more effective in the inhibition of tumor cell proliferation as each individual inhibitor it is derived of (JQ1 and CI994) or a combined treatment [283]. Similarly, NEO2734, a dual BET/HAT inhibitor targeting BET BDs and CBP/EP300 shows increased potency against lymphomas, leukemia and prostate cancer as compared to CBP/EP300 inhibitors alone [284]. BRDs share key roles in diseases with enzymes such as kinases making them interesting targets for dual-inhibitor treatment. A wide variety of dual kinase/BRD inhibitors has emerged [285] since 2013 when the first kinase inhibitor dinaciclib also interacting with BRDs has been identified [286].

Many of the first generation BET inhibitors held promise as anti-cancer treatments due to their effective inhibition of proliferation. However, clinical trials showed that most of them have low oral bioavailability, short half-life times and display dose-limiting toxicity [287]–[289]. Newer BET inhibitors such as ABBV-744 are designed to overcome these effects and target only one BET BD with increased selectivity [290]. However, it is not yet clearly established if BD1 or BD2 needs to be targeted to maintain the anti-proliferative effects and reduce the dose-limiting toxicity [232], [290]. Exciting new studies demonstrate the combinatory effects of dual BET/HDAC, BET/HAT or BET/kinase inhibitors, which likely hold clinical potential to overcome toxicity and drug resistance [291]–[293]. BRD4 is the primary target of most BET inhibitors due to its oncogenic properties and the many tumour types that have been identified to be dependent on BRD4 function. To date, most BET inhibitors lack selectivity for BRD4, instead targeting all BETs [294]. Therefore, a better understanding of the distinct and

overlapping functions of the BET family BRDs and their mechanism of function would be beneficial for the development of improved inhibitors.

B.1.5 Acetyl-lysine mimetics

Studying BD containing proteins in context of their native acetyl-lysine carrying ligands *in vivo* remains challenging due to the presence of HDACs. For this reason, lysine acetylation sites in histone peptides are often mimicked by substituting amino acids reflecting the charge status of the acetylation site. While arginine mimics the positively charged lysine residue, the neutral amino acid glutamine serves as replacement for acetylated lysine [295]. However, biophysical properties of the acetyl-lysine other than the charge are not maintained. Alternatively, genetically incorporated phenylselenocysteine can be used to introduce acetyl-thialysine, a L-cysteine thioether with a terminal acetamide group that mimics acetyl lysine better than glutamine or arginine [296], [297]. In contrast to KAc, Acetyl-thialysine carries a sulfur atom at the γ-carbon position, which alters the biophysical properties of the residue.

Sören Kirchgäßner (group of Prof. Schwarzer, Interfaculty Institute of Biochemistry, University of Tübingen) designed and synthesised a new acetyl lysine mimetic based on the BD binding triazole moiety of the JQ1-inhibitor [298]. He incorporated the triazole ring into a synthetic amino acid, namely aminoheptanedioic acid-ε-3-methyl-1,2,4-triazole (ApmTri), that can either be used as building block in peptide synthesis (Fig. B.6, A) or can be genetically encoded with the amber codon suppression system.

S. Kirchgäßner determined the affinities of ApmTri comprising histone 4 peptides to BRD3(2) and BRD4(1) by microscale thermophoresis (MST) measurements (Fig. B.6, B) [298]. The affinity of H4K20ApmTri to BRD3(2) is comparable to the native-like acetyl lysine comprising peptide H4K20Ac. In contrast to BRD3(2), BRD4(1) is able to bind tandem acetyl lysine motifs of the K5 and K8 position of histone 4. S. Kirchgäßner obtained affinities for BRD4(1) and peptides with acetyl lysine, ApmTri or lysine in one or both acetyl lysine positions. The affinity of peptides with ApmTri in the K5 position to BRD4(1) is reduced approximately by 10 fold, whereas ApmTri in the K8 position has no effect on the affinity. Interestingly, a peptide with ApmTri in both the K5 and K8 position has a higher affinity to BRD4(1) than the H4K5ApmTriK8Ac peptide, indicating that ApmTri can replace KAc in the K8 position. In conclusion, histone tail-derived peptides carrying ApmTri hold potential as tools to study the BET family BDs.

In recent years, the need for inhibitors that cover large protein-protein interaction surfaces has shifted the attention towards peptide inhibitors. Although peptide-based drug candidates usually display low proteolytic stability, several strategies have been implemented to overcome this issue [299]. Peptide-based inhibitors can be cyclised and the backbone structure can be modified to effectively reduce the effects of proteolysis [300]. One possibility for the incorporation of ApmTri in such a peptide-based

inhibitor could be naturally occurring miniproteins [301], [302]. Miniproteins are oligopeptides with a well-defined disulfide-bond stabilised three-dimensional structure that include animal toxins, antimicrobial cyclotides and defensins [303]. The exchange of single amino acids within the scaffold is not problematic as long as the disulfide bridge network is maintained [304].Moreover, the combination of several ApmTri moieties could allow for the simultaneous inhibition of two BDs, thereby further increasing the selectivity of the inhibitor for individual BRDs. Miniprotein-based compounds have a high biological compatibility and they are promising candidates for drug development due to their extended structural complexity [305], [306].

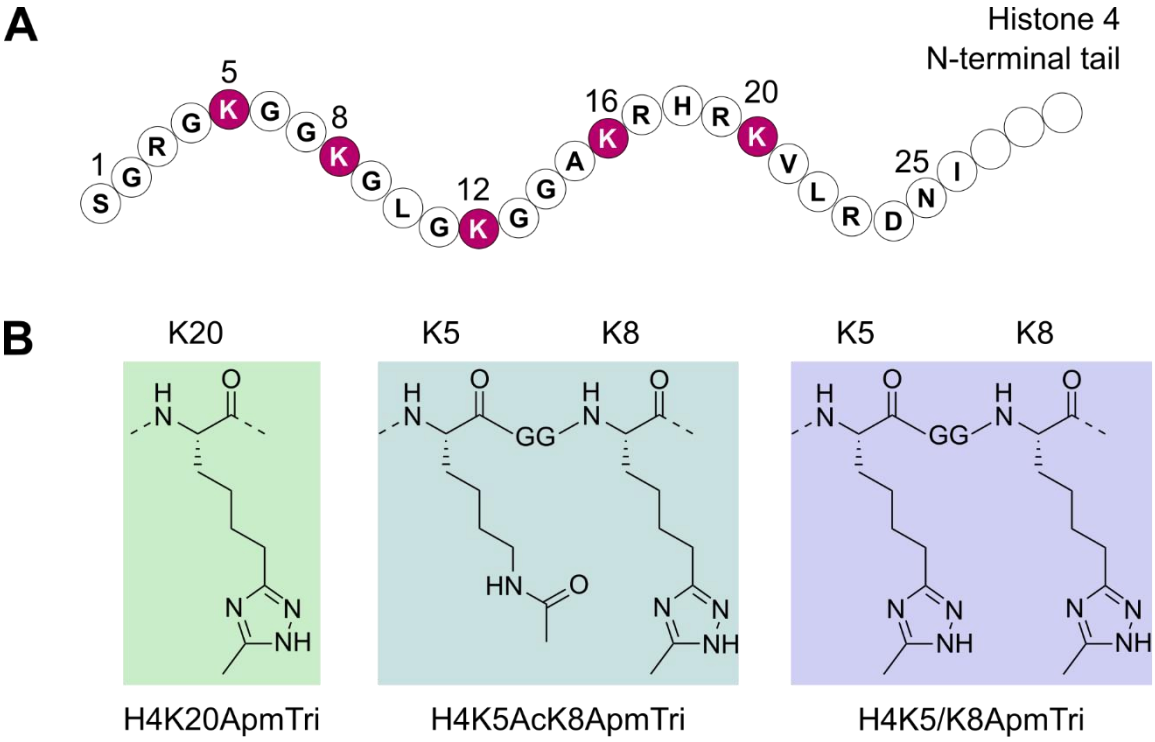

C

Peptide name	BRD	Sequence	Affinity [µM]
H4K20Ac	3(2)	*Ac*-AKRHR-**KAc**-VLRDNY-Ahx-C-NH_2	3.2 ± 0.3
H4K20ApmTri	3(2)	*Ac*-AKRHR-**ApmTri**-VLRDNY-Ahx-C-NH_2	6.5 ± 0.5
H4K5AcK8ApmTri	4(1)	*Ac*-SGRG-**KAc**-GG-**ApmTri**-GLGK-Ahx-C-NH_2	6.7 ± 0.5
H4K5/K8Ac	4(1)	*Ac*-SGRG-**KAc**-GG-**KAc**-GLGK-Ahx-C-NH_2	7.3 ± 0.5
H4K5/K8ApmTri	4(1)	*Ac*-SGRG-**ApmTri**-GG-**ApmTri**-GLGK-Ahx-C-NH_2	26.9 ± 2
H4K5ApmTriK8Ac	4(1)	*Ac*-SGRG-**ApmTri**-GG-**KAc**-GLGK-Ahx-C-NH_2	62.9 ± 5
H4K5AcK8	4(1)	*Ac*-SGRG-**KAc**-GG**K**GLGK-Ahx-C-NH_2	303 ± 32
H4K5K8Ac	4(1)	*Ac*-SGRG**K**GG-**KAc**-GLGK-Ahx-C-NH_2	675 ± 58
H4K5ApmTriK8	4(1)	*Ac*-SGRG-**ApmTri**-GG**K**GLGK-Ahx-C-NH_2	880 ± 108
H4K5K8ApmTri	4(1)	*Ac*-SGRG**K**GG-**ApmTri**-GLGK-Ahx-C-NH_2	No binding
H4K5K8	4(1)	*Ac*-SGRG**K**GG**K**-GLGK-Ahx-C-NH_2	No binding

Figure B.6: Acetyl lysine mimetic carrying peptides. (**A**) Sequence of the N-terminal tail of H4 with highlighted lysine acetylation sites (pink). (**B**) Acetyl lysine mimetic ApmTri and acetyl lysine incorporated in histone 4 tail-derived peptides [298]. The respective lysine position is indicated above. (**C**) Affinities of ApmTri histone peptides with the respective BD of the BET family [298]. S. Kirchgäßner determined the affinities by microscale thermophoresis.

B.2 OBJECTIVES

The second project of this dissertation focusses on the structural characterisation of peptides comprising the acetyl lysine mimetic ApmTri bound to BET family BDs. To analyse the potential of ApmTri as acetyl lysine mimetic in the context of bromodomains that recognise single or tandem acetyl lysine motifs, we aimed to determine structures of BRD3(2) and BRD4(1) bound to ApmTri. For this purpose, we collaborated with S. Kirchgäßner, who synthesised histone 4 tail-derived peptides comprising ApmTri and determined affinities for the BDs. A former member of the Stehle group, Dr. C. Koç (Department of Infection, Immunity and Cardiovascular Disease, University of Sheffield) collected an initial data set of BRD3(2) bound to H4K20ApmTri. Proceeding from this starting point, the objectives of this project included:

- Data processing and refinement of the BRD3(2)/H4K20ApmTri data set
- Crystallisation and structure determination of BRD4(1) bound to two acetyl lysine mimetic comprising peptides, namely H4K5AcK8ApmTri and H4K5/K8ApmTri

The previously collected data set of BRD3(2) with the H4K20ApmTri peptide had low completeness and contained diffraction rings originating from ice crystals. Several data processing strategies were tested to obtain the best possible data statistics. In parallel, BRD3(2)/H4K20ApmTri was crystallised in new conditions with the aim of determining a second data set, thereby confirming the mode of interaction between BRD3(2) and H4K20ApmTri.

B.3 MATERIALS AND METHODS

B.3.1 Materials

B.3.1.1 Chemicals

Table B.1: List of chemicals and corresponding manufacturers.

1,3-bis(tris(hydroxymethyl)methylamino)propane	Sigma-Aldrich
Dithiothreitol (DTT)	Sigma-Aldrich
Ethylene glycol	Sigma-Aldrich
L-Glycine	Sigma-Aldrich
(4-(2-hydroxyethyl)-1-piperazineethanesulfonic acid (HEPES)	Roth
2-Methyl-2,4-pentanediol (MPD)	Sigma-Aldrich
Polyethylene glycol 3350 (PEG 3350)	Sigma-Aldrich
Sodium chloride (NaCl)	Roth
Sodium fluoride (NaF)	Sigma-Aldrich

B.3.1.2 Buffers

Table B.2: Protein purification buffer.

BRD SEC buffer	10 mM HEPES pH 7.4, 150 mM NaCl, 1 mM DTT

B.3.1.3 Proteins and peptides

Table B.3: Acetyl lysine mimicking peptides. Synthesised by S. Kirchgäßner.

H4K20ApmTri	*Ac*-AKRHR-**ApmTri**-VLRDNY-Ahx-C-NH_2
H4K5AcK8ApmTri	*Ac*-SGRG-KAc-GG-**ApmTri**-GLGK-Ahx-C-NH_2
H4K5/K8ApmTri	*Ac*-SGRG-**ApmTri**-GG-**ApmTri**-GLGK-Ahx-C-NH_2

Table B.4: Protein construct overview.

Protein construct	Calculated molecular mass	Number of amino acids	Vector	Affinity tag
BRD3(2)	13.5 kDa	115	pET28a(+)	His_6-tag
BRD4(1)	15.3 kDa	129	pET28a(+)	His_6-tag

B.3.1.4 Consumables

Table B.5: List of consumable material used.

Amicon® Ultra-15 centrifugal filters (MWCO 3 kDa, 10 kDa)	Merck
Amicon® Ultra 0.5 mL centrifugal filters (MWCO 10 kDa)	Merck
Corning®-Costar®-Spin-X® centrifugal filters (0.22 µM)	Corning
Cover slides 12-542-C	Fischer Band
INTELLI-PLATE® 96	Art Robbins Instruments
Membrane filter (0.22 µM)	Millipore
Microtiter plate, 96-well	Greiner Bio-One
Pipette tips	Herbe Plus
Polyolefin cover foil	HJ-Bioanalytik GmbH
Reaction tubes (1.5 mL, 2.0 mL)	Greiner Bio-One
Serological pipettes (5 mL, 10 mL, 25 mL, 50 mL)	Greiner Bio-One
Syringes (1 mL, 5 mL, 10 mL, 30 mL)	Greiner Bio-One
Syringe-top filters (0.22 µM)	VWR international

B.3.1.5 Screens

Table B.6: Commercial crystallisation screens.

Crystal Screen HT™	Hampton Research
JCSG+ Suite	Qiagen
Morpheus®	Molecular Dimensions
Wizard Classic 1 and 2 Block	Molecular Dimensions

B.3.1.6 Instruments

Table B.7: List of hardware and instruments.

ÄKTA Basic	Amersham Pharmacia Biotech
ÄKTA Micro (Ettan LC)	GE Healthcare
Centrifuge 5415 D	Eppendorf
Centrifuge Heraeus™ multifuge 1 L-R	Thermo Fisher Scientific
CP323S-0CE scale	Sartorius
Cryo loops (0.05-0.5 mm)	Molecular dimensions
Freedom EVO™	TECAN
HiLoad Superdex™ 75 16/600 column	Cytiva
HiLoad Superdex™ 200 16/600 column	Cytiva
IKAMAG® magnetic stirrer Mini MR standard	VWR International
Microscope Leica MZ 16	Meyer Instruments
Microscope Leica MZ 95	Meyer Instruments
Milli-Q-Nerj	Millipore
Nanodrop ND-1000	Thermo Fisher Scientific
Nylon and pins	GE Healthcare
pH meter BP11	Sartorius
Sartorius ME premium semi micro scale	Sartorius
Superdex™ 75 PC 3.2/30	GE Healthcare

B.3.1.7 Software

Table B.8: Software and online tools.

Adxv	[307]
Albula	[308]
CCP4 (7.1.002 Suite)	Collaborative Computaional Project number 4, 7.1.002 Suite [309]
COOT (0.9.6.1)	[310]
ExPASy Protparam	Swiss Institute of Bioinformatics [134]
MATTHEW_COEF	[311], [312]
Molprobity	[313]–[315]
PHASER MR	CCP4, 7.1.002 Suite [316]
Phenix 1.16	Phyton-based Hierarchical ENvironment for Integrated Xtallography [317]
Phenix.eLBOW	[318]
Phenix.refine	[319]
Phenix.xtriage	[320]
POLYGON	[321]
PyMOL 2.5	DeLano Scientific LLC [135]
Unicorn™ chromatography software	Cytiva
XDS	[322]
XDSCONV	[322]
XDSGUI	[323]
XDSSTAT	[324]

B.3.2 Methods

B.3.2.1 Protein purification

All steps of the protein purification process described here were carried out at 4 °C with BRD SEC buffer (Table B.2).

Preparative size exclusion chromatography

BRD3(2) and BRD4(1) were expressed in *E. coli* and purified using a nickel IMAC. Afterwards, the His_6-tag was cleaved through thrombin digest by S. Kirchgäßner. C. Koç froze BRD3(2) after the preparative SEC for future usage and the protein was purified again by preparative SEC prior to crystallisation to remove any aggregates formed during the freezing process.

In preparation of the subsequent preparative SEC, BRD3(2) and BRD4(1) were concentrated in Amicon® Ultra-15 concentrators with a molecular weight cut-off (MWCO) of 3 kDa in several centrifugation steps each for 10 min at 2,000x g. Thereafter, the proteins were filtered (0.22 µM). BRD4(1) was loaded on an equilibrated HiLoad Superdex™ 75 16/600 column and BRD3(2) was loaded on an equilibrated HiLoad Superdex™ 200 16/600 column, installed on an ÄKTA Basic system. The proteins were eluted with 1.2 CV BRD SEC buffer and the elution process was monitored via the UV absorbance at 280 nm. Protein containing fractions were pooled and concentrated in Amicon® Ultra-15 concentrators (MWCO 3 kDa) at 2,000x g. BRD3(2) was concentrated to 13.5 mg/mL and BRD4(1) was concentrated to 11.8 mg/mL for assembling of complexes with the peptides and subsequent crystallisation.

Analytical size exclusion chromatography

To assess the quality of BRD3(2) samples for crystallisation after being frozen for several years at -20 °C, 40 µL of BRD3(2) at a concentration of 6.7 mg/mL were analysed by analytical SEC. For this purpose, aggregates in the thawed BRD3(2) sample were removed by centrifugation at 16,100x g for 5 min. The protein was loaded on a Superdex™ 75 PC 3.2/30 column installed on an ÄKTA Micro system. BRD3(2) was eluted with BRD SEC buffer while the protein's UV absorption at 280 nm was monitored.

B.3.2.2 Crystallisation

Crystallisation

The artificial amino acid ApmTri and the ApmTri-containing peptides were synthesised by S. Kirchgäßner. H4K20ApmTri was diluted in BRD SEC Buffer at a concentration of 20 mg/mL and stored at -20 °C. The quality of the thawed peptide was analysed via mass spectrometry by

S. Kirchgäßner. H4K5AcK8ApmTri and H4K5/K8ApmTri were diluted in BRD SEC buffer to 16.4 mg/mL or 16.7 mg/mL, respectively, and used right away. H4K20ApmTri and BRD3(2) were mixed in a 3:1 ratio, incubated for 1 h and centrifuged at 16.100x g, 10 min prior to crystallisation. H4K5AcK8ApmTri and H4K5/K8ApmTri were mixed with BRD4(1) in a 2:1 ratio, incubated for at least 30 min on ice and filtered to remove aggregates. Crystals of BRD4(1) co-crystallised with H4K5/K8ApmTri (mixed in a 1:2 ratio) did not contain any peptide, therefore BRD4(1) was mixed with H4K5/K8ApmTri in a 1:20 ratio for further crystallisation trials and after 1 h of incubation centrifuged at 16,100x g for 10 min. Crystallisation conditions for BRD4(1) with H4K5AcK8ApmTri and H4K5/K8ApmTri were screened in 96-well sitting drop plates with commercial screens (Table B.6). BRD3(2) with H4K20ApmTri crystallisation conditions were screened in a custom screen based on the crystallisation condition of unliganded BRD3(2) [214] with 80-280 mM sodium fluoride, 100 mM 1,3-bis(tris(hydroxymethyl)methylamino)propane pH 7 or 8, 14-25% (w/v) polyethylene glycol 3350 (PEG3350) and 9-12% (w/v) ethylene glycol [214]. Moreover, commercial screens (Table B.6) were used to identify additional crystallisation conditions. Plates were set up with a Tecan Freedom EVO™ crystallisation robot with a drop size of 600 nL and a drop ratio of 1:1, and incubated at 4 °C and 20 °C until crystal growth. The final data sets were obtained from crystals grown in initial screens at RT in 4 M sodium formate in case of BRD3(2)/H4K20ApmTri and in 0.2 M sodium acetate trihydrate, 0.1 M Tris hydrochloride pH 8.5, 30% PEG 4,000 for both BRD4(1) data sets.

Crystal harvesting and cryo-protection

Crystals of BRD3(2) with H4K20ApmTri and BRD4(1) with H4K5AcK8ApmTri or H4K5/K8ApmTri were either directly mounted in 0.05-0.5 mm loops or cryo-protected before mounting them. For cryo-protection, crystals were transferred into drops containing 30% glycerol or 2-methyl-2,4-pentanediol (MPD) and 20 mg/mL of the corresponding peptide in mother liquor before being mounted in cryo loops. All crystals were frozen in liquid nitrogen for storage, transport to the Swiss Light Source (SLS) and data collection.

B.3.2.3 Structure determination

Data collection

Data collection of all data sets and test shots in this project was performed at the SLS (Paul Scherer Institute, Villigen, Switzerland). Test shots of BRD4(1) with the H4K5AcK8ApmTri or H4K5/K8ApmTri peptide were collected at beam line X06DA at a wavelength of 1 Å, 100% beam transmission, an exposure time of 0.5 s and a 90° rotation between single images. Diffraction spots were recorded with a PILATUS 2M-F detector. For the BRD4(1) data sets with the H4K5AcK8ApmTri or H4K5/K8ApmTri peptide data was similarly collected at beam line X06DA with an exposure time of

0.1 s and an increment of 0.1° between images. To obtain a complete data set, images were collected over 240° at a detector distance of 0.165 m for BRD4(1) with H4K5AcK8ApmTri and 0.135 m for BRD4(1) with H4K5/K8ApmTri, respectively. The BRD3(2) data set with the H4K20ApmTri peptide obtained by C. Koç was collected at beam line X06DA at a wavelength of 1 Å, a beam transmission of 85%, a detector distance of 0.185 m, 0.5 s exposure time per image and 0.1° increments between single images, covering a total rotation of 244.3°. Test shots and data sets of BRD3(2) crystals with H4K20ApmTri obtained as a result of an additional initial screening were collected at beam line X06SA with a beam transmission of 10% and an EIGER 16M-X detector. Test shots were collected at a wavelength of 1 Å, 0.2 s exposure time and 90° increments between images. For the final data set, images of 360° were collected at a wavelength of 1 Å, an exposure time of 0.1 s, 0.1° rotation between single images and a detector distance of 0.205 m.

Data processing

All obtained data sets of BRD3(2) with H4K20ApmTri and BRD4(1) with H4K5AcK8ApmTri or H4K5/K8ApmTri were processed with the X-ray Detector Software (XDS) program package [322] and the XDS Graphical user interface (XDSGUI) [323]. First, the spatial distortion for each detector pixel is calculated to account for tilting of the individual detector plates. Then, the background at each pixel of the image is estimated based on the background noise of the detector in absence of X-rays. Strong diffraction spots and their coordinates are identified in a subset of the data images. These diffraction spots are used to determine the orientation, dimensions and symmetry of the crystal lattice and for indexing. All possible lattice types are tested and the likelihood for each possible lattice symmetrie is determined. Regions outside the user-defined resolution range and shaded areas of the dectector according to the initial background are removed. Each pixel of the dectector is assigned to the closest predicted reflection in reciprocal space. Based on strong reflextions, a three-dimensonal profile for each reflection is estimated and used to integrate the intensities at each reflection location. Finally, correction factors are applied to the determined intensities and standard deviations to account for radiation damage and absorption effects. The unit cell constants are refined and possible space groups are assigned. Finally, reflections are merged according to the determined symmetry of the space group and the resolution-dependent quality and completeness of the data set is evaluated.

During data processing, images were analysed for radiation damage with XDSSTAT [324] and corresponding frames were excluded. Areas on the images affected by severe ice rings were also excluded. Space groups with a high probability were tested with special emphasis on the assignment of screw axis based on systematic absents of certain reflections. The quality of the data set was evaluated based on the completeness of the data, an overall low R_{meas} (multiplicity independent quality indicating R-factor), a high signal-to-noise ratio ($I/\sigma(I)$) and the correlation of two random half data sets as given by $CC_{1/2}$. The resolution was cut at $I/\sigma(I) > 1.01$ and $CC_{1/2} > 50\%$, however, the aforementioned

parameters were also taken into account. Especially during the processing of the BRD3(2)/H4K20ApmTri data set collected by C. Koç, the resolution limit was re-evaluated as the initially chosen cut-off did not account for the low completeness of the data. Inclusion of the ice ring areas significantly improved the overall completeness and allowed the data set to be cut at 1.92 Å. Finally, XDSCONV was used to convert the finalised reflection data file into the subsequently needed mtz file format and to select a randomised subset of >1000 reflections (R-free flag set) for structure validation during the refinement process. The quality of the structure factor data was thereafter analysed with the help of phenix.xtriage [320], [325] which can detect the presence of ice rings, twinning, and pseudosymmetry the crystal might have had.

Molecular replacement

During data processing the structure factor amplitude of a given reflection condition is obtained from the intensity and the position on the detector. However, the phase angle of each reflection can not be obtained from the measured intensities and for this reason initial phases were estimated from a structurally similar model by molecular replacement. The electron density map is calculated based on the obtained structure factor amplitudes and the corresponding phases by Fourier transformation.

First, the Matthews coefficient was determined with MATTHEWS_COEF [311], [312], a program of the CCP4 Suite [309]. The Matthews coefficient and solvent content are calculated based on the determined unit cell volume and the molecular weight of the molecule, thereby allowing an estimation of the number of molecules in the asymmetric unit (ASU) of the crystal. The correct number of molecules in the ASU was determined by testing the suggestions from the Matthews coefficient with the highest probability. To obtain the required phases, molecular replacement was performed with PHASER MR [316]. The inital phases were taken from the model of the unliganded structures of BRD3(2) (PDB-ID: 2OO1) and BRD4(1) (PDB-ID: 2OSS) [214] from which all water molecules were removed. The determined solvent content and the corresponding number of molecules in the ASU was used together with the prepared unliganded structure and the calculated molecular weight of the protein for automated molecular replacement with PHASER MR [316]. In molecular replacement, the used structure model is first rotated and then translated in the ASU until the diffraction data calculated from the model matches best with the experimentally determined data. The quality of the found solution is reflected in the resulting rotation function scores (RFZ) and translation function scores (TFZ) and the latter should be >8 for a correctly placed model. The phases of the best solution are then used to calculate the initial electron density map.

Refinement

To improve the initially obtained phases from PHASER MR [316] and to obtain a model that closely agrees with the experimental data, several consecutive rounds of model building and refinement were performed. Initially, the model bias was reduced through a simulated annealing and rigid body refinement in phenix.refine [317], [319]. At this stage, all data sets were assessed regarding the displayed electron density of the ligand in all protomers, the resolution limit and the overall quality of the data set as determined at the end of data processing. Data sets displaying no ligand density were rejected and the most promising data sets for BRD3(2) with H4K20ApmTri and BRD4(1) with H4K5AcK8ApmTri or H4K5/K8ApmTri were further refined. Moreover, data sets showing problems, including lack of completeness, twinning or outliers were also excluded from further refinement. Hereafter, the protein chain of the initial model was adjusted to the electron density map using COOT [310]. In the following, the improved model was used to calculate an improved electron density map that in turn was matched to the experimental data in a subsequent refinement with phenix.refine [317], [319]. The protein model was further refined in consecutive rounds of model building and refinement with phenix.refine including real-space refinement, reciprocal-space refinement, individual or group B-factor refinement and TLS refinement. The improvement in the built model was monitored by the difference between the experimentally and model obtained structure factors as indicated by the R-factors, R-work and R-free. Once no significant improvement in the model could be obtained for two subsequent refinements, the ligand peptide chain was built into the model with COOT [310] with the help of the corresponding crystallographic information files (CIF) of the artificial amino acids KAc and ApmTri, which were prepared with phenix.eLBOW [318]. Thereafter, the model of the protein with the peptide was further refined using COOT and phenix.refine and water and solvent molecules were added during the process. The improvement in each refinement round was evaluated by the R-factors, the RMSD of the bond lengths and angles and the Ramachandran plot (Molprobity [313]–[315]). The R-free and R-work value are calculated from the R-free flag set (usually >1500 reflections) and the remaining reflections, respectively. The R-free flag set is not used for the calculation of the electron density map and represents a modeling-independent value [326]. The R-factors should be, dependent on the resolution cut-off, below 30% for a well-refined model. To avoid over-fitting, the difference between the R-work and the R-free should not increase beyond 5%. Finally, POLYGON [321] was used to compare the model quality indicators of our structures to similar structures in the PDB.

B.4 RESULTS

This section highlights the results of the structural analysis of bromodomains bound to ApmTri containing peptides. The determined structures are part of the following manuscript:

Kirchgäßner S., Braun M. B., Bartlick N., Koç C., Reinkemeier C., Lemke A., Stehle T., Schwarzer D., *Synthesis, biochemical characterization and genetic encoding of a 1,2,4-triazole amino acid as acetyl-lysine mimic for bromodomains of the BET-family*, Manuscript submitted, Angew. Chem., 2022

Sören Kirchgäßner (SKi), Michael B. Braun (MB), Cengiz Koç (CK) and N. Bartlick (NB) have contributed to the work below. Corresponding affiliations are listed in the appendix section.

SKi designed the study and synthesised ApmTri and ApmTri containing peptides [298]. Recombinant BRD3(2) and BRD4(1) were expressed and initially purified via nickel IMAC by SKi. CK and NB purified BRD3(2) and NB purified BRD4(1) by preparative SEC. CK crystallised BRD3(2) with H4K20ApmTri and collected a data set. MB and NB crystallised BRD3(2) with H4K20ApmTri and BRD4(1) with H4K5/K8ApmTri or H4K5AcK8ApmTri. Crystals were mounted by MB and NB, and MB collected high resolution data sets at the Swiss Light Source. NB selected suitable data sets, performed data processing and refinement of all data sets and MB continued refinement and finalised the structures for submission to the PDB.

B.4.1 Purification of BRD3(2) and BRD4(1)

The purification of BRD3(2) and BRD4(1) is well established (Extended data, Fig. B.10, A) [268] and structures in the PDB comprise unliganded structures [214], native ligand-bound structures [214], [327]–[329] and inhibitor-bound structures [268], [283] of both bromodomains. For the purpose of structure determination, S. Kirchgäßner established the purification of His_6-tagged BRD3(2) and BRD4(1) *E. coli* expression constructs (Table B.4) by nickel IMAC where the affinity tag was cleaved afterwards by thrombin digestion overnight. We further increased the purity of the protein and exchanged the buffer to BRD SEC buffer by preparative SEC. BRD4(1) eluted as single sharp peak from the HiLoad Superdex™ 75 16/600 column (Extended data, Fig. B.10, C) and was subsequently concentrated to 11.8 mg/mL for crystallisation. The protein partly formed white aggregates during the concentration prior to the preparative SEC. After the SEC, even at the high concentrations needed for crystallisation, the protein showed no signs of aggregation, indicating the successful removal of impurities. In contrast to BRD4(1) which was purified without interruption, BRD3(2) was frozen after purification at -20 °C for a longer time period. To ensure the integrity of the protein, BRD3(2) was purified again after thawing by preparative SEC with a HiLoad Superdex™ 200 16/600 column. Although the usage of a HiLoad Superdex™ 75 16/600 column would have been more suitable for the small size of the protein (13.5 kDa), the eluting peak was sharp with no significant amount of impurities

prior to the main protein peak (Extended data, Fig. B.10, B). The protein was subsequently concentrated to 13.5 mg/mL for crystallisation experiments.

B.4.2 Crystallisation of BRD3(2) and BRD4(1) with acetyl lysine mimicking peptides

To determine how the artificial amino acid ApmTri interacts with the acetyl lysine binding pocket of the bromodomains and to enable a comparison to structures with the native acetyl lysine peptides, we aimed to obtain structures of the bromodomains with the acetyl lysine mimetic containing peptides. Lyophilised ApmTri and KAc comprising peptides H4K20ApmTri, H4K5AcK8ApmTri and H4K5/K8ApmTri (Fig. B.6, A) were provided by S. Kirchgäßner.

The data collected in 2018 by C. Koç had issues due to over exposure and ice rings, therefore, we attempted to reproduce BRD3(2) crystals with H4K20ApmTri. In addition to commercial screens, we screened the crystallisation condition of the unliganded BRD3(2) structure [214] that was likely used by C. Koç. Although we used BRD3(2) at 10 times the concentration C. Koç used, we were unable to reproduce the BRD3(2)/H4K20ApmTri crystals in the unliganded crystallisation condition as more than 90% of the conditions remained clear. However, our initial screens gave rise to a variety of different crystal forms (Extended data, Fig. B.11, A) in several conditions (Extended data, Table B.11).

For crystallisation, BRD4(1) was mixed with H4K5AcK8ApmTri in a 1:2 ratio. The BRD4(1)/H4K5AcK8ApmTri complex crystallised in many different conditions (Extended data, Table B.12) giving rise to crystal shapes ranging from small needle clusters to more three-dimensional crystals that appeared to be consisting of stacked layers (Extended data, Fig. B.11, B). To our surprise, the smallest crystals (Extended data, Fig. B.11, B.a) gave rise to a 1.92 Å data set that displayed nice electron density for the ligand. In contrast, BRD4(1) with H4K5/K8ApmTri mixed in a 1:2 ratio only crystallised in the apo form without the peptide bound. Only when we mixed BRD4(1) with the peptide in a 1:20 ratio, we were able to determine data sets with electron density for the ligand, which reflects the 4-fold smaller affinity of H4K5/K8ApmTri as compared to H4K5AcK8ApmTri for BRD4(1) (Fig. B.6, C).

B.4.3 Structural analysis of BRD3(2) with the histone peptide H4K20ApmTri

The 1.9 Å data set (Table B.9, mint green) of BRD3(2) with H4K20ApmTri was collected at beam line X06DA. During data processing, areas showing ice rings from hexagonal ice were included as significant spots could be seen in these areas and removing the ice ring areas would have reduced the overall completeness by approximately 10%. The crystal diffracted to 1.92 Å and was processed in space group $P6_122$ with an $I/\sigma(I)$ of 1.74 and a $CC_{1/2}$ of 77.6% in the highest resolution shell.

Table B.9: Data processing and refinement statistics of BRD3(2) with the ApmTri containing peptide. The 1.9 Å data set (mint green) was collected by C. Koç and the 2.8 Å data set (white) was collected by M. Braun and N. Bartlick.

			BRD3(2) + H4K20ApmTri	**BRD3(2) + H4K20ApmTri**
Wavelength [Å]			0.999884	0.999998
Resolution [Å]			50-1.92 (1.97-1.92)	50-2.76 (2.93-2.76)
Space group			$P6_122$	$P2_12_12_1$
		a, b, c [Å]	79.61, 95.30	89.64, 96.10, 112.33
		α, β, γ (°)	90, 90, 120	90, 90, 90
Measured reflections			352328 (23570)	146829 (24133)
Unique reflections			14001 (1012)	25478 (4026)
Redundancy			25.2 (23.3)	5.8 (6.0)
Completeness [%]			98.9 (97.7)	99.8 (99.2)
I / σ(I)			31.84 (1.74)	12.43 (1.18)
$CC_{1/2}$			100.0 (77.6)	99.8 (55.4)
R_{meas} [%]			7.4 (385.6)	11.6 (156.7)
Wilson B [$Å^2$]			49.2	74.8
No. of Atoms	Protein	A*/B/C/D/E/F	884*	885 / 873 / 868 / 867 / 849 / 855
	Peptide	B*, G/H/I/J/K/L	76*	79 / 76 / 83 / 73 / 52 / 63
	Waters	S	76	7
Average B-Factors [$Å^2$]	Protein	A*/B/C/D/E/F	47.5*	77.7 / 84.4 / 84.3 / 80.9 / 93.9. / 100.3
	Peptide	B*, G/H/I/J/K/L	51.1*	106.5 / 112.5 / 103.5 / 117.1 / 114.3 / 119.7
	Waters	S	53.6	74.2
R_{work} / R_{free} [%]			21.36 / 24.96	20.85 / 25.51
R.m.s.d bond angles [°]			0.632	0.464
R.m.s.d bond length [Å]			0.005	0.002
Ramachandran	favored (%)		100.00	97.76
	outliers (%)		0.00	0.00

To confirm the binding mode of H4K20ApmTri, additional data sets were collected from crystals grown in 4 M sodium formate. The best data set from this condition (Table B.9, white) was processed with a resolution cut-off of 2.8 Å in space group $P2_12_12_1$ with an I/σ(I) of 1.18 and a $CC_{1/2}$ of 55.4% in the highest resolution shell.

After data processing, the quality of the obtained data sets was analysed with Phenix.xtriage. Images of the crystal of the 1.9 Å data set, taken during adjustment of the X-ray beam position, showed the formation of many ice crystals next to the protein crystal in the loop. As a result, the 1.9 Å data set displayed ice rings. In contrast, the 2.8 Å data set did not show ice rings or issues within the crystal such as twinning or pseudosymmetry. The Matthew coefficient was calculated with MATTHEW_COEF of

the CCP4 Suite to obtain the solvent content and the number of protomers in the ASU. The crystal used for the 1.9 Å data set has a solvent content of approximately 63% when calculated with 1 protomer per ASU in the hexagonal crystal. The solvent content of the crystal used for the 2.8 Å data set was calculated with 59% for 6 protomers per ASU in the orthorhombic crystal. The phase problem was solved by molecular replacement with the water-deprived BRD3(2) unliganded structure (PDB-ID: 2OO1) by PHASER MR.

For the H4K20ApmTri a CIF was created with Phenix.eLBOW that was modified, so that both COOT and Phenix.refine recognised H4K20ApmTri as an amino acid that can be incorporated into a regular peptide chain. The 1.9 Å and 2.8 Å structures were refined to R-work and R-free values of 21.4%/25.0% and 20.9/25.5%, respectively. The Wilson B factor of the 2.8 Å data set was 74.8 $Å^2$ indicating a low degree of order within the crystal. As a result, the refinement statistics of the 2.8 Å data set show high average B-factors for two of the 6 protein chains in the ASU, chain E and chain F. In addition, the average B-factors were high for all 6 peptides (chains G-L). Since the H4K20ApmTri peptide electron density is only well refined in areas where it is tightly bound to BRD3(2) such as the KAc binding pocket, high B-factors are expected. In addition, the crystal packing and the calculated amount of protomers suggest a possible tighter packing with 1-2 additional protomers and a potentially present additional symmetry axis that could not be used due to small deviations. During refinement of the BRD3(2)/H4K20ApmTri data sets, the overall restraint weight was selected to minimise the R-free value and keep a reasonable gap between R-work and R-free of <5%. Loosening of the geometric restraints led to an increase of the R-free and an increase of the gap between R-free and R-work, thus indicating over-fitting of the model. The 2.8 Å data set has a different crystal packing from the 1.9 Å data set and serves as supportive structure confirming ligand binding. The resolution limits the discussion about ligand positioning in this data set, for this reason, the following structural characterisation of BRD3(2)/H4K20ApmTri is based on the 1.9 Å structure.

The N-terminal His-tag of the BRD3(2) construct was enzymatically cleaved with thrombin. Therefore, the N-terminus of the cleaved construct contains 4 extra amino acids (Gly-Ser-His-Met) before BRD3(2) starts with amino acid Gly306 of BRD3. In the electron density, the first residue to be clearly seen is amino acid Lys307, however, the side chain is only partially visible due to its flexibility. All other residues towards the C-terminal Pro415 can be seen in the electron density. The core fold of BRD3(2) consists of a four helix bundle comprising the helices αZ, αA, αB and αC (Fig. B.7, A) [214]. The four helices are packed in an antiparallel left-handed fashion and display the for BETs typical KAc binding cavity. [214], [236], [239]. The helices αZ and αA are connected via an extensive ZA loop, which majorly contributes to the acetyl lysine binding pocket and to the ligand presented surface area that is responsible for the binding specificity. Helices αB and αC are connected by a short 3 amino acid BC loop, that similarly contributes to the KAc binding site. The conserved Asn391 is located at the transition of helix αB to the BC loop. This residue residue interacts directly with the acetyl lysine (Fig. B.7, B) [215]. The conserved Tyr348 [215] is part of a small helix formed by the extended ZA loop and points

towards the KAc binding pocket. The all-atom RMSD between our BRD3(2)/H4K20ApmTri structure and the unliganded BRD3(2) structure (PDB-ID: 2OO1) is 1.89 Å with the highest deviations in the ligand binding ZA loop. Both conserved residues, Asn391 and Tyr348, are positioned similarly in the BRD3(2)/H4K20ApmTri structure as in the unliganded structure.

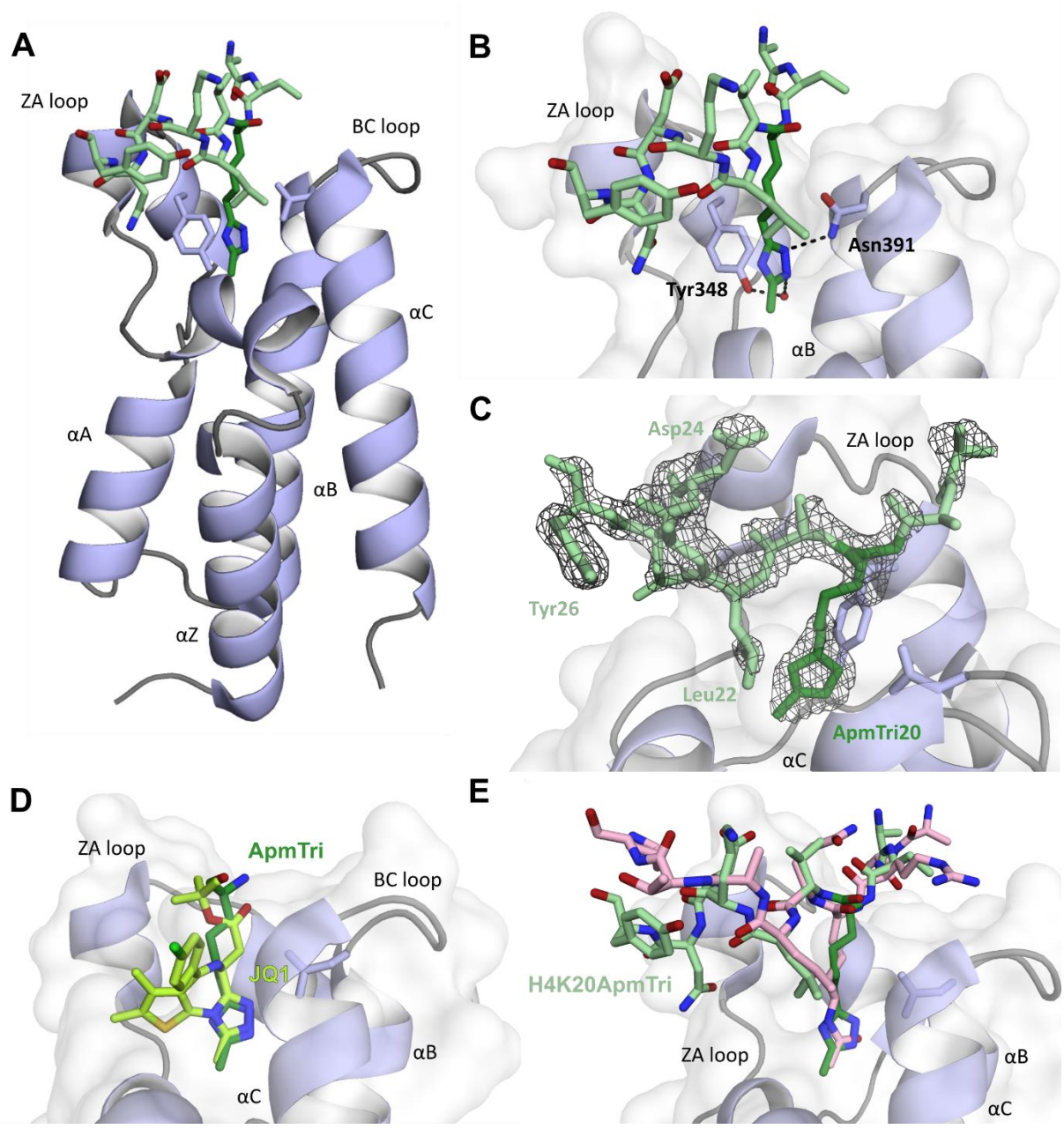

Figure B.7: 1.9 Å structure of BRD3(2) with the acetyl lysine mimetic H4K20ApmTri. (**A**) Overall structure of BRD3(2) (light blue) interacting with H4K20ApmTri (mint green). The acetyl lysine binding pocket of BRD3(2) sits on top of the four helix bundle and is mainly surrounded by the BC and ZA loops. The ApmTri in the H4K20ApmTri peptide is highlighted in green and the amino acid side chains that interact with the acetyl lysine mimetic are shown as sticks. (**B**) A close-up look on the acetyl lysine binding pocket shows the interaction of H4K20ApmTri (green) with the conserved Asn391 and an additional water mediated interaction with Thr348 (black dashed lines). (**C**) The Fo-Fc simulated annealing omit map (grey mesh) of H4K20ApmTri bound to BRD3(2) shows the placement of the model in the electron density at σ =3.0. (**D**) Structural comparison of the positioning of the ApmTri (green) and the JQ1 inhibitor (lime green, PDB-ID: 3S92) in the acetyl lysine binding pocket. The conserved Asn391 is shown as sticks. (**E**) The structural alignment of BRD3(2) bound to H4K20ApmTri (mint green) or the native ligand H3K18Ac (rose, PDB-ID: 5HJC) shows that H4K20ApmTri binds in a similar fashion in the acetyl lysine binding pocket.

The electron density of the acetyl lysine mimetic carrying peptide H4K20ApmTri is well resolved in some areas, while many side chains are only partially visible. The electron density of the ApmTri in the KAc binding pocket covers the entire residue and gives a clear indication for the positioning of the methyl group on the triazole ring system. The Leu22 residue of the peptide is located on top of the KAc binding pocket but the lack of electron density makes precise positioning difficult. Overall, the peptide backbone and sidechains are better defined towards the C-terminus, with amino acids Val21 to Tyr26 visible. Additional electron density can be seen at the N-terminus of H4K20ApmTri, however, the density is not connected and the positioning of the backbone is difficult.

In the structure of BRD3(2) bound to H4K20ApmTri, the 3-methyl-1,2,4-triazole of ApmTri is positioned deep in the KAc binding pocket and engages with the conserved Asn391 residue (Fig. B.7, B). In addition, the nitrogen atom N2 of the triazole ring contacts the conserved Tyr348 residue indirectly via a water molecule. A comparison of the binding mode of H4K20ApmTri to that of H3K18Ac, an acetyl lysine-containing histone 3-derived peptide, reveals that ApmTri and KAc bind similarly in the binding pocket of BRD3(2) (Fig. B.7, E) [327]. The hydrogen bond between the nitrogen atoms N1 and N2 and Asn391 is reminiscent of the interaction between KAc and Asn391. The triazole moiety of ApmTri is positioned in the KAc binding pocket similarly to the triazole ring of the JQ1 inhibitor bound to BRD3(2) (PDB-ID: 3S92) (Fig B.7, D) [268].

B.4.4 Structure of BRD4(1) with H4K5/K8ApmTri or H4K5AcK8ApmTri

Data sets of BRD4(1) with the ApmTri containing peptides were collected at beam line X06DA. For each complex, BRD4(1) bound to H4K5/K8ApmTri or H4K5AcK8ApmTri, several data sets were collected (Extended data, Table B.14). The best data set was chosen after initial data processing, molecular replacement and one round of simulated annealing refinement, based on ligand visibility in omit density maps in all protomers, resolution limit and overall data quality.

In the following, the described data processing and refinement focusses on the chosen data sets for BRD4(1) with one of the two peptides (Table B.10). Both data sets were derived from crystals grown in a similar condition comprising 200 mM sodium acetate trihydrate, 100 mM Tris hydrochloride pH 8.5 and 30% (w/v) polyethylene glycol 4,000.

Due to radiation damage few images had to be excluded during data processing. For the BRD4(1)/H4K5/K8ApmTri data set images of 1-203.7° and for BRD4(1)/H4K5AcK8ApmTri images of 1-210.7° were used. The BRD4(1)/H4K5/K8ApmTri crystal diffracted to 1.58 Å and the crystal of BRD4(1)/H4K5AcK8ApmTri to 1.92 Å and the data sets were processed in space group $P2_12_12_1$. The BRD4(1)/H4K5/K8ApmTri data set was processed with an I/σ(I) of 1.21 and a $CC_{1/2}$ of 52% in the highest resolution shell. The data set has a high completeness of 99.7% in the highest resolution shell. The R-free flag set was set to 9% to assign more than 1500 reflexes although the overall number of

measured reflections was low. The I/σ(I), $CC_{1/2}$ and completeness of the BRD4(1)/H4K5AcK8ApmTri data set were 1.68, 62% and 98.2% in the highest resolution shell after data processing, respectively, and the R-free flag set was assigned to 5%. Both data sets were analysed with Phenix.Xtriage after data processing and no significant issues were detected.

Table B.10: Data processing and refinement statistics of BRD4(1) with the acetyl lysine mimicking peptides H4K5/K8ApmTri or H4K5AcK8ApmTri.

			BRD4(1) + H4K5/K8ApmTri	**BRD4(1) + H4K5AcK8ApmTri**
Wavelength [Å]			0.999867	1.000029
Resolution [Å]			50-1.58 (1.67-1.58)	50-1.92 (2.04-1.92)
Space group			$P2_12_12_1$	$P2_12_12_1$
Unit cell dimension		a, b, c [Å]	42.53, 46.75, 58.90	39.51, 51.78, 170.74
		α, β, γ (°)	90, 90, 90	90, 90, 90
Measured reflections			122351 (19781)	209877 (33629)
Unique reflections			16702 (2628)	27441 (4283)
Redundancy			7.3 (7.5)	7.6 (7.9)
Completeness [%]			99.8 (99.7)	99.1 (98.2)
I / σ(I)			11.47 (1.21)	10.85 (1.68)
$CC_{1/2}$			99.9 (52.1)	99.7 (62.0)
R_{meas} [%]			14.8 (194.5)	17.2 (128.7)
Wilson B [Å²]			25.2	30.2
No. of Atoms	Protein	A*/B/C	1021*	1014 / 1025 / 1038
	Peptide	B*, D/E	76*	51 / 74
	Waters	S	78	249
	Others	F		7
Average B-Factors [Å²]	Protein	A*/B/C	19.3*	28.8/ 31.4 / 24.6
	Peptide	B*, D/E	27.9*	43.1 / 35.3
	Waters	S	29.9	31.4
	Others	F		58.5
R_{work} / R_{free} [%]			18.42 / 20.77	19.69 / 24.64
R.m.s.d bond angles [°]			0.898	0.572
R.m.s.d bond length [Å]			0.007	0.003
Ramachandran	favored (%)		99.21	98.94
	outliers (%)		0.00	0.00

The solvent content and the number of protomers in the ASU were calculated with MATTHEW_COEF for both crystals, yielding a solvent content of 36% with 1 protomer for BRD4(1)/H4K5/K8ApmTri and a solvent content of 47% with 3 protomers for BRD4(1)/K5AcK8ApmTri. To solve the phase problem, the water molecules were removed from the unliganded structure of BRD4(1) (PDB-ID: 2OSS) and the remaining coordinates were used for molecular replacement with PHASER MR. The initial refinement with phenix.refine included 10 rounds of simulated annealing to remove model bias. The BRD4(1)/H4K5/K8ApmTri data set was refined to R-work and R-free values of 18.4% and 20.8%. The refinement statistics (Table B.10, light purple) display a low average B-factor for the protein chain of 19.3 Å² and of 27.9 Å² for the peptide chain. The individual B-factors of the water molecules were analysed, to ensure only water molecules with high occupancy were placed in the model [330]. BRD4(1)/K5AcK8ApmTri was refined to R-work and R-free values of 19.7% and 24.6%. The average

B-factors of the BRD4(1)/K5AcK8ApmTri data set are comparably higher which is expected due to the lower resolution but may also indicate a larger number of residues with less occupancy. The peptide (chain D and E) was only built in two of the three proteins chains (B and C) with chain D displaying the highest B-factors indicating an overall lower occupancy of the peptide. Similar to the BRD3(2)/H4K20ApmTri data sets, the geometric restraints for the BRD4(1)/H4K5AcK8ApmTri data set were very tight after several rounds of refinement with phenix.refine. The refinement X-ray weight wxc_{scale} was adjusted to ensure the focus of the refinement was on the experimental data rather than the stereochemical restraints. However, loosening of the restraints significantly increased the R-free and the gap between the R-free and R-work value.

The construct of BRD4(1) comprises AA 44 to 168 of the BRD4 sequence with a N-terminal thrombin-cleavable His-tag. Both structures of BRD4(1) with the acetyl lysine mimicking peptides show electron density for the short linker (Gly-Ser-His-Met) that remained after thrombin cleavage. Towards the C-terminus, residues can be seen to AA 166 for both structures. The RMSD between the unliganded BRD4(1) structure (PDB-ID: 2OSS) and the ApmTri containing peptides amounts to 0.86 Å for the BRD4(1)/H4K5/K8ApmTri data set and 1.16 Å for the BRD4(1)/K5AcK8ApmTri data set. BRD4(1) in our structures closely resembles the unliganded structure with highest deviations N-terminally of the αZ helix, the BC loop and the C-terminus. Similar to BRD3(2), BRD4(1) forms an anti-parallel left-handed four helix-bundle and the deep and broad KAc binding cavity highlights the affiliation of both BDs to the BET family. In contrast to BRD3(2), the ZA loop in BRD4(1) displays less helical content. The conserved KAc interacting residues Asn140 and Tyr97 are located in the BC loop and ZA loop, respectively.

BRD4(1) interacts with diacetylated H4 peptides carrying acetyl lysine in the K5 and K8 position [214] (Fig. B.8, B). The electron density in our structures is well defined for the K5 position in the acetyl lysine mimicking peptides (Fig. B.8, E-F). Even the methyl group on the triazole ring of ApmTri in the H4K5/K8ApmTri peptide is visible. Generally, the electron density for the KAc or ApmTri comprising peptides is well defined close to the KAc binding site and less defined towards the termini, especially towards the N-terminus where most side chains can not be placed with high certainty in the model. The ApmTri acetyl lysine mimetic in the K8 position is less defined, thus the orientation of the triazole moiety is unclear and the linker to the peptide backbone is too flexible to be fully visible in the electron density.

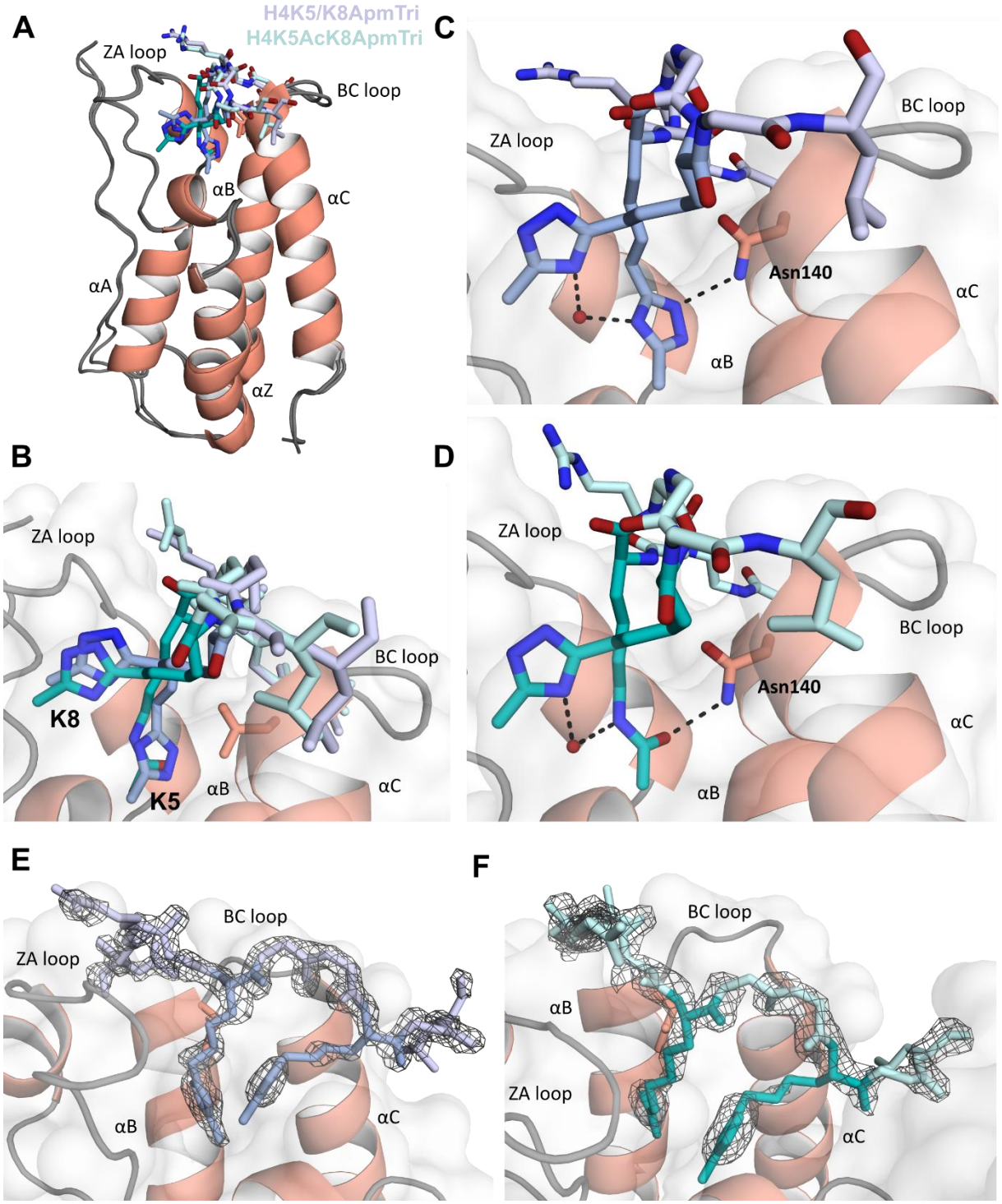

Figure B.8: Structures of BRD4(1) with the acetyl lysine mimics H4K5/K8ApmTri and H4K5AcK8ApmTri. (**A**) Structural alignment of BRD4(1) (light red) bound to the two acetyl lysine mimicking peptides H4K5/K8ApmTri (light purple) or H4K5AcK8ApmTri (cyan). Structural features comprising the four helix bundle and the binding pocket forming ZA and BC loops of BRD4(1) are indicated. (**B**) A comparison of acetyl lysine mimetics in a close-up view reveal the overall similar binding in the K5 and K8 position. The artificial amino acids ApmTri and KAc are highlighted in dark cyan and purple, respectively. (**C**-**D**) Close-up view on the acetyl lysine binding pocket of BRD4(1) shows the interaction (black dashed lines) between the conserved Asn140 of the protein and the artificial amino acids. The ApmTri or KAc in the K5 position is stabilised in the binding pocket via a water mediated interaction with the ApmTri in the K8 position. (**E**-**F**) Fo-Fc omit map (grey mesh) of (**E**) H4K5/K8ApmTri (purple) or (**F**) H4K5AcK8ApmTri (cyan) contured at σ = 3.0. The electron density in protomer C is displayed for H4K5AcK8ApmTri. (**A**, **B**, **D** and **F**) Chain C of the BRD4(1)/K5AcK8ApmTri data set was used for figures and discussion as it displays the most refined ligand density.

The KAc residue in the K5 position of H4 peptides engages with the conserved asparagine in the KAc binding pocket. The KAc in the K8 position does not insert into the binding pocket. The residue is instead positioned on the surface at the entrance of the binding pocket in a diagonal fashion. The structures of BRD4(1) with the ApmTri-containing peptides H4K5/K8ApmTri and H4K5AcK8ApmTri reveal the binding of ApmTri in this context at atomic detail. ApmTri in position K5 bound to BRD4(1) interacts with the conserved Asn140 but the position of the triazole ring is slightly tilted with respect to KAc in this position. A superposition of our BRD4(1)/H4K5/K8ApmTri structure with structures of JQ1 (PDB-ID: 3MXF) or H4K5/K8Ac (PDB-ID: 3UVW) bound to BRD4(1) highlights the rotation of the triazole ring (Fig. B.9, A, C). ApmTri in position K8 reaches diagonally across the surface of the KAc binding pocket. A bridging water molecule forms a connection between the triazole ring of ApmTri in the K8 position and the amide nitrogen of KAc or the nitrogen atom N4 of ApmTri in the K5 position. The connection is reminiscent of a water-mediated interaction between the K5Ac amide and the K8Ac carbonyl oxygen in the structure of H4K5/K8Ac bound to BRD4(1) [214]. The KAc in positon K5 of the BRD4(1)/H4K5AcK8ApmTri structure forms a hydrogen bond with the amide group of Asn140 via its carbonyl oxygen and superimposes fully with KAc in the BRD4(1)/H4K5/K8Ac structure.

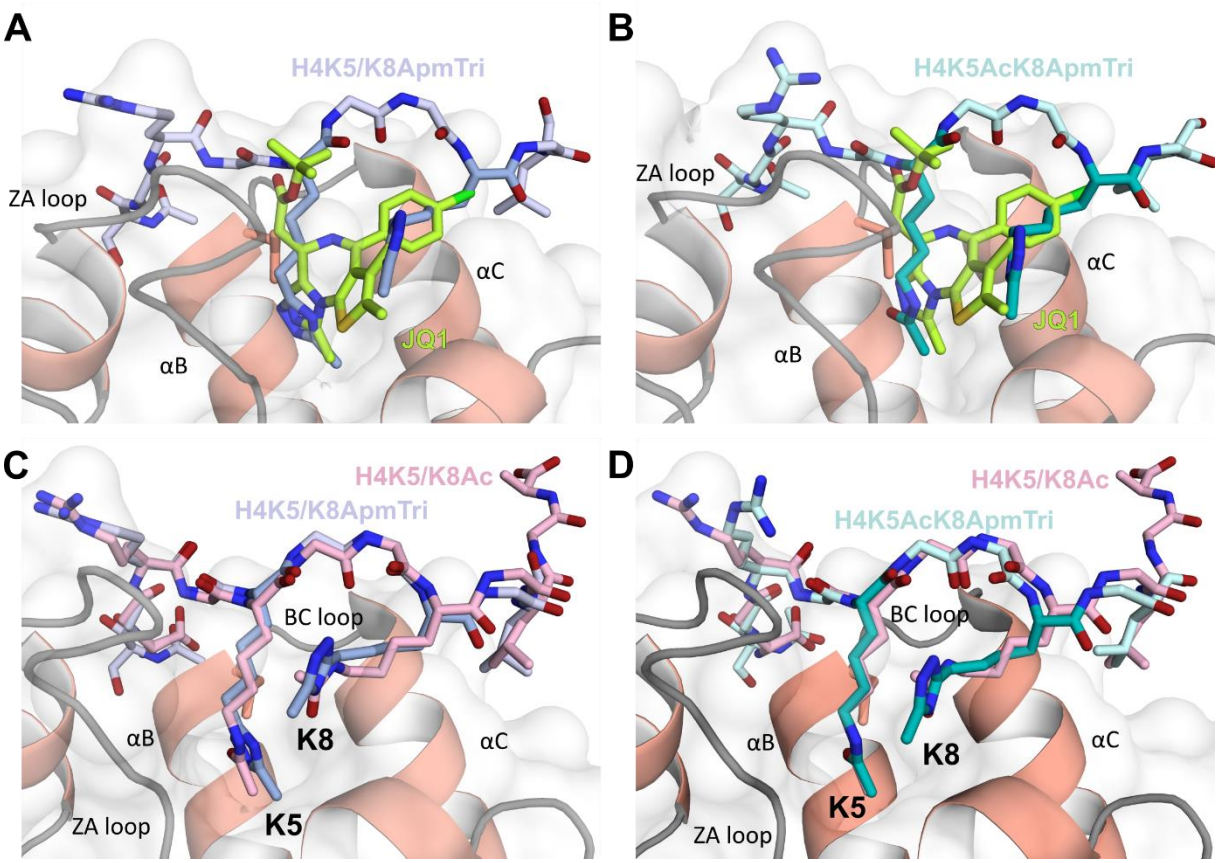

Figure B.9: Structural comparison of the positing of the acetyl lysine mimetics, the native peptide H4K5/K8ac and the JQ1 inhibitor in the acetyl lysine binding pocket of BRD4(1). (**A**-**B**) Structural alignment of BRD4(1) (light red) bound to the JQ1 inhibitor (lime green, PDB-ID: 3MXF) or (A) H4K5/K8ApmTri (purple) or (B) H4K5AcK8ApmTri (cyan). The triazole ring of artificial amino acid ApmTri is slightly tilted in the K5 position compared to the JQ1 inhibitor. (**C**-**D**) Overlay of the native tandem acetyl lysine ligand H4K5/K8Ac (rose, PDB-ID: 3UVW) with the ApmTri comprising peptides. (B, D) Chain C of the BRD4(1)/K5AcK8ApmTri structure was used to prepare the displayed images.

B.5 DISCUSSION AND OUTLOOK

ApmTri was designed as novel acetyl lysine mimetic to serve as probe for BDs of the BET family. Our structures of BRD3(2) and BRD4(1) with peptides containing ApmTri enabled the analysis of the binding mode of ApmTri at atomic level. We were able to confirm that important interactions between KAc and two conserved residues of the BDs are maintained. The ability of ApmTri to substitute for KAc is further supported by the superposition of both residues in the BRD3(2)/H4K20ApmTri structure. Furthermore, the observed resemblance of the binding mode explained the similar affinities between BRD3(2) and peptides containing either KAc or ApmTri.

We could show that tandem ApmTri peptides interact with BRD4(1) similarly to K5/K8Ac peptides with ApmTri replacing KAc in the K5 and K8 position, which is an important prerequisite for the usage of ApmTri as KAc mimetic. The electron density of ApmTri in the K8 position was less defined when compared to ApmTri in the K5 position in our structures. The comparison of ApmTri in the K8 position in both the BRD4(1)/H4K5/K8ApmTri and BRD4(1)/H4K5AcK8ApmTri structure revealed that the triazole moiety does not fully superimpose, indicating conformational flexibility in this position. Interestingly, the affinity of H4K5AcK8ApmTri to BRD4(1) is similar to H4K5/K8Ac, highlighting that ApmTri can replace KAc in the K8 position. In comparison, H4K5/K8ApmTri displays a 4-fold reduced binding affinity, likely due to the distorted positioning of ApmTri as compared to KAc. Taken together, our structures offer an explanation regarding the determined affinities and highlight differences between the K5 and K8 binding position of BDs.

The comparison of our structures to structures of BRD3(2) and BRD4(1) bound to the JQ1 inhibitor revealed that the triazole moiety of ApmTri and JQ1 superimpose fully. For this reason, ApmTri is likely a BET family BD specific KAc mimetic. Further experiments are needed to confirm the binding specificity of ApmTri. Studying BDs *in vivo* has proved to be challenging due to present deacetylases and the limited availability of suitable acetyl lysine subsitutes. In contrast to the traditional lysine and acetyl lysine substitutes, arginine and glutamine, ApmTri displays clear advantages as it does not only mimic the charge status of KAc but has a similar binding mode. The required chemical modification of phenylselenocystein to generate acetyl-lysine disqualifies the mimetic as probe for *in vivo* studies, making ApmTri the only suitable BD probe for this type of studies. For instance, ApmTri comprising peptides show potential for protein-protein interaction studies. C. Reinkemeier and E. Lemke successfully genetically encoded ApmTri in HEK cells with the amber codon suppression system [298]. HEK cells transfected with the respective pyrrolysyl-tRNA synthetase showed successful incorporation of ApmTri into a mCerulean3 labelled H4K20 peptide sequence and co-transfection with YFP-BRD3(2) will enabled future *in vivo* fluorescence resonance energy transfer (FRET) experiments on the protein interaction.

Overall, ApmTri proves to be a versatile acetyl lysine mimetic which offers new prospects for the research on BRDs.

B.6 EXTENDED DATA

B.6.1 Tables

Table B.11: Crystallisation conditions of BRD3(2) with H4K20ApmTri.

Protein	Peptide	Ratio	Temperature	Buffer	Salt	Precipitant 1	Crystal
BRD3(2)	H4K20ApmTri	1:3	20 °C	-	-	4.0 M Sodium formate	**Aa**
			20 °C	0.1 M MES/Sodium hydroxide pH 6.0	0.2 M Calcium acetate	20% (w/v) PEG 8.000	**Ab**
			20 °C	0.1 M Sodium cacodylate trihydrate pH 6.5	0.2 M Ammonium sulfate	30% (w/v) PEG 8.000	**Ac**
			20 °C	0.1 M Sodium cacodylate/ Hydrochloric acid pH 6.5	0.2 M Zinc acetate	10% (v/v) 2-propanol	**Ad**
			20 °C	0.1 M Sodium citrate tribasic dehydrate pH 5.6	0.2 M Potassium sodium tartrate tetrahydrate	2.0 M Ammonium sulfate	**Ae**
			20 °C	0.1 M Sodium citrate tribasic dehydrate pH 5.6	0.2 M Ammonium acetate	30% (w/v) PEG 4.000	**Af**
			20 °C	0.1 M BICINE pH 9.0	-	2.0 M Magnesium chloride hexahydrate	-
			20 °C	0.1 M Sodium citrate/ Citric acid pH 5.5	-	2.0 M Ammonium sulfate	-

Table B.12: Crystallisation conditions of BRD4(1) with H4K5/K8ApmTri.

Protein	Peptide	Ratio	Tempe-rature	Buffer	Salt	Precipitant 1	Cry-stal
BRD4(1)	H4K5/K8-ApmTri	1:20	20 °C	0.1 M TRIS hydrochloride pH 8.5	0.2 M Sodium acetate trihydrate	30% (w/v) PEG 4.000	**Ba**
			20 °C	0.1 M Tris hydrochloride pH 8.5	0.2 M Magnesium chloride hexahydrate	30% (w/v) PEG 4.000	**Bb**
			20 °C	0.1 M HEPES sodium pH 7.5	-	1.4 M Sodium citrate tribasic dihydrate	**Bc**
			20 °C	0.03 M Sodium fluoride, 0.03 M Sodium bromide, 0.03 M Sodium iodide	0.1 M Tris base, BICINE pH 8.5	12.5% (v/v) MPD, 12.5 % (v/v) PEG 1.000, 12.5 % (w/v) PEG 3.350	**Bd**
			20 °C	0.03 M Diethylene glycol, 0.03 M Triethylene glycol, 0.03 M Tetraethylene glycol, 0.03 M Pentaethylene glycol	0.1 M Tris base, BICINE pH 8.5	12.5% (v/v) MPD, 12.5 % (v/v) PEG 1.000, 12.5 % (w/v) PEG 3.350	**Be**
			20 °C	0.02 M 1,6-Hexanediol, 0.02 M 1-Butanol, 0.02 M 1,2-Propanediol, 0.02 M 2-Propanol, 0.02 M 1,4-Butanediol, 0.02 M 1,3-Propanediol	0.1 M Tris base, BICINE pH 8.5	20% (v/v) PEG MME 500, 10% (w/v) PEG 20.000	**Bf**
			20 °C	0.1 M Sodium citrate tribasic dehydrate pH 5.6	0.5 M Sodium chloride	2% (v/v) Ethylene imine polymer	-
			4 °C	0.1 M Tris hydrochloride pH 8.5	0.2 M Magnesium chloride hexahydrate	30% (w/v) PEG 4.000	-
			4 °C	0.1 M MES monohydrate pH 6.5	-	12% (w/v) PEG 20.000	-
			4 °C	0.02 M 1,6-Hexanediol, 0.02 M 1-Butanol, 0.02 M 1,2-Propanediol, 0.02 M 2-Propanol, 0.02 M 1,4-Butanediol, 0.02 M 1,3-Propanediol	0.1 M Tris base, BICINE pH 8.5	20% (v/v) Glycerol, 10% (w/v) PEG 4.000	-
			4 °C	0.02 M Sodium formate, 0.02 M Ammonium acetate, 0.02 M Sodium citrate tribasic dihydrate, 0.02 M Sodium potassium tartrate tetrahydrate, 0.02M Sodium oxamate	0.1 M Sodium HEPES, MOPS acid pH 7.5	12.5% (v/v) MPD, 12.5 % (v/v) PEG 1.000, 12.5 % (w/v) PEG 3.350	-

Table B.12, continued: Crystallisation conditions of BRD4(1) with H4K5/K8ApmTri.

Protein	Peptide	Ratio	Tempe-rature	Buffer	Salt	Precipitant 1	Crystal
BRD4(1)	H4K5/K8L-ApmTri	1:20	4 °C	0.02 M Sodium formate, 0.02 M Ammonium acetate, 0.02 M Sodium citrate tribasic dihydrate, 0.02 M Sodium potassium tartrate tetrahydrate, 0.02M Sodium oxamate	0.1 M Tris base, BICINE pH 8.5	20% (v/v) Ethylene glycol, 10 % (w/v) PEG 8.000	-
			4 °C	0.03 M Diethylene glycol, 0.03 M Triethylene glycol, 0.03 M Tetraethylene glycol, 0.03 M Pentaethylene glycol	0.1 M Tris base, BICINE pH 8.5	20% (v/v) Glycerol, 10% (w/v) PEG 4.000	-
			4 °C	0.03 M Diethylene glycol, 0.03 M Triethylene glycol, 0.03 M Tetraethylene glycol, 0.03 M Pentaethylene glycol	0.1 M Tris base, BICINE pH 8.5	20% (v/v) PEG MME 500, 10% (w/v) PEG 20.000	-
		1:2	20 °C	0.03 M Sodium fluoride, 0.03 M Sodium bromide, 0.03 M Sodium iodide	0.1 M Sodium HEPES, MOPS acid pH 7.5	12.5% (v/v) MPD, 12.5 % (v/v) PEG 1.000, 12.5 % (w/v) PEG 3.350	**Bg**
			20 °C	0.03 M Sodium nitrate, 0.03 M Sodium phosphate dibasic, 0.03 M Ammonium sulfate	0.1 M Tris base, BICINE pH 8.5	12.5% (v/v) MPD, 12.5 % (v/v) PEG 1.000, 12.5 % (w/v) PEG 3.350	**Bh**
			20 °C	0.02 M D-Glucose, 0.02 M D-Mannose, 0.02 M D-Galactose, 0.02 M L-Fucose, 0.02 M D-Xylose, 0.02 M N-Acetyl-D-Glucosamine	0.1 M Imidazole, MES monohydrate acid pH 6.5	20% (v/v) PEG MME 500, 10% (w/v) PEG 20.000	**Bi**
			20 °C	0.1 M Imidazole/ Hydrochloric acid pH 8.0	-	1 M Sodium citrate tribasic	**Bj**
			20 °C	0.1 M Tris base/ Hydrochloric acid pH 7.0	0.2 M Sodium chloride	1 M Sodium citrate tribasic	**Bk**
			20 °C	-	-	4.0 M Sodium formate	**Bl**
			20 °C	0.1 M Sodium cacodylate trihydrate pH 6.5	-	1.4 M Sodium acetate trihydrate	**Bm**
			20 °C	-	0.15 M Potassium bromide	30% (w/v) PEG MME 2.000	**Bn**

Table B.13: Crystallisation conditions of BRD4(1) with H4K5AcK8ApmTri.

Protein	Peptide	Ratio	Temperature	Buffer	Salt	Precipitant 1	Crystal
BRD4(1)	H4K5AcK8ApmTri	1:2	20 °C	0.1 M TRIS hydrochloride pH 8.5	0.2 M Sodium acetate trihydrate	30% (w/v) PEG 4.000	**Ca**
			20 °C	0.1 M Tris hydrochloride pH 8.5	0.2 M Magnesium chloride hexahydrate	30% (w/v) PEG 4.000	**Cb**
			20 °C	0.2 M Sodium thiocyanate pH 6.9	-	20% (w/v) PEG 3.350	**Cc**
			20 °C	0.1 M BICINE pH 9	-	20% (w/v) PEG 6.000	**Cd**
			20 °C	0.03 M Diethylene glycol, 0.03 M Triethylene glycol, 0.03 M Tetraethylene glycol, 0.03 M Pentaethylene glycol	0.1 M Sodium HEPES, MOPS acid pH 7.5	20% (v/v) PEG MME 500, 10% (w/v) PEG 20.000	**Ce**
			20 °C	0.02 M 1,6-Hexanediol, 0.02 M 1-Butanol, 0.02 M 1,2-Propanediol, 0.02 M 2-Propanol, 0.02 M 1,4-Butanediol, 0.02 M 1,3-Propanediol	0.1 M Tris base, BICINE pH 8.5	20% (v/v) PEG MME 500, 10% (w/v) PEG 20.000	**Cf**
			20 °C	0.1 M HEPES/ Sodium hydroxide pH 7.5	0.2 M Sodium chloride	20% (w/v) PEG 3.000	**Cg**
			20 °C	0.1 M HEPES/ Sodium hydroxide pH 7.5	-	20% (w/v) PEG 8.000	**Ch**
			20 °C	0.03 M Sodium fluoride, 0.03 M Sodium bromide, 0.03 M Sodium iodide	0.1 M Tris base, 0.1 M BICINE pH 8.5	12.5% (v/v) MPD, 12.5 % (v/v) PEG 1.000, 12.5 % PEG 3.350	**Ci**

Table B.14: Sorting of the collected data sets of BRD3(2) and BRD4(1) with ApmTri containing peptides.

Protein	Peptide	Data set	Resolution limit [Å] (proximately)	Initial R-free/R-work [%]	Issues (basis for choice of data set)	Ligand visible
BRD3(2)	H4K20ApmTri	1	2.8		Ligand not in all protomers	Yes
		2	3.2		Ligand not in all protomers	Yes
		3	2.9		-	Yes
		4	3.2		Ligand only visible in KAc binding site	Yes
		5	3.3		Low resolution	Yes
		6	3.4		Low resolution	Yes
		7	2.8		Radiation damage	Yes
		8	3.0		Ligand not in all protomers	Yes
		9	3.1		Ligand not in all protomers	Yes
		10	3.4		Low resolution	Yes
BRD4(1)	H4K5AcK8ApmTri	1	1.9	23.1/26.4	-	Yes
		2	1.6	-	Low completness	
		3	1.4	26.7/29.6	No protomer with ligand density in K5 and K8 position	Yes
		4	1.5	-	30° Chi to data set 3, ligand only partially visible	Yes
		5	1.3	-	Intensities for one screw axis missing	Yes
BRD4(1)	H4K5/K8ApmTri	1	1.6	21.9/25.8	-	Yes
		2	1.4	22.9/25.4	Ligand not connected between K5 and K8 position	Yes
		3	1.3	34.9/37.4	Ligand not nicely connected, unusual intensity statistic	Partially
		4	1.6	32.9/41.3	Twinning, ice rings, outliers	No
		5	1.3	30.7/35.7	Low completeness, ligand not well connected	Partially
		6	1.8	-	Low completeness	No
		7	1.3	27.7/29.0	Twinning, Intensities for one screw axis missing	Yes

B.6.2 Figures

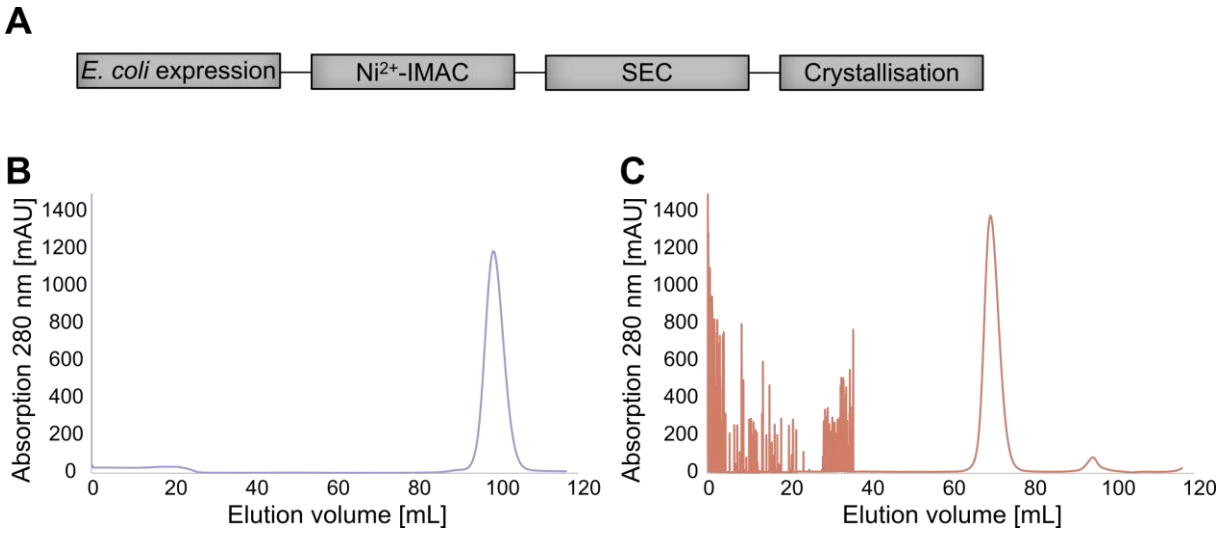

Figure B.10: Purification of BRD3(2) and BRD4(1). (**A**) The purification protocol for His_6-tagged bromodomains from *E. coli* is well established and comprises an initial nickel IMAC followed by a polishing preparative SEC. Thereafter the bromodomains were concentrated for the following crystallisation. (**B**) Elution profile of BRD3(2) purified by preparative SEC after thawing. (**C**) Chromatogram of the purification of BRD4(1) by preparative SEC. Spikes between 0 and 40 mL elution volume occurred due to pressure issues with the used HiLoad Superdex™ 75 16/600 and are not related to the protein sample.

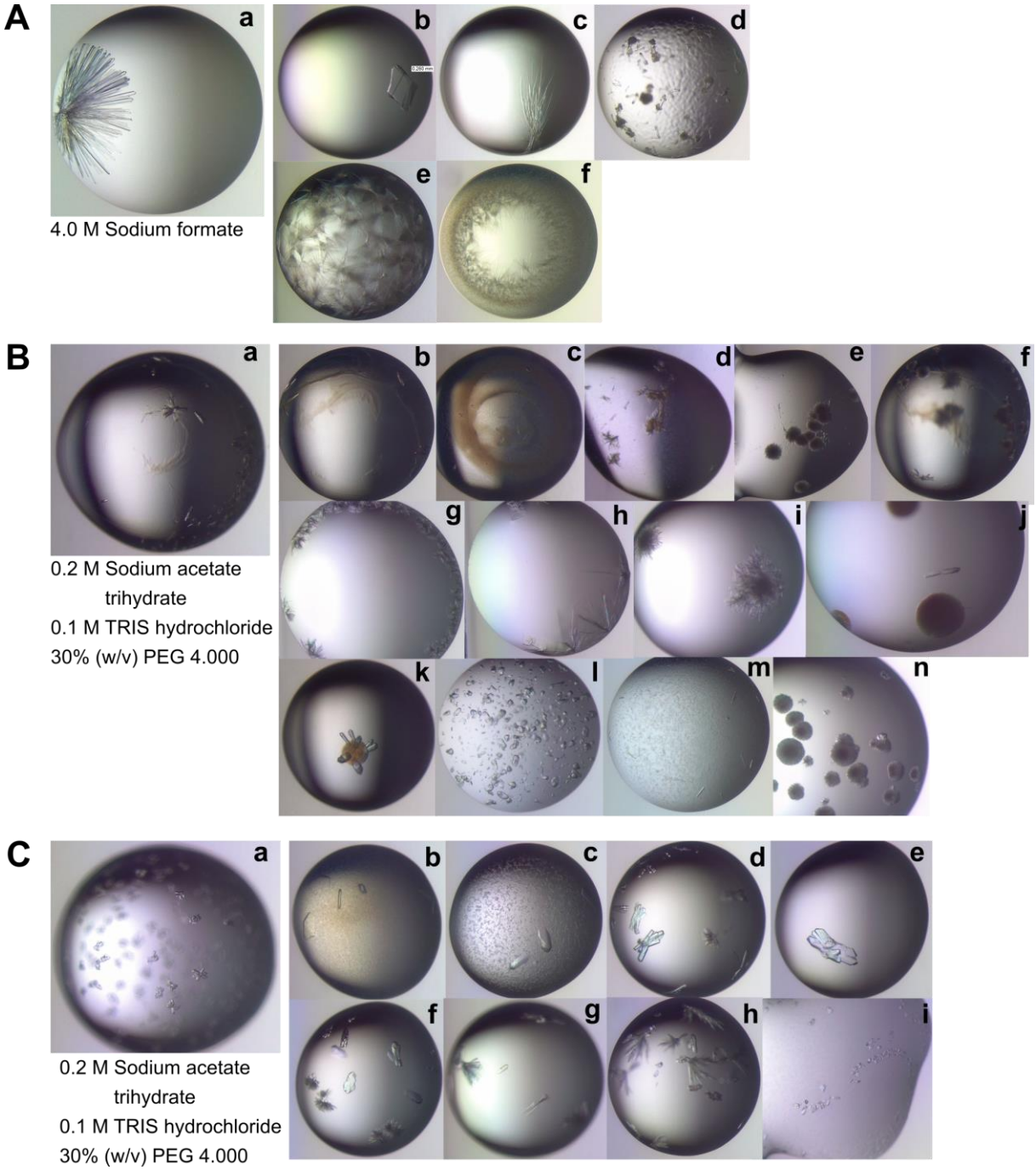

Figure B.11: Crystallisation of BRD(3)2 and BRD4(1) with acetyl lysine mimicking peptides. (**A**) Crystals of BRD3(2) with H4K20ApmTri obtained from initial screens. The 2.8 Å data set was collected from crystal (**A.a**) grown in 4.0 M sodium formate. (**B**) BRD4(1) crystals grown in the presence of 2 times access H4K5AcK8ApmTri. The data set chosen for refinement and PDB submission was obtained from crystal (**B.a**). (**C**) Crystals of BRD4(1) with H4K5/K8ApmTri mixed in a 1:20 ratio grown in initial screens. The final data set was collected from crystal (**C.a**) with a resolution cut-off of 1.58 Å. (**A**-**C**) Corresponding crystallisation conditions can be found in Table B.11, B.12 and B.13, respectively.

C. Structural interaction studies of human adenovirus hexons with the CD46 receptor

C.1 INTRODUCTION

Human adenoviruses (HAdVs) are non-enveloped double-stranded (ds) DNA viruses of icosahedral shape. The virions measure approximately 95 nm in diameter and encompass a 26-48 kb linear ds DNA genome [331], [332] that encodes 30-40 distinct proteins [333]. The first 13 HAdV strains were isolated in 1953 from human pharyngeal tonsils, also called adenoids, and identified as adenoid degeneration agents [334]. In 1954, an independent study established a connection between a HAdV strain and clinical syndromes [335] and soon after, this new category of viruses was named adenovirus group [336]. As of March 2022, 113 HAdV strains have been assigned into 7 species, A to G, with the majority belonging to species D [337]. Ongoing recombination between the capsid genes majorly contributes to the ever increasing number of unique HAdV-D types [338]. During viral cell entry, HAdV initially interact with virus attachment receptors prior to engaging with virus entry receptors before they finally gain entry into the host cell by clathrin-mediated endocytosis. After undergoing structural alterations, HAdV particles escape from the endosomal compartment and travel along microtubules towards the nucleus for replication. Most HAdV infections remain subclinical including mild infections of the respiratory and gastrointestinal tract and ocular infections. However, more severe cases can be seen in immunocompromised patients [339]. While the organisation of the HAdV capsid was unveiled early on by electron microscopy [340], [341], the details of the inner HAdV organisation did remain unknown until recent advances in cryoEM techniques enabled the revelation of a near-atomic resolution structure of the HAdV-C5 virion [342]. A simultaneously published crystal structure of a recombinant HAdV-C5 vector carrying the HAdV-B35 short fiber protein, provided further insights into the association between the capsid proteins [343]. The HAdV transcriptome is one of the most complex of viruses with alternative splicing sites on almost all transcripts leading to as many as 11,000 recorded distinct splicing patterns [344]. Despite the complexity of the virus, HAdV vectors, incompetent of replicating, are nowadays widely used as gene delivery vehicles and recent advances in vaccine development due to the COVID-19 pandemic have highlighted their potential for the preventive treatment of diseases [345]–[348].

C.1.1 HAdV genotypes in diseases

HAdVs belong to the family of *Adenoviridae*, which infects all kinds of vertebrates and comprises 6 genera: *Atadenovirus* (predominantly reptiles), *Aviadenovirus* (birds), *Ichtadenovirus* (fish), *Mastadenovirus* (mammals), *Siadenovirus* (vertebrates except mammals) and *Testadenovirus* (tortoise) [349]. The HAdVs belong to the genus of *Mastadenovirus*, which can exclusively be found in mammals and distinguish themselves through the genus-specific core protein pV and minor protein pIX [350]. To

date, seven species of HAdVs, namely A to G (Fig. C.1), have been classified based on whole-genome data-derived phylogenetic distances whereas traditional classifications relied on neutralisation assay-based serology [337]. The majority of HAdV types belong to species D followed by the HAdV-B species. Surprisingly, genotypes of the species with less members are more frequently associated with diseases. The constant evolution of the HAdV genome through recombination complicates the classification, especially when the recombinatory effects lead to significant changes in the pathogenesis of an HAdV species [344].

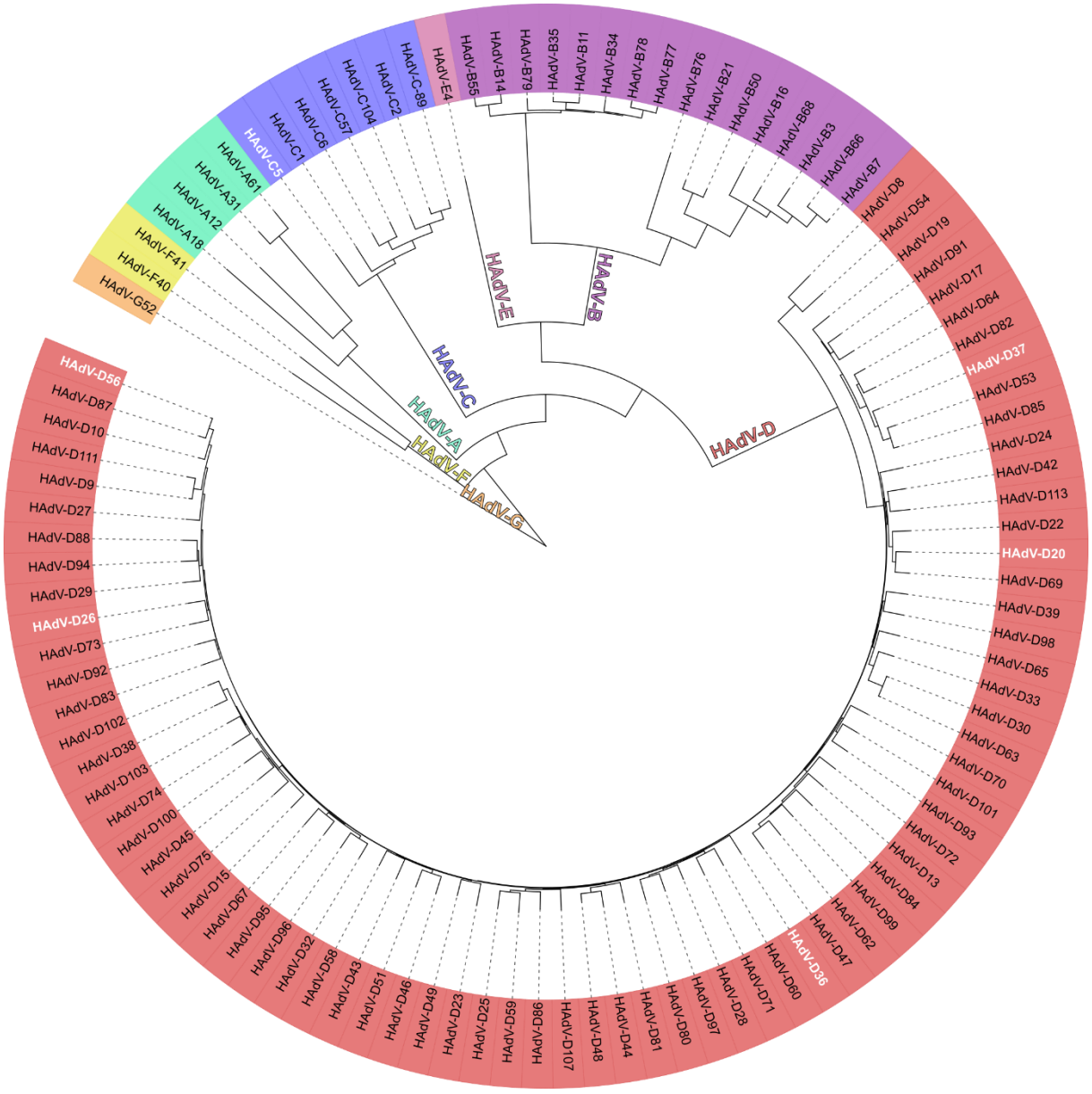

Figure C.1: Phylogenetic tree of the human *Mastadenoviruses*. Displayed are 106 distinct HAdV genotypes [337]. The HAdV are grouped into 7 species based on a whole-genome sequence alignment. Most HAdV belong to species D (80 genotypes) followed by species B (17 genotypes) and C (8 genotypes). Species A (4 genotypes), E (HAdV-E4), F (HAdV-F40, -F41) and G (HAdV-G52) have only few members. HAdV species used in this study are highlighted in white. BLAST®[132] was used to align the HAdV genotypes based on their accession code [337]. HAdV-D90, -D105, B-106, -C108, -D109, -D110, and -D112 were excluded as they have not been assigned an NCBI accession code yet. The distance tree of result was displayed with the online tool interactive tree of life [351] in order to create the depicted phylogenetic tree. The design of the tree has been taken from [352].

HAdV cause a wide variety of diseases, including respiratory diseases such as the common cold, bronchitis or pneumonia but also gastroenteritis, conjunctivitis, carditis and cystitis [353]. While HAdV can infect patients at any age, they show a prevalence for children with less than two years of age due to the lack of humoral immunity [354]. The most common respiratory tract infection causing species in children are types 1 to 7 and 55 with symptoms ranging from fever, pharyngitis, tonsillitis, cough and sore throat to in severe cases bronchiectasis, bronchiolitis obliterans and hyperlucent lung [355]. In adults, febrile respiratory illness is often linked to species 1 to 7, 14, 21 and 55 [356]–[359]. D-types 8, 19 and 37 are most commonly associated with ocular HAdV-infections leading to keratoconjunctivits [360]–[363]. HAdV-F40 and -F41 show a significant affinity for the gastrointestinal tract with symptoms of gastroenteritis and diarrhoea [364]–[366]. HAdVs are also cause of urinary tract infections with typical manifestations including dysuria, haematuria, renal allograft and haemorrhagic cystitis [367], [368]. Associated HAdV types include 3, 7, 11, 21 and 33 to 35. Infections with types 1 to 3, 5 and 7 have been reported to cause hepatitis [369], [370]. Globally, the HAdV species most commonly linked with human disease are genotypes 1 to 5, 7, 21 and 41, however, the prevalence of a certain genotype might change over time [353]. HAdV infections can cause severe issues during stem cell and solid organ transplantation [370], in HIV infected patients and other immunocompromised patients [369], [371]. Traditionally, viral infections were determined via viral cultures [372] but modern PCR-based approaches superseded conventional approaches due to their high sensitivity, quick execution and detailed results [373], [374].

C.1.2 The structural composition of HAdV

The HAdV ds DNA genome is protected by the capsid surrounding the viral core. The capsid is built by the major and minor capsid proteins (Fig. C.2, A). The DNA associated proteins pV, pVII, pMu (also named pX or pμ), terminal protein (TP), pIVa2, and the adenovirus encoded protease (AVP) are located inside the viral core [350]. The polypeptides pV, pVII and pMu are responsible for the DNA condensation which is required to fit the DNA inside the small viral core [375], [376]. They are able to tightly associate with the DNA as they carry many positively charged basic amino acids. pV acts as bridging factor between the DNA-associated core proteins and the viral capsid [377]. The C-terminus of pV interacts with the minor capsid protein pVI and it additionally interacts with the C-terminus of pVIII thus forming a complex which connects peripentonal hexons to the adjacent hexons [378], [379]. pV is Mastadenovirus-specific and not essential for adenovirus (AdV) assembly [380]. TP is a non-basic core protein which is covalently bound to the 5’ ends of the ds DNA. The HAdV protein pIVa2 assists the DNA packaging with its ATP hydrolysing ability [381], [382] and has together with TP and AVP important roles during the life cycle of HAdVs.

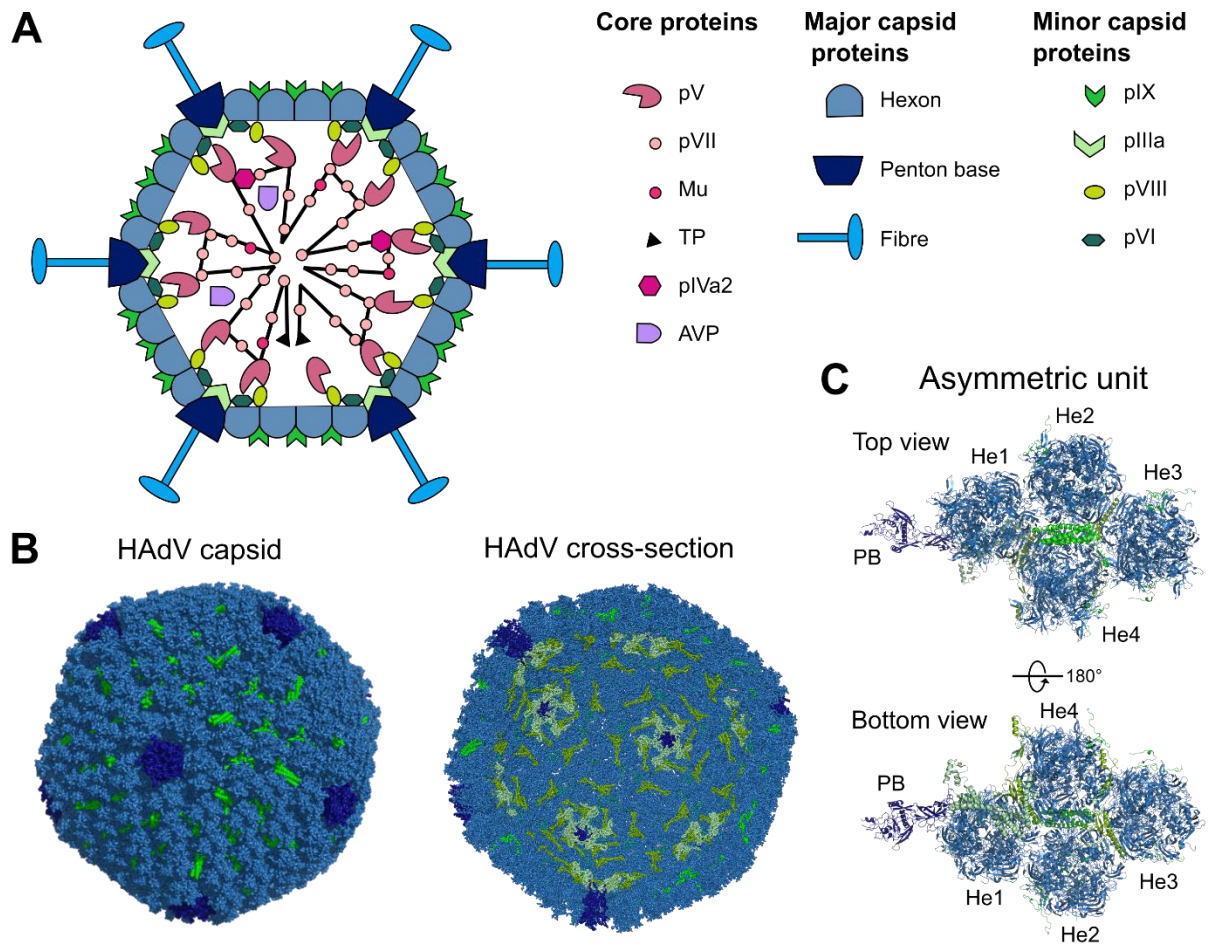

Figure C.2: Structural composition of the HAdV core and the surrounding capsid. (**A**) Schematic cross-section of the HAdV. [383] (**B**) Crystal structure of HAdV-C5 (PDB-ID: 6B1T). The icosahedral capsid is formed by the trimeric hexon protein (light blue) that has a pseudo-hexagonal shape and the pentameric penton base (dark blue). The trimeric fibre protein (not shown) protrudes from the exterior side of the penton base. While the capsid view shows how pIX (light green) neatly fills the gaps between the hexon, the cross section reveals the arrangement of pVIII (lime green) and pIIIa (pale green) on the inside of the capsid. (**C**) The asymmetric unit of the HAdV-C5 crystal structure comprising 4 hexons (He) and 1 penton base (PB) monomer (blue) as well as pIX, pIIIa, pVIII and pVI minor capsid proteins (green) (PDB-ID: 6BIT).

The HAdV capsid (Fig. C.2, B) has an overall icosahedral shape with a diameter of approximately 95 nm [340]. The asymmetric unit (Fig. C.2, C) is composed of 4 hexon trimers, one penton base monomer and the associated minor capsid proteins pIX, pIIIa, pVIII and pVI [384], [385]. The hexon, the major coat protein, covers the biggest proportion of the surface and accounts for more than half of the viral mass. The capsid comprises 240 hexon trimers in four unique locations (He1-He4), 12 per icosahedral facet of which 60 classify as peripentonal hexons (He1 in the ASU) [386]. The gap between five peripentonal hexons is filled by the pentameric penton base, a self-associating two domain protein comprising a jellyroll fold coupled to a solvent-exposed domain [387]. The trimeric fibre protein consisting of the fibre shaft, fibre knob and N-terminal tail, protrudes from the penton base [388]. The flexibility of the fiber protein prevents it from being visible in its entirety in adenovirus structures. However, electron density originating from the penton base pore at the center of the 5-fold symmetry axis has been assigned to the fiber shaft [343]. The fibre knob is formed by an antiparallel β-sandwich which is responsible for the trimerisation of the fibre [389]. The length of the trimeric β-spiral fibre shaft

depends on the virus type and plays a role in cell entry [390]. The N-terminal peptide of the fibre protein binds at a cleft within the penton base thus anchoring the fibre to the capsid structure [387]. The minor capsid proteins pIIIa, pVI, pVIII and pIX support the capsid structure from the inside and outside. pIIIa is arranged underneath the penton base vertex and connects peripentonal hexons together and to the penton base [342], [391], [392]. While pVIII mediates contacts between pIIIa and the peripentonal hexons as well as between hexons on the inner surface of the capsid, pIX connects the capsid from the outside [342], [393]–[396].

C.1.3 The HAdV hexon is a trimeric protein

The major building block of the HAdV capsid is the hexon protein, a ~950 AA, trimer-forming protein (Fig. C.3). The basis of the hexon monomer is formed by a tandem viral jellyroll domain [397]–[399]. The jellyroll domains, V1 and V2, are built by eight-stranded β-barrels which are positioned and clamped together via a small jellyroll connector domain (VC) at the bottom of the protein. The upper part of the tandem jellyrolls is stabilised and kept apart by the small DE2 loop. The DE1 loop extends from two strands of the V1 jellyroll and represents the most variable hexon region, located at the top of the hexon monomer. The FG1 loop, also smaller than the DE1 loop, similarly contributes to the variable regions of the virus and emerges from the V1 jellyroll. The FG2 loop, extending from between two strands of V2 forms a solvent-accessible pocket underneath FG1 and DE1. The N-terminal domain (NTD) of the monomer is also located at the bottom side of the hexon stretching towards the other two monomers thus increasing the stability of the trimer. The conformation of the N- and C-terminus of the hexon changes based on its position in the icosahedral capsid and establishes interactions with the minor capsid proteins pIIIa and pVIII [342]. The HAdV capsid has a pseudo T=25 icosahedral lattice as the trimeric tandem-jellyroll hexon protein has a pseudo-hexagonal shape at its base (Fig. C.3, C) [384]. On the other side of the hexon protein, the three towers formed by the DE1, FG1 and FG2 loops of the individual monomers emerge in a twisted fashion with respect to the hexagonal base (Fig. C.3, C, side view).

Among the AdV family the architecture of the hexon is highly conserved. The sequence conservation between hexon proteins of the same HAdV species is very high with approximately 90 % identity whereas the hexon protein diverges more between species. HAdV-C5 hexon and the D species HAdV-D36, -D20, -D56, -D26 or -D37 hexon have approximately 80 % sequence identity. The largest alterations can be found in the hyper variable regions (HVR) in the monomer towers. Alterations in the HVR of the hexon might reflect adaptation of the virus to environmental conditions as these regions are exposed and have been considered to play a role in determining viral tropism [395], [400].

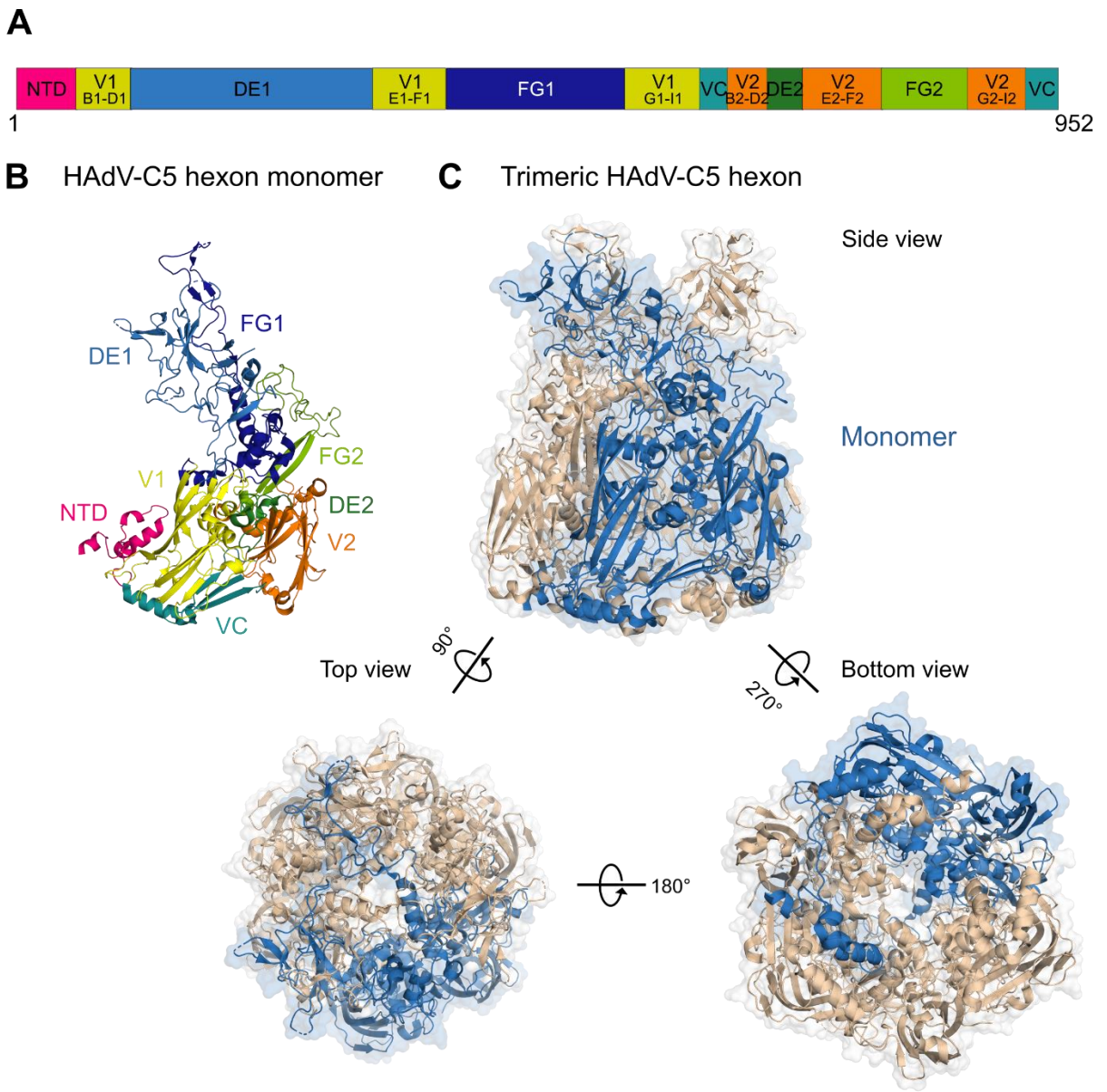

Figure C.3: The HAdV-C5 hexon is a trimeric protein with a pseudo-hexagonal appearance. (**A**) Domain architecture and (**B**) crystal structure of the HAdV-C5 monomer (PDB-ID: 3TG7). The viral jellyroll domains V1 (yellow) and V2 (orange) form the basis of the monomer and majorly contribute to the pseudo-hexagonal shape of the hexon trimer. The loops emerging from the jellyroll folds (DE1 (light blue) and FG1 (dark blue) from V1, FG2 (light green) from V2) present as tower on top of the protein and comprise the HVRs of the protein. The jellyrolls are separated and stabilised by the DE2 loop (dark green) and the VC domain (teal). The NTD (pink) connects the individual monomers to stabilise the trimeric assemble. (**C**) The trimeric arrangement of the HAdV-C5 hexon (PDB-ID: 3TG7) shows the twisted towers emerging from the jellyrole fold base and the pseudo-hexagonal fold at the bottom.

C.1.4 Viral attachment and life cycle of HAdV

Like other viruses, HAdVs rely on the host cell for reproduction. The viral DNA has to be transported to the nucleus for viral gene expression, genome replication and subsequent assembly of new virus particles. In order to reproduce and multiply, the HAdV has to undergo a series of events to cross the well-defended host cell membrane and escape the immune response [401]. The HAdV infection starts

with the attachment of the virus particle to specific host cell surface receptors. The protruding fibre protein interacts with primary receptors such as the coxsackievirus and adenovirus receptor (CAR), thus establishing an initial contact [402]. A variety of different molecules on the host cell surface have been shown to interact with HAdVs, including CAR [402]–[404], the membrane cofactor CD46 [405], [406], CD80, CD86 [407], the major histocompatibility complex (MHC) class I [408], desmoglein-2 (DSG2) [409], heparan sulfate proteoglycans [410], integrins [411], the scavenger receptor A-II [412], sialylated glycans such as GD1a [413]. The interaction between HAdV and the target cell can additionally be established in a receptor-independent fashion by lactoferrin [414] or coagulation zymogens [415]. The presence of HAdV receptors on specific cell types defines HAdV tropism as the major capsid proteins engage in serotype-specific interactions with a broad variety of receptors [416]. Recent research has established that, in addition to the fibre and the penton base proteins, the hexon of D-species HAdVs can engage in host cell receptor interactions [417].

Once the initial contact is established, the HAdV penton base interacts with active integrin adhesion receptors, thereby promoting virus internalisation [418], [419]. Consequently, the HAdV capsid is partially disassembled as the fibre is released (fibre shedding) to ensure efficient delivery of the virus to the cytosol [420]. Finally, the fibreless virus particles are internalised by clathrin-mediated endocytosis [421], [422].

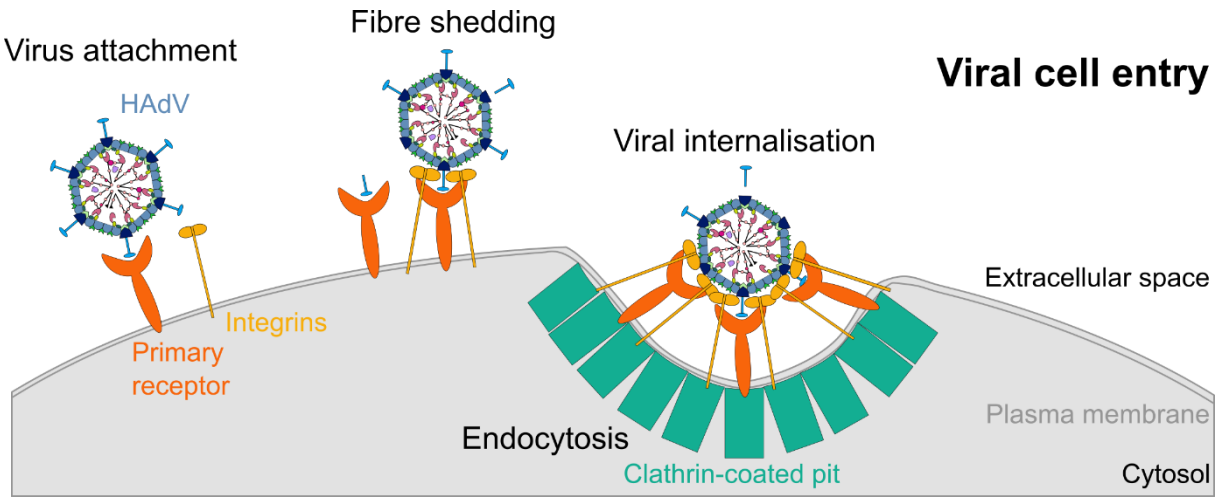

Figure C.4: The early steps of viral infection – attachment and endocytosis. Incoming virions (blue) interact via their major capsid proteins with primary receptors (orange) on host cells. Through this interaction, the attached virus can surf laterally on the host cell membrane. The additional interaction with integrin receptors (yellow) triggers virus internalisation and cell signalling. Prior to cell entry, the shedding of the virion fibres occurs and the membrane lytic pVI minor capsid protein is partially exposed. The virus particles get rapidly internalised by clathrin-mediated endocytosis.

Internalised virions escape from endosomes with the help of the membrane lytic minor capsid protein pVI and ceramide lipids [423], [424]. Cytosolic virions utilise microtubule-dependent transport systems to travel to the nucleus where they detach and interact with the nuclear pore complex (NPC) [425], [426]. Once docked to the NPC, the viral DNA is released from virus particles through disassembly and imported into the nucleus [427], [428]. Inside the nucleus, the viral DNA gets transcribed by RNA polymerase 2 in order to produce viral proteins [429]. The early E1A transactivator drives the cell into

S-phase for efficient viral DNA replication and the early E2, E3 and E4 transcripts mediate the escape from the host immune response. The structural proteins of the HAdV are expressed during late stages of DNA replication. Large clusters of virions are formed during virus assembly when the viral DNA is condensed and packed and precursor proteins are processed by AVP for virus maturation [376], [430], [431]. Finally, matured virus particles are released during cell lysis.

C.1.5 CD46, a HAdV host cell binding receptor

Viral cell entry requires the interaction of the HAdV capsid proteins with receptors on the target cell. Which HAdV species infects a specific cell type is determined by the presence of the corresponding receptors. HAdV-D species interact with CAR, CD46 and sialic acid and use the coagulation factor X for ocular and enteric infections [416]. CD46 is also a receptor for HAdV-B types together with DSG2, CD80 and CD86. CD46 is a type one transmembrane complement regulatory protein that can be found in almost all cell types, except erythrocytes [432], [433]. The complement system is a powerful initial immune response that releases millions of complement activation fragments minutes after pathogen recognition [434]. To prevent host damage, activation of complement is controlled by a tight regulatory system including CD46 [435], [436]. Two key activation fragments, namely C3b and C4b, are bound by CD46 and subsequently cleaved by serine protease factor I.

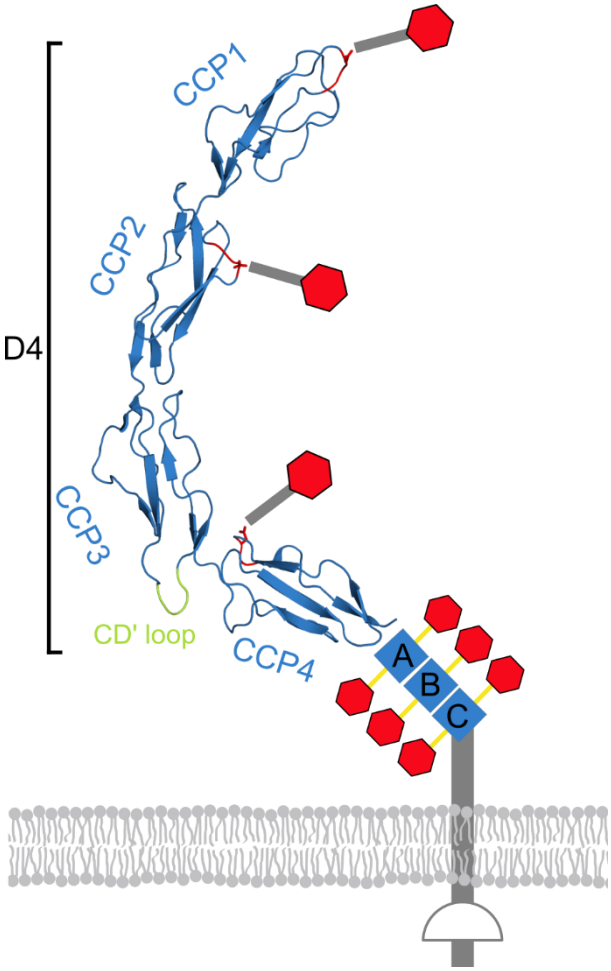

Figure C.5: The membrane cofactor protein CD46. Schematic of CD46 including the structure of CD46 D4 (PDB-ID: 3O8E). CD46 D4 comprises four complement control protein domains (CCP1-CCP4). The alternatively spliced extracellular region of CD46 is indicated (A, B and C). CD46 D4 possess 3 distinct N-glycosylation sites: Asn83, Asn114 and Asn273. Extensive O-glycosylation can be found in the Ser/Thr-rich domains (A, B and C) near the cell membrane. Both N- and O-linked carbohydrates can be capped with sialic acids (red hexagon). The proline-rich CD' loop (light green) is part of CCP3 and introduces a kink in the structure of CD46 D4.

The N-terminal extracellular part of CD46 comprises four complement control protein (CCP) domains (CCP1-CCP4) [437]. Four long β-strands forming a barrel-like structure are accompanied by a set of smaller β-strands in the CCP domain fold [438]. CCP3 carries a hydrophobic region in the protruding loop connecting β-strands C and D' [439]. The interface between CCP3 and CCP4 is notably larger than the other interdomain interfaces and exhibits a remarkable kink due to the protruding hydrophobic proline-rich CD' loop [439]. A region of alternatively spliced serine-threonine-proline (STP)-rich stretches is located between the CCP domains and the transmembrane helix. Most tissues express CD46 isoforms comprising one or two STP domains [432], [440]. On the cytoplasmic side of the membrane, two alternate tails can be found that together with the alternative splicing region give rise to multiple isoforms of the protein [432]. The CCP domains of CD46 possess three N-glycosylation sites, Asn83 in CCP1, Asn114 in CCP2 and Asn273 in CCP4 [441], whereas O-linked carbohydrates are presented on the STP domains. The N- and O-linked carbohydrates on CD46 can be capped with sialic acid which might promote additional contact sites for sialic acid binding HAdV species [441]. The HAdV-B species interacts with the CCP1 and CCP2 domain of CD46 via the fibre knob domain. HAdV genotypes of the D-species have also been reported to interact with CD46 including -D37, -D56 and -D26 [417], [442]–[450]. Recent data demonstrated a novel mode of receptor recognition for D-species HAdV independent of the fibre knob domain [417]. In contrast to HAdV-B35 which interacts with CD46 through the fibre knob, HAdV-D56 and -D26 engage in the interaction via the major capsid hexon protein [417]. Infection assays with A549 cells and soluble CD46 suggest a broader relevance for the hexon protein as the infection of many HAdV-D genotypes depends on CD46 [417]. CryoEM analysis of whole HAdV-D56 virion particles in complex with CD46 suggest binding of CD46 at the cleft between the three towers of the hexon trimer, however a detailed analysis of the binding mode remains to be determined. Whether the interaction between CD46 and the HAdV hexon is exclusive or the hexon participates in interactions with other primary or secondary HAdV receptors needs to be established.

C.1.6 HAdV vaccine and drug development

The high-density living conditions of military recruits regularly trigger epidemic respiratory HAdV infections during winter months. Since 1963, live oral adenovirus type -E4 and -B7 enteric-coated vaccines are used to treat US military personnel thus successfully reducing the rates of acute respiratory diseases [451]–[453]. The danger of environmental spreading of stable adenovirus types and the occurrence of local prevalent strains required the development of suitable alternatives. Early on, inactivated adenovirus vaccines have been considered as alternatives which increases safety while maintaining the effectiveness [451], [452], [454], [455]. However, cross-contaminations with simian virus SV-40 and potential tumorigenic properties of the inactivating agent formaldehyde significantly slowed the development [456], [457]. Neutralising antibodies (NAbs) isolated from vaccinated or naturally-exposed humans contain predominantly NAbs against the HVRs of the hexon protein and only subdominantly NAbs against the fibre knob [458]–[460]. The high variability between HAdV fibre

knobs and its ability to distinguish species-specific antibodies, renders the fibre knob a candidate with potential for the development of serotype-specific epitope-based vaccines [461], [462].

Cidofovir (CDV), a cytosine analogue is used as antiviral drug to fight HAdV infections, especially in immunocompromised patients [372], [463], [464]. Once entering cells, the prodrug CDV becomes phosphorylated by kinases to Cidofovirdiphosphat. The incorporation of CDV into the viral DNA inhibits the DNA polymerase and the subsequent virus replication. However, the poor bioavailability and nephrotoxicity of CDV are limiting possible applications [369], [372]. Other strategies against HAdV infections include the reconstitution of the immune system, which has been associated with the clearance of HAdV infections [465], [466].

C.1.7 The emerging role of HAdV vectors in preventive disease treatment

The ongoing COVID-19 pandemic [467] has boosted the development of AdV vector-based vaccines. AdV vectors are incapable of replication due to the deletion of the early-transcribed E1A gene. A variety of new vaccines is currently under development, including an HAdV-D26-based mosaic HIV vaccine (Ad26.Mos4.HIV, Janssen) [468], an HAdV-D26-based Zika virus vaccine (Ad26.ZIKV.001, Janssen) [469] and an HAdV-E4-based influenza virus vaccine (Ad4-H5-Vtn, National Institute of Allergy and Infectious Diseases) [470]. The limited availability of anti-Ebola virus agents has led to the approval of a vaccine (Zabdeno, Ad26.ZEBOV-GP, Janssen) based on the HAdV-D26 vector expressing the envelope glycoprotein of the Ebola virus [471], [472]. Four AdV vector-based vaccines against SARS-CoV-2 have been approved to date: ChAdOx1 nCoV-19 (AstraZeneca/University of Oxford), Ad26.COV2-S (Janssen), Sputnik V (Gamaleya Research Institute) and Ad5-nCOV (CanSino Biologics Inc.) [473], [474]. In contrast to the other three vaccines, which express the full-length spike protein, Ad26.COV2-S expresses a pre-fusion stabilised spike protein [346]. Additional research on less studied HAdV strains will be beneficial for the development of new HAdV-based vectors capable of interacting with a broad range of receptors.

C.2 OBJECTIVES

The aim of the third project of this thesis is the structural characterisation of the interaction between the HAdV hexon and the CD46 receptor. CD46 has long been established as a receptor for several HAdV types and structures of CD46 in complex with HAdV fibre knobs are available [439], [475], [476]. These show that the fibre knob engages several CD46 domains. Recent data provide evidence for an additional, fibre-independent CD46-interaction mode requiring the HAdV major capsid hexon protein [417]. A cryoEM structure of HAdV-D56 virions bound to CD46 indicates the possible location of CD46 at the cleft between the trimeric hexon towers, however, the visible density was not defined enough to allow for a fit of the CD46 structure. Proceeding from the results of this study, the project presented here focusses on gaining additional structural data on the details of the HAdV hexon/CD46 interaction. This project was established in collaboration with the laboratory of Prof. Niklas Arnberg in Umeå. His PhD student K. Danskog established the purification of the hexon protein from several different HAdV genotypes. The purification of CD46 from CHO cell culture supernatant has been established by Prof. Dr. Thilo Stehle, and supernatant produced in 2008 was readily available. The tasks at hand included:

- Purification of CD46 D4 from frozen CHO cell culture supernatant according to established protocols.
- Establishing the formation of a stable complex between CD46 D4 and the HAdV-D species (-D20, -D26, -D36, -D37 and -D56) hexons.
- Determining the minimal amount of CD46 D4 needed to fully saturate the complex via titration.
- Optimisation of the sample preparation procedure for negative staining and subsequent cryoEM structure determination.

To determine if the hexon protein of more HAdV-D species participates in the interaction with the CD46 receptor, we planned to analyse several HAdV hexons in parallel. Understanding virus-receptor relationships is of special importance for HAdV-D26 as it is used as vector in COVID-19 and Ebola virus vaccines and the HAdV-D20 is a promising candidate for future vaccine vectors [346], [471]. The HAdV-D37 hexon was studied because HAdV-D37 causes epidemic keratoconjunctivits [477] and it was the only D-species HAdV that showed limited interaction with CD46 in infection studies [417]. HAdV-D36 has been linked to human obesity [478], and ongoing studies in our group have left open questions about receptor interactions (*unpublished data*) which might be answered by corresponding structural data. Finally, the hexon of HAdV-D56 and -C5 were included as positive and negative controls, respectively. The available cryoEM structure of HAdV-D56 with CD46 [417] gives an indication as to where CD46 might bind to the hexon, but a more detailed analysis is clearly necessary to determine a binding interface.

C.3 MATERIALS AND METHODS

C.3.1 Materials

C.3.1.1 Chemicals

Table C.1: List of chemicals used in the HAdV hexon project.

Acrylamide-bisacrylamide solution Rotiphorese® 30% (v/w) gel	Roth
APS	Roth
Bromphenol blue	Roth
Calcium chloride ($CaCl_2$)	Sigma-Aldrich
Ethylenediaminetetraacetic acid (EDTA)	Roth
Glycerol	Sigma-Aldrich
(4-(2-hydroxyethyl)-1-piperazineethanesulfonic acid (HEPES)	Roth
Maganese chloride ($MnCl_2$)	Sigma-Aldrich
Magnesium chloride ($MgCl_2$)	Sigma-Aldrich
β-Mercaptoethanol	Sigma-Aldrich
Methyl-α-D-mannopyranoside	Sigma-Aldrich
Sodium chloride (NaCl)	Roth
Sodium dodecyl sulfate (SDS)	Roth
Tetramethylethylenediamine (TEMED)	Roth
Tris(hydroxymethyl)aminomethane hydrochloride (Tris-hydrochloride)	Sigma-Aldrich

C.3.1.2 Consumables

Table C.2: Consumables used for the purification of CD46.

Amicon® Ultra 0.5 mL centrifugal filters (MWCO 10 kDa)	Merck
Amicon® Ultra-15 centrifugal filters (MWCO 10 kDa, 50 kDa)	Merck
Corning®-Costar®-Spin-X® centrifugal filters (0.22 µM)	Corning
HiTrap™ Con A 4B column 5 mL	Cytiva
HiTrap™ Q FF column 5 mL	Cytiva
Membrane filter (0.22 µM)	Millipore
Microtiter plate, 96-well	Greiner Bio-One
Pipette tips	Herbe Plus
Reaction tubes (1.5 mL, 2.0 mL, 15 mL, 50 mL)	Greiner Bio-One
Serological pipettes (5 mL, 10 mL, 25 mL, 50 mL, 100 mL)	Greiner Bio-One
Steritop-GP polyethersulfone filter (0.22 µm)	Millipore
Syringes (1 mL, 5 mL, 10 mL, 30 mL)	Greiner Bio-One

C.3.1.3 Buffers and Reagents

Table C.3: Protein purification and other buffers.

Analytical SEC buffer	20 mM HEPES pH 7.5, 100 mM NaCl, 5 mM $CaCl_2$
CD46 D4 SEC buffer	20 mM HEPES pH 7.4, 100 mM NaCl
Con A elution buffer	20 mM HEPES pH 7.4, 500 mM NaCl, 1 mM $MgCl_2$, 1 mM $CaCl_2$, 1 mM $MnCl_2$, 12.5% methyl-α-D-mannopyranoside
Con A loading buffer	20 mM HEPES pH 7.4, 500 mM NaCl, 1 mM $MgCl_2$, 1 mM $CaCl_2$, 1 mM $MnCl_2$
Con A wash buffer	20 mM HEPES pH 7.4, 1 M NaCl, 1 mM $CaCl_2$, 1 mM MnCl
IEx elution buffer	20 mM HEPES pH 7.4, 1 M NaCl
IEx loading buffer	20 mM HEPES pH 7.4
4x SDS sample buffer	30 mL glycerol, 10 mL 10% SDS, 1.63 mL 0.5 M EDTA pH 8.0, 4 mL β-mercaptoethanol, 20 mg bromphenol blue, 13 mL H_2O

Table C.4: List of the used reagents.

Gel Filtration Calibration Kits (Low/High molecular weight)	GE Healthcare
Instant blue®	Abcam
Page Ruler™ unstained protein ladder	Fermentas
Rotiphorese® 10x running buffer	Roth

C.3.1.4 Instruments

Table C.5: Overview of instruments used in the HAdV hexon project.

ÄKTA Basic	Amersham Pharmacia Biotech
ÄKTA Micro (Ettan LC)	GE Healthcare
ÄKTA Prime Plus	GE Healthcare
Centrifuge 5415 D	Eppendorf
Centrifuge Heraeus™ multifuge 1 L-R	Thermo Fisher Scientific
Fiberlite™ bottle for SLC4000 rotor	VWR International
Heating block Neoblock 1	neoLab
HiLoad Superdex™ 200 16/600 column	Cytiva
IKAMAG® magnetic stirrer Mini MR standard	VWR International
Milli-Q-Nerj	Millipore
Mini-PROTEAN electrophoresis system	Bio-Rad
Nanodrop ND-1000	Thermo Fisher Scientific
Peristaltic pump (EconoPump)	Bio-Rad
pH meter BP11	Sartorius
Sartorius ME premium semi micro scale	Sartorius
SLC4000 rotor	Thermo Fisher Scientific
Sorvall™ RC 6 Plus centrifuge	Thermo Fisher Scientific
Superdex™ Increase 3.2/300 column	Cytiva
Superose® 6 Increase 3.2/300 column	Cytiva

C.3.1.5 SDS-PAGE

Table C.6: Protocol for the casting of SDS gels.

Chemicals	Stacking gel	Separating gel 12%	Separating gel 15%
Rotiphorese® gel 30%	5.85 mL	27 mL	33.8 mL
1.5 M Tris/HCl pH 8.8		16.9 mL	16.9 mL
1.5 M Tris/HCl pH 6.8	7.5 mL		
10% SDS (w/v)	450 µL	677 µL	677 µL
TEMED	45 µL	67.5 µL	67.5 µL
10% APS (w/v)	450 µL	677 µL	677 µL
H_2O	27.5 mL	22.5 mL	15.7 mL

C.3.1.6 Software

Table C.7: List of software and online tools.

BLAST®	National Center for Biotechnology Information [132]
Interactive Tree of Life (iTOL)	EMBL [351]
Unicorn™ chromatography software	Cytiva

C.3.2 Methods

C.3.2.1 Protein purification

HAdV hexon samples were obtained from infected A549 cells and purified via CsCl gradient ultracentrifugation and subsequent IEx and preparative SEC by K. Danskog (group of Prof. Arnberg, Division of Virology, Umeå University). Small quantities of flash frozen HAdV hexon samples were shipped to our lab.

The protocol for the purification of CD46 D2 has been established in 1999 by Casasnovas et al. [438] and was thereafter adapted for the purification of CD46 D4 [439]. The purification of CD46 D4 as described below was carried out at 4°C with pre-chilled and filtered buffers (Table C. 3).

Concanavalin A (Con A) affinity chromatography

CD46 D4 (AS 35-288) was purified from frozen CHO cell culture supernatant. 1 L supernatant from the heterologous expression of CD46 D4 was thawed in a 10 °C water bath for approximately 4 hours. To separate remaining cells and cell debris, the supernatant was subsequently centrifuged at 7,000x g for 15 min at 4 °C. The cleared supernatant was transferred into a fresh bottle with a 100 mL pipette and $MgCl_2$, $CaCl_2$ and $MnCl_2$ were added to a final concentration of 1 mM. Hereafter, the supernatant was filtered into a fresh bottle with 0.22 µM Steritop-GP polyethersulfone filters. A 5 mL HiTrap™ Con A 4B column was equilibrated with Con A loading buffer and the supernatant was loaded cyclic for ≥12 h. The column was installed on an Äkta Prime Plus system and washed with 100 mL Con A wash buffer containing 1 M NaCl and eluted with 12.5 % methyl-α-D-mannopyranoside in 100 mL Con A elution buffer. The collected fractions were analysed for protein content by SDS-PAGE and fractions containing protein were pooled for subsequent protein purification steps.

Preparative size exclusion chromatography

The CD46 D4 containing samples obtained after Con A affinity purification were concentrated with equilibrated Amicon® Ultra-15 centrifugal filters with a molecular weight cut-off (MWCO) of 10 kDa in several 30 min steps at 2,000x g. The NaCl and methyl-α-D-mannopyranoside concentrations in the samples was reduced by diluting the sample three times in a 1:4 ratio with CD46 D4 SEC buffer. The protein was further concentrated to a final volume of approximately 3 mL. Any protein aggregates were removed by centrifugation at 16,000x g for 10 min and transfer into a fresh reaction tube. Thereafter, the protein sample was loaded onto an equilibrated HiLoad Superdex™ 200 16/600 column installed on an ÄKTA Basic system and eluted over 1.2 CV with CD46 D4 SEC buffer. Fractions containing protein were identified via absorption at 280 nm and by SDS-PAGE. In preparation of the subsequent ion exchange chromatography, CD46 D4 containing fractions were pooled.

Ion exchange chromatography

To increase the purity of CD46 D4, SEC purified samples were further purified by IEx. For this purpose, CD46 D4 was loaded cyclic for ≥15 h onto an equilibrated HiTrap™ Q FF 5 mL column. Subsequently, the column was installed on an Äkta prime plus system and washed with 30 mL IEx loading buffer and 30 mL 20 mM NaCl IEx loading buffer. The protein was eluted with a 20-1000 mM NaCl gradient over 20 CV. Fractions containing protein were identified by SDS-PAGE and pooled prior to concentrating. For subsequent experiments, CD46 D4 was concentrated with Amicon® Ultra-15 centrifugal filters (MWCO 10 kDa) at 2,000x g for 3x 15 min to a final concentration of about 3 mg/mL. Protein aliquots of 100 µL were flash frozen in liquid nitrogen and stored at -80 °C until usage.

C.3.2.2 Analytics

SDS-PAGE

During protein purifications, samples were analysed at each step by SDS-PAGE in order to identify fractions containing protein and to ensure sufficient purity. Samples were prepared by adding 25% 4x SDS sample buffer (Table C.3), boiling at 98 °C for 5 min and subsequent centrifugation at 16,100x g for 2 min. For each sample, 10 µL were loaded onto 12% SDS polyacrylamide gels and 5 µL Page Ruler™ unstained protein ladder was loaded as control. The SDS-PAGE was run for 45 min at 220 V in 1x SDS-PAGE buffer prepared from Rotiphorese® 10x running buffer. SDS polyacrylamide gels were stained with Instant blue® overnight.

Complex formation

For complex formation, HAdV hexon samples were thawed, pooled and concentrated with Amicon® Ultra 0.5 mL centrifugal filters to concentrations ranging from 1.1 to 2.6 mg/mL. The HAdV hexon samples were mixed with CD46 D4 in 1:1 to 1:9 ratios, with a 1:1 ratio corresponding to one CD46 D4 molecule per trimer of HAdV hexon and a 1:3 ratio corresponding to one CD46 D4 molecule per monomer of HAdV hexon. Samples were mixed in analytical SEC buffer containing 5 mM $CaCl_2$ needed for complex formation. As control, samples with the same HAdV hexon or CD46 concentration were prepared to enable the comparison of chromatograms, and to show the reduction of the individual peaks upon complex formation. Hereafter, the samples were incubated for 12 to 16 h at 4 °C and further incubated for 1 h at RT to enhance complex formation. Finally, the prepared samples were filtered with 0.22 µM Corning®-Costar®-Spin-X® centrifugal filters to remove any aggregates prior to analytical SEC.

Analytical SEC

HAdV hexon/CD46 D4 samples were analysed for potential complex formation by analytical SEC. For this purpose, 25 µL sample containing HAdV hexon, CD46 D4 or both were loaded with a syringe onto a Superdex™ 200 Increase 3.2/300 column installed on an Äkta Micro Ettan LC system. The analytical SEC was run with analytical SEC buffer over 1.1-1.2 CV, and the elution volume of the proteins was compared to a protein standard to estimate the size of the proteins and protein complexes. Complex formation was monitored via UV absorption at 280 nm.

C.3.2.3 Structure determination

Negative staining

HAdV-D26, HAdV-D37 and HAdV-D56 hexon samples with CD46 D4 were prepared for negative staining from analytical SEC elutions. For this purpose, peak fractions containing potential complexes were pooled and frozen from analytical SEC runs with a 1:2, 1:3 or 1:6 ratio of HAdV hexon and CD46 D4. Samples were thawed before usage, filtered with 0.22 µM Corning®-Costar®-Spin-X® centrifugal filters and the concentration was determined with a Nanodrop ND-1000 using the calculated molecular mass and the extinction coefficient (Table C.8). In contrast, samples of HAdV-D20 and HAdV-D36 hexon with CD46 D4 were prepared by mixing the respective hexon in a 1:2 ratio with CD46 D4, incubating fro 12 to 16 h at 4 °C and 1 h at RT. Thereafter samples were filtered to remove aggregates.

Table C.8: Molecular weight and extinction coefficient of HAdV hexons and CD46 D4.

Protein	Calculated molecular mass [kDa]	Extinction coefficient $[\frac{1}{M*cm}]$	Number of amino acids
HAdV-C5 hexon	324.0	466070	2,856
-D20 hexon	324.9	443595	2,829
-D26 hexon	321.5	461225	2,856
-D36 hexon	319.4	465570	2,832
-D37 hexon	316.8	456630	2,817
-D56 hexon	319.4	461600	2,823
CD46 D4	28.6	49820	254

Negative staining grids were prepared with the respective samples at RT by K. Hipp (Electron microscopy, Max-Planck-Institute for Biology). Samples at concentrations of 10 µg/mL or 40 µg/mL were loaded onto glow-discharged EM grids coated with a continuous carbon film and incubated for 2 min. Remaining sample liquid was removed with filter paper and 3 consecutive drops of water were applied and removed with filter paper. Subsequently, 3 drops of 1% uranium acetate were similarly applied and removed. Finally, the sample loaded grid was incubated with 1 drop of 1% uranyl acetate for 5 min until dry. Grids were imaged with a 120 kV Tecnai G2 Sprit BioTWIN and a TVIPS F416 camera by K. Hipp at the Electron Microscopy facility of the Max Planck Institute for Biology Tübingen.

C.4 RESULTS

In this chapter the results of the HAdV hexon project will be discussed. Katarina Danskog (KD), Lars Frängsmyr (LF), Katharina Hipp (KH) and N. Bartlick (NB) have contributed to the work below. Corresponding affiliations are listed in the appendix section.

The study was designed by KD and NB. KD purified HAdV hexons from infected A549 cells. NB purified CD46 D4 from frozen CHO cell culture supernatant. LF analysed the interaction between the HAdV-D56 and HAdV-D26 hexon and full-length CD46 or CD46 D4 by SPR. NB established the complex formation of CD46 D4 with the HAdV hexons by analytical SEC. NB prepared complex samples for negative staining and cryoEM and KH was responsible for grid preparation and freezing. Negative staining and cryoEM data collection was taken care of by KH.

C.4.1 Purification of CD46 D4

The foundation for the work presented here has been laid by the recognition of the hexon protein as a receptor interaction factor [417]. Based on the results of that study, we sought to identify and analyse the binding epitopes of CD46 and characterise differences among selected D-species HAdV hexons. For this purpose, CD46 D4, comprising the four extracellular CCP domains of CD46, was purified from frozen Chinese hamster ovary (CHO) Lec 3.2.8.1 cell supernatant according to established protocols from our group [439], [475], [476]. CHO Lec 3.2.8.1 cells secret glycoproteins with high-mannose type glycans and minimal carbohydrate heterogeneity [479]. The supernatant was harvested in 2008 from cells grown in roller bottles with 3.5% FBS added to the medium. In accordance with the original protocol by T. Stehle, CD46 D4 was purified via three steps including a Con A affinity purification, a preparative SEC and a polishing ion exchange chromatography. The proteins did not elute in a sharp peak from the Con A column but over a large elution volume (Fig. C.6, A-B). In an SDS-PAGE, CD46 D4 runs as a double band between the 30 kDa and 40 kDa marker, due to two types of glycosylation (tested with *EndoH* by D. Persson in 2008). During the preparative SEC, performed via a HiLoad Superdex™ 200 16/600 column, most impurities, especially glycosylated proteins of larger size, were separated from CD46 D4 (Fig. C.6, C-D). CD46 D4 eluted in a second sharp peak and the corresponding SDS-PAGE (Fig. C.6, D) revealed the increase in sample quality. Peak 2 was pooled and loaded overnight onto a 5 mL HiTrap™ Q FF column. A flat NaCl gradient of 20-1000 mM over 20 CV was used to elute CD46 D4 (Fig. C.6, E-F). As is apparent from the SDS-PAGE, the IEx did not increase the purity of the CD46 D4 sample. The use of a bigger Mono Q 5/50 column likely could improve this result, however, the quality and quantity of the protein was judged to be sufficient for further experiments. Fractions of the eluting peak were concentrated to 3.4 mg/mL, flash frozen in liquid nitrogen and stored at -80 °C. In summary, the purification was straightforward and could be repeated several times with similar results.

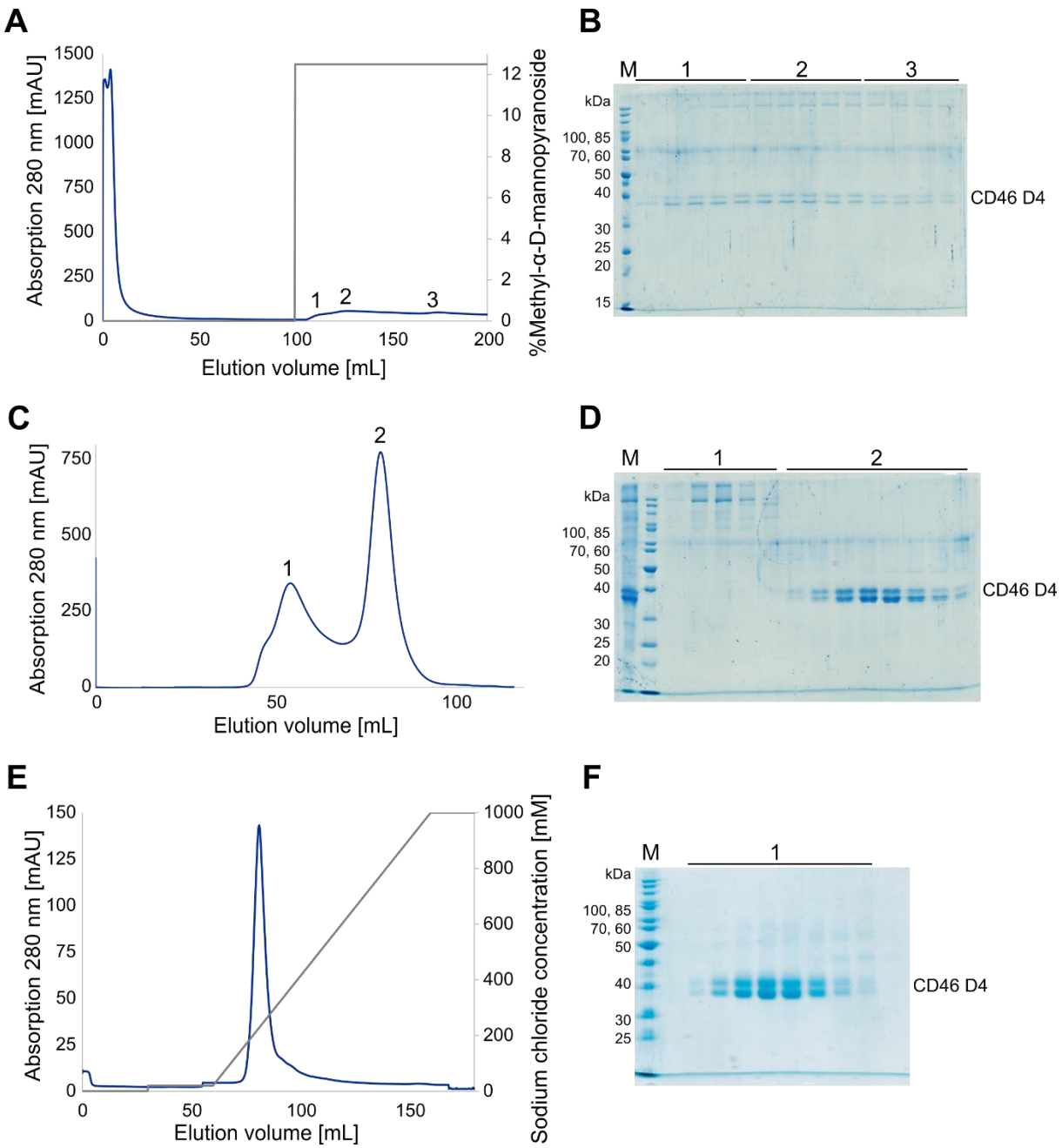

Figure C.6: Purification of the membrane cofactor protein CD46 D4. (**A**-**B**) Concanavalin A affinity purification of heterologously expressed CD46 D4. Glycosylated proteins elute over 100 mL at 12.5 % methyl-α-D-mannopyranoside. (**C**-**D**) During the subsequent preparative SEC, larger glycosylated proteins are separated from CD46 D4 which elutes mainly in peak 2. (**E**-**F**) CD46 D4 elutes as sharp peak from the HiTrap™ Q FF column with a 20-1000 mM NaCl gradient. (**A**-**F**) For each of the purification steps both the elution profile and the corresponding SDS-gel are displayed. M = marker.

C.4.2 Establishing a stable complex between HAdV D-species hexons and CD46

With the aim of obtaining structural data on the interaction epitopes of HAdV D-species hexons and CD46, K. Danskog purified HAdV hexons of the following strains: -D20, -D26, -D36, -D37, -D56 and -C5, according to existing protocols for the purification of -D26 and -D56 [417]. Initial experiments to establish a complex between the HAdV-D37 and -D26 hexon and CD46 D4 by analytical SEC were not

successful. For this reason, L. Frängsmyr determined the equilibrium dissociation constant K_D with immobilised full-length human CD46 (Nordic Biosite) by SPR experiments (*unpublished data*). For the HAdV-D26 and -D56 hexons K_Ds of 4.2 µM and 6.7 µM were determined, respectively. In contrast, the HAdV-C5 hexon did not bind at all. L. Frängsmyr determined a K_D of 0.25 µM for CD46 (Nordic Biosite) run over immobilised HAdV-D56 hexon and a similar K_D of 0.14 µM for CD46 D4 purified by N. Bartlick as described here. The SPR experiments also revealed that the interaction between the HAdV hexon and CD46 is calcium-dependent. Hereafter, complex formation was analysed in the presence of 5 mM $CaCl_2$ by analytical SEC with HAdV -D26, -D36, -D37, -D56 and -C5 hexons mixed in a 1:1 ratio with CD46 D4, which corresponds to one molecule CD46 D4 (28.6 kDa) per hexon trimer (~320 kDa). To establish if complex formation was successful, samples of CD46 D4 alone, the HAdV hexons alone and the putative complexes were analysed with a Superdex™ 200 Increase 3.2/300 column with special emphasis placed on loading comparable amounts. While we were confident that HAdV-D37 and HAdV-D36 hexons formed a complex with CD46 D4 based on the occurring significant peak shift, the results were more difficult to interpret for HAdV-D26 and HAdV-D56, for which the peak shift was subtler (Extended data, Fig. C9). In this particular experiment, the HAdV-C5 hexon control could not be trusted because the loading valve of the instrument did not load the HAdV-C5/CD46 D4 sample properly (Extended data, Fig. C9, E).

With the aim of determining complex formation for all HAdV D-species used in this study and to establish the amount of CD46 D4 needed to saturate the hexons, we tested ratios between hexon and CD46 D4 ranging from 1:1 to 1:9 (Fig. C.7). A ratio of 1:1 corresponds to one CD46 D4 molecule per hexon trimer and a ratio of 1:3 corresponds to one CD46 D4 molecule per hexon monomer, which should saturate the complex if CD46 D4 binds to a single epitope of the hexon. We tested hexons from HAdV types -D26 (321.5 kDa), -D36 (319.4 kDa), -D37 (316.8 kDa), -D56 (322.0 kDa) and -C5 (324.0 kDa) and additionally included the -D20 (324.9 kDa) hexon in our analytical SEC experiments. As expected, HAdV-C5 did not interact with CD46 D4 at all, shown by hexon peak eluting at an elution volume corresponding to approximately 280 kDa (Fig. C.7, A). The elution volume of the hexon peak varies for the individual hexons as it is dependent on the size, shape but also the surface properties of the hexon. Some hexon samples (HAdV-D26, -D36 and -D56) display more than one peak likely due to variations in the sample quality. For the HAdV-D20, -D26, -D36 and -D37 hexons we see significant shifts ranging from 45 to 90 kDa. The HAdV-D56 hexon was supposed to serve as positive control in our experiments, as its interaction with CD46 has been established before [417]. However, the peak shift of the HAdV-D56 hexon upon interaction with CD46 D4 amounts to 21 kDa, which is too small to verify complex formation. For all D-species hexons, except HAdV-D20, a 1:2 excess of CD46 D4 was sufficient to saturate complex formation, indicating that only 1-2 copies of CD46 bind per hexon trimer.

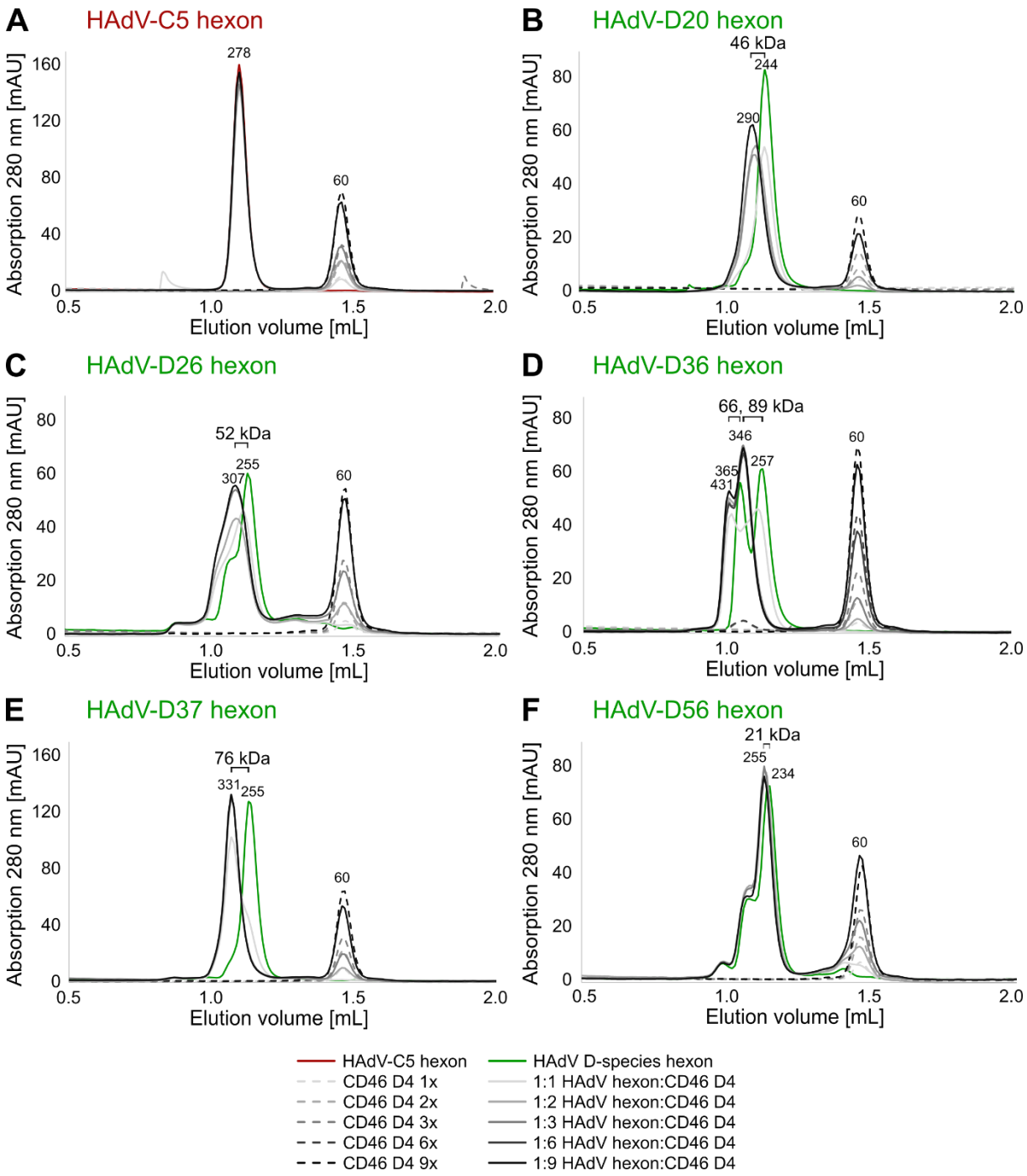

Figure C.7: Complex formation between HAdV hexons and CD46 D4 via analytical SEC titrations. (**A**) Control experiment with HAdV-C5 incubated with CD46 D4. The peak of the HAdV-C5 hexon does not shift indicating that as expected no binding took place. (**B-F**) Analytical SEC runs of HAdV D-species hexons with CD46 D4 in ratios ranging from 1:1 to 1:9. The peak position on the Superdex™ 200 Increase 3.2/300 column was correlated to the protein size according to the elution volume of protein standards. Control runs include the individual hexons (green) and CD46 D4 (dashed lines) loaded in similar amounts to the complex samples (solid lines, greyscale). Peak shifts and the reduction of free CD46 in the HAdV-D20, -D26, -D36 and -D37 samples clearly indicate binding. HAdV-D56 hexon still holds the potential for binding, as the peak shifting is dependent on surface properties of the hexon. This is also highlighted by the different elution volumes of the hexons which all have similar size and shape.

C.4.3 Negative staining results of HAdV hexons with CD46

Although samples of both CD46 D4 or HAdV hexons can be concentrated beyond the concentration of 1 mg/mL without any visible signs of precipitation, once we attempted to form a complex, the corresponding samples could not be concentrated without precipitation of the majority of the protein. For this reason, we initially decided to use peak fractions of the analytical SEC runs of HAdV-D26, -D37 and -D56 hexon with CD46 D4. Fractions containing complexes were pooled from analytical SEC runs with excess CD46 D4. Determining the exact concentration of the sample was difficult due to the limited resolution capacity of the device. Therefore, the measured concentration was considered a rough estimate and grids were subsequently prepared at a variety of concentrations to find the ideal concentration at which particles are spread densely but without touching each other. In contrast, samples of -D20 and -D36 hexon with CD46 D4 were prepared from hexon and CD46 D4 samples mixed in a 1:2 ratio without further purification of the putative complex by analytical SEC.

Negative staining grids of CD46 D4 bound to HAdV hexons were prepared by K. Hipp. Representative sections of the obtained negative staining images (Fig. C.8) show the distribution of hexon particles on the corresponding grids. A concentration of 10 µg/mL was determined to be ideal for densely packed grids while maintaining separated hexon particles. That the concentration could not be determined exactly is visible when comparing the different samples (Fig. C.8, A and B). Although the contrast varies between different samples prepared and imaged on separate dates (Fig. C8, A and C together, D and E together), the HAdV D-type hexon particles are nicely visible. The top/bottom view was distinguished from the side view, due to its round, sometimes even hexagonal appearance and the darker shaded cleft at the centre of the hexon. In contrast, the side view appears cone-shaped and in case of good contrast tooth-shaped. HAdV-D20 and HAdV-D26 hexons display a prevalent top/bottom orientation whereas the other hexons have a more mixed population. Samples of HAdV-D37 and HAdV-D56 hexons display the formation of trimers of trimers which is likely an artefact of the freezing and thawing process as all thawed complex samples showed severe signs of precipitation. Therefore, subsequent samples of complexes were prepared fresh and only the individual components were frozen. The HAdV hexon and CD46 D4 complex samples shown here (Fig. C.8) will need further investigation by three-dimensional reconstruction to determine if the 10 times smaller CD46 D4 is bound to the hexons. In order to determine details of the binding epitope of CD46, we aim to obtain high-resolution cryoEM structures of the samples displayed here.

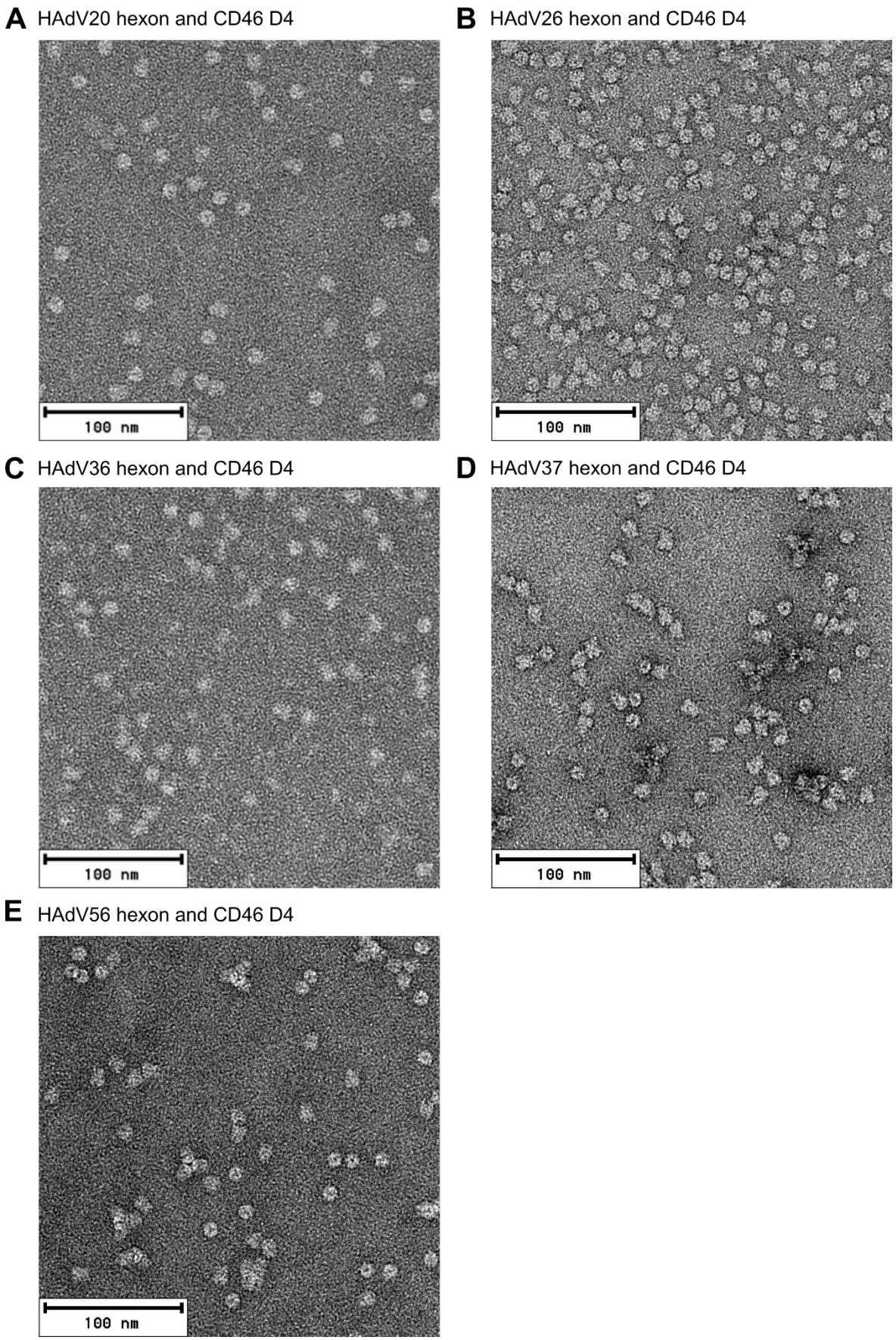

Figure C.8: Negative staining images of HAdV hexons with CD46 D4. (**A**-**E**) Samples were prepared on glow-discharged carbon-coated EM grids and incubated with uranyl acetate for contrast. Exemplary sections are displayed from samples at 10 µg/mL. HAdV-D26 and HAdV-D20 hexons display a prevalent top/bottom view orientation, whereas HAdV-D37 and HAdV-D56 hexons appear to be mainly side view oriented.

C.5 DISCUSSION

The aim of the project presented here was the investigation of the recently discovered novel type of interaction between the HAdV D-species and the CD46 receptor. Revealing the binding epitope and interaction mode of the hexon with CD46 will shed light onto this unexpected interaction and enable the analysis of the relevance of the interaction for viral cell entry.

For this purpose, we analysed the complex formation between HAdV D-species hexons and CD46 D4 and found that HAdV-D20, -D26, -D36 and -D37 hexons form stable complexes with CD46. Analytical SEC titration experiments revealed that for HAdV-D26, -D36 and -D37 a two-time excess of CD46 was required to saturate the complex, indicating that the hexon trimer binds more than one copy of CD46. In case of the HAdV-D20 hexon even a three-time excess of CD46 D4 was needed to saturate the peak shift. This contradicts the cryoEM reconstruction of the HAdV-D56 virion [417] which showed a potential single epitope at the cavity formed by the three towers formed by the trimeric hexon. This could be an indication, that the binding mode for CD46 differs between the different HAdV species, which remains to be determined. The saturation of all 240 hexon proteins of the HAdV by CD46 is highly unlikely *in vivo*, due to steric hindrance and the one-sided docking of the virion. However, binding of CD46 to more than one epitope could increase infectivity and contribute to the manifestation of the corresponding diseases. *Persson et al.* demonstrated that, in contrast to D-species HAdVs, HAdV-B35 interacts with CD46 via the fibre knob domain [417]. Nevertheless, it still needs to be established if the contribution of the hexon major capsid protein to the receptor binding is a D-species unique feature or if the hexon may be able to engage with a variety of receptors by so far unknown mechanisms. Our negative staining results highlight the potential of the HAdV hexon for cryoEM structure determination. The trimeric hexon protein has a globular fold with high contrast, and it is thus a good candidate for cryoEM. We have laid a solid foundation for the subsequent structural analysis of the interaction between the hexon and CD46 which will reveal the novel mode of interaction between HAdV D-species and their receptor.

C.6 OUTLOOK

The work presented in this thesis is the basis for the structural characterisation of the interaction between the HAdV hexon and the CD46 receptor. The obtained negative staining images could be used to reconstruct low-resolution three-dimensional structures of the hexon receptor complexes. However, the purpose of the negative staining experiments was the examination of the sample quality. From those images, the ideal sample concentration was determined and the sample preparation was optimised as described. The negative staining micrographs comprise only a couple of hundred particles, which would be of limited use for reconstructions especially due to the preference for a specific orientation. Nevertheless, based on the results presented here, samples were submitted for the collection of cryoEM data sets by K. Hipp. To date, two full data sets of HAdV-D26 and -D37 (only recently obtained) with CD46 D4 were collected. Initial analysis of the HAdV-D26/CD46 data set showed that the data processing is not trivial as more than 90% of all particles are in the preferred top/bottom orientation. Side view particles are not only rare but also much harder to spot by eye, making the initial particle picking a challenging task. These issues lead to significant noise in the data set which complicates the three-dimensional refinement and likely requires the optimisation of the two-dimensional classification. To this date, we cannot confirm the presence of CD46 in the sample, which is why this data set was not analysed as part of this thesis. Based on the negative staining images, we guess that the HAdV-D37 hexon/CD46 D4 data set should display a better distribution of particle orientations. In addition, the data sets of HAdV-D20, -D37 and -D56 hexon will be obtained over the course of the next year. In case we continue having issues with the identification of CD46, we consider submitting additional samples of the hexons without CD46 in order to calculate difference maps. In summary, the identification and analysis of the CD46 binding epitopes on the hexon require additional refinement of the current and any future data sets. Further research will be needed to analyse details of the interaction mechanism with the help of suitable mutants, thus broadening our understanding of how the HAdV engages with receptors.

C.7 EXTENDED DATA

C.7.1 Figures

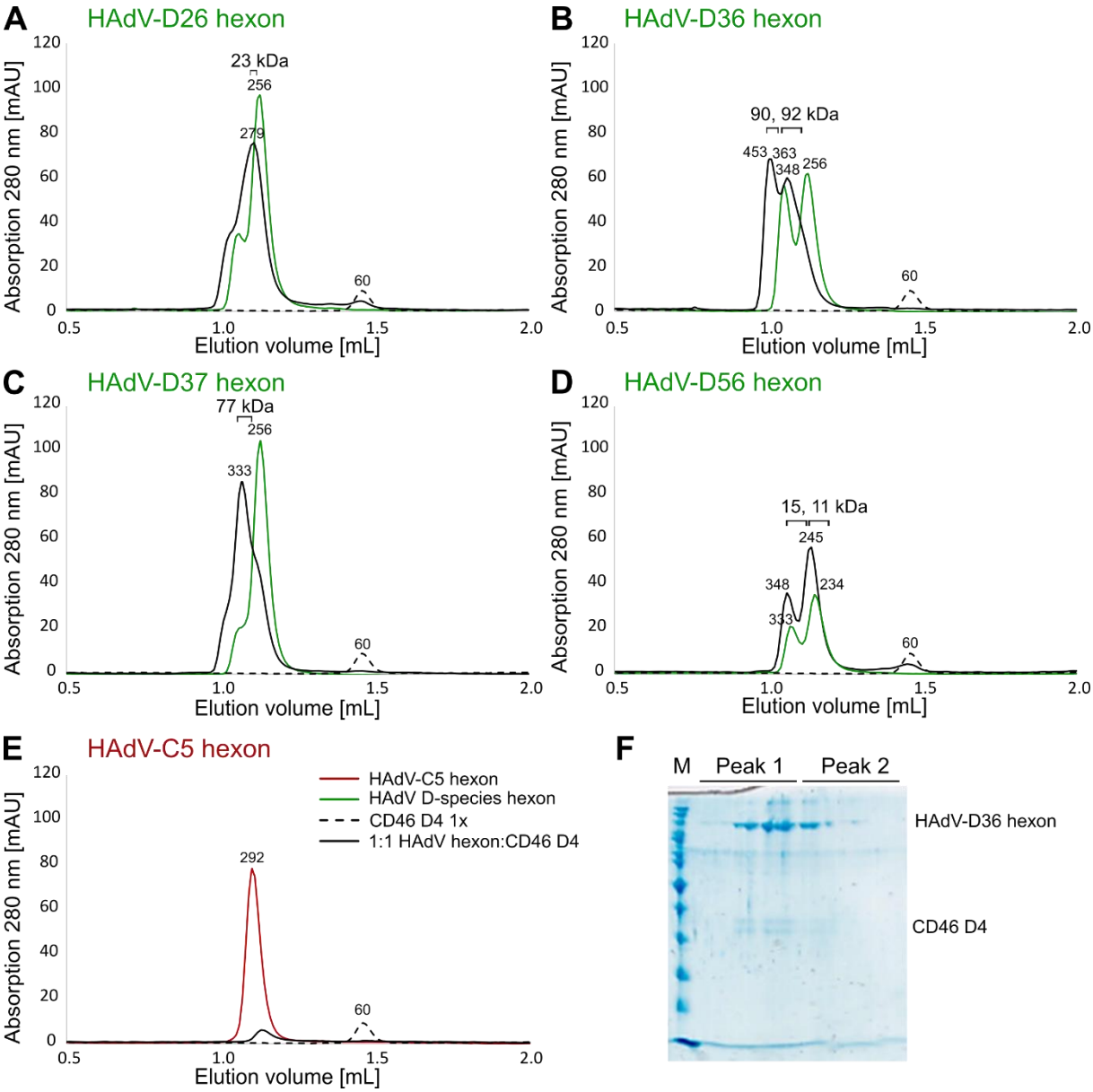

Figure C.9: Analytical SEC of HAdV hexons with CD46 D4. (**A**-**D**) Initial analytical SEC experiments to establish complex formation between HAdV D-species hexons and CD46 D4. Hexon samples and CD46 D4 were mixed in a 1:1 ratio in the presence of 5 mM $CaCl_2$ and incubated overnight. A 1:1 ratio equals one molecule CD46 D4 per hexon trimer, therefore likely not fully saturating the putative complex. Samples were run on a Superdex™ 200 Increase 3.2/300 column to achieve optimal separation of hexon and complex samples. While both HAdV-D36 and HAdV-D37 hexons display significant shifts upon interaction with CD46 D4, the peak shifts are subtler for HAdV-D26 and HAdV-D56. (**E**) During the control runs with HAdV-C5 hexon, the mixed sample of the hexon and CD46 D4 was lost due to a faulty circuit of a valve in the Äkta Micro Ettan LC system. (**F**) The complex between HAdV-D36 and CD46 D4 was the only one that could be confirmed by SDS-PAGE due to the small amounts of protein loaded for analytical SEC. M = marker.

D. References

[1] J. Szymański, J. Janikiewicz, B. Michalska, P. Patalas-Krawczyk, M. Perrone, W. Ziółkowski, J. Duszyński, P. Pinton, A. Dobrzyń, and M. R. Więckowski, "Interaction of Mitochondria with the Endoplasmic Reticulum and Plasma Membrane in Calcium Homeostasis, Lipid Trafficking and Mitochondrial Structure.," *Int. J. Mol. Sci.*, vol. 18, no. 7, Jul. 2017, doi: 10.3390/ijms18071576.

[2] D. Hockenbery, G. Nuñez, C. Milliman, R. D. Schreiber, and S. J. Korsmeyer, "Bcl-2 is an inner mitochondrial membrane protein that blocks programmed cell death.," *Nature*, vol. 348, no. 6299, pp. 334–336, Nov. 1990, doi: 10.1038/348334a0.

[3] M. R. Lewis and W. H. Lewis, "Mitochondria in Tissue Culture," *Science (80-.).*, vol. 39, no. 1000, pp. 330–333, Feb. 1914, doi: 10.1126/science.39.1000.330.

[4] J. Bereiter-Hahn and M. Vöth, "Dynamics of mitochondria in living cells: shape changes, dislocations, fusion, and fission of mitochondria.," *Microsc. Res. Tech.*, vol. 27, no. 3, pp. 198–219, Feb. 1994, doi: 10.1002/jemt.1070270303.

[5] P. Mishra and D. C. Chan, "Mitochondrial dynamics and inheritance during cell division, development and disease.," *Nat. Rev. Mol. Cell Biol.*, vol. 15, no. 10, pp. 634–646, Oct. 2014, doi: 10.1038/nrm3877.

[6] C. A. Mannella, "The relevance of mitochondrial membrane topology to mitochondrial function.," *Biochim. Biophys. Acta*, vol. 1762, no. 2, pp. 140–147, Feb. 2006, doi: 10.1016/j.bbadis.2005.07.001.

[7] C. A. Mannella, "Structure and dynamics of the mitochondrial inner membrane cristae.," *Biochim. Biophys. Acta*, vol. 1763, no. 5–6, pp. 542–548, 2006, doi: 10.1016/j.bbamcr.2006.04.006.

[8] E. Fernández-Vizarra, J. A. Enríquez, A. Pérez-Martos, J. Montoya, and P. Fernández-Silva, "Tissue-specific differences in mitochondrial activity and biogenesis," *Mitochondrion*, vol. 11, no. 1, pp. 207–213, 2011, doi: 10.1016/j.mito.2010.09.011.

[9] S. C. Leary, B. J. Battersby, and C. D. Moyes, "Inter-tissue differences in mitochondrial enzyme activity, RNA and DNA in rainbow trout (Oncorhynchus mykiss)," *J. Exp. Biol.*, vol. 201, no. 24, pp. 3377–3384, 1998, doi: 10.1242/jeb.201.24.3377.

[10] A. Melkov and U. Abdu, "Regulation of long-distance transport of mitochondria along microtubules," *Cell. Mol. Life Sci.*, vol. 75, no. 2, pp. 163–176, 2018, doi: 10.1007/s00018-017-2590-1.

[11] R. L. Morris and P. J. Hollenbeck, "The regulation of bidirectional mitochondrial transport is coordinated with axonal outgrowth.," *J. Cell Sci.*, vol. 104 (Pt 3, pp. 917–927, Mar. 1993.

[12] S. R. Heidemann, J. M. Landers, and M. A. Hamborg, "Polarity orientation of axonal microtubules.," *J. Cell Biol.*, vol. 91, no. 3 Pt 1, pp. 661–665, Dec. 1981, doi: 10.1083/jcb.91.3.661.

[13] P. R. Burton and J. L. Paige, "Polarity of axoplasmic microtubules in the olfactory nerve of the frog.," *Proc. Natl. Acad. Sci. U. S. A.*, vol. 78, no. 5, pp. 3269–3273, May 1981, doi: 10.1073/pnas.78.5.3269.

[14] P. W. Baas, J. S. Deitch, M. M. Black, and G. A. Banker, "Polarity orientation of microtubules in hippocampal neurons: uniformity in the axon and nonuniformity in the dendrite.," *Proc. Natl. Acad. Sci. U. S. A.*, vol. 85, no. 21, pp. 8335–8339, Nov. 1988, doi: 10.1073/pnas.85.21.8335.

[15] M. C. Stone, F. Roegiers, and M. M. Rolls, "Microtubules have opposite orientation in axons and dendrites of Drosophila neurons.," *Mol. Biol. Cell*, vol. 19, no. 10, pp. 4122–4129, Oct. 2008, doi: 10.1091/mbc.e07-10-1079.

[16] S. Deheshi, B. A. Pasqualotto, and G. L. Rintoul, "Mitochondrial trafficking in neuropsychiatric diseases.," *Neurobiol. Dis.*, vol. 51, pp. 66–71, Mar. 2013, doi: 10.1016/j.nbd.2012.06.015.

[17] A. Bose and M. F. Beal, "Mitochondrial dysfunction in Parkinson's disease.," *J. Neurochem.*, vol. 139 Suppl, pp. 216–231, Oct. 2016, doi: 10.1111/jnc.13731.

[18] J. Johnson, E. Mercado-Ayon, Y. Mercado-Ayon, Y. N. Dong, S. Halawani, L. Ngaba, and D. R. Lynch, "Mitochondrial dysfunction in the development and progression of neurodegenerative diseases.," *Arch. Biochem. Biophys.*, vol. 702, p. 108698, May 2021, doi: 10.1016/j.abb.2020.108698.

[19] R. D. Allen, J. Metuzals, I. Tasaki, S. T. Brady, and S. P. Gilbert, "Fast axonal transport in squid giant axon.," *Science*, vol. 218, no. 4577, pp. 1127–1129, Dec. 1982, doi: 10.1126/science.6183744.

[20] P. J. Hollenbeck, “The pattern and mechanism of mitochondrial transport in axons.,” *Front. Biosci.*, vol. 1, pp. d91-102, Jul. 1996, doi: 10.2741/a118.

[21] X. Wang and T. L. Schwarz, “The Mechanism of Ca 2 + -Dependent Regulation of Kinesin-Mediated Mitochondrial Motility,” *Cell*, vol. 136, pp. 1–13, 2009.

[22] Y. Chen and Z. H. Sheng, “Kinesin-1-syntaphilin coupling mediates activity-dependent regulation of axonal mitochondrial transport,” *J. Cell Biol.*, vol. 202, no. 2, pp. 351–364, 2013, doi: 10.1083/jcb.201302040.

[23] M. Yi, D. Weaver, and G. Hajnóczky, “Control of mitochondrial motility and distribution by the calcium signal: A homeostatic circuit,” *J. Cell Biol.*, vol. 167, no. 4, pp. 661–672, 2004, doi: 10.1083/jcb.200406038.

[24] D. T. W. Chang and I. J. Reynolds, “Differences in mitochondrial movement and morphology in young and mature primary cortical neurons in culture.,” *Neuroscience*, vol. 141, no. 2, pp. 727–736, Aug. 2006, doi: 10.1016/j.neuroscience.2006.01.034.

[25] M. van Spronsen, M. Mikhaylova, J. Lipka, M. A. Schlager, D. J. van den Heuvel, M. Kuijpers, P. S. Wulf, N. Keijzer, J. Demmers, L. C. Kapitein, D. Jaarsma, H. C. Gerritsen, A. Akhmanova, and C. C. Hoogenraad, “TRAK/Milton Motor-Adaptor Proteins Steer Mitochondrial Trafficking to Axons and Dendrites,” *Neuron*, vol. 77, no. 3, pp. 485–502, 2013, doi: 10.1016/j.neuron.2012.11.027.

[26] O. A. Quintero, M. M. DiVito, R. C. Adikes, M. B. Kortan, L. B. Case, A. J. Lier, N. S. Panaretos, S. Q. Slater, M. Rengarajan, M. Feliu, and R. E. Cheney, “Human Myo19 Is a Novel Myosin that Associates with Mitochondria,” *Curr. Biol.*, vol. 19, no. 23, pp. 2008–2013, 2009, doi: 10.1016/j.cub.2009.10.026.

[27] J. L. Bocanegra, B. M. Fujita, N. R. Melton, J. M. Cowan, E. L. Schinski, T. Y. Tamir, M. B. Major, and O. A. Quintero, “The MyMOMA domain of MYO19 encodes for distinct Miro-dependent and Miro-independent mechanisms of interaction with mitochondrial membranes,” *Cytoskeleton*, vol. 77, no. 3–4, pp. 149–166, 2020, doi: 10.1002/cm.21560.

[28] G. López-Doménech, C. Covill-Cooke, D. Ivankovic, E. F. Halff, D. F. Sheehan, R. Norkett, N. Birsa, and J. T. Kittler, “Miro proteins coordinate microtubule- and actin-dependent mitochondrial transport and distribution,” *EMBO J.*, vol. 37, no. 3, pp. 321–336, 2018, doi: 10.15252/embj.201696380.

[29] A. F. MacAskill, J. E. Rinholm, A. E. Twelvetrees, I. L. Arancibia-Carcamo, J. Muir, A. Fransson, P. Aspenstrom, D. Attwell, and J. T. Kittler, “Miro1 Is a Calcium Sensor for Glutamate Receptor-Dependent Localization of Mitochondria at Synapses,” *Neuron*, vol. 61, no. 4, pp. 541–555, 2009, doi: 10.1016/j.neuron.2009.01.030.

[30] Å. Fransson, A. Ruusala, and P. Aspenström, “Atypical Rho GTPases have roles in mitochondrial homeostasis and apoptosis,” *J. Biol. Chem.*, vol. 278, no. 8, pp. 6495–6502, 2003, doi: 10.1074/jbc.M208609200.

[31] K. Brickley, M. J. Smith, M. Beck, and F. A. Stephenson, “GRIF-1 and OIP106, members of a novel gene family of coiled-coil domain proteins: Association in vivo and in vitro with kinesin,” *J. Biol. Chem.*, vol. 280, no. 15, pp. 14723–14732, 2005, doi: 10.1074/jbc.M409095200.

[32] M. J. Smith, K. Pozo, K. Brickley, and F. A. Stephenson, “Mapping the GRIF-1 binding domain of the kinesin, KIF5C, substantiates a role for GRIF-1 as an adaptor protein in the anterograde trafficking of cargoes,” *J. Biol. Chem.*, vol. 281, no. 37, pp. 27216–27228, 2006, doi: 10.1074/jbc.M600522200.

[33] J. S. Kang, J. H. Tian, P. Y. Pan, P. Zald, C. Li, C. Deng, and Z. H. Sheng, “Docking of Axonal Mitochondria by Syntaphilin Controls Their Mobility and Affects Short-Term Facilitation,” *Cell*, vol. 132, no. 1, pp. 137–148, 2008, doi: 10.1016/j.cell.2007.11.024.

[34] S. J. Oeding, K. Majstrowicz, X. P. Hu, V. Schwarz, A. Freitag, U. Honnert, P. Nikolaus, and M. Bähler, “Identification of Miro1 and Miro2 as mitochondrial receptors for myosin XIX,” *J. Cell Sci.*, vol. 131, no. 17, 2018, doi: 10.1242/jcs.219469.

[35] V. Henrichs, L. Grycova, C. Barinka, Z. Nahacka, J. Neuzil, S. Diez, J. Rohlena, M. Braun, and Z. Lansky, “Mitochondria-adaptor TRAK1 promotes kinesin-1 driven transport in crowded environments,” *Nat. Commun.*, vol. 11, no. 1, pp. 1–44, 2020, doi: 10.1038/s41467-020-16972-5.

[36] E. E. Glater, L. J. Megeath, R. S. Stowers, and T. L. Schwarz, “Axonal transport of mitochondria requires milton to recruit kinesin heavy chain and is light chain independent,” *J. Cell Biol.*, vol. 173, no. 4, pp. 545–557, 2006, doi: 10.1083/jcb.200601067.

[37] G. López-Doménech, N. F. Higgs, V. Vaccaro, H. Roš, I. L. Arancibia-Cárcamo, A. F. MacAskill, and J. T. Kittler, “Loss of Dendritic Complexity Precedes Neurodegeneration in a Mouse Model with Disrupted Mitochondrial Distribution in Mature Dendrites.,” *Cell Rep.*, vol. 17, no. 2, pp. 317–327, Oct. 2016, doi: 10.1016/j.celrep.2016.09.004.

[38] A. Misko, S. Jiang, I. Wegorzewska, J. Milbrandt, and R. H. Baloh, “Mitofusin 2 is necessary for transport of axonal mitochondria and interacts with the Miro/Milton complex,” *J. Neurosci.*, vol. 30, no. 12, pp. 4232–4240, 2010, doi: 10.1523/JNEUROSCI.6248-09.2010.

[39] C. A. Lee, L.-S. Chin, and L. Li, “Hypertonia-linked protein Trak1 functions with mitofusins to promote mitochondrial tethering and fusion.,” *Protein Cell*, vol. 9, no. 8, pp. 693–716, Aug. 2018, doi: 10.1007/s13238-017-0469-4.

[40] J. L. Klosowiak, S. Park, K. P. Smith, M. E. French, P. J. Focia, D. M. Freymann, and S. E. Rice, “Structural insights into Parkin substrate lysine targeting from minimal Miro substrates,” *Sci. Rep.*, vol. 6, no. April, pp. 1–13, 2016, doi: 10.1038/srep33019.

[41] K. P. Smith, P. J. Focia, S. Chakravarthy, E. C. Landahl, J. L. Klosowiak, S. E. Rice, and D. M. Freymann, “Insight into human Miro1/2 domain organization based on the structure of its N-terminal GTPase,” *J. Struct. Biol.*, 2020, doi: 10.1016/j.jsb.2020.107656.

[42] P. Aspenström, A. Fransson, and J. Saras, “Rho GTPases have diverse effects on the organization of the actin filament system.,” *Biochem. J.*, vol. 377, no. Pt 2, pp. 327–337, Jan. 2004, doi: 10.1042/BJ20031041.

[43] K. Wennerberg and C. J. Der, “Rho-family GTPases: it’s not only Rac and Rho (and I like it).,” *J. Cell Sci.*, vol. 117, no. Pt 8, pp. 1301–1312, Mar. 2004, doi: 10.1242/jcs.01118.

[44] D. T. Peters, L. Kay, J. Eswaran, J. H. Lakey, and M. Soundararajan, “Human miro proteins act as NTP hydrolases through a novel, non-canonical catalytic mechanism,” *Int. J. Mol. Sci.*, 2018, doi: 10.3390/ijms19123839.

[45] J. L. Klosowiak, P. J. Focia, S. Chakravarthy, E. C. Landahl, D. M. Freymann, and S. E. Rice, “Structural coupling of the EF hand and C-terminal GTPase domains in the mitochondrial protein Miro,” *EMBO Rep.*, vol. 14, no. 11, pp. 968–974, 2013, doi: 10.1038/embor.2013.151.

[46] P. O. Heidarsson, I. J. Bjerrum-Bohr, G. A. Jensen, O. Pongs, B. E. Finn, F. M. Poulsen, and B. B. Kragelund, “The C-terminal tail of human neuronal calcium sensor 1 regulates the conformational stability of the Ca2+-activated state,” *J. Mol. Biol.*, vol. 417, no. 1–2, pp. 51–64, 2012, doi: 10.1016/j.jmb.2011.12.049.

[47] T. Koshiba, H. A. Holman, K. Kubara, K. Yasukawa, S. I. Kawabata, K. Okamoto, J. Macfarlane, and J. M. Shaw, “Structure-function analysis of the yeast mitochondrial Rho GTPase, Gem1p: Implications for mitochondrial inheritance,” *J. Biol. Chem.*, vol. 286, no. 1, pp. 354–362, 2011, doi: 10.1074/jbc.M110.180034.

[48] M. Saotome, D. Safiulina, G. Szabadkai, S. Das, Å. Fransson, P. Aspenstrom, R. Rizzuto, and G. Hajnóczky, “Bidirectional Ca2+-dependent control of mitochondrial dynamics by the Miro GTPase,” *Proc. Natl. Acad. Sci. U. S. A.*, vol. 105, no. 52, pp. 20728–20733, 2008, doi: 10.1073/pnas.0808953105.

[49] S. Modi, G. López-Doménech, E. F. Halff, C. Covill-Cooke, D. Ivankovic, D. Melandri, I. L. Arancibia-Cárcamo, J. J. Burden, A. R. Lowe, and J. T. Kittler, “Miro clusters regulate ER-mitochondria contact sites and link cristae organization to the mitochondrial transport machinery,” *Nat. Commun.*, vol. 10, no. 1, pp. 17–19, 2019, doi: 10.1038/s41467-019-12382-4.

[50] R. S. Stowers, L. J. Megeath, J. Górska-Andrzejak, I. A. Meinertzhagen, and T. L. Schwarz, “Axonal transport of mitochondria to synapses depends on Milton, a novel Drosophila protein,” *Neuron*, vol. 36, no. 6, pp. 1063–1077, 2002, doi: 10.1016/S0896-6273(02)01094-2.

[51] S. P. N. Iyer, Y. Akimoto, and G. W. Hart, “Identification and cloning of a novel family of coiled-coil domain proteins that interact with O-GlcNac transferase,” *J. Biol. Chem.*, vol. 278, no. 7, pp. 5399–5409, 2003, doi: 10.1074/jbc.M209384200.

[52] M. Beck, K. Brickley, H. L. Wilkinson, S. Sharma, M. Smith, P. L. Chazot, S. Pollard, and F. A. Stephenson, "Identification, molecular cloning, and characterization of a novel GABAA receptor-associated protein, GRIF-1.," *J. Biol. Chem.*, vol. 277, no. 33, pp. 30079–30090, 2002, doi: 10.1074/jbc.M200438200.

[53] S. P. N. Iyer and G. W. Hart, "Roles of the Tetratricopeptide Repeat Domain in O-GlcNAc Transferase Targeting and Protein Substrate Specificity," *J. Biol. Chem.*, vol. 278, no. 27, pp. 24608–24616, 2003, doi: 10.1074/jbc.M300036200.

[54] M. Varadi, S. Anyango, M. Deshpande, S. Nair, C. Natassia, G. Yordanova, D. Yuan, O. Stroe, G. Wood, A. Laydon, A. Žídek, T. Green, K. Tunyasuvunakool, S. Petersen, J. Jumper, E. Clancy, R. Green, A. Vora, M. Lutfi, *et al.*, "AlphaFold Protein Structure Database: massively expanding the structural coverage of protein-sequence space with high-accuracy models," *Nucleic Acids Res.*, vol. 50, no. D1, pp. D439–D444, 2022, doi: 10.1093/nar/gkab1061.

[55] J. Jumper, R. Evans, A. Pritzel, T. Green, M. Figurnov, O. Ronneberger, K. Tunyasuvunakool, R. Bates, A. Žídek, A. Potapenko, A. Bridgland, C. Meyer, S. A. A. Kohl, A. J. Ballard, A. Cowie, B. Romera-Paredes, S. Nikolov, R. Jain, J. Adler, *et al.*, "Highly accurate protein structure prediction with AlphaFold," *Nature*, vol. 596, no. 7873, pp. 583–589, 2021, doi: 10.1038/s41586-021-03819-2.

[56] Å. Fransson, A. Ruusala, and P. Aspenström, "The atypical Rho GTPases Miro-1 and Miro-2 have essential roles in mitochondrial trafficking," *Biochem. Biophys. Res. Commun.*, vol. 344, no. 2, pp. 500–510, 2006, doi: 10.1016/j.bbrc.2006.03.163.

[57] A. F. MacAskill, K. Brickley, F. A. Stephenson, and J. T. Kittler, "GTPase dependent recruitment of Grif-1 by Miro1 regulates mitochondrial trafficking in hippocampal neurons," *Mol. Cell. Neurosci.*, vol. 40, no. 3, pp. 301–312, 2009, doi: 10.1016/j.mcn.2008.10.016.

[58] C. Ott, K. Ross, S. Straub, B. Thiede, M. Götz, C. Goosmann, M. Krischke, M. J. Mueller, G. Krohne, T. Rudel, and V. Kozjak-Pavlovic, "Sam50 functions in mitochondrial intermembrane space bridging and biogenesis of respiratory complexes.," *Mol. Cell. Biol.*, vol. 32, no. 6, pp. 1173–1188, Mar. 2012, doi: 10.1128/MCB.06388-11.

[59] V. Kozjak-Pavlovic, "The MICOS complex of human mitochondria.," *Cell Tissue Res.*, vol. 367, no. 1, pp. 83–93, Jan. 2017, doi: 10.1007/s00441-016-2433-7.

[60] M. Darshi, K. N. Trinh, A. N. Murphy, and S. S. Taylor, "Targeting and import mechanism of coiled-coil helix coiled-coil helix domain-containing protein 3 (ChChd3) into the mitochondrial intermembrane space.," *J. Biol. Chem.*, vol. 287, no. 47, pp. 39480–39491, Nov. 2012, doi: 10.1074/jbc.M112.387696.

[61] R. L. Frederick and J. M. Shaw, "Moving mitochondria: Establishing distribution of an essential organelle," *Traffic*, vol. 8, no. 12, pp. 1668–1675, 2007, doi: 10.1111/j.1600-0854.2007.00644.x.

[62] J. Xie, M. F. Marusich, P. Souda, J. Whitelegge, and R. A. Capaldi, "The mitochondrial inner membrane protein mitofilin exists as a complex with SAM50, metaxins 1 and 2, coiled-coil-helix coiled-coil-helix domain-containing protein 3 and 6 and DnaJC11.," *FEBS Lett.*, vol. 581, no. 18, pp. 3545–3549, Jul. 2007, doi: 10.1016/j.febslet.2007.06.052.

[63] S. A. Paschen, T. Waizenegger, T. Stan, M. Preuss, M. Cyrklaff, K. Hell, D. Rapaport, and W. Neupert, "Evolutionary conservation of biogenesis of beta-barrel membrane proteins.," *Nature*, vol. 426, no. 6968, pp. 862–866, Dec. 2003, doi: 10.1038/nature02208.

[64] N. Wiedemann, V. Kozjak, A. Chacinska, B. Schönfisch, S. Rospert, M. T. Ryan, N. Pfanner, and C. Meisinger, "Machinery for protein sorting and assembly in the mitochondrial outer membrane.," *Nature*, vol. 424, no. 6948, pp. 565–571, Jul. 2003, doi: 10.1038/nature01753.

[65] Z. Yu, K. SoHee, Y. Teppei, C. Fabien, R. Sophie, K. Michaela, C. Chun, L. Na, C. Hwei-Ling, C. Katrin, L. David, M. Adam, M. Gabriele, A. F. W., K. Saadi, and M. Patrick, "Mice Lacking Histone Deacetylase 6 Have Hyperacetylated Tubulin but Are Viable and Develop Normally," *Mol. Cell. Biol.*, vol. 28, no. 5, pp. 1688–1701, Mar. 2008, doi: 10.1128/MCB.01154-06.

[66] C. Hubbert, A. Guardiola, R. Shao, Y. Kawaguchi, A. Ito, A. Nixon, M. Yoshida, X.-F. Wang, and T.-P. Yao, "HDAC6 is a microtubule-associated deacetylase.," *Nature*, vol. 417, no. 6887, pp. 455–458, May 2002, doi: 10.1038/417455a.

[67] A. Lahm, P. C., P. M., N. M. C., J. P., N. P., S. S., B. M. J., L. S. P., C. A., K. U., D. F. R., S. C., and G. P., "Unraveling the hidden catalytic activity of vertebrate class IIa histone deacetylases," *Proc. Natl. Acad. Sci.*, vol. 104, no. 44, pp. 17335–17340, Oct. 2007, doi: 10.1073/pnas.0706487104.

[68] M. A. Rivieccio, B. Camille, W. D. E., W. B. A., D. M. A., M. Kathryn, S. Ambreena, K. A. P., J. S. R., T. J. L., R. R. R., and L. Brett, "HDAC6 is a target for protection and regeneration following injury in the nervous system," *Proc. Natl. Acad. Sci.*, vol. 106, no. 46, pp. 19599–19604, Nov. 2009, doi: 10.1073/pnas.0907935106.

[69] V. S. C. Wong, C. Picci, M. Swift, M. Levinson, D. Willis, and B. Langley, "α-Tubulin Acetyltransferase Is a Novel Target Mediating Neurite Growth Inhibitory Effects of Chondroitin Sulfate Proteoglycans and Myelin-Associated Glycoprotein.," *eNeuro*, vol. 5, no. 1, 2018, doi: 10.1523/ENEURO.0240-17.2018.

[70] R. Schweigreiter, A. R. Walmsley, B. Niederöst, D. R. Zimmermann, T. Oertle, E. Casademunt, S. Frentzel, G. Dechant, A. Mir, and C. E. Bandtlow, "Versican V2 and the central inhibitory domain of Nogo-A inhibit neurite growth via p75NTR/NgR-independent pathways that converge at RhoA.," *Mol. Cell. Neurosci.*, vol. 27, no. 2, pp. 163–174, Oct. 2004, doi: 10.1016/j.mcn.2004.06.004.

[71] A. L. Kalinski, A. N. Kar, J. Craver, A. P. Tosolini, J. N. Sleigh, S. J. Lee, A. Hawthorne, P. Brito-Vargas, S. Miller-Randolph, R. Passino, L. Shi, V. S. C. Wong, C. Picci, D. S. Smith, D. E. Willis, L. A. Havton, G. Schiavo, R. J. Giger, B. Langley, *et al.*, "Deacetylation of Miro1 by HDAC6 blocks mitochondrial transport and mediates axon growth inhibition," *J. Cell Biol.*, vol. 218, no. 6, 2019, doi: 10.1083/jcb.201702187.

[72] J. W. Hammond, K. Griffin, G. T. Jih, J. Stuckey, and K. J. Verhey, "Co-operative versus independent transport of different cargoes by Kinesin-1.," *Traffic*, vol. 9, no. 5, pp. 725–741, May 2008, doi: 10.1111/j.1600-0854.2008.00722.x.

[73] A. Lundby, K. Lage, B. T. Weinert, D. B. Bekker-Jensen, A. Secher, T. Skovgaard, C. D. Kelstrup, A. Dmytriyev, C. Choudhary, C. Lundby, and J. V Olsen, "Proteomic analysis of lysine acetylation sites in rat tissues reveals organ specificity and subcellular patterns.," *Cell Rep.*, vol. 2, no. 2, pp. 419–431, Aug. 2012, doi: 10.1016/j.celrep.2012.07.006.

[74] C. Choudhary, C. Kumar, F. Gnad, M. L. Nielsen, M. Rehman, T. C. Walther, J. V Olsen, and M. Mann, "Lysine acetylation targets protein complexes and co-regulates major cellular functions.," *Science*, vol. 325, no. 5942, pp. 834–840, Aug. 2009, doi: 10.1126/science.1175371.

[75] M. Fransen, C. Lismont, and P. Walton, "The Peroxisome-Mitochondria Connection: How and Why?," *Int. J. Mol. Sci.*, vol. 18, no. 6, May 2017, doi: 10.3390/ijms18061126.

[76] K. Okumoto, T. Ono, R. Toyama, A. Shimomura, A. Nagata, and Y. Fujiki, "New splicing variants of mitochondrial Rho GTPase-1 (Miro1) transport peroxisomes.," *J. Cell Biol.*, vol. 217, no. 2, pp. 619–633, Feb. 2018, doi: 10.1083/jcb.201708122.

[77] K. Götte, W. Girzalsky, M. Linkert, E. Baumgart, S. Kammerer, W. H. Kunau, and R. Erdmann, "Pex19p, a farnesylated protein essential for peroxisome biogenesis.," *Mol. Cell. Biol.*, vol. 18, no. 1, pp. 616–628, Jan. 1998, doi: 10.1128/MCB.18.1.616.

[78] I. G. Castro, D. M. Richards, J. Metz, J. L. Costello, J. B. Passmore, T. A. Schrader, A. Gouveia, D. Ribeiro, and M. Schrader, "A role for Mitochondrial Rho GTPase 1 (MIRO1) in motility and membrane dynamics of peroxisomes.," *Traffic*, vol. 19, no. 3, pp. 229–242, Mar. 2018, doi: 10.1111/tra.12549.

[79] D. Dietrich, F. Seiler, F. Essmann, and G. Dodt, "Identification of the kinesin KifC3 as a new player for positioning of peroxisomes and other organelles in mammalian cells.," *Biochim. Biophys. Acta*, vol. 1833, no. 12, pp. 3013–3024, Dec. 2013, doi: 10.1016/j.bbamcr.2013.08.002.

[80] R. J. Youle and A. M. van der Bliek, "Mitochondrial fission, fusion, and stress.," *Science*, vol. 337, no. 6098, pp. 1062–1065, Aug. 2012, doi: 10.1126/science.1219855.

[81] H. Chen, A. Chomyn, and D. C. Chan, "Disruption of fusion results in mitochondrial heterogeneity and dysfunction.," *J. Biol. Chem.*, vol. 280, no. 28, pp. 26185–26192, Jul. 2005, doi: 10.1074/jbc.M503062200.

[82] H. Chen and D. C. Chan, "Physiological functions of mitochondrial fusion.," *Ann. N. Y. Acad. Sci.*, vol. 1201, pp. 21–25, Jul. 2010, doi: 10.1111/j.1749-6632.2010.05615.x.

[83] R. L. Frederick, J. M. McCaffery, K. W. Cunningham, K. Okamoto, and J. M. Shaw, “Yeast Miro GTPase, Gem1p, regulates mitochondrial morphology via a novel pathway,” *J. Cell Biol.*, vol. 167, no. 1, pp. 87–98, 2004, doi: 10.1083/jcb.200405100.

[84] G. J. Russo, K. Louie, A. Wellington, G. T. Macleod, F. Hu, S. Panchumarthi, and K. E. Zinsmaier, “Drosophila Miro is required for both anterograde and retrograde axonal mitochondrial transport,” *J. Neurosci.*, vol. 29, no. 17, pp. 5443–5455, 2009, doi: 10.1523/JNEUROSCI.5417-08.2009.

[85] C. Covill-Cooke, V. S. Toncheva, J. Drew, N. Birsa, G. López-Doménech, and J. T. Kittler, “Peroxisomal fission is modulated by the mitochondrial Rho-GTPases, Miro1 and Miro2,” *EMBO Rep.*, vol. 21, no. 2, p. e49865, Feb. 2020, doi: https://doi.org/10.15252/embr.201949865.

[86] W. Bernhard and C. Rouiller, “Close topographical relationship between mitochondria and ergastoplasm of liver cells in a definite phase of cellular activity.,” *J. Biophys. Biochem. Cytol.*, vol. 2, no. 4 Suppl, pp. 73–78, Jul. 1956, doi: 10.1083/jcb.2.4.73.

[87] M. Eisenberg-Bord, N. Shai, M. Schuldiner, and M. Bohnert, “A Tether Is a Tether Is a Tether: Tethering at Membrane Contact Sites.,” *Dev. Cell*, vol. 39, no. 4, pp. 395–409, Nov. 2016, doi: 10.1016/j.devcel.2016.10.022.

[88] A. H. Michel and B. Kornmann, “The ERMES complex and ER-mitochondria connections.,” *Biochem. Soc. Trans.*, vol. 40, no. 2, pp. 445–450, Apr. 2012, doi: 10.1042/BST20110758.

[89] B. Kornmann, E. Currie, S. R. Collins, M. Schuldiner, J. Nunnari, J. S. Weissman, and P. Walter, “An ER-mitochondria tethering complex revealed by a synthetic biology screen.,” *Science*, vol. 325, no. 5939, pp. 477–481, Jul. 2009, doi: 10.1126/science.1175088.

[90] B. Kornmann, C. Osman, and P. Walter, “The conserved GTPase Gem1 regulates endoplasmic reticulum-mitochondria connections.,” *Proc. Natl. Acad. Sci. U. S. A.*, vol. 108, no. 34, pp. 14151–14156, Aug. 2011, doi: 10.1073/pnas.1111314108.

[91] D. A. Stroud, S. Oeljeklaus, S. Wiese, M. Bohnert, U. Lewandrowski, A. Sickmann, B. Guiard, M. van der Laan, B. Warscheid, and N. Wiedemann, “Composition and topology of the endoplasmic reticulum-mitochondria encounter structure.,” *J. Mol. Biol.*, vol. 413, no. 4, pp. 743–750, Nov. 2011, doi: 10.1016/j.jmb.2011.09.012.

[92] R. Norkett, S. Modi, N. Birsa, T. A. Atkin, D. Ivankovic, M. Pathania, S. V Trossbach, C. Korth, W. D. Hirst, and J. T. Kittler, “DISC1-dependent Regulation of Mitochondrial Dynamics Controls the Morphogenesis of Complex Neuronal Dendrites.,” *J. Biol. Chem.*, vol. 291, no. 2, pp. 613–629, Jan. 2016, doi: 10.1074/jbc.M115.699447.

[93] Y.-U. Park, J. Jeong, H. Lee, J. Y. Mun, J.-H. Kim, J. S. Lee, M. D. Nguyen, S. S. Han, P.-G. Suh, and S. K. Park, “Disrupted-in-schizophrenia 1 (DISC1) plays essential roles in mitochondria in collaboration with Mitofilin.,” *Proc. Natl. Acad. Sci. U. S. A.*, vol. 107, no. 41, pp. 17785–17790, Oct. 2010, doi: 10.1073/pnas.1004361107.

[94] S. J. Park, J. Jeong, Y.-U. Park, K.-S. Park, H. Lee, N. Lee, S.-M. Kim, K. Kuroda, M. D. Nguyen, K. Kaibuchi, and S. K. Park, “Disrupted-in-schizophrenia-1 (DISC1) Regulates Endoplasmic Reticulum Calcium Dynamics.,” *Sci. Rep.*, vol. 5, p. 8694, Mar. 2015, doi: 10.1038/srep08694.

[95] K. Palikaras, E. Lionaki, and N. Tavernarakis, “Mechanisms of mitophagy in cellular homeostasis, physiology and pathology.,” *Nat. Cell Biol.*, vol. 20, no. 9, pp. 1013–1022, Sep. 2018, doi: 10.1038/s41556-018-0176-2.

[96] L. Galluzzi, I. Vitale, S. A. Aaronson, J. M. Abrams, D. Adam, P. Agostinis, E. S. Alnemri, L. Altucci, I. Amelio, D. W. Andrews, M. Annicchiarico-Petruzzelli, A. V Antonov, E. Arama, E. H. Baehrecke, N. A. Barlev, N. G. Bazan, F. Bernassola, M. J. M. Bertrand, K. Bianchi, *et al.*, “Molecular mechanisms of cell death: recommendations of the Nomenclature Committee on Cell Death 2018.,” *Cell Death Differ.*, vol. 25, no. 3, pp. 486–541, Mar. 2018, doi: 10.1038/s41418-017-0012-4.

[97] S. Pickles, P. Vigié, and R. J. Youle, “Mitophagy and Quality Control Mechanisms in Mitochondrial Maintenance.,” *Curr. Biol.*, vol. 28, no. 4, pp. R170–R185, Feb. 2018, doi: 10.1016/j.cub.2018.01.004.

[98] M. Lazarou, S. M. Jin, L. A. Kane, and R. J. Youle, “Role of PINK1 binding to the TOM complex and alternate intracellular membranes in recruitment and activation of the E3 ligase Parkin.,” *Dev. Cell*, vol. 22, no. 2, pp. 320–333, Feb. 2012, doi: 10.1016/j.devcel.2011.12.014.

[99] E. Deas, H. Plun-Favreau, S. Gandhi, H. Desmond, S. Kjaer, S. H. Y. Loh, A. E. M. Renton, R. J. Harvey, A. J. Whitworth, L. M. Martins, A. Y. Abramov, and N. W. Wood, "PINK1 cleavage at position A103 by the mitochondrial protease PARL.," *Hum. Mol. Genet.*, vol. 20, no. 5, pp. 867–879, Mar. 2011, doi: 10.1093/hmg/ddq526.

[100] Z. Y. Gan, S. Callegari, S. A. Cobbold, T. R. Cotton, M. J. Mlodzianoski, A. F. Schubert, N. D. Geoghegan, K. L. Rogers, A. Leis, G. Dewson, A. Glukhova, and D. Komander, "Activation mechanism of PINK1.," *Nature*, vol. 602, no. 7896, pp. 328–335, Feb. 2022, doi: 10.1038/s41586-021-04340-2.

[101] Z. Yi, G. Jun, C. K. K. K., H. Hui, D. V. L., and D. T. M., "Parkin functions as an E2-dependent ubiquitin– protein ligase and promotes the degradation of the synaptic vesicle-associated protein, CDCrel-1," *Proc. Natl. Acad. Sci.*, vol. 97, no. 24, pp. 13354–13359, Nov. 2000, doi: 10.1073/pnas.240347797.

[102] C.-H. Hsieh, A. Shaltouki, A. E. Gonzalez, A. Bettencourt da Cruz, L. F. Burbulla, E. St Lawrence, B. Schüle, D. Krainc, T. D. Palmer, and X. Wang, "Functional Impairment in Miro Degradation and Mitophagy Is a Shared Feature in Familial and Sporadic Parkinson's Disease.," *Cell Stem Cell*, vol. 19, no. 6, pp. 709–724, Dec. 2016, doi: 10.1016/j.stem.2016.08.002.

[103] X. Wang, D. Winter, G. Ashrafi, J. Schlehe, Y. L. Wong, D. Selkoe, S. Rice, J. Steen, M. J. Lavoie, and T. L. Schwarz, "PINK1 and Parkin target miro for phosphorylation and degradation to arrest mitochondrial motility," *Cell*, vol. 147, no. 4, pp. 893–906, 2011, doi: 10.1016/j.cell.2011.10.018.

[104] E. Shlevkov, T. Kramer, J. Schapansky, M. J. Lavoie, and T. L. Schwarz, "Miro phosphorylation sites regulate Parkin recruitment and mitochondrial motility," *Proc. Natl. Acad. Sci. U. S. A.*, vol. 113, no. 41, pp. E6097–E6106, 2016, doi: 10.1073/pnas.1612283113.

[105] G. López-Doménech, C. Covill-Cooke, J. H. Howden, N. Birsa, C. Morfill, N. J. Brandon, and J. T. Kittler, "Miro ubiquitination is critical for efficient damage-induced PINK1/Parkin-mediated mitophagy," *bioRxiv*, no. September, 2018, doi: 10.1101/414664.

[106] A. Kazlauskaite, V. Kelly, C. Johnson, C. Baillie, C. J. Hastie, M. Peggie, T. Macartney, H. I. Woodroof, D. R. Alessi, P. G. A. Pedrioli, and M. M. K. Muqit, "Phosphorylation of Parkin at Serine65 is essential for activation: elaboration of a Miro1 substrate-based assay of Parkin E3 ligase activity.," *Open Biol.*, vol. 4, no. 3, p. 130213, Mar. 2014, doi: 10.1098/rsob.130213.

[107] D. Safiulina, M. Kuum, V. Choubey, N. Gogichaishvili, J. Liiv, M. A. Hickey, M. Cagalinec, M. Mandel, A. Zeb, M. Liiv, and A. Kaasik, "Miro proteins prime mitochondria for Parkin translocation and mitophagy.," *EMBO J.*, vol. 38, no. 2, Jan. 2019, doi: 10.15252/embj.201899384.

[108] J.-Q. Wang, S. Zhu, Y. Wang, F. Wang, C. An, D. Jiang, L. Gao, Y. Tu, X. Zhu, Y. Wang, H. Liu, J. Gong, Z. Sun, X. Wang, L. Liu, K. Yang, C. Guo, and T.-S. Tang, "Miro2 supplies a platform for Parkin translocation to damaged mitochondria," *Sci. Bull.*, vol. 64, no. 11, pp. 730–747, 2019, doi: https://doi.org/10.1016/j.scib.2019.04.033.

[109] E. M. Valente, P. M. Abou-Sleiman, V. Caputo, M. M. K. Muqit, K. Harvey, S. Gispert, Z. Ali, D. Del Turco, A. R. Bentivoglio, D. G. Healy, A. Albanese, R. Nussbaum, R. González-Maldonado, T. Deller, S. Salvi, P. Cortelli, W. P. Gilks, D. S. Latchman, R. J. Harvey, *et al.*, "Hereditary early-onset Parkinson's disease caused by mutations in PINK1.," *Science*, vol. 304, no. 5674, pp. 1158–1160, May 2004, doi: 10.1126/science.1096284.

[110] T. Kitada, S. Aakawa, N. Hattori, H. Matsumine, M. Yokochi, Y. Mizuno, and N. Shimizu, "Mutations in the parkin gene cause autosomal recessive juvenile parkinsonism," in *Nature Letters*, vol. 169, no. 1993, 1998, pp. 166–169. [Online]. Available: https://www.nature.com/articles/33416.pdf

[111] D. Grossmann, C. Berenguer-Escuder, M. E. Bellet, D. Scheibner, J. Bohler, F. Massart, D. Rapaport, A. Skupin, A. Fouquier d'Hérouël, M. Sharma, J. Ghelfi, A. Raković, P. Lichtner, P. Antony, E. Glaab, P. May, K. S. Dimmer, J. C. Fitzgerald, A. Grünewald, *et al.*, "Mutations in RHOT1 Disrupt Endoplasmic Reticulum-Mitochondria Contact Sites Interfering with Calcium Homeostasis and Mitochondrial Dynamics in Parkinson's Disease.," *Antioxid. Redox Signal.*, vol. 31, no. 16, pp. 1213–1234, Dec. 2019, doi: 10.1089/ars.2018.7718.

[112] C. Berenguer-Escuder, D. Grossmann, F. Massart, P. Antony, L. F. Burbulla, E. Glaab, S. Imhoff, J. Trinh, P. Seibler, A. Grünewald, and R. Krüger, "Variants in Miro1 Cause Alterations of ER-Mitochondria Contact Sites in Fibroblasts from Parkinson's Disease Patients.," *J. Clin. Med.*, vol. 8, no. 12, Dec. 2019, doi: 10.3390/jcm8122226.

[113] L. Schwarz, N. Casadei, and J. C. Fitzgerald, “Generation of R272Q, S156A and K572R RHOT1/Miro1 point mutations in iPSCs from a healthy individual using FACS-assisted CRISPR/Cas9 genome editing.,” *Stem Cell Res.*, vol. 55, p. 102469, Aug. 2021, doi: 10.1016/j.scr.2021.102469.

[114] V. Zimorski, C. Ku, W. F. Martin, and S. B. Gould, “Endosymbiotic theory for organelle origins.,” *Curr. Opin. Microbiol.*, vol. 22, pp. 38–48, Dec. 2014, doi: 10.1016/j.mib.2014.09.008.

[115] K. Tucker and E. Park, “Cryo-EM structure of the mitochondrial protein-import channel TOM complex at near-atomic resolution,” *Nat. Struct. Mol. Biol.*, vol. 26, no. 12, pp. 1158–1166, 2019, doi: 10.1038/s41594-019-0339-2.

[116] T. Bausewein, H. Naveed, J. Liang, and S. Nussberger, “The structure of the TOM core complex in the mitochondrial outer membrane.,” *Biol. Chem.*, vol. 401, no. 6–7, pp. 687–697, May 2020, doi: 10.1515/hsz-2020-0104.

[117] N. Pfanner, N. Wiedemann, C. Meisinger, and T. Lithgow, “Assembling the mitochondrial outer membrane.,” *Nat. Struct. Mol. Biol.*, vol. 11, no. 11, pp. 1044–1048, Nov. 2004, doi: 10.1038/nsmb852.

[118] S. A. Paschen, W. Neupert, and D. Rapaport, “Biogenesis of beta-barrel membrane proteins of mitochondria.,” *Trends Biochem. Sci.*, vol. 30, no. 10, pp. 575–582, Oct. 2005, doi: 10.1016/j.tibs.2005.08.009.

[119] T. Becker, L.-S. Wenz, V. Krüger, W. Lehmann, J. M. Müller, L. Goroncy, N. Zufall, T. Lithgow, B. Guiard, A. Chacinska, R. Wagner, C. Meisinger, and N. Pfanner, “The mitochondrial import protein Mim1 promotes biogenesis of multispanning outer membrane proteins.,” *J. Cell Biol.*, vol. 194, no. 3, pp. 387–395, Aug. 2011, doi: 10.1083/jcb.201102044.

[120] D. Papic, K. Krumpe, J. Dukanovic, K. S. Dimmer, and D. Rapaport, “Multispan mitochondrial outer membrane protein Ugo1 follows a unique Mim1-dependent import pathway.,” *J. Cell Biol.*, vol. 194, no. 3, pp. 397–405, Aug. 2011, doi: 10.1083/jcb.201102041.

[121] K. S. Dimmer, D. Papić, B. Schumann, D. Sperl, K. Krumpe, D. M. Walther, and D. Rapaport, “A crucial role for Mim2 in the biogenesis of mitochondrial outer membrane proteins,” *J. Cell Sci.*, vol. 125, no. 14, pp. 3464–3473, Jul. 2012, doi: 10.1242/jcs.103804.

[122] K. N. Doan, A. Grevel, C. U. Mårtensson, L. Ellenrieder, N. Thornton, L.-S. Wenz, Ł. Opaliński, B. Guiard, N. Pfanner, and T. Becker, “The Mitochondrial Import Complex MIM Functions as Main Translocase for α-Helical Outer Membrane Proteins,” *Cell Rep.*, vol. 31, no. 4, p. 107567, 2020, doi: https://doi.org/10.1016/j.celrep.2020.107567.

[123] T. Becker, S. Pfannschmidt, B. Guiard, D. Stojanovski, D. Milenkovic, S. Kutik, N. Pfanner, C. Meisinger, and N. Wiedemann, “Biogenesis of the mitochondrial TOM complex: Mim1 promotes insertion and assembly of signal-anchored receptors.,” *J. Biol. Chem.*, vol. 283, no. 1, pp. 120–127, Jan. 2008, doi: 10.1074/jbc.M706997200.

[124] T. Becker, B. Guiard, N. Thornton, N. Zufall, D. A. Stroud, N. Wiedemann, and N. Pfanner, “Assembly of the mitochondrial protein import channel: role of Tom5 in two-stage interaction of Tom40 with the SAM complex.,” *Mol. Biol. Cell*, vol. 21, no. 18, pp. 3106–3113, Sep. 2010, doi: 10.1091/mbc.E10-06-0518.

[125] J. M. Hulett, F. Lueder, N. C. Chan, A. J. Perry, P. Wolynec, V. A. Likić, P. R. Gooley, and T. Lithgow, “The transmembrane segment of Tom20 is recognized by Mim1 for docking to the mitochondrial TOM complex.,” *J. Mol. Biol.*, vol. 376, no. 3, pp. 694–704, Feb. 2008, doi: 10.1016/j.jmb.2007.12.021.

[126] J. Popov-Celeketić, T. Waizenegger, and D. Rapaport, “Mim1 functions in an oligomeric form to facilitate the integration of Tom20 into the mitochondrial outer membrane.,” *J. Mol. Biol.*, vol. 376, no. 3, pp. 671–680, Feb. 2008, doi: 10.1016/j.jmb.2007.12.006.

[127] F. Lueder and T. Lithgow, “The three domains of the mitochondrial outer membrane protein Mim1 have discrete functions in assembly of the TOM complex.,” *FEBS Lett.*, vol. 583, no. 9, pp. 1475–1480, May 2009, doi: 10.1016/j.febslet.2009.03.064.

[128] D. G. Vitali, S. Käser, A. Kolb, K. S. Dimmer, A. Schneider, and D. Rapaport, “Independent evolution of functionally exchangeable mitochondrial outer membrane import complexes.,” *Elife*, vol. 7, Jun. 2018, doi: 10.7554/eLife.34488.

[129] A. Guna, T. A. Stevens, A. J. Inglis, J. M. Replogle, T. K. Esantsi, G. Muthukumar, K. C. L. Shaffer, M. L. Wang, A. N. Pogson, J. J. Jones, B. Lomenick, T.-F. Chou, J. S. Weissman, and R. M. Voorhees, "MTCH2 is a mitochondrial outer membrane protein insertase," *bioRxiv*, p. 2022.09.15.508165, Jan. 2022, doi: 10.1101/2022.09.15.508165.

[130] D. Ishikawa, H. Yamamoto, Y. Tamura, K. Moritoh, and T. Endo, "Two novel proteins in the mitochondrial outer membrane mediate beta-barrel protein assembly.," *J. Cell Biol.*, vol. 166, no. 5, pp. 621–627, Aug. 2004, doi: 10.1083/jcb.200405138.

[131] T. Waizenegger, S. Schmitt, J. Zivkovic, W. Neupert, and D. Rapaport, "Mim1, a protein required for the assembly of the TOM complex of mitochondria.," *EMBO Rep.*, vol. 6, no. 1, pp. 57–62, Jan. 2005, doi: 10.1038/sj.embor.7400318.

[132] S. F. Altschul, W. Gish, W. Miller, E. W. Myers, and D. J. Lipman, "Basic local alignment search tool.," *J. Mol. Biol.*, vol. 215, no. 3, pp. 403–410, Oct. 1990, doi: 10.1016/S0022-2836(05)80360-2.

[133] F. Madeira, M. Pearce, A. R. N. Tivey, P. Basutkar, J. Lee, O. Edbali, N. Madhusoodanan, A. Kolesnikov, and R. Lopez, "Search and sequence analysis tools services from EMBL-EBI in 2022.," *Nucleic Acids Res.*, Apr. 2022, doi: 10.1093/nar/gkac240.

[134] M. R. Wilkins, E. Gasteiger, A. Bairoch, J. C. Sanchez, K. L. Williams, R. D. Appel, and D. F. Hochstrasser, "Protein identification and analysis tools in the ExPASy server.," *Methods Mol. Biol.*, vol. 112, pp. 531–552, 1999, doi: 10.1385/1-59259-584-7:531.

[135] Schrödinger, LLC, "The {PyMOL} Molecular Graphics System, Version~1.8," Nov. 2015.

[136] Sigma-Aldrich, "GenElute™ HP Plasmid Midiprep Kit," *GenElute™ HP Plasmid Midiprep Kit*, 2014, [Online]. Available: http://www.sigmaaldrich.com/catalog/product/sigma/na0200?lang=en&region=GB

[137] Invitrogen, "Bac-to-Bac® Baculovirus Expression System," *User Guid.*, no. August, pp. 1–78, 2015, [Online]. Available: http://tools.thermofisher.com/content/sfs/manuals/bactobac_man.pdf

[138] Invitrogen, "PureLink HiPure Plasmid DNA (Mini. Midi. Maxi)," *Manual*, no. 25, pp. 1–42, 2013.

[139] Q. Kit and U. Guide, "baculo QUANT TM," 2019.

[140] A. Jenner, A. Peña-Blanco, R. Salvador-Gallego, B. Ugarte-Uribe, C. Zollo, T. Ganief, J. Bierlmeier, M. Mund, J. E. Lee, J. Ries, D. Schwarzer, B. Macek, and A. J. Garcia-Saez, "DRP1 interacts directly with BAX to induce its activation and apoptosis," *EMBO J.*, pp. 1–19, 2022, doi: 10.15252/embj.2021108587.

[141] F. O. Fagbadebo, P. D. Kaiser, K. Zittlau, N. Bartlick, T. R. Wagner, T. Froehlich, G. Jarjour, S. Nueske, A. Scholz, B. Traenkle, B. Macek, and U. Rothbauer, "A Nanobody-Based Toolset to Monitor and Modify the Mitochondrial GTPase Miro1.," *Front. Mol. Biosci.*, vol. 9, p. 835302, 2022, doi: 10.3389/fmolb.2022.835302.

[142] Life Technologies, "Protein Thermal Shift ™ Studies," *Protein Therm. Shift Stud.*, no. 4461808, pp. 7–34, 2011.

[143] C. Panel and H. Tab, "Malachite Green Phosphate Assay Kit MAK307," *Sigma-Aldrich*, pp. 2–5, 2006.

[144] B. Bingol, J. S. Tea, L. Phu, M. Reichelt, C. E. Bakalarski, Q. Song, O. Foreman, D. S. Kirkpatrick, and M. Sheng, "The mitochondrial deubiquitinase USP30 opposes parkin-mediated mitophagy," *Nature*, vol. 510, no. 7505, pp. 370–375, 2014, doi: 10.1038/nature13418.

[145] S. Liu, T. Sawada, S. Lee, W. Yu, G. Silverio, P. Alapatt, I. Millan, A. Shen, W. Saxton, T. Kanao, R. Takahashi, N. Hattori, Y. Imai, and B. Lu, "Parkinson's disease-associated kinase PINK1 regulates miro protein level and axonal transport of mitochondria," *PLoS Genet.*, vol. 8, no. 3, pp. 15–17, 2012, doi: 10.1371/journal.pgen.1002537.

[146] X. Guo, G. T. Macleod, A. Wellington, F. Hu, S. Panchumarthi, M. Schoenfield, L. Marin, M. P. Charlton, H. L. Atwood, and K. E. Zinsmaier, "The GTPase dMiro is required for axonal transport of mitochondria to drosophila synapses," *Neuron*, vol. 47, no. 3, pp. 379–393, 2005, doi: 10.1016/j.neuron.2005.06.027.

[147] N. Nemani, E. Carvalho, D. Tomar, Z. Dong, A. Ketschek, S. L. Breves, F. Jaña, A. M. Worth, J. Heffler, P. Palaniappan, A. Tripathi, R. Subbiah, M. F. Riitano, A. Seelam, T. Manfred, K. Itoh, S. Meng, H. Sesaki, W. J. Craigen, *et al.*, "MIRO-1 Determines Mitochondrial Shape Transition upon GPCR Activation and Ca2+ Stress," *Cell Rep.*, vol. 23, no. 4, pp. 1005–1019, 2018, doi: 10.1016/j.celrep.2018.03.098.

[148] S. M. Kelly, T. J. Jess, and N. C. Price, "How to study proteins by circular dichroism," *Biochim. Biophys. Acta - Proteins Proteomics*, vol. 1751, no. 2, pp. 119–139, 2005, doi: 10.1016/j.bbapap.2005.06.005.

[149] C. McMahon, A. S. Baier, R. Pascolutti, M. Wegrecki, S. Zheng, J. X. Ong, S. C. Erlandson, D. Hilger, S. G. F. Rasmussen, A. M. Ring, A. Manglik, and A. C. Kruse, "Yeast surface display platform for rapid discovery of conformationally selective nanobodies," *Nat. Struct. Mol. Biol.*, vol. 25, no. 3, pp. 289–296, 2018, doi: 10.1038/s41594-018-0028-6.

[150] E. Smirnova, L. Griparic, D. L. Shurland, and A. M. van der Bliek, "Dynamin-related protein Drp1 is required for mitochondrial division in mammalian cells.," *Mol. Biol. Cell*, vol. 12, no. 8, pp. 2245–2256, Aug. 2001, doi: 10.1091/mbc.12.8.2245.

[151] D. J. Weihofen, Andreas; Thomas, Kelly J.; Ostaszewski, Beth L.; Cookson, Mark R.; Selkoe, "Pink1 forms a multi-protein complex with Miro and Milton, linking Pink1 function to mitochondrial trafficking," *Biochemistry*, vol. 23, no. 1, pp. 1–7, 2009, doi: 10.1021/bi8019178.Pink1.

[152] S. A. Sarraf, M. Raman, V. Guarani-Pereira, M. E. Sowa, E. L. Huttlin, S. P. Gygi, and J. W. Harper, "Landscape of the PARKIN-dependent ubiquitylome in response to mitochondrial depolarization.," *Nature*, vol. 496, no. 7445, pp. 372–376, Apr. 2013, doi: 10.1038/nature12043.

[153] A. Ordureau, S. A. Sarraf, D. M. Duda, J.-M. Heo, M. P. Jedrychowski, V. O. Sviderskiy, J. L. Olszewski, J. T. Koerber, T. Xie, S. A. Beausoleil, J. A. Wells, S. P. Gygi, B. A. Schulman, and J. W. Harper, "Quantitative proteomics reveal a feedforward mechanism for mitochondrial PARKIN translocation and ubiquitin chain synthesis.," *Mol. Cell*, vol. 56, no. 3, pp. 360–375, Nov. 2014, doi: 10.1016/j.molcel.2014.09.007.

[154] S. Muyldermans, "A guide to: generation and design of nanobodies.," *FEBS J.*, vol. 288, no. 7, pp. 2084–2102, Apr. 2021, doi: 10.1111/febs.15515.

[155] D. S. Waugh, "Crystal structures of MBP fusion proteins.," *Protein Sci.*, vol. 25, no. 3, pp. 559–571, Mar. 2016, doi: 10.1002/pro.2863.

[156] T. T. Nguyen, S. S. Oh, D. Weaver, A. Lewandowska, D. Maxfield, M.-H. Schuler, N. K. Smith, J. Macfarlane, G. Saunders, C. A. Palmer, V. Debattisti, T. Koshiba, S. Pulst, E. L. Feldman, G. Hajnóczky, and J. M. Shaw, "Loss of Miro1-directed mitochondrial movement results in a novel murine model for neuron disease.," *Proc. Natl. Acad. Sci. U. S. A.*, vol. 111, no. 35, pp. E3631-40, Sep. 2014, doi: 10.1073/pnas.1402449111.

[157] K. T. Chang, R. F. Niescier, and K. T. Min, "Mitochondrial matrix Ca 2+ as an intrinsic signal regulating mitochondrial motility in axons," *Proc. Natl. Acad. Sci. U. S. A.*, vol. 108, no. 37, pp. 15456–15461, 2011, doi: 10.1073/pnas.1106862108.

[158] L. A. Feig, "Tools of the trade: use of dominant-inhibitory mutants of Ras-family GTPases.," *Nat. Cell Biol.*, vol. 1, no. 2, pp. E25-7, Jun. 1999, doi: 10.1038/10018.

[159] L. Walch, E. Pellier, W. Leng, G. Lakisic, A. Gautreau, V. Contremoulins, J.-M. Verbavatz, and C. L. Jackson, "GBF1 and Arf1 interact with Miro and regulate mitochondrial positioning within cells.," *Sci. Rep.*, vol. 8, no. 1, p. 17121, Nov. 2018, doi: 10.1038/s41598-018-35190-0.

[160] Y. Zhao, E. Song, W. Wang, C.-H. Hsieh, X. Wang, W. Feng, X. Wang, and K. Shen, "Metaxins are core components of mitochondrial transport adaptor complexes.," *Nat. Commun.*, vol. 12, no. 1, p. 83, Jan. 2021, doi: 10.1038/s41467-020-20346-2.

[161] T. König, H. Nolte, M. J. Aaltonen, T. Tatsuta, M. Krols, T. Stroh, T. Langer, and H. M. McBride, "MIROs and DRP1 drive mitochondrial-derived vesicle biogenesis and promote quality control.," *Nat. Cell Biol.*, vol. 23, no. 12, pp. 1271–1286, Dec. 2021, doi: 10.1038/s41556-021-00798-4.

[162] K. Luger, A. W. Mäder, R. K. Richmond, D. F. Sargent, and T. J. Richmond, "Crystal structure of the nucleosome core particle at 2.8 Å resolution," *Nature*, vol. 389, no. 6648, pp. 251–260, 1997, doi: 10.1038/38444.

[163] A. D. Mirzabekov and A. Rich, “Asymmetric lateral distribution of unshielded phosphate groups in nucleosomal DNA and its role in DNA bending.,” *Proc. Natl. Acad. Sci. U. S. A.*, vol. 76, no. 3, pp. 1118–1121, Mar. 1979, doi: 10.1073/pnas.76.3.1118.

[164] T. M. Okonogi, S. C. Alley, E. A. Harwood, P. B. Hopkins, and B. H. Robinson, “Phosphate backbone neutralization increases duplex DNA flexibility: a model for protein binding.,” *Proc. Natl. Acad. Sci. U. S. A.*, vol. 99, no. 7, pp. 4156–4160, Apr. 2002, doi: 10.1073/pnas.072067799.

[165] D. M. PHILLIPS, “The presence of acetyl groups of histones.,” *Biochem. J.*, vol. 87, no. 2, pp. 258–263, May 1963, doi: 10.1042/bj0870258.

[166] V. G. ALLFREY, R. FAULKNER, and A. E. MIRSKY, “ACETYLATION AND METHYLATION OF HISTONES AND THEIR POSSIBLE ROLE IN THE REGULATION OF RNA SYNTHESIS.,” *Proc. Natl. Acad. Sci. U. S. A.*, vol. 51, no. 5, pp. 786–794, May 1964, doi: 10.1073/pnas.51.5.786.

[167] J. Thomas and A. C. David, “Translating the Histone Code,” *Science (80-.).*, vol. 293, no. 5532, pp. 1074–1080, Aug. 2001, doi: 10.1126/science.1063127.

[168] R. N. Dutnall, “Cracking the histone code: one, two, three methyls, you’re out!,” *Mol. Cell*, vol. 12, no. 1, pp. 3–4, Jul. 2003, doi: 10.1016/s1097-2765(03)00282-x.

[169] M. Garcia-Ramirez, C. Rocchini, and J. Ausio, “Modulation of chromatin folding by histone acetylation.,” *J. Biol. Chem.*, vol. 270, no. 30, pp. 17923–17928, Jul. 1995, doi: 10.1074/jbc.270.30.17923.

[170] C. Tse, T. Sera, A. P. Wolffe, and J. C. Hansen, “Disruption of higher-order folding by core histone acetylation dramatically enhances transcription of nucleosomal arrays by RNA polymerase III.,” *Mol. Cell. Biol.*, vol. 18, no. 8, pp. 4629–4638, Aug. 1998, doi: 10.1128/MCB.18.8.4629.

[171] J. Taunton, C. A. Hassig, and S. L. Schreiber, “A mammalian histone deacetylase related to the yeast transcriptional regulator Rpd3p.,” *Science*, vol. 272, no. 5260, pp. 408–411, Apr. 1996, doi: 10.1126/science.272.5260.408.

[172] J. E. Brownell, J. Zhou, T. Ranalli, R. Kobayashi, D. G. Edmondson, S. Y. Roth, and C. D. Allis, “Tetrahymena histone acetyltransferase A: a homolog to yeast Gcn5p linking histone acetylation to gene activation.,” *Cell*, vol. 84, no. 6, pp. 843–851, Mar. 1996, doi: 10.1016/s0092-8674(00)81063-6.

[173] S. R. Haynes, C. Dollard, F. Winston, S. Beck, J. Trowsdale, and I. B. Dawid, “The bromodomain: a conserved sequence found in human, Drosophila and yeast proteins.,” *Nucleic Acids Res.*, vol. 20, no. 10, p. 2603, May 1992, doi: 10.1093/nar/20.10.2603.

[174] C. Dhalluin, J. E. Carlson, L. Zeng, C. He, A. K. Aggarwal, and M. M. Zhou, “Structure and ligand of a histone acetyltransferase bromodomain.,” *Nature*, vol. 399, no. 6735, pp. 491–496, Jun. 1999, doi: 10.1038/20974.

[175] S. Singh, P. Senapati, and T. K. Kundu, “Metabolic Regulation of Lysine Acetylation: Implications in Cancer.,” *Subcell. Biochem.*, vol. 100, pp. 393–426, 2022, doi: 10.1007/978-3-031-07634-3_12.

[176] S. C. Kim, R. Sprung, Y. Chen, Y. Xu, H. Ball, J. Pei, T. Cheng, Y. Kho, H. Xiao, L. Xiao, N. V Grishin, M. White, X.-J. Yang, and Y. Zhao, “Substrate and functional diversity of lysine acetylation revealed by a proteomics survey.,” *Mol. Cell*, vol. 23, no. 4, pp. 607–618, Aug. 2006, doi: 10.1016/j.molcel.2006.06.026.

[177] C. Choudhary, C. Kumar, F. Gnad, M. L. Nielsen, M. Rehman, T. C. Walther, J. V. Olsen, and M. Mann, “Lysine acetylation targets protein complexes and co-regulates major cellular functions,” *Science (80-.).*, vol. 325, no. 5942, pp. 834–840, 2009, doi: 10.1126/science.1175371.

[178] B. T. Weinert, T. Narita, S. Satpathy, B. Srinivasan, B. K. Hansen, C. Schölz, W. B. Hamilton, B. E. Zucconi, W. W. Wang, W. R. Liu, J. M. Brickman, E. A. Kesicki, A. Lai, K. D. Bromberg, P. A. Cole, and C. Choudhary, “Time-Resolved Analysis Reveals Rapid Dynamics and Broad Scope of the CBP/p300 Acetylome.,” *Cell*, vol. 174, no. 1, pp. 231-244.e12, Jun. 2018, doi: 10.1016/j.cell.2018.04.033.

[179] J. G. Meyer, A. K. D’Souza, D. J. Sorensen, M. J. Rardin, A. J. Wolfe, B. W. Gibson, and B. Schilling, “Quantification of Lysine Acetylation and Succinylation Stoichiometry in Proteins Using Mass Spectrometric Data-Independent Acquisitions (SWATH).,” *J. Am. Soc. Mass Spectrom.*, vol. 27, no. 11, pp. 1758–1771, Nov. 2016, doi: 10.1007/s13361-016-1476-z.

[180] B. K. Hansen, R. Gupta, L. Baldus, D. Lyon, T. Narita, M. Lammers, C. Choudhary, and B. T. Weinert, "Analysis of human acetylation stoichiometry defines mechanistic constraints on protein regulation.," *Nat. Commun.*, vol. 10, no. 1, p. 1055, Mar. 2019, doi: 10.1038/s41467-019-09024-0.

[181] R. W. Burlingame, W. E. Love, and E. N. Moudrianakis, "Crystals of the octameric histone core of the nucleosome.," *Science*, vol. 223, no. 4634, pp. 413–414, Jan. 1984, doi: 10.1126/science.6691154.

[182] Z. Fang, X. Wang, X. Sun, W. Hu, and Q. R. Miao, "The Role of Histone Protein Acetylation in Regulating Endothelial Function.," *Front. cell Dev. Biol.*, vol. 9, p. 672447, 2021, doi: 10.3389/fcell.2021.672447.

[183] Y.-M. Xu, J.-Y. Du, and A. T. Y. Lau, "Posttranslational modifications of human histone H3: an update.," *Proteomics*, vol. 14, no. 17–18, pp. 2047–2060, Sep. 2014, doi: 10.1002/pmic.201300435.

[184] M. Tan, H. Luo, S. Lee, F. Jin, J. S. Yang, E. Montellier, T. Buchou, Z. Cheng, S. Rousseaux, N. Rajagopal, Z. Lu, Z. Ye, Q. Zhu, J. Wysocka, Y. Ye, S. Khochbin, B. Ren, and Y. Zhao, "Identification of 67 histone marks and histone lysine crotonylation as a new type of histone modification.," *Cell*, vol. 146, no. 6, pp. 1016–1028, Sep. 2011, doi: 10.1016/j.cell.2011.08.008.

[185] C. E. Barnes, D. M. English, and S. M. Cowley, "Acetylation & Co: an expanding repertoire of histone acylations regulates chromatin and transcription.," *Essays Biochem.*, vol. 63, no. 1, pp. 97–107, Apr. 2019, doi: 10.1042/EBC20180061.

[186] C. D. Allis, S. L. Berger, J. Cote, S. Dent, T. Jenuwien, T. Kouzarides, L. Pillus, D. Reinberg, Y. Shi, R. Shiekhattar, A. Shilatifard, J. Workman, and Y. Zhang, "New nomenclature for chromatin-modifying enzymes.," *Cell*, vol. 131, no. 4. United States, pp. 633–636, Nov. 2007. doi: 10.1016/j.cell.2007.10.039.

[187] A. F. Neuwald and D. Landsman, "GCN5-related histone N-acetyltransferases belong to a diverse superfamily that includes the yeast SPT10 protein.," *Trends Biochem. Sci.*, vol. 22, no. 5, pp. 154–155, May 1997, doi: 10.1016/s0968-0004(97)01034-7.

[188] V. V Ogryzko, R. L. Schiltz, V. Russanova, B. H. Howard, and Y. Nakatani, "The transcriptional coactivators p300 and CBP are histone acetyltransferases.," *Cell*, vol. 87, no. 5, pp. 953–959, Nov. 1996, doi: 10.1016/s0092-8674(00)82001-2.

[189] A. J. Bannister and T. Kouzarides, "The CBP co-activator is a histone acetyltransferase.," *Nature*, vol. 384, no. 6610, pp. 641–643, Dec. 1996, doi: 10.1038/384641a0.

[190] Y. Tang, M. A. Holbert, H. Wurtele, K. Meeth, W. Rocha, M. Gharib, E. Jiang, P. Thibault, A. Verreault, P. A. Cole, and R. Marmorstein, "Fungal Rtt109 histone acetyltransferase is an unexpected structural homolog of metazoan p300/CBP.," *Nat. Struct. Mol. Biol.*, vol. 15, no. 7, pp. 738–745, Jul. 2008, doi: 10.1038/nsmb.1448.

[191] T. E. Spencer, G. Jenster, M. M. Burcin, C. D. Allis, J. Zhou, C. A. Mizzen, N. J. McKenna, S. A. Onate, S. Y. Tsai, M. J. Tsai, and B. W. O'Malley, "Steroid receptor coactivator-1 is a histone acetyltransferase.," *Nature*, vol. 389, no. 6647, pp. 194–198, Sep. 1997, doi: 10.1038/38304.

[192] T. Thomas and A. K. Voss, "The diverse biological roles of MYST histone acetyltransferase family proteins.," *Cell Cycle*, vol. 6, no. 6, pp. 696–704, Mar. 2007, doi: 10.4161/cc.6.6.4013.

[193] I. V Gregoretti, Y.-M. Lee, and H. V Goodson, "Molecular evolution of the histone deacetylase family: functional implications of phylogenetic analysis.," *J. Mol. Biol.*, vol. 338, no. 1, pp. 17–31, Apr. 2004, doi: 10.1016/j.jmb.2004.02.006.

[194] P. Bjerling, R. A. Silverstein, G. Thon, A. Caudy, S. Grewal, and K. Ekwall, "Functional divergence between histone deacetylases in fission yeast by distinct cellular localization and in vivo specificity.," *Mol. Cell. Biol.*, vol. 22, no. 7, pp. 2170–2181, Apr. 2002, doi: 10.1128/MCB.22.7.2170-2181.2002.

[195] J. J. Buggy, M. L. Sideris, P. Mak, D. D. Lorimer, B. McIntosh, and J. M. Clark, "Cloning and characterization of a novel human histone deacetylase, HDAC8.," *Biochem. J.*, vol. 350 Pt 1, no. Pt 1, pp. 199–205, Aug. 2000.

[196] P. J. Watson, L. Fairall, G. M. Santos, and J. W. R. Schwabe, "Structure of HDAC3 bound to co-repressor and inositol tetraphosphate.," *Nature*, vol. 481, no. 7381, pp. 335–340, Jan. 2012, doi: 10.1038/nature10728.

[197] P. Gujral, V. Mahajan, A. C. Lissaman, and A. P. Ponnampalam, “Histone acetylation and the role of histone deacetylases in normal cyclic endometrium,” *Reprod. Biol. Endocrinol.*, vol. 18, no. 1, p. 84, 2020, doi: 10.1186/s12958-020-00637-5.

[198] C. M. Grozinger, C. A. Hassig, and S. L. Schreiber, “Three proteins define a class of human histone deacetylases related to yeast Hda1p.,” *Proc. Natl. Acad. Sci. U. S. A.*, vol. 96, no. 9, pp. 4868–4873, Apr. 1999, doi: 10.1073/pnas.96.9.4868.

[199] W. Fischle, F. Dequiedt, M. J. Hendzel, M. G. Guenther, M. A. Lazar, W. Voelter, and E. Verdin, “Enzymatic activity associated with class II HDACs is dependent on a multiprotein complex containing HDAC3 and SMRT/N-CoR.,” *Mol. Cell*, vol. 9, no. 1, pp. 45–57, Jan. 2002, doi: 10.1016/s1097-2765(01)00429-4.

[200] D. D. Fischer, R. Cai, U. Bhatia, F. A. M. Asselbergs, C. Song, R. Terry, N. Trogani, R. Widmer, P. Atadja, and D. Cohen, “Isolation and characterization of a novel class II histone deacetylase, HDAC10.,” *J. Biol. Chem.*, vol. 277, no. 8, pp. 6656–6666, Feb. 2002, doi: 10.1074/jbc.M108055200.

[201] H.-Y. Kao, C.-H. Lee, A. Komarov, C. C. Han, and R. M. Evans, “Isolation and characterization of mammalian HDAC10, a novel histone deacetylase.,” *J. Biol. Chem.*, vol. 277, no. 1, pp. 187–193, Jan. 2002, doi: 10.1074/jbc.M108931200.

[202] L. Gao, M. A. Cueto, F. Asselbergs, and P. Atadja, “Cloning and functional characterization of HDAC11, a novel member of the human histone deacetylase family.,” *J. Biol. Chem.*, vol. 277, no. 28, pp. 25748–25755, Jul. 2002, doi: 10.1074/jbc.M111871200.

[203] J. Cao, L. Sun, P. Aramsangtienchai, N. A. Spiegelman, X. Zhang, W. Huang, E. Seto, and H. Lin, “HDAC11 regulates type I interferon signaling through defatty-acylation of SHMT2.,” *Proc. Natl. Acad. Sci. U. S. A.*, vol. 116, no. 12, pp. 5487–5492, Mar. 2019, doi: 10.1073/pnas.1815365116.

[204] A. Villagra, F. Cheng, H.-W. Wang, I. Suarez, M. Glozak, M. Maurin, D. Nguyen, K. L. Wright, P. W. Atadja, K. Bhalla, J. Pinilla-Ibarz, E. Seto, and E. M. Sotomayor, “The histone deacetylase HDAC11 regulates the expression of interleukin 10 and immune tolerance.,” *Nat. Immunol.*, vol. 10, no. 1, pp. 92–100, Jan. 2009, doi: 10.1038/ni.1673.

[205] Y. Nakahata, M. Kaluzova, B. Grimaldi, S. Sahar, J. Hirayama, D. Chen, L. P. Guarente, and P. Sassone-Corsi, “The NAD+-dependent deacetylase SIRT1 modulates CLOCK-mediated chromatin remodeling and circadian control.,” *Cell*, vol. 134, no. 2, pp. 329–340, Jul. 2008, doi: 10.1016/j.cell.2008.07.002.

[206] S. Imai, C. M. Armstrong, M. Kaeberlein, and L. Guarente, “Transcriptional silencing and longevity protein Sir2 is an NAD-dependent histone deacetylase.,” *Nature*, vol. 403, no. 6771, pp. 795–800, Feb. 2000, doi: 10.1038/35001622.

[207] J. Landry, A. Sutton, S. T. Tafrov, R. C. Heller, J. Stebbins, L. Pillus, and R. Sternglanz, “The silencing protein SIR2 and its homologs are NAD-dependent protein deacetylases.,” *Proc. Natl. Acad. Sci. U. S. A.*, vol. 97, no. 11, pp. 5807–5811, May 2000, doi: 10.1073/pnas.110148297.

[208] J. S. Smith, C. B. Brachmann, I. Celic, M. A. Kenna, S. Muhammad, V. J. Starai, J. L. Avalos, J. C. Escalante-Semerena, C. Grubmeyer, C. Wolberger, and J. D. Boeke, “A phylogenetically conserved NAD+-dependent protein deacetylase activity in the Sir2 protein family.,” *Proc. Natl. Acad. Sci. U. S. A.*, vol. 97, no. 12, pp. 6658–6663, Jun. 2000, doi: 10.1073/pnas.97.12.6658.

[209] C. B. Brachmann, J. M. Sherman, S. E. Devine, E. E. Cameron, L. Pillus, and J. D. Boeke, “The SIR2 gene family, conserved from bacteria to humans, functions in silencing, cell cycle progression, and chromosome stability.,” *Genes Dev.*, vol. 9, no. 23, pp. 2888–2902, Dec. 1995, doi: 10.1101/gad.9.23.2888.

[210] R. A. Frye, “Characterization of five human cDNAs with homology to the yeast SIR2 gene: Sir2-like proteins (sirtuins) metabolize NAD and may have protein ADP-ribosyltransferase activity.,” *Biochem. Biophys. Res. Commun.*, vol. 260, no. 1, pp. 273–279, Jun. 1999, doi: 10.1006/bbrc.1999.0897.

[211] A. J. Bannister and T. Kouzarides, “Regulation of chromatin by histone modifications,” *Cell Res.*, vol. 21, no. 3, pp. 381–395, Mar. 2011, doi: 10.1038/cr.2011.22.

[212] E. Seto and M. Yoshida, “Erasers of histone acetylation: the histone deacetylase enzymes,” *Cold Spring Harb. Perspect. Biol.*, vol. 6, no. 4, pp. a018713–a018713, Apr. 2014, doi: 10.1101/cshperspect.a018713.

[213] J. W. Tamkun, R. Deuring, M. P. Scott, M. Kissinger, A. M. Pattatucci, T. C. Kaufman, and J. A. Kennison, "brahma: a regulator of Drosophila homeotic genes structurally related to the yeast transcriptional activator SNF2/SWI2.," *Cell*, vol. 68, no. 3, pp. 561–572, Feb. 1992, doi: 10.1016/0092-8674(92)90191-e.

[214] P. Filippakopoulos, S. Picaud, M. Mangos, T. Keates, J.-P. Lambert, D. Barsyte-Lovejoy, I. Felletar, R. Volkmer, S. Müller, T. Pawson, A.-C. Gingras, C. H. Arrowsmith, and S. Knapp, "Histone recognition and large-scale structural analysis of the human bromodomain family.," *Cell*, vol. 149, no. 1, pp. 214–231, Mar. 2012, doi: 10.1016/j.cell.2012.02.013.

[215] D. J. Owen, P. Ornaghi, J. C. Yang, N. Lowe, P. R. Evans, P. Ballario, D. Neuhaus, P. Filetici, and A. A. Travers, "The structural basis for the recognition of acetylated histone H4 by the bromodomain of histone acetyltransferase gcn5p.," *EMBO J.*, vol. 19, no. 22, pp. 6141–6149, Nov. 2000, doi: 10.1093/emboj/19.22.6141.

[216] E. M. Flynn, O. W. Huang, F. Poy, M. Oppikofer, S. F. Bellon, Y. Tang, and A. G. Cochran, "A Subset of Human Bromodomains Recognizes Butyryllysine and Crotonyllysine Histone Peptide Modifications.," *Structure*, vol. 23, no. 10, pp. 1801–1814, Oct. 2015, doi: 10.1016/j.str.2015.08.004.

[217] R. H. Jacobson, A. G. Ladurner, D. S. King, and R. Tjian, "Structure and function of a human TAFII250 double bromodomain module.," *Science*, vol. 288, no. 5470, pp. 1422–1425, May 2000, doi: 10.1126/science.288.5470.1422.

[218] F. Gong, L.-Y. Chiu, B. Cox, F. Aymard, T. Clouaire, J. W. Leung, M. Cammarata, M. Perez, P. Agarwal, J. S. Brodbelt, G. Legube, and K. M. Miller, "Screen identifies bromodomain protein ZMYND8 in chromatin recognition of transcription-associated DNA damage that promotes homologous recombination.," *Genes Dev.*, vol. 29, no. 2, pp. 197–211, Jan. 2015, doi: 10.1101/gad.252189.114.

[219] M.-S. Kim, S. M. Pinto, D. Getnet, R. S. Nirujogi, S. S. Manda, R. Chaerkady, A. K. Madugundu, D. S. Kelkar, R. Isserlin, S. Jain, J. K. Thomas, B. Muthusamy, P. Leal-Rojas, P. Kumar, N. A. Sahasrabuddhe, L. Balakrishnan, J. Advani, B. George, S. Renuse, *et al.*, "A draft map of the human proteome.," *Nature*, vol. 509, no. 7502, pp. 575–581, May 2014, doi: 10.1038/nature13302.

[220] M. Wilhelm, J. Schlegl, H. Hahne, A. M. Gholami, M. Lieberenz, M. M. Savitski, E. Ziegler, L. Butzmann, S. Gessulat, H. Marx, T. Mathieson, S. Lemeer, K. Schnatbaum, U. Reimer, H. Wenschuh, M. Mollenhauer, J. Slotta-Huspenina, J.-H. Boese, M. Bantscheff, *et al.*, "Mass-spectrometry-based draft of the human proteome.," *Nature*, vol. 509, no. 7502, pp. 582–587, May 2014, doi: 10.1038/nature13319.

[221] T. Fujisawa and P. Filippakopoulos, "Functions of bromodomain-containing proteins and their roles in homeostasis and cancer.," *Nat. Rev. Mol. Cell Biol.*, vol. 18, no. 4, pp. 246–262, Apr. 2017, doi: 10.1038/nrm.2016.143.

[222] N. Zaware and M.-M. Zhou, "Bromodomain biology and drug discovery," *Nat. Struct. Mol. Biol.*, vol. 26, no. 10, pp. 870–879, Oct. 2019, doi: 10.1038/s41594-019-0309-8.

[223] M. A. Dawson, R. K. Prinjha, A. Dittmann, G. Giotopoulos, M. Bantscheff, W.-I. Chan, S. C. Robson, C. Chung, C. Hopf, M. M. Savitski, C. Huthmacher, E. Gudgin, D. Lugo, S. Beinke, T. D. Chapman, E. J. Roberts, P. E. Soden, K. R. Auger, O. Mirguet, *et al.*, "Inhibition of BET recruitment to chromatin as an effective treatment for MLL-fusion leukaemia.," *Nature*, vol. 478, no. 7370, pp. 529–533, Oct. 2011, doi: 10.1038/nature10509.

[224] A. C. Groner, L. Cato, J. de Tribolet-Hardy, T. Bernasocchi, H. Janouskova, D. Melchers, R. Houtman, A. C. B. Cato, P. Tschopp, L. Gu, A. Corsinotti, Q. Zhong, C. Fankhauser, C. Fritz, C. Poyet, U. Wagner, T. Guo, R. Aebersold, L. A. Garraway, *et al.*, "TRIM24 Is an Oncogenic Transcriptional Activator in Prostate Cancer.," *Cancer Cell*, vol. 29, no. 6, pp. 846–858, Jun. 2016, doi: 10.1016/j.ccell.2016.04.012.

[225] J. Zuber, J. Shi, E. Wang, A. R. Rappaport, H. Herrmann, E. A. Sison, D. Magoon, J. Qi, K. Blatt, M. Wunderlich, M. J. Taylor, C. Johns, A. Chicas, J. C. Mulloy, S. C. Kogan, P. Brown, P. Valent, J. E. Bradner, S. W. Lowe, *et al.*, "RNAi screen identifies Brd4 as a therapeutic target in acute myeloid leukaemia.," *Nature*, vol. 478, no. 7370, pp. 524–528, Aug. 2011, doi: 10.1038/nature10334.

[226] Z. Yang, N. He, and Q. Zhou, "Brd4 recruits P-TEFb to chromosomes at late mitosis to promote G1 gene expression and cell cycle progression.," *Mol. Cell. Biol.*, vol. 28, no. 3, pp. 967–976, Feb. 2008, doi: 10.1128/MCB.01020-07.

[227] C. A. French, J. L. Kutok, W. C. Faquin, J. A. Toretsky, C. R. Antonescu, C. A. Griffin, V. Nose, S. O. Vargas, M. Moschovi, F. Tzortzatou-Stathopoulou, I. Miyoshi, A. R. Perez-Atayde, J. C. Aster, and J. A. Fletcher, "Midline carcinoma of children and young adults with NUT rearrangement.," *J. Clin. Oncol. Off. J. Am. Soc. Clin. Oncol.*, vol. 22, no. 20, pp. 4135–4139, Oct. 2004, doi: 10.1200/JCO.2004.02.107.

[228] R. J. Greenwald, J. R. Tumang, A. Sinha, N. Currier, R. D. Cardiff, T. L. Rothstein, D. V Faller, and G. V Denis, "E mu-BRD2 transgenic mice develop B-cell lymphoma and leukemia.," *Blood*, vol. 103, no. 4, pp. 1475–1484, Feb. 2004, doi: 10.1182/blood-2003-06-2116.

[229] B. Huang, X.-D. Yang, M.-M. Zhou, K. Ozato, and L.-F. Chen, "Brd4 coactivates transcriptional activation of NF-kappaB via specific binding to acetylated RelA.," *Mol. Cell. Biol.*, vol. 29, no. 5, pp. 1375–1387, Mar. 2009, doi: 10.1128/MCB.01365-08.

[230] A. C. Belkina and G. V Denis, "BET domain co-regulators in obesity, inflammation and cancer.," *Nat. Rev. Cancer*, vol. 12, no. 7, pp. 465–477, Jun. 2012, doi: 10.1038/nrc3256.

[231] P. Filippakopoulos and S. Knapp, "Next-generation epigenetic inhibitors.," *Science*, vol. 368, no. 6489, pp. 367–368, Apr. 2020, doi: 10.1126/science.abb5060.

[232] O. Gilan, I. Rioja, K. Knezevic, M. J. Bell, M. M. Yeung, N. R. Harker, E. Y. N. Lam, C.-W. Chung, P. Bamborough, M. Petretich, M. Urh, S. J. Atkinson, A. K. Bassil, E. J. Roberts, D. Vassiliadis, M. L. Burr, A. G. S. Preston, C. Wellaway, T. Werner, *et al.*, "Selective targeting of BD1 and BD2 of the BET proteins in cancer and immunoinflammation.," *Science*, vol. 368, no. 6489, pp. 387–394, Apr. 2020, doi: 10.1126/science.aaz8455.

[233] H. Mahdi, B. A. Fisher, H. Källberg, D. Plant, V. Malmström, J. Rönnelid, P. Charles, B. Ding, L. Alfredsson, L. Padyukov, D. P. M. Symmons, P. J. Venables, L. Klareskog, and K. Lundberg, "Specific interaction between genotype, smoking and autoimmunity to citrullinated alpha-enolase in the etiology of rheumatoid arthritis.," *Nat. Genet.*, vol. 41, no. 12, pp. 1319–1324, Dec. 2009, doi: 10.1038/ng.480.

[234] G. LeRoy, B. Rickards, and S. J. Flint, "The double bromodomain proteins Brd2 and Brd3 couple histone acetylation to transcription.," *Mol. Cell*, vol. 30, no. 1, pp. 51–60, Apr. 2008, doi: 10.1016/j.molcel.2008.01.018.

[235] M. Ullah, N. Pelletier, L. Xiao, S. P. Zhao, K. Wang, C. Degerny, S. Tahmasebi, C. Cayrou, Y. Doyon, S.-L. Goh, N. Champagne, J. Côté, and X.-J. Yang, "Molecular architecture of quartet MOZ/MORF histone acetyltransferase complexes.," *Mol. Cell. Biol.*, vol. 28, no. 22, pp. 6828–6843, Nov. 2008, doi: 10.1128/MCB.01297-08.

[236] J. Morinière, S. Rousseaux, U. Steuerwald, M. Soler-López, S. Curtet, A.-L. Vitte, J. Govin, J. Gaucher, K. Sadoul, D. J. Hart, J. Krijgsveld, S. Khochbin, C. W. Müller, and C. Petosa, "Cooperative binding of two acetylation marks on a histone tail by a single bromodomain.," *Nature*, vol. 461, no. 7264, pp. 664–668, Oct. 2009, doi: 10.1038/nature08397.

[237] S. Ohno, U. Wolf, and N. B. Atkin, "Evolution from fish to mammals by gene duplication.," *Hereditas*, vol. 59, no. 1, pp. 169–187, 1968, doi: 10.1111/j.1601-5223.1968.tb02169.x.

[238] Y. Nakamura, T. Umehara, K. Nakano, M. K. Jang, M. Shirouzu, S. Morita, H. Uda-Tochio, H. Hamana, T. Terada, N. Adachi, T. Matsumoto, A. Tanaka, M. Horikoshi, K. Ozato, B. Padmanabhan, and S. Yokoyama, "Crystal structure of the human BRD2 bromodomain: insights into dimerization and recognition of acetylated histone H4.," *J. Biol. Chem.*, vol. 282, no. 6, pp. 4193–4201, Feb. 2007, doi: 10.1074/jbc.M605971200.

[239] R. Gamsjaeger, S. R. Webb, J. M. Lamonica, A. Billin, G. A. Blobel, and J. P. Mackay, "Structural basis and specificity of acetylated transcription factor GATA1 recognition by BET family bromodomain protein Brd3.," *Mol. Cell. Biol.*, vol. 31, no. 13, pp. 2632–2640, Jul. 2011, doi: 10.1128/MCB.05413-11.

[240] N. Wang, R. Wu, D. Tang, and R. Kang, "The BET family in immunity and disease," *Signal Transduct. Target. Ther.*, vol. 6, no. 1, p. 23, Jan. 2021, doi: 10.1038/s41392-020-00384-4.

[241] F. Wang, H. Liu, W. P. Blanton, A. Belkina, N. K. Lebrasseur, and G. V Denis, "Brd2 disruption in mice causes severe obesity without Type 2 diabetes.," *Biochem. J.*, vol. 425, no. 1, pp. 71–83, Dec. 2009, doi: 10.1042/BJ20090928.

[242] S. Sarkar, E. B. Dammer, E. Malovic, A. L. Olsen, S. A. Raza, T. Gao, H. Xiao, D. L. Oliver, D. Duong, V. Joers, N. Seyfried, M. Huang, T. Kukar, M. G. Tansey, A. G. Kanthasamy, and S. Rangaraju, "Molecular Signatures of Neuroinflammation Induced by αSynuclein Aggregates in Microglial Cells.," *Front. Immunol.*, vol. 11, p. 33, 2020, doi: 10.3389/fimmu.2020.00033.

[243] R. Malhotra, N. Kurian, X.-H. Zhou, F. Jiang, S. Monkley, A. DeMicco, I. G. Clausen, G. Dellgren, G. Edenro, M. J. Ahdesmäki, M. Clausen, L. Öberg, E. Israelsson, G. Belfield, and O. Vaarala, "Altered regulation and expression of genes by BET family of proteins in COPD patients.," *PLoS One*, vol. 12, no. 3, p. e0173115, 2017, doi: 10.1371/journal.pone.0173115.

[244] L. Jin, Z. Wu, W. Xu, X. Hu, J. Zhang, Z. Xue, and L. Cheng, "Identifying gene expression profile of spinal cord injury in rat by bioinformatics strategy.," *Mol. Biol. Rep.*, vol. 41, no. 5, pp. 3169–3177, May 2014, doi: 10.1007/s11033-014-3176-8.

[245] H. Ishii, K. Mimori, M. Mori, and A. Vecchione, "Differentially expressed genes in endothelial differentiation.," *DNA Cell Biol.*, vol. 24, no. 7, pp. 432–437, Jul. 2005, doi: 10.1089/dna.2005.24.432.

[246] J. Cho, Y. H. Chang, Y. J. Heo, S. Kim, N. K. Kim, J. O. Park, W. K. Kang, J. Lee, and K.-M. Kim, "Four distinct immune microenvironment subtypes in gastric adenocarcinoma with special reference to microsatellite instability.," *ESMO open*, vol. 3, no. 3, p. e000326, 2018, doi: 10.1136/esmoopen-2018-000326.

[247] K. Klein, P. A. Kabala, A. M. Grabiec, R. E. Gay, C. Kolling, L.-L. Lin, S. Gay, P. P. Tak, R. K. Prinjha, C. Ospelt, and K. A. Reedquist, "The bromodomain protein inhibitor I-BET151 suppresses expression of inflammatory genes and matrix degrading enzymes in rheumatoid arthritis synovial fibroblasts.," *Ann. Rheum. Dis.*, vol. 75, no. 2, pp. 422–429, Feb. 2016, doi: 10.1136/annrheumdis-2014-205809.

[248] Y. W. Jiang, P. Veschambre, H. Erdjument-Bromage, P. Tempst, J. W. Conaway, R. C. Conaway, and R. D. Kornberg, "Mammalian mediator of transcriptional regulation and its possible role as an end-point of signal transduction pathways.," *Proc. Natl. Acad. Sci. U. S. A.*, vol. 95, no. 15, pp. 8538–8543, Jul. 1998, doi: 10.1073/pnas.95.15.8538.

[249] M. K. Jang, K. Mochizuki, M. Zhou, H.-S. Jeong, J. N. Brady, and K. Ozato, "The bromodomain protein Brd4 is a positive regulatory component of P-TEFb and stimulates RNA polymerase II-dependent transcription.," *Mol. Cell*, vol. 19, no. 4, pp. 523–534, Aug. 2005, doi: 10.1016/j.molcel.2005.06.027.

[250] Z. Yang, J. H. N. Yik, R. Chen, N. He, M. K. Jang, K. Ozato, and Q. Zhou, "Recruitment of P-TEFb for stimulation of transcriptional elongation by the bromodomain protein Brd4.," *Mol. Cell*, vol. 19, no. 4, pp. 535–545, Aug. 2005, doi: 10.1016/j.molcel.2005.06.029.

[251] J. Lovén, H. A. Hoke, C. Y. Lin, A. Lau, D. A. Orlando, C. R. Vakoc, J. E. Bradner, T. I. Lee, and R. A. Young, "Selective inhibition of tumor oncogenes by disruption of super-enhancers," *Cell*, vol. 153, no. 2, pp. 320–334, Apr. 2013, doi: 10.1016/j.cell.2013.03.036.

[252] C. A. French, I. Miyoshi, J. C. Aster, I. Kubonishi, T. G. Kroll, P. Dal Cin, S. O. Vargas, A. R. Perez-Atayde, and J. A. Fletcher, "BRD4 bromodomain gene rearrangement in aggressive carcinoma with translocation t(15;19).," *Am. J. Pathol.*, vol. 159, no. 6, pp. 1987–1992, Dec. 2001, doi: 10.1016/S0002-9440(10)63049-0.

[253] C. A. French, I. Miyoshi, I. Kubonishi, H. E. Grier, A. R. Perez-Atayde, and J. A. Fletcher, "BRD4-NUT fusion oncogene: a novel mechanism in aggressive carcinoma.," *Cancer Res.*, vol. 63, no. 2, pp. 304–307, Jan. 2003.

[254] C. A. French, C. L. Ramirez, J. Kolmakova, T. T. Hickman, M. J. Cameron, M. E. Thyne, J. L. Kutok, J. A. Toretsky, A. K. Tadavarthy, U. R. Kees, J. A. Fletcher, and J. C. Aster, "BRD-NUT oncoproteins: a family of closely related nuclear proteins that block epithelial differentiation and maintain the growth of carcinoma cells.," *Oncogene*, vol. 27, no. 15, pp. 2237–2242, Apr. 2008, doi: 10.1038/sj.onc.1210852.

[255] S. Shatavi, A. Fawole, K. Haberichter, I. Jaiyesimi, and C. French, "Nuclear protein in testis (NUT) midline carcinoma with a novel three-way translocation (4;15;19)(q13;q14;p13.1).," *Pathology*, vol. 48, no. 6. England, pp. 620–623, Oct. 2016. doi: 10.1016/j.pathol.2016.06.010.

[256] M. D. Rudman, J. S. Choi, H. E. Lee, S. K. Tan, N. G. Ayad, and J. K. Lee, "Bromodomain and extraterminal domain-containing protein inhibition attenuates acute inflammation after spinal cord injury.," *Exp. Neurol.*, vol. 309, pp. 181–192, Nov. 2018, doi: 10.1016/j.expneurol.2018.08.005.

[257] J. Wang, G.-L. Li, S.-L. Ming, C.-F. Wang, L.-J. Shi, B.-Q. Su, H.-T. Wu, L. Zeng, Y.-Q. Han, Z.-H. Liu, D.-W. Jiang, Y.-K. Du, X.-D. Li, G.-P. Zhang, G.-Y. Yang, and B.-B. Chu, "BRD4 inhibition exerts anti-viral activity through DNA damage-dependent innate immune responses.," *PLoS Pathog.*, vol. 16, no. 3, p. e1008429, Mar. 2020, doi: 10.1371/journal.ppat.1008429.

[258] E. Shang, H. D. Nickerson, D. Wen, X. Wang, and D. J. Wolgemuth, "The first bromodomain of Brdt, a testis-specific member of the BET sub-family of double-bromodomain-containing proteins, is essential for male germ cell differentiation.," *Development*, vol. 134, no. 19, pp. 3507–3515, Oct. 2007, doi: 10.1242/dev.004481.

[259] B. D. Berkovits and D. J. Wolgemuth, "The first bromodomain of the testis-specific double bromodomain protein Brdt is required for chromocenter organization that is modulated by genetic background.," *Dev. Biol.*, vol. 360, no. 2, pp. 358–368, Dec. 2011, doi: 10.1016/j.ydbio.2011.10.005.

[260] L. Chen, S. Cai, J.-M. Wang, Y.-Y. Huai, P.-H. Lu, and Q. Chu, "BRDT promotes ovarian cancer cell growth," *Cell Death Dis.*, vol. 11, no. 11, p. 1021, Nov. 2020, doi: 10.1038/s41419-020-03225-y.

[261] K. I. Aston, C. Krausz, I. Laface, E. Ruiz-Castané, and D. T. Carrell, "Evaluation of 172 candidate polymorphisms for association with oligozoospermia or azoospermia in a large cohort of men of European descent.," *Hum. Reprod.*, vol. 25, no. 6, pp. 1383–1397, Jun. 2010, doi: 10.1093/humrep/deq081.

[262] L. Zeng, J. Li, M. Muller, S. Yan, S. Mujtaba, C. Pan, Z. Wang, and M. M. Zhou, "Selective small molecules blocking HIV-1 tat and coactivator PCAF association," *J. Am. Chem. Soc.*, vol. 127, no. 8, pp. 2376–2377, 2005, doi: 10.1021/ja044885g.

[263] Sachchidanand, L. Resnick-Silverman, S. Yan, S. Mutjaba, W.-J. Liu, L. Zeng, J. J. Manfredi, and M.-M. Zhou, "Target structure-based discovery of small molecules that block human p53 and CREB binding protein association.," *Chem. Biol.*, vol. 13, no. 1, pp. 81–90, Jan. 2006, doi: 10.1016/j.chembiol.2005.10.014.

[264] J. Endoh, "(12) United States Patent," vol. 2, no. 12, 2011.

[265] H. Hikawa and K. Sugahara, "(12) United States Patent," vol. 2, no. 12, 2013, doi: 10.1038/sjonc.1210852.

[266] S. G. Smith, R. Sanchez, and M.-M. Zhou, "Privileged diazepine compounds and their emergence as bromodomain inhibitors.," *Chem. Biol.*, vol. 21, no. 5, pp. 573–583, May 2014, doi: 10.1016/j.chembiol.2014.03.004.

[267] M. Brand, A. M. Measures, B. G. Wilson, W. A. Cortopassi, R. Alexander, M. Höss, D. S. Hewings, T. P. C. Rooney, R. S. Paton, and S. J. Conway, "Small molecule inhibitors of bromodomain - Acetyl-lysine interactions," *ACS Chem. Biol.*, vol. 10, no. 1, pp. 22–39, 2015, doi: 10.1021/cb500996u.

[268] P. Filippakopoulos, J. Qi, S. Picaud, Y. Shen, W. B. Smith, O. Fedorov, E. M. Morse, T. Keates, T. T. Hickman, I. Felletar, M. Philpott, S. Munro, M. R. McKeown, Y. Wang, A. L. Christie, N. West, M. J. Cameron, B. Schwartz, T. D. Heightman, *et al.*, "Selective inhibition of BET bromodomains.," *Nature*, vol. 468, no. 7327, pp. 1067–1073, Dec. 2010, doi: 10.1038/nature09504.

[269] G. Zhang, R. Liu, Y. Zhong, A. N. Plotnikov, W. Zhang, L. Zeng, E. Rusinova, G. Gerona-Nevarro, N. Moshkina, J. Joshua, P. Y. Chuang, M. Ohlmeyer, J. C. He, and M.-M. Zhou, "Down-regulation of NF-κB transcriptional activity in HIV-associated kidney disease by BRD4 inhibition.," *J. Biol. Chem.*, vol. 287, no. 34, pp. 28840–28851, Aug. 2012, doi: 10.1074/jbc.M112.359505.

[270] C. Wong, S. V Laddha, L. Tang, E. Vosburgh, A. J. Levine, E. Normant, P. Sandy, C. R. Harris, C. S. Chan, and E. Y. Xu, "The bromodomain and extra-terminal inhibitor CPI203 enhances the antiproliferative effects of rapamycin on human neuroendocrine tumors.," *Cell Death Dis.*, vol. 5, no. 10, p. e1450, Oct. 2014, doi: 10.1038/cddis.2014.396.

[271] A. Moros, V. Rodríguez, I. Saborit-Villarroya, A. Montraveta, P. Balsas, P. Sandy, A. Martínez, A. Wiestner, E. Normant, E. Campo, P. Pérez-Galán, D. Colomer, and G. Roué, "Synergistic antitumor activity of lenalidomide with the BET bromodomain inhibitor CPI203 in bortezomib-resistant mantle cell lymphoma.," *Leukemia*, vol. 28, no. 10, pp. 2049–2059, Oct. 2014, doi: 10.1038/leu.2014.106.

[272] M. E. Riveiro, L. Astorgues-Xerri, R. Vazquez, R. Frapolli, I. Kwee, A. Rinaldi, E. Odore, K. Rezai, M. Bekradda, G. Inghirami, M. D'Incalci, K. Noel, E. Cvitkovic, E. Raymond, and F. Bertoni, "OTX015 (MK-8628), a novel BET inhibitor, exhibits antitumor activity in non-small cell and small cell lung cancer models harboring different oncogenic mutations," *Oncotarget*, vol. 7, no. 51, pp. 84675–84687, Dec. 2016, doi: 10.18632/oncotarget.13181.

[273] J. K. Noel, K. Iwata, S. Ooike, K. Sugahara, H. Nakamura, and M. Daibata, "Abstract C244: Development of the BET bromodomain inhibitor OTX015.," *Mol. Cancer Ther.*, vol. 12, no. 11_Supplement, pp. C244–C244, Nov. 2013, doi: 10.1158/1535-7163.TARG-13-C244.

[274] R. Gosmini, V. L. Nguyen, J. Toum, C. Simon, J.-M. G. Brusq, G. Krysa, O. Mirguet, A. M. Riou-Eymard, E. V Boursier, L. Trottet, P. Bamborough, H. Clark, C. Chung, L. Cutler, E. H. Demont, R. Kaur, A. J. Lewis, M. B. Schilling, P. E. Soden, *et al.*, "The discovery of I-BET726 (GSK1324726A), a potent tetrahydroquinoline ApoA1 up-regulator and selective BET bromodomain inhibitor.," *J. Med. Chem.*, vol. 57, no. 19, pp. 8111–8131, Oct. 2014, doi: 10.1021/jm5010539.

[275] S. Picaud, C. Wells, I. Felletar, D. Brotherton, S. Martin, P. Savitsky, B. Diez-Dacal, M. Philpott, C. Bountra, H. Lingard, O. Fedorov, S. Müller, P. E. Brennan, S. Knapp, and P. Filippakopoulos, "RVX-208, an inhibitor of BET transcriptional regulators with selectivity for the second bromodomain.," *Proc. Natl. Acad. Sci. U. S. A.*, vol. 110, no. 49, pp. 19754–19759, Dec. 2013, doi: 10.1073/pnas.1310658110.

[276] S. Picaud, D. Da Costa, A. Thanasopoulou, P. Filippakopoulos, P. V Fish, M. Philpott, O. Fedorov, P. Brennan, M. E. Bunnage, D. R. Owen, J. E. Bradner, P. Taniere, B. O'Sullivan, S. Müller, J. Schwaller, T. Stankovic, and S. Knapp, "PFI-1, a highly selective protein interaction inhibitor, targeting BET Bromodomains.," *Cancer Res.*, vol. 73, no. 11, pp. 3336–3346, Jun. 2013, doi: 10.1158/0008-5472.CAN-12-3292.

[277] D. S. Hewings, M. Wang, M. Philpott, O. Fedorov, S. Uttarkar, P. Filippakopoulos, S. Picaud, C. Vuppusetty, B. Marsden, S. Knapp, S. J. Conway, and T. D. Heightman, "3,5-dimethylisoxazoles act as acetyl-lysine-mimetic bromodomain ligands.," *J. Med. Chem.*, vol. 54, no. 19, pp. 6761–6770, Oct. 2011, doi: 10.1021/jm200640v.

[278] M. Gacias, G. Gerona-Navarro, A. N. Plotnikov, G. Zhang, L. Zeng, J. Kaur, G. Moy, E. Rusinova, Y. Rodriguez, B. Matikainen, A. Vincek, J. Joshua, P. Casaccia, and M.-M. Zhou, "Selective chemical modulation of gene transcription favors oligodendrocyte lineage progression.," *Chem. Biol.*, vol. 21, no. 7, pp. 841–854, Jul. 2014, doi: 10.1016/j.chembiol.2014.05.009.

[279] G. Zhang, A. N. Plotnikov, E. Rusinova, T. Shen, K. Morohashi, J. Joshua, L. Zeng, S. Mujtaba, M. Ohlmeyer, and M.-M. Zhou, "Structure-guided design of potent diazobenzene inhibitors for the BET bromodomains.," *J. Med. Chem.*, vol. 56, no. 22, pp. 9251–9264, Nov. 2013, doi: 10.1021/jm401334s.

[280] K. Cheung, G. Lu, R. Sharma, A. Vincek, R. Zhang, A. N. Plotnikov, F. Zhang, Q. Zhang, Y. Ju, Y. Hu, L. Zhao, X. Han, J. Meslamani, F. Xu, A. Jaganathan, T. Shen, H. Zhu, E. Rusinova, L. Zeng, *et al.*, "BET N-terminal bromodomain inhibition selectively blocks Th17 cell differentiation and ameliorates colitis in mice.," *Proc. Natl. Acad. Sci. U. S. A.*, vol. 114, no. 11, pp. 2952–2957, Mar. 2017, doi: 10.1073/pnas.1615601114.

[281] R. P. Law, S. J. Atkinson, P. Bamborough, C.-W. Chung, E. H. Demont, L. J. Gordon, M. Lindon, R. K. Prinjha, A. J. B. Watson, and D. J. Hirst, "Discovery of Tetrahydroquinoxalines as Bromodomain and Extra-Terminal Domain (BET) Inhibitors with Selectivity for the Second Bromodomain.," *J. Med. Chem.*, vol. 61, no. 10, pp. 4317–4334, May 2018, doi: 10.1021/acs.jmedchem.7b01666.

[282] E. J. Faivre, K. F. McDaniel, D. H. Albert, S. R. Mantena, J. P. Plotnik, D. Wilcox, L. Zhang, M. H. Bui, G. S. Sheppard, L. Wang, V. Sehgal, X. Lin, X. Huang, X. Lu, T. Uziel, P. Hessler, L. T. Lam, R. J. Bellin, G. Mehta, *et al.*, "Selective inhibition of the BD2 bromodomain of BET proteins in prostate cancer.," *Nature*, vol. 578, no. 7794, pp. 306–310, Feb. 2020, doi: 10.1038/s41586-020-1930-8.

[283] X. Zhang, T. Zegar, T. Weiser, F. H. Hamdan, B.-T. Berger, R. Lucas, D.-Ii. Balourdas, S. Ladigan, P. F. Cheung, S.-T. Liffers, M. Trajkovic-Arsic, B. Scheffler, A. C. Joerger, S. A. Hahn, S. A. Johnsen, S. Knapp, and J. T. Siveke, "Characterization of a dual BET/HDAC inhibitor for treatment of pancreatic ductal adenocarcinoma.," *Int. J. cancer*, vol. 147, no. 10, pp. 2847–2861, Nov. 2020, doi: 10.1002/ijc.33137.

[284] F. Spriano, E. Gaudio, L. Cascione, C. Tarantelli, F. Melle, G. Motta, V. Priebe, A. Rinaldi, G. Golino, A. A. Mensah, L. Aresu, E. Zucca, S. Pileri, M. Witcher, B. Brown, C. Wahlestedt, F. Giles, A. Stathis, and F. Bertoni, "Antitumor activity of the dual BET and CBP/EP300 inhibitor NEO2734.," *Blood Adv.*, vol. 4, no. 17, pp. 4124–4135, Sep. 2020, doi: 10.1182/bloodadvances.2020001879.

[285] L. Carlino and G. Rastelli, "Dual Kinase-Bromodomain Inhibitors in Anticancer Drug Discovery: A Structural and Pharmacological Perspective," *J. Med. Chem.*, vol. 59, no. 20, pp. 9305–9320, 2016, doi: 10.1021/acs.jmedchem.6b00438.

[286] M. P. Martin, S. H. Olesen, G. I. Georg, and E. Schönbrunn, "Cyclin-dependent kinase inhibitor dinaciclib interacts with the acetyl-lysine recognition site of bromodomains.," *ACS Chem. Biol.*, vol. 8, no. 11, pp. 2360–2365, Nov. 2013, doi: 10.1021/cb4003283.

[287] M. Boi, E. Gaudio, P. Bonetti, I. Kwee, E. Bernasconi, C. Tarantelli, A. Rinaldi, M. Testoni, L. Cascione, M. Ponzoni, A. A. Mensah, A. Stathis, G. Stussi, M. E. Riveiro, P. Herait, G. Inghirami, E. Cvitkovic, E. Zucca, and F. Bertoni, "The BET Bromodomain Inhibitor OTX015 Affects Pathogenetic Pathways in Preclinical B-cell Tumor Models and Synergizes with Targeted Drugs.," *Clin. cancer Res. an Off. J. Am. Assoc. Cancer Res.*, vol. 21, no. 7, pp. 1628–1638, Apr. 2015, doi: 10.1158/1078-0432.CCR-14-1561.

[288] S. Postel-Vinay, K. Herbschleb, C. Massard, V. Woodcock, J.-C. Soria, A. O. Walter, F. Ewerton, M. Poelman, N. Benson, M. Ocker, G. Wilkinson, and M. Middleton, "First-in-human phase I study of the bromodomain and extraterminal motif inhibitor BAY 1238097: emerging pharmacokinetic/pharmacodynamic relationship and early termination due to unexpected toxicity.," *Eur. J. Cancer*, vol. 109, pp. 103–110, Mar. 2019, doi: 10.1016/j.ejca.2018.12.020.

[289] S. A. Piha-Paul, C. L. Hann, C. A. French, S. Cousin, I. Braña, P. A. Cassier, V. Moreno, J. S. de Bono, S. D. Harward, G. Ferron-Brady, O. Barbash, A. Wyce, Y. Wu, T. Horner, M. Annan, N. J. Parr, R. K. Prinjha, C. L. Carpenter, J. Hilton, *et al.*, "Phase 1 Study of Molibresib (GSK525762), a Bromodomain and Extra-Terminal Domain Protein Inhibitor, in NUT Carcinoma and Other Solid Tumors.," *JNCI cancer Spectr.*, vol. 4, no. 2, p. pkz093, Apr. 2020, doi: 10.1093/jncics/pkz093.

[290] G. S. Sheppard, L. Wang, S. D. Fidanze, L. A. Hasvold, D. Liu, J. K. Pratt, C. H. Park, K. Longenecker, W. Qiu, M. Torrent, P. J. Kovar, M. Bui, E. Faivre, X. Huang, X. Lin, D. Wilcox, L. Zhang, Y. Shen, D. H. Albert, *et al.*, "Discovery of N-Ethyl-4-[2-(4-fluoro-2,6-dimethyl-phenoxy)-5-(1-hydroxy-1-methyl-ethyl)phenyl]-6-methyl-7-oxo-1H-pyrrolo[2,3-c]pyridine-2-carboxamide (ABBV-744), a BET Bromodomain Inhibitor with Selectivity for the Second Bromodomain.," *J. Med. Chem.*, vol. 63, no. 10, pp. 5585–5623, May 2020, doi: 10.1021/acs.jmedchem.0c00628.

[291] E. E. Stratikopoulos, M. Dendy, M. Szabolcs, A. J. Khaykin, C. Lefebvre, M.-M. Zhou, and R. Parsons, "Kinase and BET Inhibitors Together Clamp Inhibition of PI3K Signaling and Overcome Resistance to Therapy.," *Cancer Cell*, vol. 27, no. 6, pp. 837–851, Jun. 2015, doi: 10.1016/j.ccell.2015.05.006.

[292] I. M. Echevarría-Vargas, P. I. Reyes-Uribe, A. N. Guterres, X. Yin, A. V Kossenkov, Q. Liu, G. Zhang, C. Krepler, C. Cheng, Z. Wei, R. Somasundaram, G. Karakousis, W. Xu, J. J. Morrissette, Y. Lu, G. B. Mills, R. J. Sullivan, M. Benchun, D. T. Frederick, *et al.*, "Co-targeting BET and MEK as salvage therapy for MAPK and checkpoint inhibitor-resistant melanoma.," *EMBO Mol. Med.*, vol. 10, no. 5, May 2018, doi: 10.15252/emmm.201708446.

[293] A. M. Kurimchak, C. Shelton, K. E. Duncan, K. J. Johnson, J. Brown, S. O'Brien, R. Gabbasov, L. S. Fink, Y. Li, N. Lounsbury, M. Abou-Gharbia, W. E. Childers, D. C. Connolly, J. Chernoff, J. R. Peterson, and J. S. Duncan, "Resistance to BET Bromodomain Inhibitors Is Mediated by Kinome Reprogramming in Ovarian Cancer.," *Cell Rep.*, vol. 16, no. 5, pp. 1273–1286, Aug. 2016, doi: 10.1016/j.celrep.2016.06.091.

[294] T. Shorstova, W. D. Foulkes, and M. Witcher, "Achieving clinical success with BET inhibitors as anti-cancer agents," *Br. J. Cancer*, vol. 124, no. 9, pp. 1478–1490, 2021, doi: 10.1038/s41416-021-01321-0.

[295] K. Kamieniarz and R. Schneider, "Tools to tackle protein acetylation.," *Chem. Biol.*, vol. 16, no. 10, pp. 1027–1029, Oct. 2009, doi: 10.1016/j.chembiol.2009.10.002.

[296] J. Guo, J. Wang, J. S. Lee, and P. G. Schultz, "Site-specific incorporation of methyl- and acetyl-lysine analogues into recombinant proteins.," *Angew. Chem. Int. Ed. Engl.*, vol. 47, no. 34, pp. 6399–6401, 2008, doi: 10.1002/anie.200802336.

[297] G. Proietti, G. Rainone, J. C. J. Hintzen, and J. Mecinović, "Exploring the Histone Acylome through Incorporation of γ-Thialysine on Histone Tails.," *Bioconjug. Chem.*, vol. 31, no. 3, pp. 844–851, Mar. 2020, doi: 10.1021/acs.bioconjchem.0c00012.

[298] S. B. Kirchgäßner, "Synthesis , biochemical characterization and genetic encoding of acetyl-lysine mimicking amino acids for bromodomains and deacetylases," 2021.

[299] P. Wójcik and Ł. Berlicki, "Peptide-based inhibitors of protein-protein interactions," *Bioorganic Med. Chem. Lett.*, vol. 26, no. 3, pp. 707–713, 2016, doi: 10.1016/j.bmcl.2015.12.084.

[300] A. Bhat, L. R. Roberts, and J. J. Dwyer, "Lead discovery and optimization strategies for peptide macrocycles," *Eur. J. Med. Chem.*, vol. 94, pp. 471–479, 2015, doi: 10.1016/j.ejmech.2014.07.083.

[301] F. Stricher, L. Martin, and C. Vita, "Design of miniproteins by the transfer of active sites onto small-size scaffolds.," *Methods Mol. Biol.*, vol. 340, pp. 113–149, 2006, doi: 10.1385/1-59745-116-9:113.

[302] F. Zoller, A. Markert, P. Barthe, W. Zhao, W. Weichert, V. Askoxylakis, A. Altmann, W. Mier, and U. Haberkorn, "Combination of phage display and molecular grafting generates highly specific tumor-targeting miniproteins.," *Angew. Chem. Int. Ed. Engl.*, vol. 51, no. 52, pp. 13136–13139, Dec. 2012, doi: 10.1002/anie.201203857.

[303] D. J. Craik, J. E. Swedberg, J. S. Mylne, and M. Cemazar, "Cyclotides as a basis for drug design.," *Expert Opin. Drug Discov.*, vol. 7, no. 3, pp. 179–194, Mar. 2012, doi: 10.1517/17460441.2012.661554.

[304] Y. Ji, S. Majumder, M. Millard, R. Borra, T. Bi, A. Y. Elnagar, N. Neamati, A. Shekhtman, and J. A. Camarero, "In vivo activation of the p53 tumor suppressor pathway by an engineered cyclotide.," *J. Am. Chem. Soc.*, vol. 135, no. 31, pp. 11623–11633, Aug. 2013, doi: 10.1021/ja405108p.

[305] D. S. Daniels and A. Schepartz, "Intrinsically cell-permeable miniature proteins based on a minimal cationic PPII motif.," *J. Am. Chem. Soc.*, vol. 129, no. 47, pp. 14578–14579, Nov. 2007, doi: 10.1021/ja0772445.

[306] B. A. Smith, D. S. Daniels, A. E. Coplin, G. E. Jordan, L. M. McGregor, and A. Schepartz, "Minimally cationic cell-permeable miniature proteins via alpha-helical arginine display.," *J. Am. Chem. Soc.*, vol. 130, no. 10, pp. 2948–2949, Mar. 2008, doi: 10.1021/ja800074v.

[307] A. Arvai, "Adxv." https://www.scripps.edu/tainer/arvai/adxv.html (accessed Jun. 09, 2022).

[308] Dectris, "ALBULA Software." https://www.dectris.com/detectors/albula-software/ (accessed Jun. 09, 2022).

[309] M. D. Winn, C. C. Ballard, K. D. Cowtan, E. J. Dodson, P. Emsley, P. R. Evans, R. M. Keegan, E. B. Krissinel, A. G. W. Leslie, A. McCoy, S. J. McNicholas, G. N. Murshudov, N. S. Pannu, E. A. Potterton, H. R. Powell, R. J. Read, A. Vagin, and K. S. Wilson, "Overview of the CCP4 suite and current developments.," *Acta Crystallogr. D. Biol. Crystallogr.*, vol. 67, no. Pt 4, pp. 235–242, Apr. 2011, doi: 10.1107/S0907444910045749.

[310] P. Emsley, B. Lohkamp, W. G. Scott, and K. Cowtan, "Features and development of Coot.," *Acta Crystallogr. D. Biol. Crystallogr.*, vol. 66, no. Pt 4, pp. 486–501, Apr. 2010, doi: 10.1107/S0907444910007493.

[311] B. W. Matthews, "Solvent content of protein crystals.," *J. Mol. Biol.*, vol. 33, no. 2, pp. 491–497, Apr. 1968, doi: 10.1016/0022-2836(68)90205-2.

[312] K. A. Kantardjieff and B. Rupp, "Matthews coefficient probabilities: Improved estimates for unit cell contents of proteins, DNA, and protein-nucleic acid complex crystals.," *Protein Sci.*, vol. 12, no. 9, pp. 1865–1871, Sep. 2003, doi: 10.1110/ps.0350503.

[313] C. J. Williams, J. J. Headd, N. W. Moriarty, M. G. Prisant, L. L. Videau, L. N. Deis, V. Verma, D. A. Keedy, B. J. Hintze, V. B. Chen, S. Jain, S. M. Lewis, W. B. 3rd Arendall, J. Snoeyink, P. D. Adams, S. C. Lovell, J. S. Richardson, and D. C. Richardson, "MolProbity: More and better reference data for improved all-atom structure validation.," *Protein Sci.*, vol. 27, no. 1, pp. 293–315, Jan. 2018, doi: 10.1002/pro.3330.

[314] I. W. Davis, A. Leaver-Fay, V. B. Chen, J. N. Block, G. J. Kapral, X. Wang, L. W. Murray, W. B. 3rd Arendall, J. Snoeyink, J. S. Richardson, and D. C. Richardson, "MolProbity: all-atom contacts and structure validation for proteins and nucleic acids.," *Nucleic Acids Res.*, vol. 35, no. Web Server issue, pp. W375-83, Jul. 2007, doi: 10.1093/nar/gkm216.

[315] V. B. Chen, W. B. 3rd Arendall, J. J. Headd, D. A. Keedy, R. M. Immormino, G. J. Kapral, L. W. Murray, J. S. Richardson, and D. C. Richardson, "MolProbity: all-atom structure validation for macromolecular crystallography.," *Acta Crystallogr. D. Biol. Crystallogr.*, vol. 66, no. Pt 1, pp. 12–21, Jan. 2010, doi: 10.1107/S0907444909042073.

[316] A. J. McCoy, R. W. Grosse-Kunstleve, P. D. Adams, M. D. Winn, L. C. Storoni, and R. J. Read, "Phaser crystallographic software.," *J. Appl. Crystallogr.*, vol. 40, no. Pt 4, pp. 658–674, Aug. 2007, doi: 10.1107/S0021889807021206.

[317] P. D. Adams, P. V Afonine, G. Bunkóczi, V. B. Chen, I. W. Davis, N. Echols, J. J. Headd, L.-W. Hung, G. J. Kapral, R. W. Grosse-Kunstleve, A. J. McCoy, N. W. Moriarty, R. Oeffner, R. J. Read, D. C. Richardson, J. S. Richardson, T. C. Terwilliger, and P. H. Zwart, "PHENIX: a comprehensive Python-based system for macromolecular structure solution.," *Acta Crystallogr. D. Biol. Crystallogr.*, vol. 66, no. Pt 2, pp. 213–221, Feb. 2010, doi: 10.1107/S0907444909052925.

[318] N. W. Moriarty, R. W. Grosse-Kunstleve, and P. D. Adams, "electronic Ligand Builder and Optimization Workbench (eLBOW): a tool for ligand coordinate and restraint generation.," *Acta Crystallogr. D. Biol. Crystallogr.*, vol. 65, no. Pt 10, pp. 1074–1080, Oct. 2009, doi: 10.1107/S0907444909029436.

[319] P. V Afonine, R. W. Grosse-Kunstleve, N. Echols, J. J. Headd, N. W. Moriarty, M. Mustyakimov, T. C. Terwilliger, A. Urzhumtsev, P. H. Zwart, and P. D. Adams, "Towards automated crystallographic structure refinement with phenix.refine.," *Acta Crystallogr. D. Biol. Crystallogr.*, vol. 68, no. Pt 4, pp. 352–367, Apr. 2012, doi: 10.1107/S0907444912001308.

[320] P. H. Zwart, R. W. Grosse-Kunstleve, and P. D. Adams, "Xtriage and Fest: automatic assessment of X-ray data and substructure structure factor estimation," *CCP4 newsletter No. 43*, 2005.

[321] L. Urzhumtseva, P. V Afonine, P. D. Adams, and A. Urzhumtsev, "Crystallographic model quality at a glance.," *Acta Crystallogr. D. Biol. Crystallogr.*, vol. 65, no. Pt 3, pp. 297–300, Mar. 2009, doi: 10.1107/S0907444908044296.

[322] W. Kabsch, "XDS.," *Acta Crystallogr. D. Biol. Crystallogr.*, vol. 66, no. Pt 2, pp. 125–132, Feb. 2010, doi: 10.1107/S0907444909047337.

[323] "XDSGUI." https://strucbio.biologie.uni-konstanz.de/xdswiki/index.php/XDSGUI (accessed Jun. 09, 2022).

[324] K. Diederichs, "Some aspects of quantitative analysis and correction of radiation damage.," *Acta Crystallogr. D. Biol. Crystallogr.*, vol. 62, no. Pt 1, pp. 96–101, Jan. 2006, doi: 10.1107/S0907444905031537.

[325] P. H. Zwart, R. W. Grosse-kunsteleve, and P. D. Adams, "Characterization of X-ray data sets," *CCP4 newsletter No. 42*, 2005.

[326] B. AT, "Free R value: a novel statistical quantity for assessing the accuracy of crystal structures," *Nature*, vol. 355, no. 6359, pp. 472–5, 1992.

[327] Y. Li, B. R. Sabari, T. Panchenko, H. Wen, D. Zhao, H. Guan, L. Wan, H. Huang, Z. Tang, Y. Zhao, R. G. Roeder, X. Shi, C. D. Allis, and H. Li, "Molecular Coupling of Histone Crotonylation and Active Transcription by AF9 YEATS Domain.," *Mol. Cell*, vol. 62, no. 2, pp. 181–193, Apr. 2016, doi: 10.1016/j.molcel.2016.03.028.

[328] F. Vollmuth, W. Blankenfeldt, and M. Geyer, "Structures of the dual bromodomains of the P-TEFb-activating protein Brd4 at atomic resolution.," *J. Biol. Chem.*, vol. 284, no. 52, pp. 36547–36556, Dec. 2009, doi: 10.1074/jbc.M109.033712.

[329] J.-P. Lambert, S. Picaud, T. Fujisawa, H. Hou, P. Savitsky, L. Uusküla-Reimand, G. D. Gupta, H. Abdouni, Z.-Y. Lin, M. Tucholska, J. D. R. Knight, B. Gonzalez-Badillo, N. St-Denis, J. A. Newman, M. Stucki, L. Pelletier, N. Bandeira, M. D. Wilson, P. Filippakopoulos, *et al.*, "Interactome Rewiring Following Pharmacological Targeting of BET Bromodomains.," *Mol. Cell*, vol. 73, no. 3, pp. 621-638.e17, Feb. 2019, doi: 10.1016/j.molcel.2018.11.006.

[330] O. Carugo, "Correlation between occupancy and B factor of water molecules in protein crystal structures," *Protein Eng. Des. Sel.*, vol. 12, no. 12, pp. 1021–1024, Dec. 1999, doi: 10.1093/protein/12.12.1021.

[331] A. Doszpoly, B. Harrach, S. LaPatra, and M. Benkő, "Unconventional gene arrangement and content revealed by full genome analysis of the white sturgeon adenovirus, the single member of the genus Ichtadenovirus.," *Infect. Genet. Evol. J. Mol. Epidemiol. Evol. Genet. Infect. Dis.*, vol. 75, p. 103976, Nov. 2019, doi: 10.1016/j.meegid.2019.103976.

[332] A. J. Davison, K. M. Wright, and B. Harrach, "DNA sequence of frog adenovirus.," *J. Gen. Virol.*, vol. 81, no. Pt 10, pp. 2431–2439, Oct. 2000, doi: 10.1099/0022-1317-81-10-2431.

[333] R. C. Hoeben and T. G. Uil, "Adenovirus DNA replication.," *Cold Spring Harb. Perspect. Biol.*, vol. 5, no. 3, p. a013003, Mar. 2013, doi: 10.1101/cshperspect.a013003.

[334] W. P. ROWE, R. J. HUEBNER, L. K. GILMORE, R. H. PARROTT, and T. G. WARD, "Isolation of a cytopathogenic agent from human adenoids undergoing spontaneous degeneration in tissue culture.," *Proc. Soc. Exp. Biol. Med. Soc. Exp. Biol. Med. (New York, N.Y.)*, vol. 84, no. 3, pp. 570–573, Dec. 1953, doi: 10.3181/00379727-84-20714.

[335] M. R. HILLEMAN and J. H. WERNER, "Recovery of new agent from patients with acute respiratory illness.," *Proc. Soc. Exp. Biol. Med. Soc. Exp. Biol. Med. (New York, N.Y.)*, vol. 85, no. 1, pp. 183–188, Jan. 1954, doi: 10.3181/00379727-85-20825.

[336] J. F. ENDERS, J. A. BELL, J. H. DINGLE, T. J. FRANCIS, M. R. HILLEMAN, R. J. HUEBNER, and A. M. PAYNE, "Adenoviruses: group name proposed for new respiratory-tract viruses.," *Science*, vol. 124, no. 3212, pp. 119–120, Jul. 1956, doi: 10.1126/science.124.3212.119.

[337] HAdV working group, "HAdV working group," *HAdV working group*. 2019.

[338] M. P. Walsh, A. Chintakuntlawar, C. M. Robinson, I. Madisch, B. Harrach, N. R. Hudson, D. Schnurr, A. Heim, J. Chodosh, D. Seto, and M. S. Jones, "Evidence of molecular evolution driven by recombination events influencing tropism in a novel human adenovirus that causes epidemic keratoconjunctivitis.," *PLoS One*, vol. 4, no. 6, p. e5635, Jun. 2009, doi: 10.1371/journal.pone.0005635.

[339] A. M. Leen and C. M. Rooney, "Adenovirus as an emerging pathogen in immunocompromised patients.," *Br. J. Haematol.*, vol. 128, no. 2, pp. 135–144, Jan. 2005, doi: 10.1111/j.1365-2141.2004.05218.x.

[340] R. W. Horne, S. Brenner, A. P. Waterson, and P. Wildy, "The icosahedral form of an adenovirus," *J. Mol. Biol.*, vol. 1, no. 1, pp. 84-IN15, 1959, doi: https://doi.org/10.1016/S0022-2836(59)80011-5.

[341] R. C. Valentine and H. G. Pereira, "Antigens and structure of the adenovirus.," *J. Mol. Biol.*, vol. 13, no. 1, pp. 13–20, Aug. 1965, doi: 10.1016/s0022-2836(65)80076-6.

[342] H. Liu, L. Jin, S. B. S. Koh, I. Atanasov, S. Schein, L. Wu, and Z. H. Zhou, "Atomic structure of human adenovirus by cryo-EM reveals interactions among protein networks.," *Science*, vol. 329, no. 5995, pp. 1038–1043, Aug. 2010, doi: 10.1126/science.1187433.

[343] V. S. Reddy, S. K. Natchiar, P. L. Stewart, and G. R. Nemerow, "Crystal structure of human adenovirus at 3.5 A resolution.," *Science*, vol. 329, no. 5995, pp. 1071–1075, Aug. 2010, doi: 10.1126/science.1187292.

[344] I. Donovan-Banfield, A. S. Turnell, J. A. Hiscox, K. N. Leppard, and D. A. Matthews, "Deep splicing plasticity of the human adenovirus type 5 transcriptome drives virus evolution.," *Commun. Biol.*, vol. 3, no. 1, p. 124, Mar. 2020, doi: 10.1038/s42003-020-0849-9.

[345] F.-C. Zhu, X.-H. Guan, Y.-H. Li, J.-Y. Huang, T. Jiang, L.-H. Hou, J.-X. Li, B.-F. Yang, L. Wang, W.-J. Wang, S.-P. Wu, Z. Wang, X.-H. Wu, J.-J. Xu, Z. Zhang, S.-Y. Jia, B.-S. Wang, Y. Hu, J.-J. Liu, *et al.*, "Immunogenicity and safety of a recombinant adenovirus type-5-vectored COVID-19 vaccine in healthy adults aged 18 years or older: a randomised, double-blind, placebo-controlled, phase 2 trial.," *Lancet (London, England)*, vol. 396, no. 10249, pp. 479–488, Aug. 2020, doi: 10.1016/S0140-6736(20)31605-6.

[346] J. Sadoff, G. Gray, A. Vandebosch, V. Cárdenas, G. Shukarev, B. Grinsztejn, P. A. Goepfert, C. Truyers, H. Fennema, B. Spiessens, K. Offergeld, G. Scheper, K. L. Taylor, M. L. Robb, J. Treanor, D. H. Barouch, J. Stoddard, M. F. Ryser, M. A. Marovich, *et al.*, "Safety and Efficacy of Single-Dose Ad26.COV2.S Vaccine against Covid-19.," *N. Engl. J. Med.*, vol. 384, no. 23, pp. 2187–2201, Jun. 2021, doi: 10.1056/NEJMoa2101544.

[347] D. Y. Logunov, I. V Dolzhikova, D. V Shcheblyakov, A. I. Tukhvatulin, O. V Zubkova, A. S. Dzharullaeva, A. V Kovyrshina, N. L. Lubenets, D. M. Grousova, A. S. Erokhova, A. G. Botikov, F. M. Izhaeva, O. Popova, T. A. Ozharovskaya, I. B. Esmagambetov, I. A. Favorskaya, D. I. Zrelkin, D. V Voronina, D. N. Shcherbinin, *et al.*, "Safety and efficacy of an rAd26 and rAd5 vector-based heterologous prime-boost COVID-19 vaccine: an interim analysis of a randomised controlled phase 3 trial in Russia.," *Lancet (London, England)*, vol. 397, no. 10275, pp. 671–681, Feb. 2021, doi: 10.1016/S0140-6736(21)00234-8.

[348] K. R. W. Emary, T. Golubchik, P. K. Aley, C. V Ariani, B. Angus, S. Bibi, B. Blane, D. Bonsall, P. Cicconi, S. Charlton, E. A. Clutterbuck, A. M. Collins, T. Cox, T. C. Darton, C. Dold, A. D. Douglas, C. J. A. Duncan, K. J. Ewer, A. L. Flaxman, *et al.*, "Efficacy of ChAdOx1 nCoV-19 (AZD1222) vaccine against SARS-CoV-2 variant of concern 202012/01 (B.1.1.7): an exploratory analysis of a randomised controlled trial.," *Lancet (London, England)*, vol. 397, no. 10282, pp. 1351–1362, Apr. 2021, doi: 10.1016/S0140-6736(21)00628-0.

[349] G. Hardwick, "Master Species List," *Academia.Edu*. [Online]. Available: https://www.academia.edu/download/60117342/Northern_Species_List__3rd_Edition__6_July_2019201 90725-89097-12rwi5d.pdf

[350] A. J. Davison, M. Benko, and B. Harrach, "Genetic content and evolution of adenoviruses," *J. Gen. Virol.*, vol. 84, no. 11, pp. 2895–2908, 2003, doi: 10.1099/vir.0.19497-0.

[351] I. Letunic, "ITOL: Interactive tree of life."

[352] C. M. Robinson, G. Singh, J. Y. Lee, S. Dehghan, J. Rajaiya, E. B. Liu, M. A. Yousuf, R. A. Betensky, M. S. Jones, D. W. Dyer, D. Seto, and J. Chodosh, "Molecular evolution of human adenoviruses," *Sci. Rep.*, vol. 3, no. 1, p. 1812, 2013, doi: 10.1038/srep01812.

[353] J. P. Lynch 3rd and A. E. Kajon, "Adenovirus: Epidemiology, Global Spread of Novel Serotypes, and Advances in Treatment and Prevention," *Semin. Respir. Crit. Care Med.*, vol. 37, no. 4, pp. 586–602, Aug. 2016, doi: 10.1055/s-0036-1584923.

[354] S.-Y. Chang, C.-N. Lee, P.-H. Lin, H.-H. Huang, L.-Y. Chang, W. Ko, S.-F. Chang, P.-I. Lee, L.-M. Huang, and C.-L. Kao, "A community-derived outbreak of adenovirus type 3 in children in Taiwan between 2004 and 2005.," *J. Med. Virol.*, vol. 80, no. 1, pp. 102–112, Jan. 2008, doi: 10.1002/jmv.21045.

[355] J. Lee, E. H. Choi, and H. J. Lee, "Comprehensive serotyping and epidemiology of human adenovirus isolated from the respiratory tract of Korean children over 17 consecutive years (1991-2007).," *J. Med. Virol.*, vol. 82, no. 4, pp. 624–631, Apr. 2010, doi: 10.1002/jmv.21701.

[356] D. D. Erdman, W. Xu, S. I. Gerber, G. C. Gray, D. Schnurr, A. E. Kajon, and L. J. Anderson, "Molecular epidemiology of adenovirus type 7 in the United States, 1966-2000.," *Emerg. Infect. Dis.*, vol. 8, no. 3, pp. 269–277, Mar. 2002, doi: 10.3201/eid0803.010190.

[357] J. L. Sanchez, L. N. Binn, B. L. Innis, R. D. Reynolds, T. Lee, F. Mitchell-Raymundo, S. C. Craig, J. P. Marquez, G. A. Shepherd, C. S. Polyak, J. Conolly, and K. F. Kohlhase, "Epidemic of adenovirus-induced respiratory illness among US military recruits: epidemiologic and immunologic risk factors in healthy, young adults.," *J. Med. Virol.*, vol. 65, no. 4, pp. 710–718, Dec. 2001, doi: 10.1002/jmv.2095.

[358] A. E. Kajon, X. Lu, D. D. Erdman, J. Louie, D. Schnurr, K. S. George, M. P. Koopmans, T. Allibhai, and D. Metzgar, "Molecular epidemiology and brief history of emerging adenovirus 14-associated respiratory disease in the United States.," *J. Infect. Dis.*, vol. 202, no. 1, pp. 93–103, Jul. 2010, doi: 10.1086/653083.

[359] "Civilian outbreak of adenovirus acute respiratory disease--South Dakota, 1997.," *MMWR. Morb. Mortal. Wkly. Rep.*, vol. 47, no. 27, pp. 567–570, Jul. 1998.

[360] E. Percivalle, A. Sarasini, M. Torsellini, L. Bruschi, E. Antoniazzi, M. Grazia Revello, and G. Gerna, "A comparison of methods for detecting adenovirus type 8 keratoconjunctivitis during a nosocomial outbreak in a Neonatal Intensive Care Unit.," *J. Clin. Virol. Off. Publ. Pan Am. Soc. Clin. Virol.*, vol. 28, no. 3, pp. 257–264, Dec. 2003, doi: 10.1016/s1386-6532(03)00011-8.

[361] N. Hamada, K. Gotoh, K. Hara, J. Iwahashi, Y. Imamura, S. Nakamura, C. Taguchi, M. Sugita, R. Yamakawa, Y. Etoh, N. Sera, T. Ishibashi, K. Chijiwa, and H. Watanabe, "Nosocomial outbreak of epidemic keratoconjunctivitis accompanying environmental contamination with adenoviruses.," *J. Hosp. Infect.*, vol. 68, no. 3, pp. 262–268, Mar. 2008, doi: 10.1016/j.jhin.2007.12.012.

[362] H. Ishiko and K. Aoki, “Spread of epidemic keratoconjunctivitis due to a novel serotype of human adenovirus in Japan.,” *Journal of clinical microbiology*, vol. 47, no. 8. pp. 2678–2679, Aug. 2009. doi: 10.1128/JCM.r00313-09.

[363] K. F. Tabbara, N. Omar, E. Hammouda, M. Akanuma, T. Ohguchi, T. Ariga, Y. Tagawa, N. Kitaichi, S. Ishida, K. Aoki, H. Ishiko, and S. Ohno, “Molecular epidemiology of adenoviral keratoconjunctivitis in Saudi Arabia.,” *Mol. Vis.*, vol. 16, pp. 2132–2136, Oct. 2010.

[364] L. Li, H. Shimizu, L. T. P. Doan, P. G. Tung, S. Okitsu, O. Nishio, E. Suzuki, J. K. Seo, K. S. Kim, W. E. G. Müller, and H. Ushijima, “Characterizations of adenovirus type 41 isolates from children with acute gastroenteritis in Japan, Vietnam, and Korea.,” *J. Clin. Microbiol.*, vol. 42, no. 9, pp. 4032–4039, Sep. 2004, doi: 10.1128/JCM.42.9.4032-4039.2004.

[365] S. Fukuda, M. Kuwayama, S. Takao, Y. Shimazu, and K. Miyazaki, “Molecular epidemiology of subgenus F adenoviruses associated with pediatric gastroenteritis during eight years in Hiroshima Prefecture as a limited area.,” *Arch. Virol.*, vol. 151, no. 12, pp. 2511–2517, Dec. 2006, doi: 10.1007/s00705-006-0816-x.

[366] K. Sdiri-Loulizi, H. Gharbi-Khelifi, A. de Rougemont, M. Hassine, S. Chouchane, N. Sakly, P. Pothier, M. N. Guédiche, M. Aouni, and K. Ambert-Balay, “Molecular epidemiology of human astrovirus and adenovirus serotypes 40/41 strains related to acute diarrhea in Tunisian children.,” *J. Med. Virol.*, vol. 81, no. 11, pp. 1895–1902, Nov. 2009, doi: 10.1002/jmv.21586.

[367] A. M. Lachiewicz, R. Cianciolo, M. B. Miller, and V. K. Derebail, “Adenovirus causing fever, upper respiratory infection, and allograft nephritis complicated by persistent asymptomatic viremia.,” *Transpl. Infect. Dis. an Off. J. Transplant. Soc.*, vol. 16, no. 4, pp. 648–652, Aug. 2014, doi: 10.1111/tid.12248.

[368] N. Yokose, T. Hirakawa, and K. Inokuchi, “Adenovirus-associated hemorrhagic cystitis in a patient with plasma cell myeloma treated with bortezomib.,” *Leukemia research*, vol. 33, no. 8. England, p. e106, Aug. 2009. doi: 10.1016/j.leukres.2009.02.021.

[369] M. Echavarría, “Adenoviruses in immunocompromised hosts.,” *Clin. Microbiol. Rev.*, vol. 21, no. 4, pp. 704–715, Oct. 2008, doi: 10.1128/CMR.00052-07.

[370] M. G. Ison and M. Green, “Adenovirus in solid organ transplant recipients.,” *Am. J. Transplant. Off. J. Am. Soc. Transplant. Am. Soc. Transpl. Surg.*, vol. 9 Suppl 4, pp. S161-5, Dec. 2009, doi: 10.1111/j.1600-6143.2009.02907.x.

[371] Y.-J. Kim, M. Boeckh, and J. A. Englund, “Community respiratory virus infections in immunocompromised patients: hematopoietic stem cell and solid organ transplant recipients, and individuals with human immunodeficiency virus infection.,” *Semin. Respir. Crit. Care Med.*, vol. 28, no. 2, pp. 222–242, Apr. 2007, doi: 10.1055/s-2007-976494.

[372] M. G. Ison, “Adenovirus infections in transplant recipients.,” *Clin. Infect. Dis. an Off. Publ. Infect. Dis. Soc. Am.*, vol. 43, no. 3, pp. 331–339, Aug. 2006, doi: 10.1086/505498.

[373] V. Erard, M.-L. Huang, J. Ferrenberg, L. Nguy, T. L. Stevens-Ayers, R. C. Hackman, L. Corey, and M. Boeckh, “Quantitative real-time polymerase chain reaction for detection of adenovirus after T cell-replete hematopoietic cell transplantation: viral load as a marker for invasive disease.,” *Clin. Infect. Dis. an Off. Publ. Infect. Dis. Soc. Am.*, vol. 45, no. 8, pp. 958–965, Oct. 2007, doi: 10.1086/521851.

[374] M. Leruez-Ville, V. Minard, F. Lacaille, A. Buzyn, E. Abachin, S. Blanche, F. Freymuth, and C. Rouzioux, “Real-time blood plasma polymerase chain reaction for management of disseminated adenovirus infection.,” *Clin. Infect. Dis. an Off. Publ. Infect. Dis. Soc. Am.*, vol. 38, no. 1, pp. 45–52, Jan. 2004, doi: 10.1086/380450.

[375] A. J. Pérez-Berná, S. Marion, F. J. Chichón, J. J. Fernández, D. C. Winkler, J. L. Carrascosa, A. C. Steven, A. Šiber, and C. San Martín, “Distribution of DNA-condensing protein complexes in the adenovirus core.,” *Nucleic Acids Res.*, vol. 43, no. 8, pp. 4274–4283, Apr. 2015, doi: 10.1093/nar/gkv187.

[376] N. Martín-González, M. Hernando-Pérez, G. N. Condezo, M. Pérez-Illana, A. Šiber, D. Reguera, P. Ostapchuk, P. Hearing, C. San Martín, and P. J. de Pablo, “Adenovirus major core protein condenses DNA in clusters and bundles, modulating genome release and capsid internal pressure.,” *Nucleic Acids Res.*, vol. 47, no. 17, pp. 9231–9242, Sep. 2019, doi: 10.1093/nar/gkz687.

[377] J. Pérez-Vargas, R. C. Vaughan, C. Houser, K. M. Hastie, C. C. Kao, and G. R. Nemerow, "Isolation and characterization of the DNA and protein binding activities of adenovirus core protein V.," *J. Virol.*, vol. 88, no. 16, pp. 9287–9296, Aug. 2014, doi: 10.1128/JVI.00935-14.

[378] V. S. Reddy and G. R. Nemerow, "Structures and organization of adenovirus cement proteins provide insights into the role of capsid maturation in virus entry and infection.," *Proc. Natl. Acad. Sci. U. S. A.*, vol. 111, no. 32, pp. 11715–11720, Aug. 2014, doi: 10.1073/pnas.1408462111.

[379] P. K. Chatterjee, M. E. Vayda, and S. J. Flint, "Interactions among the three adenovirus core proteins.," *J. Virol.*, vol. 55, no. 2, pp. 379–386, Aug. 1985, doi: 10.1128/JVI.55.2.379-386.1985.

[380] H. Ugai, A. V Borovjagin, L. P. Le, M. Wang, and D. T. Curiel, "Thermostability/infectivity defect caused by deletion of the core protein V gene in human adenovirus type 5 is rescued by thermo-selectable mutations in the core protein X precursor.," *J. Mol. Biol.*, vol. 366, no. 4, pp. 1142–1160, Mar. 2007, doi: 10.1016/j.jmb.2006.11.090.

[381] D. D. Leipe, E. V Koonin, and L. Aravind, "Evolution and classification of P-loop kinases and related proteins.," *J. Mol. Biol.*, vol. 333, no. 4, pp. 781–815, Oct. 2003, doi: 10.1016/j.jmb.2003.08.040.

[382] P. Ostapchuk and P. Hearing, "Adenovirus IVa2 protein binds ATP.," *J. Virol.*, vol. 82, no. 20, pp. 10290–10294, Oct. 2008, doi: 10.1128/JVI.00882-08.

[383] S. Kulanayake and S. K. Tikoo, "Adenovirus core proteins: Structure and function," *Viruses*, vol. 13, no. 3, pp. 1–16, 2021, doi: 10.3390/v13030388.

[384] C. San Martín, "Latest insights on adenovirus structure and assembly.," *Viruses*, vol. 4, no. 5, pp. 847–877, May 2012, doi: 10.3390/v4050847.

[385] J. V. J. Maizel, D. O. White, and M. D. Scharff, "The polypeptides of adenovirus. I. Evidence for multiple protein components in the virion and a comparison of types 2, 7A, and 12.," *Virology*, vol. 36, no. 1, pp. 115–125, Sep. 1968, doi: 10.1016/0042-6822(68)90121-9.

[386] R. M. Burnett, M. G. Grütter, and J. L. White, "The structure of the adenovirus capsid. I. An envelope model of hexon at 6 A resolution.," *J. Mol. Biol.*, vol. 185, no. 1, pp. 105–123, Sep. 1985, doi: 10.1016/0022-2836(85)90186-x.

[387] C. Zubieta, G. Schoehn, J. Chroboczek, and S. Cusack, "The Structure of the Human Adenovirus 2 Penton," *Mol. Cell*, vol. 17, no. 1, pp. 121–135, 2005, doi: https://doi.org/10.1016/j.molcel.2004.11.041.

[388] M. J. van Raaij, A. Mitraki, G. Lavigne, and S. Cusack, "A triple beta-spiral in the adenovirus fibre shaft reveals a new structural motif for a fibrous protein.," *Nature*, vol. 401, no. 6756, pp. 935–938, Oct. 1999, doi: 10.1038/44880.

[389] D. Xia, L. J. Henry, R. D. Gerard, and J. Deisenhofer, "Crystal structure of the receptor-binding domain of adenovirus type 5 fiber protein at 1.7 A resolution.," *Structure*, vol. 2, no. 12, pp. 1259–1270, Dec. 1994, doi: 10.1016/s0969-2126(94)00126-x.

[390] S. A. Nicklin, E. Wu, G. R. Nemerow, and A. H. Baker, "The influence of adenovirus fiber structure and function on vector development for gene therapy.," *Mol. Ther.*, vol. 12, no. 3, pp. 384–393, Sep. 2005, doi: 10.1016/j.ymthe.2005.05.008.

[391] C. San Martín, J. N. Glasgow, A. Borovjagin, M. S. Beatty, E. A. Kashentseva, D. T. Curiel, R. Marabini, and I. P. Dmitriev, "Localization of the N-terminus of minor coat protein IIIa in the adenovirus capsid.," *J. Mol. Biol.*, vol. 383, no. 4, pp. 923–934, Nov. 2008, doi: 10.1016/j.jmb.2008.08.054.

[392] S. D. Saban, M. Silvestry, G. R. Nemerow, and P. L. Stewart, "Visualization of alpha-helices in a 6-angstrom resolution cryoelectron microscopy structure of adenovirus allows refinement of capsid protein assignments.," *J. Virol.*, vol. 80, no. 24, pp. 12049–12059, Dec. 2006, doi: 10.1128/JVI.01652-06.

[393] R. Marabini, G. N. Condezo, M. Krupovic, R. Menéndez-Conejero, J. Gómez-Blanco, and C. San Martín, "Near-atomic structure of an atadenovirus reveals a conserved capsid-binding motif and intergenera variations in cementing proteins.," *Sci. Adv.*, vol. 7, no. 14, Mar. 2021, doi: 10.1126/sciadv.abe6008.

[394] X. Yu, D. Veesler, M. G. Campbell, M. E. Barry, F. J. Asturias, M. A. Barry, and V. S. Reddy, "Cryo-EM structure of human adenovirus D26 reveals the conservation of structural organization among human adenoviruses.," *Sci. Adv.*, vol. 3, no. 5, p. e1602670, May 2017, doi: 10.1126/sciadv.1602670.

[395] M. Pérez-Illana, M. Martínez, G. N. Condezo, M. Hernando-Pérez, C. Mangroo, M. Brown, R. Marabini, and C. San Martín, "Cryo-EM structure of enteric adenovirus HAdV-F41 highlights structural variations among human adenoviruses.," *Sci. Adv.*, vol. 7, no. 9, Feb. 2021, doi: 10.1126/sciadv.abd9421.

[396] X. Dai, L. Wu, R. Sun, and Z. H. Zhou, "Atomic Structures of Minor Proteins VI and VII in Human Adenovirus.," *J. Virol.*, vol. 91, no. 24, Dec. 2017, doi: 10.1128/JVI.00850-17.

[397] F. K. Athappilly, R. Murali, J. J. Rux, Z. Cai, and R. M. Burnett, "The refined crystal structure of hexon, the major coat protein of adenovirus type 2, at 2.9 Å resolution," *Journal of Molecular Biology*, vol. 242, no. 4. pp. 430–455, 1994. doi: 10.1006/jmbi.1994.1593.

[398] J. J. Rux and R. M. Burnett, "Type-Specific Epitope Locations Revealed by X-Ray Crystallographic Study of Adenovirus Type 5 Hexon," *Mol. Ther.*, vol. 1, no. 1, pp. 18–30, 2000, doi: https://doi.org/10.1006/mthe.1999.0001.

[399] R. J. J., K. P. R., and B. R. M., "Structural and Phylogenetic Analysis of Adenovirus Hexons by Use of High-Resolution X-Ray Crystallographic, Molecular Modeling, and Sequence-Based Methods," *J. Virol.*, vol. 77, no. 17, pp. 9553–9566, Sep. 2003, doi: 10.1128/JVI.77.17.9553-9566.2003.

[400] K. Diaz, C. T. Hu, Y. Sul, B. A. Bromme, N. D. Myers, K. V Skorohodova, A. P. Gounder, and J. G. Smith, "Defensin-driven viral evolution," *PLOS Pathog.*, vol. 16, no. 11, p. e1009018, Nov. 2020, [Online]. Available: https://doi.org/10.1371/journal.ppat.1009018

[401] N. Pied and H. Wodrich, "Imaging the adenovirus infection cycle," *FEBS Lett.*, vol. 593, no. 24, pp. 3419–3448, 2019, doi: 10.1002/1873-3468.13690.

[402] J. M. Bergelson, J. A. Cunningham, G. Droguett, E. A. Kurt-Jones, A. Krithivas, J. S. Hong, M. S. Horwitz, R. L. Crowell, and R. W. Finberg, "Isolation of a common receptor for Coxsackie B viruses and adenoviruses 2 and 5.," *Science*, vol. 275, no. 5304, pp. 1320–1323, Feb. 1997, doi: 10.1126/science.275.5304.1320.

[403] I. Kirby, R. Lord, E. Davison, T. J. Wickham, P. W. Roelvink, I. Kovesdi, B. J. Sutton, and G. Santis, "Adenovirus type 9 fiber knob binds to the coxsackie B virus-adenovirus receptor (CAR) with lower affinity than fiber knobs of other CAR-binding adenovirus serotypes.," *J. Virol.*, vol. 75, no. 15, pp. 7210–7214, Aug. 2001, doi: 10.1128/JVI.75.15.7210-7214.2001.

[404] P. W. Roelvink, A. Lizonova, J. G. Lee, Y. Li, J. M. Bergelson, R. W. Finberg, D. E. Brough, I. Kovesdi, and T. J. Wickham, "The coxsackievirus-adenovirus receptor protein can function as a cellular attachment protein for adenovirus serotypes from subgroups A, C, D, E, and F.," *J. Virol.*, vol. 72, no. 10, pp. 7909–7915, Oct. 1998, doi: 10.1128/JVI.72.10.7909-7915.1998.

[405] A. Segerman, J. P. Atkinson, M. Marttila, V. Dennerquist, G. Wadell, and N. Arnberg, "Adenovirus type 11 uses CD46 as a cellular receptor.," *J. Virol.*, vol. 77, no. 17, pp. 9183–9191, Sep. 2003, doi: 10.1128/jvi.77.17.9183-9191.2003.

[406] A. Gaggar, D. M. Shayakhmetov, and A. Lieber, "CD46 is a cellular receptor for group B adenoviruses.," *Nat. Med.*, vol. 9, no. 11, pp. 1408–1412, Nov. 2003, doi: 10.1038/nm952.

[407] J. J. Short, C. Vasu, M. J. Holterman, D. T. Curiel, and A. Pereboev, "Members of adenovirus species B utilize CD80 and CD86 as cellular attachment receptors.," *Virus Res.*, vol. 122, no. 1–2, pp. 144–153, Dec. 2006, doi: 10.1016/j.virusres.2006.07.009.

[408] S. S. Hong, L. Karayan, J. Tournier, D. T. Curiel, and P. A. Boulanger, "Adenovirus type 5 fiber knob binds to MHC class I alpha2 domain at the surface of human epithelial and B lymphoblastoid cells.," *EMBO J.*, vol. 16, no. 9, pp. 2294–2306, May 1997, doi: 10.1093/emboj/16.9.2294.

[409] H. Wang, Z.-Y. Li, Y. Liu, J. Persson, I. Beyer, T. Möller, D. Koyuncu, M. R. Drescher, R. Strauss, X.-B. Zhang, J. K. 3rd Wahl, N. Urban, C. Drescher, A. Hemminki, P. Fender, and A. Lieber, "Desmoglein 2 is a receptor for adenovirus serotypes 3, 7, 11 and 14.," *Nat. Med.*, vol. 17, no. 1, pp. 96–104, Jan. 2011, doi: 10.1038/nm.2270.

[410] T. A. G. Smith, N. Idamakanti, M. L. Rollence, J. Marshall-Neff, J. Kim, K. Mulgrew, G. R. Nemerow, M. Kaleko, and S. C. Stevenson, "Adenovirus serotype 5 fiber shaft influences in vivo gene transfer in mice.," *Hum. Gene Ther.*, vol. 14, no. 8, pp. 777–787, May 2003, doi: 10.1089/104303403765255165.

[411] P. Mathias, T. Wickham, M. Moore, and G. Nemerow, "Multiple adenovirus serotypes use alpha v integrins for infection.," *J. Virol.*, vol. 68, no. 10, pp. 6811–6814, Oct. 1994, doi: 10.1128/JVI.68.10.6811-6814.1994.

[412] H. J. Haisma, M. Boesjes, A. M. Beerens, B. W. A. van der Strate, D. T. Curiel, A. Plüddemann, S. Gordon, and A. R. Bellu, "Scavenger receptor A: a new route for adenovirus 5.," *Mol. Pharm.*, vol. 6, no. 2, pp. 366–374, 2009, doi: 10.1021/mp8000974.

[413] E. C. Nilsson, R. J. Storm, J. Bauer, S. M. C. Johansson, A. Lookene, J. Ångström, M. Hedenström, T. L. Eriksson, L. Frängsmyr, S. Rinaldi, H. J. Willison, F. Pedrosa Domellöf, T. Stehle, and N. Arnberg, "The GD1a glycan is a cellular receptor for adenoviruses causing epidemic keratoconjunctivitis.," *Nat. Med.*, vol. 17, no. 1, pp. 105–109, Jan. 2011, doi: 10.1038/nm.2267.

[414] C. Johansson, M. Jonsson, M. Marttila, D. Persson, X.-L. Fan, J. Skog, L. Frängsmyr, G. Wadell, and N. Arnberg, "Adenoviruses use lactoferrin as a bridge for CAR-independent binding to and infection of epithelial cells.," *J. Virol.*, vol. 81, no. 2, pp. 954–963, Jan. 2007, doi: 10.1128/JVI.01995-06.

[415] A. L. Parker, S. N. Waddington, C. G. Nicol, D. M. Shayakhmetov, S. M. Buckley, L. Denby, G. Kemball-Cook, S. Ni, A. Lieber, J. H. McVey, S. A. Nicklin, and A. H. Baker, "Multiple vitamin K-dependent coagulation zymogens promote adenovirus-mediated gene delivery to hepatocytes.," *Blood*, vol. 108, no. 8, pp. 2554–2561, Oct. 2006, doi: 10.1182/blood-2006-04-008532.

[416] N. Arnberg, "Adenovirus receptors: implications for targeting of viral vectors.," *Trends Pharmacol. Sci.*, vol. 33, no. 8, pp. 442–448, Aug. 2012, doi: 10.1016/j.tips.2012.04.005.

[417] B. D. Persson, L. John, K. Rafie, M. Strebl, L. Frängsmyr, M. Z. Ballmann, K. Mindler, M. Havenga, A. Lemckert, T. Stehle, L.-A. Carlson, and N. Arnberg, "Human species D adenovirus hexon capsid protein mediates cell entry through a direct interaction with CD46.," *Proc. Natl. Acad. Sci. U. S. A.*, vol. 118, no. 3, Jan. 2021, doi: 10.1073/pnas.2020732118.

[418] T. J. Wickham, P. Mathias, D. A. Cheresh, and G. R. Nemerow, "Integrins alpha v beta 3 and alpha v beta 5 promote adenovirus internalization but not virus attachment.," *Cell*, vol. 73, no. 2, pp. 309–319, Apr. 1993, doi: 10.1016/0092-8674(93)90231-e.

[419] H. Nagel, S. Maag, A. Tassis, F. O. Nestlé, U. F. Greber, and S. Hemmi, "The alphavbeta5 integrin of hematopoietic and nonhematopoietic cells is a transduction receptor of RGD-4C fiber-modified adenoviruses.," *Gene Ther.*, vol. 10, no. 19, pp. 1643–1653, Sep. 2003, doi: 10.1038/sj.gt.3302058.

[420] M. Y. Nakano, K. Boucke, M. Suomalainen, R. P. Stidwill, and U. F. Greber, "The First Step of Adenovirus Type 2 Disassembly Occurs at the Cell Surface, Independently of Endocytosis and Escape to the Cytosol," *J. Virol.*, vol. 74, no. 15, pp. 7085–7095, 2000, doi: 10.1128/jvi.74.15.7085-7095.2000.

[421] U. F. Greber, M. Willetts, P. Webster, and A. Helenius, "Stepwise dismantling of adenovirus 2 during entry into cells.," *Cell*, vol. 75, no. 3, pp. 477–486, Nov. 1993, doi: 10.1016/0092-8674(93)90382-z.

[422] O. Meier, K. Boucke, S. V. Hammer, S. Keller, R. P. Stidwill, S. Hemmi, and U. F. Greber, "Adenovirus triggers macropinocytosis and endosomal leakage together with its clathrin-mediated uptake.," *J. Cell Biol.*, vol. 158, no. 6, pp. 1119–1131, Sep. 2002, doi: 10.1083/jcb.200112067.

[423] C. M. Wiethoff, H. Wodrich, L. Gerace, and G. R. Nemerow, "Adenovirus protein VI mediates membrane disruption following capsid disassembly.," *J. Virol.*, vol. 79, no. 4, pp. 1992–2000, Feb. 2005, doi: 10.1128/JVI.79.4.1992-2000.2005.

[424] M. Suomalainen, S. Luisoni, K. Boucke, S. Bianchi, D. A. Engel, and U. F. Greber, "A direct and versatile assay measuring membrane penetration of adenovirus in single cells.," *J. Virol.*, vol. 87, no. 22, pp. 12367–12379, Nov. 2013, doi: 10.1128/JVI.01833-13.

[425] L. C. Trotman, N. Mosberger, M. Fornerod, R. P. Stidwill, and U. F. Greber, "Import of adenovirus DNA involves the nuclear pore complex receptor CAN/Nup214 and histone H1.," *Nat. Cell Biol.*, vol. 3, no. 12, pp. 1092–1100, Dec. 2001, doi: 10.1038/ncb1201-1092.

[426] M. Gazzola, C. J. Burckhardt, B. Bayati, M. Engelke, U. F. Greber, and P. Koumoutsakos, "A stochastic model for microtubule motors describes the in vivo cytoplasmic transport of human adenovirus.," *PLoS Comput. Biol.*, vol. 5, no. 12, p. e1000623, Dec. 2009, doi: 10.1371/journal.pcbi.1000623.

[427] M. Bauer, J. W. Flatt, D. Seiler, B. Cardel, M. Emmenlauer, K. Boucke, M. Suomalainen, S. Hemmi, and U. F. Greber, "The E3 Ubiquitin Ligase Mind Bomb 1 Controls Adenovirus Genome Release at the Nuclear Pore Complex.," *Cell Rep.*, vol. 29, no. 12, pp. 3785-3795.e8, Dec. 2019, doi: 10.1016/j.celrep.2019.11.064.

[428] S. Strunze, M. F. Engelke, I.-H. Wang, D. Puntener, K. Boucke, S. Schleich, M. Way, P. Schoenenberger, C. J. Burckhardt, and U. F. Greber, "Kinesin-1-mediated capsid disassembly and disruption of the nuclear pore complex promote virus infection.," *Cell Host Microbe*, vol. 10, no. 3, pp. 210–223, Sep. 2011, doi: 10.1016/j.chom.2011.08.010.

[429] A. J. Berk, "Recent lessons in gene expression, cell cycle control, and cell biology from adenovirus.," *Oncogene*, vol. 24, no. 52, pp. 7673–7685, Nov. 2005, doi: 10.1038/sj.onc.1209040.

[430] U. F. Greber, "Virus assembly and disassembly: the adenovirus cysteine protease as a trigger factor.," *Rev. Med. Virol.*, vol. 8, no. 4, pp. 213–222, Oct. 1998, doi: 10.1002/(sici)1099-1654(1998100)8:4<213::aid-rmv225>3.0.co;2-w.

[431] U. F. Greber, P. Webster, J. Weber, and A. Helenius, "The role of the adenovirus protease on virus entry into cells.," *EMBO J.*, vol. 15, no. 8, pp. 1766–1777, Apr. 1996.

[432] B. T. W. Post, M. K. Liszewski, E. M. Adams, I. Tedja, E. A. Miller, and J. P. Atkinson, "Membrane Cofactor Protein of the Complement System: Alternative Splicing of Serine/Threonine/Prohne-rich Exons and Cytoplasmic Tails Produces Multiple Isoforms that Correlate with Protein Phenotype," *J. Exp. Med.*, vol. 174, no. July, 1991.

[433] D. M. Lublin, M. K. Liszewski, T. W. Post, M. A. Arce, M. M. Le Beau, M. B. Rebentisch, R. S. Lemons, T. Seya, and J. P. Atkinson, "Molecular cloning and chromosomal localization of human membrane cofactor protein (MCP): Evidence for inclusion in the multigene family of complement-regulatory proteins," *J. Exp. Med.*, vol. 168, no. 1, pp. 181–194, 1988, doi: 10.1084/jem.168.1.181.

[434] R. Lubbers, M. F. van Essen, C. van Kooten, and L. A. Trouw, "Production of complement components by cells of the immune system.," *Clin. Exp. Immunol.*, vol. 188, no. 2, pp. 183–194, May 2017, doi: 10.1111/cei.12952.

[435] M. K. Liszewski and C. Kemper, "Complement in Motion: The Evolution of CD46 from a Complement Regulator to an Orchestrator of Normal Cell Physiology.," *J. Immunol.*, vol. 203, no. 1, pp. 3–5, Jul. 2019, doi: 10.4049/jimmunol.1900527.

[436] H. Yamamoto, A. F. Fara, P. Dasgupta, and C. Kemper, "CD46: The 'multitasker' of complement proteins," *Int. J. Biochem. Cell Biol.*, vol. 45, no. 12, pp. 2808–2820, 2013, doi: 10.1016/j.biocel.2013.09.016.

[437] M. K. Liszewski, T. W. Post, and J. P. Atkinson, "Membrane cofactor protein (MCP or CD46): newest member of the regulators of complement activation gene cluster.," *Annu. Rev. Immunol.*, vol. 9, pp. 431–455, 1991, doi: 10.1146/annurev.iy.09.040191.002243.

[438] J. M. Casasnovas, M. Larvie, and T. Stehle, "Crystal structure of two CD46 domains reveals an extended measles virus-binding surface.," *EMBO J.*, vol. 18, no. 11, pp. 2911–2922, Jun. 1999, doi: 10.1093/emboj/18.11.2911.

[439] B. D. Persson, N. B. Schmitz, C. Santiago, G. Zocher, M. Larvie, U. Scheu, J. M. Casasnovas, and T. Stehle, "Structure of the extracellular portion of CD46 provides insights into its interactions with complement proteins and pathogens," *PLoS Pathog.*, vol. 6, no. 9, 2010, doi: 10.1371/journal.ppat.1001122.

[440] R. W. Johnstone, S. M. Russell, B. E. Loveland, and I. F. C. McKenzie, "Polymorphic expression of CD46 protein isoforms due to tissue-specific RNA splicing," *Mol. Immunol.*, vol. 30, no. 14, pp. 1231–1241, 1993, doi: https://doi.org/10.1016/0161-5890(93)90038-D.

[441] L. L. Ballard, N. S. Bora, G. H. Yu, and J. P. Atkinson, "Biochemical characterization of membrane cofactor protein of the complement system.," *J. Immunol.*, vol. 141, no. 11, pp. 3923–3929, Dec. 1988.

[442] H. Li, E. G. Rhee, K. Masek-Hammerman, J. E. Teigler, P. Abbink, and D. H. Barouch, "Adenovirus serotype 26 utilizes CD46 as a primary cellular receptor and only transiently activates T lymphocytes following vaccination of rhesus monkeys.," *J. Virol.*, vol. 86, no. 19, pp. 10862–10865, Oct. 2012, doi: 10.1128/JVI.00928-12.

[443] J. Liu, P. Boehme, W. Zhang, J. Fu, R. Yumul, K. Mese, R. Tsoukas, M. Solanki, M. Kaufmann, R. Lu, A. Schmidtko, A. F. Stewart, A. Lieber, and A. Ehrhardt, "Human adenovirus type 17 from species D transduces endothelial cells and human CD46 is involved in cell entry.," *Sci. Rep.*, vol. 8, no. 1, p. 13442, Sep. 2018, doi: 10.1038/s41598-018-31713-x.

[444] N. Belousova, G. Mikheeva, C. Xiong, L. J. Stagg, M. Gagea, P. S. Fox, R. L. Bassett, J. E. Ladbury, M. B. Braun, T. Stehle, C. Li, and V. Krasnykh, "Native and engineered tropism of vectors derived from a rare species D adenovirus serotype 43.," *Oncotarget*, vol. 7, no. 33, pp. 53414–53429, Aug. 2016, doi: 10.18632/oncotarget.10800.

[445] A. A. C. Lemckert, J. Grimbergen, S. Smits, E. Hartkoorn, L. Holterman, B. Berkhout, D. H. Barouch, R. Vogels, P. Quax, J. Goudsmit, and M. J. E. Havenga, "Generation of a novel replication-incompetent adenoviral vector derived from human adenovirus type 49: manufacture on PER.C6 cells, tropism and immunogenicity.," *J. Gen. Virol.*, vol. 87, no. Pt 10, pp. 2891–2899, Oct. 2006, doi: 10.1099/vir.0.82079-0.

[446] E. Wu, S. A. Trauger, L. Pache, T.-M. Mullen, D. J. von Seggern, G. Siuzdak, and G. R. Nemerow, "Membrane cofactor protein is a receptor for adenoviruses associated with epidemic keratoconjunctivitis.," *J. Virol.*, vol. 78, no. 8, pp. 3897–3905, Apr. 2004, doi: 10.1128/jvi.78.8.3897-3905.2004.

[447] P. Abbink, A. A. C. Lemckert, B. A. Ewald, D. M. Lynch, M. Denholtz, S. Smits, L. Holterman, I. Damen, R. Vogels, A. R. Thorner, K. L. O'Brien, A. Carville, K. G. Mansfield, J. Goudsmit, M. J. E. Havenga, and D. H. Barouch, "Comparative seroprevalence and immunogenicity of six rare serotype recombinant adenovirus vaccine vectors from subgroups B and D.," *J. Virol.*, vol. 81, no. 9, pp. 4654–4663, May 2007, doi: 10.1128/JVI.02696-06.

[448] C. A. Kahl, J. Bonnell, S. Hiriyanna, M. Fultz, C. Nyberg-Hoffman, P. Chen, C. R. King, and J. G. D. Gall, "Potent immune responses and in vitro pro-inflammatory cytokine suppression by a novel adenovirus vaccine vector based on rare human serotype 28.," *Vaccine*, vol. 28, no. 35, pp. 5691–5702, Aug. 2010, doi: 10.1016/j.vaccine.2010.06.050.

[449] S. Lecollinet, F. Gavard, M. J. E. Havenga, O. B. Spiller, A. Lemckert, J. Goudsmit, M. Eloit, and J. Richardson, "Improved gene delivery to intestinal mucosa by adenoviral vectors bearing subgroup B and d fibers.," *J. Virol.*, vol. 80, no. 6, pp. 2747–2759, Mar. 2006, doi: 10.1128/JVI.80.6.2747-2759.2006.

[450] S. A. Trauger, E. Wu, S. J. Bark, G. R. Nemerow, and G. Siuzdak, "The identification of an adenovirus receptor by using affinity capture and mass spectrometry.," *Chembiochem*, vol. 5, no. 8, pp. 1095–1099, Aug. 2004, doi: 10.1002/cbic.200400037.

[451] F. H. J. Top, E. L. Buescher, W. H. Bancroft, and P. K. Russell, "Immunization with live types 7 and 4 adenovirus vaccines. II. Antibody response and protective effect against acute respiratory disease due to adenovirus type 7.," *J. Infect. Dis.*, vol. 124, no. 2, pp. 155–160, Aug. 1971, doi: 10.1093/infdis/124.2.155.

[452] F. H. J. Top, R. A. Grossman, P. J. Bartelloni, H. E. Segal, B. A. Dudding, P. K. Russell, and E. L. Buescher, "Immunization with live types 7 and 4 adenovirus vaccines. I. Safety, infectivity, antigenicity, and potency of adenovirus type 7 vaccine in humans.," *J. Infect. Dis.*, vol. 124, no. 2, pp. 148–154, Aug. 1971, doi: 10.1093/infdis/124.2.148.

[453] J. M. Radin, A. W. Hawksworth, P. J. Blair, D. J. Faix, R. Raman, K. L. Russell, and G. C. Gray, "Dramatic decline of respiratory illness among US military recruits after the renewed use of adenovirus vaccines.," *Clin. Infect. Dis. an Off. Publ. Infect. Dis. Soc. Am.*, vol. 59, no. 7, pp. 962–968, Oct. 2014, doi: 10.1093/cid/ciu507.

[454] M. R. HILLEMAN, "Efficacy of and indications for use of adenovirus vaccine.," *Am. J. Public Health Nations. Health*, vol. 48, no. 2, pp. 153–158, Feb. 1958, doi: 10.2105/ajph.48.2.153.

[455] C. H. J. Hoke and C. E. J. Snyder, “History of the restoration of adenovirus type 4 and type 7 vaccine, live oral (Adenovirus Vaccine) in the context of the Department of Defense acquisition system.,” *Vaccine*, vol. 31, no. 12, pp. 1623–1632, Mar. 2013, doi: 10.1016/j.vaccine.2012.12.029.

[456] G. T. Truffelli, E. A. Timm, W. B. Beardmore, and I. W. J. McLean, “Inactivation of adenovirus and simian virus 40 tumorigenicity in hamsters by vaccine processing methods.,” *Appl. Microbiol.*, vol. 15, no. 3, pp. 516–527, May 1967, doi: 10.1128/am.15.3.516-527.1967.

[457] R. M. Chanock, W. Ludwig, R. J. Heubner, T. R. Cate, and L. W. Chu, “Immunization by selective infection with type 4 adenovirus grown in human diploid tissue cultures. I. Safety and lack of oncogenicity and tests for potency in volunteers.,” *JAMA*, vol. 195, no. 6, pp. 445–452, Feb. 1966.

[458] R. R. Bradley, D. M. Lynch, M. J. Iampietro, E. N. Borducchi, and D. H. Barouch, “Adenovirus serotype 5 neutralizing antibodies target both hexon and fiber following vaccination and natural infection.,” *J. Virol.*, vol. 86, no. 1, pp. 625–629, Jan. 2012, doi: 10.1128/JVI.06254-11.

[459] B. Yu, J. Dong, C. Wang, Y. Zhan, H. Zhang, J. Wu, W. Kong, and X. Yu, “Characteristics of neutralizing antibodies to adenovirus capsid proteins in human and animal sera.,” *Virology*, vol. 437, no. 2, pp. 118–123, Mar. 2013, doi: 10.1016/j.virol.2012.12.014.

[460] S. M. Sumida, D. M. Truitt, A. A. C. Lemckert, R. Vogels, J. H. H. V Custers, M. M. Addo, S. Lockman, T. Peter, F. W. Peyerl, M. G. Kishko, S. S. Jackson, D. A. Gorgone, M. A. Lifton, M. Essex, B. D. Walker, J. Goudsmit, M. J. E. Havenga, and D. H. Barouch, “Neutralizing antibodies to adenovirus serotype 5 vaccine vectors are directed primarily against the adenovirus hexon protein.,” *J. Immunol.*, vol. 174, no. 11, pp. 7179–7185, Jun. 2005, doi: 10.4049/jimmunol.174.11.7179.

[461] S. Lang, L. Wang, Z. Wang, R. Zhu, J. Yan, B. Wang, J. Wu, H. Zhang, H. Wu, Y. Zhou, W. Kong, B. Yu, and X. Yu, “Localization of neutralization epitopes on adenovirus fiber knob from species C.,” *J. Gen. Virol.*, vol. 97, no. 4, pp. 955–962, Apr. 2016, doi: 10.1099/jgv.0.000410.

[462] B. Yu, J. Dong, C. Wang, Z. Wang, L. Gao, H. Zhang, J. Wu, W. Kong, and X. Yu, “Trimeric knob protein specifically distinguishes neutralizing antibodies to different human adenovirus species: potential application for adenovirus seroepidemiology.,” *J. Gen. Virol.*, vol. 95, no. Pt 7, pp. 1564–1573, Jul. 2014, doi: 10.1099/vir.0.064832-0.

[463] L. Naesens, L. Lenaerts, G. Andrei, R. Snoeck, D. Van Beers, A. Holy, J. Balzarini, and E. De Clercq, “Antiadenovirus activities of several classes of nucleoside and nucleotide analogues.,” *Antimicrob. Agents Chemother.*, vol. 49, no. 3, pp. 1010–1016, Mar. 2005, doi: 10.1128/AAC.49.3.1010-1016.2005.

[464] F. Morfin, S. Dupuis-Girod, S. Mundweiler, D. Falcon, D. Carrington, P. Sedlacek, M. Bierings, P. Cetkovsky, A. C. M. Kroes, M. J. D. van Tol, and D. Thouvenot, “In vitro susceptibility of adenovirus to antiviral drugs is species-dependent.,” *Antivir. Ther.*, vol. 10, no. 2, pp. 225–229, 2005.

[465] B. Heemskerk, A. C. Lankester, T. van Vreeswijk, M. F. C. Beersma, E. C. J. Claas, L. A. Veltrop-Duits, A. C. M. Kroes, J. M. J. J. Vossen, M. W. Schilham, and M. J. D. van Tol, “Immune reconstitution and clearance of human adenovirus viremia in pediatric stem-cell recipients.,” *J. Infect. Dis.*, vol. 191, no. 4, pp. 520–530, Feb. 2005, doi: 10.1086/427513.

[466] S. Chakrabarti, V. Mautner, H. Osman, K. E. Collingham, C. D. Fegan, P. E. Klapper, P. A. H. Moss, and D. W. Milligan, “Adenovirus infections following allogeneic stem cell transplantation: incidence and outcome in relation to graft manipulation, immunosuppression, and immune recovery.,” *Blood*, vol. 100, no. 5, pp. 1619–1627, Sep. 2002, doi: 10.1182/blood-2002-02-0377.

[467] J. F.-W. Chan, K.-H. Kok, Z. Zhu, H. Chu, K. K.-W. To, S. Yuan, and K.-Y. Yuen, “Genomic characterization of the 2019 novel human-pathogenic coronavirus isolated from a patient with atypical pneumonia after visiting Wuhan.,” *Emerg. Microbes Infect.*, vol. 9, no. 1, pp. 221–236, 2020, doi: 10.1080/22221751.2020.1719902.

[468] L. R. Baden, D. J. Stieh, M. Sarnecki, S. R. Walsh, G. D. Tomaras, J. G. Kublin, M. J. McElrath, G. Alter, G. Ferrari, D. Montefiori, P. Mann, S. Nijs, K. Callewaert, P. Goepfert, S. Edupuganti, E. Karita, J. P. Langedijk, F. Wegmann, L. Corey, *et al.*, “Safety and immunogenicity of two heterologous HIV vaccine regimens in healthy, HIV-uninfected adults (TRAVERSE): a randomised, parallel-group, placebo-controlled, double-blind, phase 1/2a study.,” *lancet. HIV*, vol. 7, no. 10, pp. e688–e698, Oct. 2020, doi: 10.1016/S2352-3018(20)30229-0.

[469] N. C. Salisch, K. E. Stephenson, K. Williams, F. Cox, L. van der Fits, D. Heerwegh, C. Truyers, M. N. Habets, D. G. Kanjilal, R. A. Larocca, P. Abbink, J. Liu, L. Peter, C. Fierro, R. A. De La Barrera, K. Modjarrad, R. C. Zahn, J. Hendriks, C. P. Cahill, *et al.*, "A Double-Blind, Randomized, Placebo-Controlled Phase 1 Study of Ad26.ZIKV.001, an Ad26-Vectored Anti-Zika Virus Vaccine.," *Ann. Intern. Med.*, vol. 174, no. 5, pp. 585–594, May 2021, doi: 10.7326/M20-5306.

[470] K. Matsuda, S. A. Migueles, J. Huang, L. Bolkhovitinov, S. Stuccio, T. Griesman, A. A. Pullano, B. H. Kang, E. Ishida, M. Zimmerman, N. Kashyap, K. M. Martins, D. Stadlbauer, J. Pederson, A. Patamawenu, N. Wright, T. Shofner, S. Evans, C. J. Liang, *et al.*, "A replication-competent adenovirus-vectored influenza vaccine induces durable systemic and mucosal immunity.," *J. Clin. Invest.*, vol. 131, no. 5, Mar. 2021, doi: 10.1172/JCI140794.

[471] A. Volkmann, A.-L. Williamson, H. Weidenthaler, T. P. H. Meyer, J. S. Robertson, J.-L. Excler, R. C. Condit, E. Evans, E. R. Smith, D. Kim, and R. T. Chen, "The Brighton Collaboration standardized template for collection of key information for risk/benefit assessment of a Modified Vaccinia Ankara (MVA) vaccine platform.," *Vaccine*, vol. 39, no. 22, pp. 3067–3080, May 2021, doi: 10.1016/j.vaccine.2020.08.050.

[472] O. Tomori and M. O. Kolawole, "Ebola virus disease: current vaccine solutions.," *Curr. Opin. Immunol.*, vol. 71, pp. 27–33, Aug. 2021, doi: 10.1016/j.coi.2021.03.008.

[473] F. Sakurai, M. Tachibana, and H. Mizuguchi, "Adenovirus vector-based vaccine for infectious diseases," no. January, 2020.

[474] J. R. Teijaro and D. L. Farber, "COVID-19 vaccines: modes of immune activation and future challenges.," *Nat. Rev. Immunol.*, vol. 21, no. 4, pp. 195–197, Apr. 2021, doi: 10.1038/s41577-021-00526-x.

[475] B. D. Persson, D. M. Reiter, M. Marttila, Y.-F. Mei, J. M. Casasnovas, N. Arnberg, and T. Stehle, "Adenovirus type 11 binding alters the conformation of its receptor CD46," *Nat. Struct. Mol. Biol.*, vol. 14, no. 2, pp. 164–166, 2007, doi: 10.1038/nsmb1190.

[476] C. Karolina, M. Steffen, P. B. David, J. Marco, A. Niklas, and S. Thilo, "Structure of Adenovirus Type 21 Knob in Complex with CD46 Reveals Key Differences in Receptor Contacts among Species B Adenoviruses," *J. Virol.*, vol. 84, no. 7, pp. 3189–3200, Apr. 2010, doi: 10.1128/JVI.01964-09.

[477] J. S. Lee, S. Mukherjee, J. Y. Lee, A. Saha, J. Chodosh, D. F. Painter, and J. Rajaiya, "Entry of Epidemic Keratoconjunctivitis-Associated Human Adenovirus Type 37 in Human Corneal Epithelial Cells.," *Invest. Ophthalmol. Vis. Sci.*, vol. 61, no. 10, p. 50, Aug. 2020, doi: 10.1167/iovs.61.10.50.

[478] N. V Dhurandhar, L. D. Whigham, D. H. Abbott, N. J. Schultz-Darken, B. A. Israel, S. M. Bradley, J. W. Kemnitz, D. B. Allison, and R. L. Atkinson, "Human adenovirus Ad-36 promotes weight gain in male rhesus and marmoset monkeys.," *J. Nutr.*, vol. 132, no. 10, pp. 3155–3160, Oct. 2002, doi: 10.1093/jn/131.10.3155.

[479] P. Stanley, "Chinese hamster ovary cell mutants with multiple glycosylation defects for production of glycoproteins with minimal carbohydrate heterogeneity.," *Mol. Cell. Biol.*, vol. 9, no. 2, pp. 377–383, Feb. 1989, doi: 10.1128/mcb.9.2.377-383.1989.

E. Appendix

LIST OF TABLES AND FIGURES

Tables

Figures

AUTHOR AFFILIATIONS

Andreas Jenner	Garcia-Saez group, Institute for Genetics, CECAD Research center, University of Cologne, Cologne, Germany
Annkathrin Scheck	Institute for Immunology, Biomedical Center (BMC), Faculty of Medicine, LMU Munich, Munich, Germany
	Former: master student, Biochemistry, University of Tübingen, Tübingen, Germany
Boris Maček	Proteome Center Tübingen, University of Tübingen, Tübingen, Germany
Cengiz Koç	Department of Infection, Immunity and Cardiovascular Disease, University of Sheffield, Sheffield, United Kingdom
Christopher Reinkemeier	Platt group, Biologial Engineering, Department Biosystems Basel, ETH Zürich, Basel, Switzerland
	Former: Lemke group, Institute for Moleculare Physiology, Johannes Gutenberg-University, Mainz, Germany
Dirk Schwarzer	Interfaculty Institute of Biochemistry, University of Tübingen, Tübingen, Germany
Doron Rapaport	Interfaculty Institute of Biochemistry, University of Tübingen, Tübingen, Germany
Edward A. Lemke	Institute for Moleculare Physiology, Johannes Gutenberg-University, Mainz, Germany
Funmi Fagbadebo	Scientist, BioNTech SE, Munich, Germany
	Former: Rothbauer group, Pharmaceutical Biotechnology, University of Tübingen, Tübingen, Germany
Hsin-Yin Chang	Clinical Trial Coordinator, Thermo Fisher Scientific Taipei, Taipei City, Taiwan
	Former: master student, Biochemistry, University of Tübingen, Tübingen, Germany
Janani Natarjan	Alberti group, Biotechnology Center (BIOTEC), Technical University Dresden, Dresden, Germany
	Former: Rapaport group, Interfaculty Institute of Biochemistry, University of Tübingen, Tübingen, Germany
Julia Fitzgerald	Department of Neurodegeneration, Hertie Institute for Clinical Brain Research, University of Tübingen, Tübingen, Germany
Katarina Danskog	Arnberg group, Divison of Virology, Department of Clinical Microbiology, Umeå University, Umeå, Sweden
	Laboratory for Molecular Infection Medicine Sweden (MIMS) within the EMBL Nordic Partnership for Molecular Medicine, Umeå, Sweden

Katharina Hipp	Electron microscopy, Max-Planck-Institute for Biology, Tübingen, Germany
Katharina Zittlau	Proteome Center Tübingen, University of Tübingen, Tübingen, Germany
Katja Vonmetz	Stehle group, Interfaculty Institute of Biochemistry, University of Tübingen, Tübingen, Germany
Lars Frängsmyr	Arnberg group, Divison of Virology, Department of Clinical Microbiology, Umeå University, Umeå, Sweden
Leonard Jahnke	Master student, Molecular and Structural Biology, ETH Zürich, Zürich, Swiss
	Former: bachelor student, Biochemistry, University of Tübingen, Tübingen, Germany
Lisa Schwarz	Fitzgerald group, Department of Neurodegeneration, Hertie Institute for Clinical Brain Research, University of Tübingen, Tübingen, Germany
Michael Braun	Hartmann group, Interfaculty Institute of Biochemistry, University of Tübingen, Tübingen, Germany
	Former: Stehle group, Interfaculty Institute of Biochemistry, University of Tübingen, Tübingen, Germany
Niklas Arnberg	Division of Virology, Department of Clinical Microbiology, Umeå University, Umeå, Sweden
	Laboratory for Molecular Infection Medicine Sweden (MIMS) within the EMBL Nordic Partnership for Molecular Medicine, Umeå, Sweden
Ulrich Rothbauer	Pharmaceutical Biotechnology, University of Tübingen, Tübingen, Germany
	NMI Natural and Medical Sciences Institute, University of Tübingen, Reutlingen, Germany
Sophia Kieferle	Master student, Biochemistry, University of Tübingen, Tübingen, Germany
Sören Kirchgäßner	Schwarzer group, Interfaculty Institute of Biochemistry, University of Tübingen, Tübingen, Germany
Yannic Lurz	Schäffer group, Cellular Nanoscience, Center for Molecular Biology of Plants (ZMBP), University of Tübingen, Tübingen, Germany

PUBLICATIONS

Fagbadebo F. O., Kaiser P. D., Zittlau K., Bartlick N., Wagner T. R., Fröhlich T., Jarjour G., Nueske S., Scholz A., Tränkle B., Maček B., Rothbauer U., *A Nanobody-Based Toolset to Monitor and Modify the Mitochondrial GTPase Miro1,* Front Mol Biosci. 2022, 9:835302, doi: 10.3389/fmolb.2022.835302.

Author contribution as declared in the research article:

FF and UR conceived the study and analyzed the data. FF, PK, TW, BT, TF, and GJ performed all cellular and biochemical experiments including imaging studies. NB provided recombinant Miro1. SN and AS immunized the alpaca. KZ and BM performed and analyzed mass spectrometry experiments. FF and UR wrote the manuscript with the help of all authors.

Kirchgäßner S., Braun M., Bartlick N., Koç C., Reinkemeier C., Lemke A., Stehle T., Schwarzer D., *Synthesis, biochemical characterization and genetic encoding of a 1,2,4-triazole amino acid as acetyl-lysine mimic for bromodomains of the BET-family,* Angew Chem Int Ed Engl. 2022, online ahead of print, doi: 10.1002/anie.202215460.

SK and DS designed the study. SK synthesised ApmTri and ApmTri containing peptides. SK expressed BRD3(2) and BRD4(1) and SK and NB purified the proteins. SK performed all experiments for the biochemical characterisation of ApmTri peptides. MB, NB, CK and TS determined and analysed structures of bromodomains with ApmTri peptides. CR and LA genetically encoded ApmTri. SK and DS wrote the manuscript with the help of all authors.

MANUSCRIPT IN PREPARATION

Bartlick N., Scheck A., Stehle T., *A protocol for heterologous expression of the human mitochondrial GTPase Miro1,* Manuscript in preparation

NB and TS conceptualised the study. NB planned and performed the experiments. AS assisted with cloning and purified PD-related hMiro1 mutants. NB wrote the manuscript with the help of all authors.